

# Dry adhesive surfaces based on high density, high aspect ratio, hierarchical polymeric nano-structures

Ho, Audrey Yoke Yee

2012

Ho, A. Y. Y. (2012). Dry adhesive surfaces based on high density, high aspect ratio, hierarchical polymeric nano-structures. Doctoral thesis, Nanyang Technological University, Singapore.

<https://hdl.handle.net/10356/50670>

<https://doi.org/10.32657/10356/50670>

# Dry Adhesive Surfaces Based on High Density, High Aspect Ratio, Hierarchical Polymeric Nano- Structures

Audrey Ho Yoke Yee

School of Mechanical and Aerospace Engineering

A thesis submitted to the  
Nanyang Technological University in fulfillment of the  
requirement for the degree of Doctor of Philosophy

2012



# Abstract

Gecko's dry attachment system has been acknowledged to be the most efficient among all the biological attachment systems. This remarkable ability derives from the hierarchical and fibrillar structures on the gecko's foot which is composed of nearly 500,000 keratinous hairs called setae. Many attempts have been made to emulate the topographic features of the gecko feet to construct artificial dry adhesive tapes. However, many of the gecko inspired structures produced up to date consist of linear structures often made in soft polymers with relatively low density or low aspect ratio and typically have size in micron or sub micrometer range. Hitherto, the fabrication of hierarchical structures in nanometer range has not been accomplished, although theoretical studies predict an improvement on the shear adhesion properties of such mimetic structures.

Hence, in this thesis, a novel methodology has been developed to fabricate hierarchical gecko-inspired dry adhesives (adapting the topographical/geometrical features of gecko foot-hairs). The dry adhesives consisted of high density, high aspect ratio, hierarchical nano-pillars made on a stiff polymeric material. This is far superior than most of the produced hierarchical structures that are either in the micrometer range [1, 2], combination of micro- and nano-scale [3-5], low aspect ratio [3] or sparse packing structure density [1, 2].

In addition, the method is made using an inexpensive and direct approach to fabricate such molds easily as compared to sophisticated and expensive lithography and alignment tools as well as highly skilled personnel. The method developed is, the fabrication of multi-tiered branched porous anodic alumina (PAA) template using step-down voltage aluminium anodization process. The template consists of pores branching within pores. The key processing parameters to define the tiered porous structure are determined through systematically designed experiments.



Gecko inspired structures consisting of high density, high aspect ratio linear pillars and two tier hierarchical pillars are fabricated in polycarbonate (PC) and other thermoplastic polymers like poly(methyl methacrylate) (PMMA) by a capillary force mediated nano-imprinting. Till today, this process is the only methodology described that allows to fabricate the closest mimicking the topographical gecko toe pad features in a practical and low cost manner.

Numerically, the imprinting parameters for complete polymer filling, a numerical model were developed predicting the polymer pillar height. Both models take into consideration the surface tension effect, exacerbated by capillary flow in nano-scale, which hitherto, has not been taken into account in most literature. The experimental and simulation results compare well (~8.4 % difference), indicating that the model is useful to predict the attainable pillar structural dimensions.

Experimentally, hitherto, there is yet any conclusive evidence either on the advantages of hierarchical structure in aiding adhesion or any in-depth shear adhesion force characterizations. Hence, with rigorous and systematic analyses, the shear adhesion properties of the adhesive films prepared were characterized. From these analyses, it is put forth possible explanations to the two distinct phenomena observed. They are, 1) the shear adhesion force of the polymeric structured films increased progressively as the films were repeatedly tested, 2) the hierarchically-structured films of branched pillars indeed outperformed the linear pillars in experimental shear adhesion tests.

Rigorous characterization of the synthetic dry adhesives' shear adhesion performance are conducted in both the macro- and micro- scale regimes and a comprehensive understanding of the underlying shear adhesion mechanisms is presented. The experimental macro-scale shear adhesion tests indicate that the hierarchical pillared topography improves the shear adhesion force over the corresponding linear structure by 150 %. This is a result of a reduction in effective stiffness of hierarchical pillar structure which results in a more effective bending compared to the linear pillar structure. This rendered a better compliance of the hierarchical topography to a test surface, which in

turn resulted in a higher effective contact area. Consequently, as the effective contact area increased, the shear adhesion force followed.

Micro-scale shear adhesion studies are performed using a dynamic nano-mechanical probe. The tests serve to identify that there is a change in the dominance of friction mechanism from van der Waals attraction to Amontons' friction as the applied load increased.

Nano-indentation measurements are used to characterize the mechanical properties of the topographical surfaces. These include the hardness and elastic moduli as well as the deformation behavior of the polymer such as creep and recovery. In addition, using the load-penetration depth curves during the load holding period the buckling of the pillars is determined. The elastic modulus of the hierarchical pillars was found to be the lower ( $0.67 \pm 0.028$  GPa) in comparison to the linear pillars ( $1.34 \pm 0.098$  GPa) and the pristine PC film ( $3.31 \pm 0.123$  GPa).

The hydrophobic characteristics of the topography were measured. The hierarchical structure had contributed to an increase in hydrophobicity. This unique characteristic determines the self-cleaning and reusability properties of these synthetic dry adhesives.

Keywords: Gecko foot-hair, gecko adhesion, contact splitting, hierarchical structure, biological materials, nano-structured materials, surface energy, contact mechanics, shear adhesion.

# Acknowledgement

First and foremost, my deepest gratitude is to the support of Institute of Materials Research and Engineering (IMRE) of Agency for Science, Technology and Research (A\*STAR), and School of Mechanical and Aerospace Engineering (MAE) of Nanyang Technological University (NTU). The resources and facilities provided are gratefully acknowledged.

I am deeply indebted to ***Dr. Isabel Rodriguez***, my IMRE supervisor for giving me the freedom to explore the wonder of aluminum anodization. With her guidance we recognized the potential application of the multi-tiered branched porous anodic alumina templates for the fabrication of gecko mimetic adhesives. Her attention to details and constructive criticism has greatly contributed to the success of this work. She understands research is not always a bed of roses and that anything can go wrong will go wrong. Thus, when I have negative results, she would always suggest the next step to take. She is truly patient and good mentor and always gives words of encouragement. This has inspired me to not just be a good researcher but also a good mentor.

Equally important, my sincerest gratitude goes to ***Professor Lam Yee Cheong***, my supervisor in NTU who never fails to avail himself the moment I seek to meet him. He is the first person I turn to whenever I obtain unexpected and puzzling results and for discussions when I hit dead-ends. His many out-of-the-box suggestions have helped me solved many technical problems. He is a staunch advocator of the importance of having strong fundamental scientific knowledge and to conduct research with high research ethics and integrity. He constantly makes sure that I am on the right track. His call for rigorous experimentations has helped me to be a more systematic and better researcher. To help me advance this work, he has roped the expertise from his postdoctoral fellows and students to help me in various aspects of the theoretical work, without which, this work would never have completed. I hereby thank all his postdoctoral fellows;

particularly, ***Dr. Yeo Lip Pin*** and ***Dr. Chen Xing***, for their unconditional support and contributions to this thesis. My appreciation also goes to ***Dr. Wang ZhiYing***, ***Mr. Ling Siang Hooi*** and ***Mr. Tan Jun Liang***.

Many thanks to ***Dr. Gao Han*** for his generosity in allowing me to freely use his laboratory and consumables. Being an expert in template-assisted nanofabrication, he has offered many useful and practical advices regarding aluminum anodization process.

I would like to acknowledge my labmates ***Maria Chong***, ***Lee Kheng***, ***Wang Miao***, ***Thelese*** and ***Tanu*** for making my work in the laboratory a joy. I would also like to express my appreciations to ***Dr. Julian Chia*** and ***Dr. Lim Chee Tiong*** for all the useful discussions.

I would like to express my utmost gratitude to IMRE's SERC nano Fabrication, Processing and Characterisation (SnFPC) staffs ***Mr. Augustine Cheong***, ***Ms Shen Lu***, ***Ms Jane Wang***, ***Ms Tan Sze Yu*** for all the characterization equipment trainings, preparation of samples, the use of equipment, technical support and interpretation of results. Not to miss out are all my colleagues in IMRE, for their friendships have directly and indirectly helped me throughout this project; ***Wee Yang***, ***Alicia***, ***Bee Keen***, ***Hui Kim***, ***Phoi Chin***, ***XiaoSong***, and ***Nancy***.

Words cannot express my deepest gratitude to my family, my mother, ***Looi Yew Bee***, and my sisters ***Angie*** and ***Junie Ho*** for being so patient and supportive throughout all these years. They understood that I could not go home as much as I would love to and that I am guilty of neglecting them. Not forgetting the family's pet dog, ***Jacob*** for being who he is, cute little entertaining being. Seeing him relieves stress from work.

Last but not least, my utmost gratitude goes to my husband ***Soong Kar Seng*** for his unconditional love, understanding, continuous emotional and financial support, and encouragement much needed for this journey and our future journey. This piece of work is dedicated to him.

# Table of Contents

<b>Table of Contents.....</b>	<b>vi</b>
<b>List of Figures .....</b>	<b>xi</b>
<b>List of Tables .....</b>	<b>xix</b>
<b>List of Symbols .....</b>	<b>xxi</b>
 <b>Chapter 1     Introduction.....</b>	 <b>1</b>
1.1    Biomimetic-Based Dry Adhesives.....	1
1.1.1    Low Attachment Force (Preload) and Detachment Force .....	4
1.1.2    Material Independence.....	4
1.1.3    Anti-fouling / self-cleaning.....	4
1.1.4    Non-sticky by default state .....	5
1.1.5    Anti self-matting / adhering .....	5
1.2    Gecko – Inspired Dry Adhesives .....	5
1.3    Research Objective .....	7
1.4    Thesis Scope .....	7
1.5    Thesis Outline .....	8
 <b>Chapter 2     Literature Review .....</b>	 <b>11</b>
2.1    Overview.....	11
2.2    Current Fabrication Approaches for Developing Gecko Mimetic Adhesives .....	14
2.2.1    Materials Used .....	15
2.2.2    Processing Approaches .....	16
2.2.3    Approaches to Various Shapes and Morphologies .....	19
2.2.4    Mold Materials.....	26
2.3    Design Requirements for Gecko Mimetic Adhesives.....	27

2.3.1	Material Properties .....	27
2.3.2	Geometrical parameters – Individual Contact .....	28
2.3.3	Surface Morphology – Array Density.....	31
2.4	Potential Fabrication Techniques.....	31
2.4.1	Nano-imprinting Technique.....	31
2.4.2	Multi-Tiered Porous Anodic Alumina .....	33
2.5	Summary .....	33
<b>Chapter 3</b>	<b>Mold Fabrication using Porous Anodic Alumina (PAA) .....</b>	<b>35</b>
3.1	Introduction.....	35
3.2	Overview of Porous Anodic Alumina (PAA) Hole Arrays as Templates .....	37
3.3	Mechanism of Linear PAA Formation and Self-Ordering .....	38
3.4	Fabrication of Multi-Tiered Branched PAA .....	40
3.4.1	Fabrication of Two-Tiered Branched PAA on Aluminum Sheet .....	44
3.4.2	Fabrication of Three-Tiered Branched PAA on Al-on-Si Substrate.....	45
3.4.3	Fabrication of Ordered Two-Tiered Branched PAA on Aluminum Sheet ..	46
3.5	Parametric Study on the Processing Conditions of PAA.....	49
3.5.1	Interpore Distance of Sub-Pores Within ( $d_w$ ) <i>versus</i> Between ( $d_b$ ) Preceding Pores.....	54
3.5.2	Interpore Distance of Sub-Pores <i>versus</i> 2 <sup>nd</sup> – Tier Anodizing Voltage .....	58
3.5.3	Number of Sub-Pores <i>versus</i> 2 <sup>nd</sup> – Tier Anodizing Voltage.....	60
3.5.4	Anodizing Duration <i>versus</i> 2 <sup>nd</sup> Tier Anodizing Voltage .....	61
3.5.5	Effect of Electrolyte on the Formation of Sub-Pores.....	63
3.6	Wetting Properties of PAA .....	65
3.7	Summary .....	66
<b>Chapter 4</b>	<b>Polymer Characterizations .....</b>	<b>69</b>
4.1	Overview.....	69
4.2	Polycarbonate (PC) .....	70

4.3	Gel Permeation Chromatography (GPC) .....	71
4.4	Dynamic Mechanical Thermal Analysis (DMTA) .....	73
4.5	Summary .....	89
<b>Chapter 5</b>	<b>Polymer Flow Modeling during Nano-Imprinting .....</b>	<b>91</b>
5.1	Overview .....	91
5.2	Evidence of Capillary Effect.....	93
5.3	Experimental Details.....	95
5.4	Flow Analysis of an Amorphous Polymer in Nano-imprinting.....	99
5.4.1	Physical description .....	100
5.4.2	Mathematical formulation.....	101
5.4.3	Verification of Flow Model .....	118
5.4.4	Effects of Material Flow Properties on Pillar Height .....	119
5.4.5	Parametric Studies on Polymer Pillar Height .....	122
5.5	Summary .....	126
<b>Chapter 6</b>	<b>Fabrication of Gecko-Inspired Dry Adhesives.....</b>	<b>129</b>
6.1	Overview .....	129
6.2	Fabrication of High-Aspect-Ratio (HAR) Polymeric Pillars.....	130
6.3	Fabrication of Polymeric Hierarchical Nano-structure.....	134
6.4	Nano-imprint Processing Conditions for Hierarchical Nano-Structure.....	137
6.5	Challenges for Achieving High Aspect Ratio Polymeric Pillars .....	141
6.5.1	Polymer Relaxation.....	141
6.5.2	Demolding of Patterned Polymeric Pillars .....	148
6.5.3	Density of Patterned Polymeric Pillars .....	150
6.6	Summary .....	152
<b>Chapter 7</b>	<b>Macro-Scale Shear Adhesion Force Analysis of Gecko-Inspired Dry Adhesives.....</b>	<b>155</b>

7.1	Overview .....	155
7.2	Mechanisms of Gecko Adhesion .....	156
7.3	Frictional Adhesion in Gecko Attachment System.....	157
7.4	Morphology of Test Substrates .....	159
7.5	Shear Adhesion Analysis .....	160
7.5.1	Preliminary Shear Adhesion Force Measurements .....	160
7.6	Quantitative Adhesive Force Measurements .....	168
7.6.1	Shear Adhesion Testing Setup .....	168
7.6.2	Shear Adhesion Force in Repetitive Measurements .....	174
7.6.3	Shear Adhesion Force versus Applied Preloads .....	176
7.6.4	Shear Adhesion Force versus Area of Residual Deformation .....	182
7.6.5	Shear Adhesion Force per unit Area versus Preloads .....	184
7.6.6	Resolving Shear Adhesion Force into Components .....	187
7.6.7	Contact Angle Study .....	190
7.7	Summary .....	191
<b>Chapter 8</b>	<b>Micro –scale Shear Adhesion Force Analysis of Gecko-Inspired Dry Adhesives .....</b>	<b>193</b>
8.1	Overview .....	193
8.2	Micro-scale Shear Adhesion Force Measurements.....	195
8.2.1	Sample Preparation .....	197
8.2.2	Experimental Procedure.....	199
8.2.3	Results.....	202
8.3	Nano-indentation.....	211
8.4	Summary .....	219
<b>Chapter 9</b>	<b>Conclusions and Future Work.....</b>	<b>223</b>
9.1	Conclusions.....	223
9.2	Future Work .....	227



<b>Appendix A .....</b>	<b>229</b>
<b>Appendix B .....</b>	<b>231</b>
<b>Appendix C .....</b>	<b>233</b>
<b>Appendix D .....</b>	<b>241</b>
<b>Appendix E .....</b>	<b>243</b>
<b>List of Publications .....</b>	<b>245</b>
<b>References .....</b>	<b>247</b>

# List of Figures

**Figure 2.1.** a) Malaysian House gecko/ House lizard or scientifically named, *Hemidactylus frenatus*. Also locally known as *chicak* (pr: chee chuck; said quickly) derived onomatopoeically from the sounds they make [54]. The gecko is attached to an inverted ceiling (rough). b) *Gekko* gecko is adhering on a single toe to a vertical glass slide (smooth) and gradually overturned for measuring the angle at which the gecko toe detach [53]. ..... 11

**Figure 2.2.** a) *Gekko* gecko looking bottom-up [20], b) a gecko foot [20] and c) a gecko toe [34]. Each toe contains hundreds of thousands of setae and each seta contains hundreds of spatulae (SP). d) and e) Scanning electron microscopy (SEM) micrographs of two (at different magnifications) of the setae (ST) [20] and f) single stalk of hierarchically branched seta [20] and g) the terminal elements (TE), and spatulae. .... 13

**Figure 2.3.** Schematics of unconventional fabrication methods for synthetic dry adhesives a) electrically induced polymeric organo-rods [77] b) PDMS with embedded vertically-aligned Carbon Nano-tubes (VACNTs) [76] c) colloidal lithography [66] d) “rigiflex” lithography [4]. ..... 18

**Figure 2.4.** Schematics of fabrication methods for obtaining micro-structures with different shapes and orientation a) spatulate-tips [42] b) SU-8 polymeric high aspect ratio angled nano-pillars [33] c) directional polymer stalks [22]. ..... 21

**Figure 2.5.** SEM images of structures with various shapes and orientations a and b) spatulate tips [42, 64] c) angled micro-fibrils [33] d) directional polymer stalks [22]... 21

**Figure 2.6.** Schematics of fabrication methods for obtaining different shapes, orientation and hierarchical structures a) hierarchical micro- and nano-structures using “rigiflex” lithography [3] b) hierarchical micro-structures using SU-8 as mold [1] c) hierarchical micro-structure with spatulate-tips using dip-transfer technique [2] d) hierarchical micro- and nano-structures using PAA template [50]. ..... 25

**Figure 2.7.** SEM images of the terminal structures fabricated in polymers a) flat tips, b) spherical tips, c) symmetric spatulae, d) asymmetric spatulae, e) concave tubes, f) concave tips [89]. ..... 31

**Figure 3.1.** SEM micrograph of a) top and b) cross-sectional view of alumina nano-hole array [102]. ..... 37

**Figure 3.2.** Migration of  $\text{Al}^{3+}$  and  $\text{O}^{2-}$  through the metal/oxide interface and oxide/electrolyte interface respectively. .... 39

<b>Figure 3.3.</b> Set up apparatus for control production of porous alumina a) schematic of the experimental setup, b) actual experimental setup c) close-up of the electrolytic bath. ....	41
<b>Figure 3.4.</b> Schematic of the steps involved in the fabrication of 3-tiered branched NPAA. a) and b) 1 <sup>st</sup> Tier - First tier anodization pores and thinning of barrier layer step. c) and d) 2 <sup>nd</sup> Tier – Formation of sub-pores at reduced potential followed by barrier layer thinning. e) and f) 3 <sup>rd</sup> Tier – Formation of third tiered pores at further reduced anodizing potential completed by barrier layer thinning. ....	43
<b>Figure 3.5.</b> Schematic of the Masuda’s two-step anodizing method to obtain ordered porous template [101]. ....	47
<b>Figure 3.6.</b> a) Plane and b) side views of a two-tiered branched PAA, c) plane and d) side views of a three-tiered branched PAA, e) top view of ordered two-tiered branched PAA employing Masuda’s method of two-step anodization. ....	48
<b>Figure 3.7.</b> SEM images of cross-sectioned single-tier PAA on Al-on-Si substrate. a) Barrier layer thickness of samples for Set A $183 \pm 7.5$ nm. b) Samples for Set B with barrier layer thinned to $115 \pm 5$ nm using 5 wt % $H_3PO_4$ at room temperature. ....	51
<b>Figure 3.8.</b> SEM images of the experimental results based on Design of Experiment on the formation of sub-pores under the respectively conditions. a) 0.15 M Oxalic acid; 80 V; BL- $183 \pm 7.5$ nm b) 0.3 M Oxalic acid; 80 V; BL- $183 \pm 7.5$ nm c) 0.15 M Oxalic acid; 100 V; BL- $183 \pm 7.5$ nm e) 0.15M Oxalic acid; 80V; BL- $115 \pm 5$ nm f) 0.3 M Oxalic acid; 80 V; BL- $115 \pm 5$ nm g) 0.15M Oxalic acid; 100 V; BL- $115 \pm 5$ nm. ....	53
<b>Figure 3.9.</b> a) Schematic b) SEM micrograph illustrating the center-to-center interpore distance of sub-pores located between different preceding pores, $d_b$ and the interpore distance of sub-pores within its preceding pores, $d_w$ ....	55
<b>Figure 3.10.</b> T-distribution curve ....	57
<b>Figure 3.11.</b> Relationship of ratio of sub-pores’ interpore distance to anodizing voltage ( $d_w/V_a$ ) for 2 <sup>nd</sup> tier anodization with its respective voltage ratio. Goodness of fit, $R^2$ is shown in the figure and error bar indicates one standard deviation. ....	59
<b>Figure 3.12.</b> Number of sub-pores versus its respective 2 <sup>nd</sup> tier voltage ratio. Goodness of fit, $R^2$ is as shown in the figure and error bar indicates one standard deviation. ....	61
<b>Figure 3.13.</b> Anodizing duration vs. 2 <sup>nd</sup> tier anodizing voltage for the formation of sub-pores through barrier layer thickness of $115 \pm 5$ nm. Y- values of 0.02 are only approximate. Equation of fit for Y (vertical axis) versus X (horizontal axis, i.e. Anodizing Voltage) and goodness of fit, $R^2$ for each curve are shown in the figure. Error bar indicates one standard deviation. ....	63

<b>Figure 3.14.</b> PAA films subjected to a second tier anodization at 100 V using two different electrolytes. a) 0.15 M C <sub>2</sub> H <sub>2</sub> O <sub>4</sub> and b) 0.3 M H <sub>3</sub> PO <sub>4</sub> . Both were pore widened for 45 min. 1st-tier anodization was previously performed at 130 V using 0.3 M H <sub>3</sub> PO <sub>4</sub> for 30 min.....	64
<b>Figure 3.15.</b> Contact angles of water on a) aluminum-on-Si; b) single tier PAA on Si substrate; and c) shallow two-tiered PAA on Si substrate.....	66
<b>Figure 4.1.</b> Chemical structure of polycarbonate [142]. .....	70
<b>Figure 4.2.</b> Chromatogram of PC (Peak 1) and a side product (Peak 2).....	72
<b>Figure 4.3.</b> a) Typical SRF fixture in a CTD [145] b) schematic of clamp and sample dimension.....	74
<b>Figure 4.4.</b> Complex modulus versus temperature at constant frequency of 10 rad/s and 50 rad/s.....	76
<b>Figure 4.5.</b> Storage and loss modulus versus temperature at constant frequency of 10 rads <sup>-1</sup> and 50 rads <sup>-1</sup> .....	77
<b>Figure 4.6.</b> a) storage modulus b) loss modulus c) complex modulus and d) complex viscosity with respect to angular frequency.....	81
<b>Figure 4.7.</b> Master curve of complex modulus at 145 °C reference temperature for polycarbonate depicting the experimental and fitted curves.....	83
<b>Figure 4.8.</b> Fitting curves of viscosity at temperature 165°C according to Power-law model.....	85
<b>Figure 4.9.</b> A Generalized Maxwell Model. ....	88
<b>Figure 5.1.</b> Atomic force micrograph (AFM) images of the imprint performed at a) 165°C and b) 175°C respectively and subsequently demolded by wet-etching. The profiles of the imprinted feature obtained at c) 165°C and d) 175°C respectively. ....	94
<b>Figure 5.2.</b> SEM image of the commercial PAA mold used for imprinting experiments. The specifications of the PAA mold are – thickness of the membrane: 60 μm, pore density: 10.7 x 10 <sup>6</sup> pores/mm <sup>2</sup> , pore wall thickness: 80.4 ± 33.34 nm, average pore diameter: 271.4 ± 23.3 nm. ....	95
<b>Figure 5.3.</b> Schematic of the nano-imprint process for pillar height measurement. ....	97
<b>Figure 5.4.</b> a) Temperature and pressure profiles during imprint. b) Temperature profile during cooling (inset showing initial 5 min of the cooling profile).....	98

<b>Figure 5.5.</b> SEM image of cross-sectioned PC imprinted at 165 °C under pressure of 1 MPa for 150 s for pillars' heights measurements. ....	98
<b>Figure 5.6.</b> a) SEM image and b) schematic of axisymmetric unit cell as sub-domain on a PAA mold. ....	100
<b>Figure 5.7</b> Model domain, parameters and coordinate system used in theoretical simulation.....	103
<b>Figure 5.8.</b> Schematic of load and temperature profiles. ....	107
<b>Figure 5.9.</b> Comparison of pillar height achieved with and without capped effect. ....	109
<b>Figure 5.10.</b> Control volume and finite difference grid [174] .....	116
<b>Figure 5.11.</b> Comparison between experimental and predicted results with and without capillary force (surface tension).....	119
<b>Figure 5.12.</b> Pillar height evolution for three different values of material constants $m = 10$ Pa.s, 100 Pa.s and 1000 Pa.s .....	120
<b>Figure 5.13.</b> Viscosity, $\log \eta$ versus shear rate, $\log \dot{\gamma}$ [175]. ....	120
<b>Figure 5.14.</b> Pillar height evolution for three different values of surface tension $\sigma = 1.e-4$ N/mm, 1.e-5 N/mm and 1.e-6 N/mm. ....	121
<b>Figure 5.15.</b> Numerical simulation of pillar height profile at various imprint temperature. Imprint pressure and duration are kept constant at 1 MPa and 300s respectively. ....	123
<b>Figure 5.16.</b> Numerical simulation of pillar height profile at various imprint pressures. Imprint temperature and duration are kept constant at 165 °C and 300s respectively. ..	124
<b>Figure 5.17.</b> Numerical simulation of pillar height profile at various imprint duration. Imprint temperature and imprint pressure are kept constant at 165 °C and 1 MPa respectively.....	125
<b>Figure 6.1.</b> Linear PAA templates a), cross-sectional view b) top view and c) SEM image of the PAA template.....	131
<b>Figure 6.2.</b> Fabrication process of linear polymeric topographic structures.....	133
<b>Figure 6.3.</b> Multi-tiered PAA templates a), cross-sectional view b) top view and c) SEM image of the PAA template.....	135
<b>Figure 6.4.</b> Fabrication process of hierarchically branched polymeric topographic structures. ....	136

**Figure 6.5.** SEM images of imprinted hierarchically branched pillared substrates. a) Four branches (Insert shows magnified view of pillars). The base pillars' dimensions are  $280 \pm 20$  nm in diameter with aspect ratio of 8-10, and a diameter and aspect ratio of  $90 \pm 10$  nm and 5-6 respectively for the top pillars. b) Five branches. The dimensions of the hierarchical pillars are  $280 \pm 20$  nm and  $6.5 \pm 0.5$   $\mu$ m for the diameter and height of the base pillars respectively; and a diameter and aspect ratio of  $110 \pm 10$  nm and 5-6 respectively for the top pillars..... 137

**Figure 6.6.** Schematic of Poisson's ratio effect a) in tension and b) in compressive stress. .... 145

**Figure 6.7.** Schematic of PC pillar a) under tension after imprint with PAA mold still intact, b) relaxed after the removal of PAA mold by wet-etching and c) SEM image of pillar after mold removal by wet-etching..... 146

**Figure 6.8.** SEM images showing a) oblique view and b) planar view of the bunched pillars..... 149

**Figure 6.9.** SEM image a) peel-off of high aspect ratio PC pillars with a broader base, b) fibrillar attachment system of a beetle (*Hemisphaerota cyanea*) showing its broad bases [18]..... 150

**Figure 6.10.** SEM images of a) planar view and b) cross-sectional view of random AAO template, c) imprinted polymer using random AAO template, d) planar view and e) cross-sectional view of ordered AAO template, f) patterned polymer with ordered AAO template..... 151

**Figure 7.1.** SEM images of shear adhesion test substrates a) pristine PC, b) linear pillars and c) hierarchical pillars imprinted on PC. .... 160

**Figure 7.2 .** a) Polycarbonate (PC) nano-pillars sample (left) and unstructured PC sample (right) each being glued to a 5 cents coin were placed onto an ethanol cleaned glass-slide with the nano-pillars facing the glass-slide, b) Glass-slide was tilted and the coin with PC nano-pillars remain adhered to the glass-slide while the unstructured PC slipped off. .... 162

**Figure 7.3.** Preliminary shear adhesion force tests. a) linear pillared tape sliding off at  $64^\circ$  tilt c) hierarchical pillared tape still remaining on the glass slide at  $90^\circ$  tilt..... 163

**Figure 7.4** a) Schematic of coin on glass-slide being tilted, b) free body diagram of the forces acting on the tape c) closed diagram to calculate shear adhesion friction force,  $F_{Sad}$  ..... 164

**Figure 7.5.** Plot of  $(\frac{F_{Sad}}{L_N})$  vs.  $(\frac{1}{L_N})$ ..... 167

**Figure 7.6.** a) Schematic and b) actual shear adhesion force measurement setup. .... 169

**Figure 7.7.** Shear adhesion force versus the extension curve for the test conducted using preload of 45 mN ..... 170

**Figure 7.8.** Stitched images of adhesive tapes taken with optical microscope. a) control images (prior to shear adhesion test). b) images taken after a typical shear force measurement. The light contrast differences between a) and b) corresponds to contact area of pillars with the glass slide. Images of a) and b) were analyzed using image processing software (ImageJ, v1.41o) and are shown in c) and d) respectively..... 173

**Figure 7.9** Shear adhesion force of branched, linear pillars and pristine polycarbonate with repeated measurements using same preload of 30 mN..... 175

**Figure 7.10.** a) SEM image depicting the plastically deformed hierarchical pillars after a shear adhesion measurement. Circles highlight some of the side contacts of the pillars. b) Schematic illustration of pillars conditioning for consecutive shear adhesion measurements..... 176

**Figure 7.11** a) Shear adhesion force as a function of preload for branch and linear pillars, b) Area of residual deformation (effective contact area after the removal of preload) of pillars against glass slide as a function of preload. .... 178

**Figure 7.12.** Illustration of the I for a) linear and b) hierarchical pillar respectively. ... 181

**Figure 7.13.** Illustration of the effective contact area of the a) linear pillar and b) hierarchical pillar respectively..... 181

**Figure 7.14.** SEM images of samples after shear adhesive tests were performed a) linear pillars and b) branched pillars. More branched pillars bent in the direction of shear indicating more area of contact..... 182

**Figure 7.15.** Shear adhesion force of hierarchical and linear pillars as a function of area of residual deformation. .... 183

**Figure 7.16.** Shear adhesion force per unit effective contact area of hierarchical and linear pillars versus preload. .... 185

**Figure 7.17.** Various plots of  $\frac{F_{Sad}}{A}$  versus  $\frac{L_N}{A}$ . Fitting equations depicting  $Y = mX + C$

where  $Y = \frac{F_{Sad}}{A}$ ,  $X = \frac{L_N}{A}$ ,  $m$  = slope of curve,  $\mu$  and  $C$  = intercept at Y-axis,  $S_c$ . The adjusted  $R^2$  values for fitted equations are as shown. .... 189

**Figure 7.18.** Water contact angles and corresponding SEM images of a) pristine polycarbonate b) linear polycarbonate pillars, and c) hierarchical polycarbonate pillars. .... 191

**Figure 8.1.** a) and b) Images of tipless AFM cantilevers..... 195

**Figure 8.2.** Image of Nano Indenter® XP (MTS, Nano Instruments Innovation Center, USA). .... 197

**Figure 8.3.** Images of a) samples glued to holder and subsequently secured into the sample tray, b) sample tray loaded into the equipment. .... 198

**Figure 8.4.** 10  $\mu$ N load on a) linear pillars and b) hierarchical pillars against representative slide distance ..... 200

**Figure 8.5.** a) SEM images of a series of slides made by varying the applied loads, b) trail made by 2 mN normal load during sliding depicting the profiling and actual measurement section, bi) close-up of the profiling section, bii) close-up of the actual measurement section depicting the plastically deformed pillars. .... 201

**Figure 8.6.** Ratio of shear adhesion force to applied normal load ( $\frac{F_{Sad}}{L_N}$ ) of linear pillars and hierarchical pillars as a function of representative slide distance with respect to its applied normal loads a) 10 $\mu$ N, b) 25 $\mu$ N, c) 50 $\mu$ N, d) 100  $\mu$ N, e) 250  $\mu$ N, f) 500  $\mu$ N, g) 1 mN and h) 2 mN. Each set of data represents average value of three measurements. ... 205

**Figure 8.7.** Averaged ratio  $\frac{F_{Sad}}{L_N}$  for linear pillars and hierarchical pillars with its respective applied normal loads during sliding. Each set of data is an average value of three measurements. Inset a) shows the close-up values of friction coefficients for 250  $\mu$ N, 500  $\mu$ N, 1 mN and 2 mN. Error bars indicate one standard deviation. .... 207

**Figure 8.8.** Sketch of two contacting surfaces separated by a sub-monolayer of mobile atoms [222]. .... 208

**Figure 8.9.** Displacement into surface for linear pillars and hierarchical pillars with its respective applied normal loads during sliding. Each set of data is an average value of three measurements. Error bars indicate one standard deviation..... 210

**Figure 8.10.** Area of contact between indenter and pillars a) prior to loading b) upon loading [223]. .... 210

**Figure 8.11.** Image of a typical Berkovich tip used for nano-indentation tests [225]. .. 211

**Figure 8.12.** Schematic of indentation process illustrating penetration depth  $h_p$  [226].212



<b>Figure 8.13.</b> Load-displacement curve of pristine PC obtained with MTS Nano-indenter. ....	213
<b>Figure 8.14.</b> a) SEM image of some indentations performed on linear pillars. Five indentations were performed on each load. B) Close-up image of one of the indentations. ....	214
<b>Figure 8.15.</b> Overall penetration depths of the respective applied loads (100 $\mu$ N, 250 $\mu$ N, 1 mN and 2.5 mN) for pristine PC, linear pillars and hierarchical pillars. ....	215
<b>Figure 8.16.</b> Penetration depth for pristine PC, linear pillars and hierarchical pillars with applied normal load of 1 mN during indentation. Each set of data is an average value of five measurements. ....	217
<b>Figure 9.1.</b> Variations of samples according to the types of effects to be studied.....	228

# List of Tables

<b>Table 2.1.</b> Dimensions of the adhesion structures at each level of hierarchy [34].....	14
<b>Table 2.2.</b> Parameters influencing adhesion performance of split-contacts on surfaces [83].....	27
<b>Table 3.1.</b> Factors and “high” and “low” levels chosen.....	50
<b>Table 3.2.</b> List of full factorial $2^k$ “Design of Experiment” with a total of eight test combinations ( $2^3$ permutations). “Positive” response denotes successful formation of sub-pores and negative otherwise. Breakdown denotes the substrate that was burnt due to localized Joule heating.....	52
<b>Table 3.3.</b> Interpore distance of sub-pores between ( $d_b$ ) and within ( $d_w$ ) preceding pores with respective $t$ -values. Results from the statistical hypothesis $t$ -tests show that the two measures of interpore distances are significantly different.....	56
<b>Table 4.1.</b> $M_w$ and $M_n$ of commercial grade polycarbonate (Lexan).....	72
<b>Table 4.2.</b> Values of constants, ( $C_1$ and $C_2$ ) and shift factors, $a_T$ at each temperature with respect to the reference temperature. ....	82
<b>Table 4.3.</b> Summary of equations for relaxation modulus $G'$ (storage modulus) and $G''$ (loss modulus) by relaxation time $\lambda_i$ and weight factors $g_i$ . ....	86
<b>Table 4.4.</b> Values calculated for the stiffness ( $G_i$ ) and Prony coefficients ( $\lambda_i$ and $g_i$ ) of the respective Maxwell element.....	88
<b>Table 5.1.</b> Imprint parameters and pillar heights. Standard deviations are shown. ....	99
<b>Table 6.1.</b> Processing conditions to obtain various linear pillar heights of polycarbonate. ....	138
<b>Table 6.2.</b> Processing conditions for the fabrication of tiered branched polymer pillars in various polymeric materials. ....	140
<b>Table 6.3.</b> Average diameter of imprinted polymeric pillars after 1) mechanical force demolding and 2) mechanical force demolding coupled with immersion into chemical etching solution. ....	142

<b>Table 6.4.</b> Imprint parameters with the respective diameter (top, mid and bottom) of the pillars obtained. Standard deviations are shown. PAA pore diameters are approximately 270 nm .....	143
<b>Table 6.5.</b> Imprint parameters with holding pressure and its respective diameter of the pillars. Standard deviations are shown.....	147
<b>Table 7.1.</b> Data from adhesive friction measurements and calculated adhesive friction force for hierarchical pillars.....	165
<b>Table 7.2.</b> Summary of shear adhesion forces for reported natural gecko foot-hair and fabricated hierarchical structures .....	187
<b>Table 8.1.</b> Elastic modulus of pristine PC, linear pillars and hierarchical pillars at various applied loads. ....	218

# List of Symbols

$E$	Young's modulus
$F'_c$	total pull-off force
$R$	radius of terminal elements/contact points
$n$	number of sub-contacts
$P$	applied compressive preload
$R$	radius of the indenting sphere
$\delta$	indentation depth
$V_{i+1}$	successive step anodization voltage
$V_i$	preceeding anodization voltage
$k$	number of factors
$d_b$	to-center interpore distance of sub-pores between their preceding pores
$d_w$	Center-to-center interpore distance of sub-pores within their preceding pores
$\overline{d_b}$	mean of $d_b$
$\overline{d_w}$	mean of $d_w$
$S_d$	standard deviation of the difference between each pair ( $d_{bi} - d_{wi}$ )
$n$	number of measurements
$t\text{-stat}$	value of two-sample paired $t$ -test
$t_{crit}$	critical value of $t - stat$
$H_0$	Null hypothesis
$H_1$	Alternative hypothesis
$D_{int}$	center-to-center interpore distance for linear pores
$k$	proportionality constant
$V_a$	second tier anodization voltage
$\theta$	water contact angles
$T_g$	transition temperature
$T_m$	melting temperature
$M_w$	average molecular weight
$ G^* $	complex modulus
$G'$	storage modulus
$G''$	loss modulus
$\eta^*$	complex viscosity
$\omega$	frequency of oscillation
$m$	flow consistency index
$n$	power-law index
$\sigma$	surface tension
$\lambda_i$	relaxation time
$g_i$	weight factors

$Kn$	Kundsen number
$p$	fluid phase hydrostatic pressure
$I$	identity tensor
$\eta$	viscosity of fluid
$E$	local rate of strain
$B$	Material constant
$T_b$	Material constant
$\tau^*$	Material constant
$\eta_0$	Newtonian viscosity at zero shear-rate
$\dot{\gamma}$	shear rate
$S_E$	total energy
$S_0$	surface energy stored
$F_s$	equivalent capillary force
$\Delta p_{la}$	pressure drop across the liquid-air interface
$\gamma_a$	surface tension force between the liquid and air
$\bar{\tau}$	extra stress tensor
$\bar{u}$	velocity field
$S^{(l)}$	flow conductance
$D_{ik}^{(l)}$	coefficient of the nodal pressure to the net flow in element
$f_{ij}$	fill factor
$V_i$	control volume
$\Delta V_{ij}$	filled volume
$\nu$	Poisson's ratio
$F_f$	friction (lateral) force
$\mu$	coefficient of friction
$L_N$	normal applied load
$F_{Sad}$	shear adhesion force
$L_0$	the “internal” load
$A$	area of contact
$S_c$	shear strength
$\Delta\gamma$	adhesion energy hysteresis
$\varepsilon$	factor accounting for the less-than-full transfer of energy
$\delta$	atomic gap between the two contacting surfaces
	slipping angles
$M$	bending moment
$I$	moment of inertia
$\kappa$	curvature
$EI$	flexural rigidity
$D$	diameter of the pillar

# Chapter 1 Introduction

## 1.1 Biomimetic-Based Dry Adhesives

Adhesives play an important role in our everyday lives for bonding or joining a wide variety of materials (i.e. thin films, dissimilar materials, complex assemblies) both in light-weight [6] or heavy-weight applications [7]. Adhesives can be used either for permanent or detachable applications. Drying adhesives, contact adhesives and hot adhesives are usually used for permanent applications while dry adhesives such as pressure sensitive adhesives and biomimetic-based dry adhesives are for detachable applications.

One of the most widely used adhesives is pressure-sensitive adhesives (PSA) where pressure is applied to adhere the adhesive to the adherend. It is made of soft unstructured planar layer with stiffness modulus of  $< 10$  MPa. It is known as low-tack adhesives as it appears to be sticky when touched [8]. One classic example is the re-adherable or repositionable adhesive/glue used on Post-It® Notes. It is made of acrylate copolymer microspheres, an elastomeric material, therefore, inherently sticky [9]. The tacky microspheres provide pressure-sensitive adhesiveness which has a low degree of adhesion permitting separation, repositioning and rebonding to the adhered objects. During each adherence, the microspheres limit the amount of surface area contact between the adhesive and the substrate [10]. However, it exhibits a very low film or

tensile strength which is approximately less than 70 kPa. In addition, the main issue of these adhesives is fouling [11-13] of the surface after use. In addition, at microscopic level, this type of adhesives leaves a residue.

Hence, biomimetic-based dry adhesives, through the study of biological attachment systems (particularly of the smaller animals) are garnering much interest due to their self-cleaning ability which enables repeated usage with negligible wear [14]. This is made feasible by means of mechanical contact and not by chemical bonding [15].

Biomimetic-based dry adhesives are best exemplified by the gecko toe-pads. As pointed out by Arzt et al., the larger (mass) the creature, the smaller but denser the number of the terminal attachment elements are [16, 17]. Therefore, a gecko, being the heaviest animal that uses a *hairy* attachment system is most studied in dry adhesion [18]. In addition, *Gekko* gecko which is the largest species of its kind naturally garnered the most attention. These creatures have been nicknamed the *professional climbers* [19].

A gecko's superb ability to adhere to most surfaces is attributed to the adhesive mechanism on their toe pads based on cumulative van der Waals interactions [20] achieved through contact-splitting of setae [16]. This is achieved by the large attachment area of approximately  $220 \text{ mm}^2$  of *hierarchical* and *fibrillar* structures on their feet [21]. These two features, when combined, provide the necessary compliance to the gecko toe-pad to effectively engage a high percentage of the spatulae, at each step, to all kinds of surface topographies [22].

One of the first applications emerged from geckos' adhesive research is in robotics application, the wall climbing robots. These wall climbing robots are mainly aimed for inspection in nuclear reactors [23, 24] or any other facilities that are perilous for human beings.

In 2007, a project named as Nano-Attach Project [25] was launched. The objective was to explore the feasibility of synthetic dry adhesives mimicking gecko foot-hair to replace the current assembly process using the traditional solder adhesive. Gecko-inspired dry adhesives would enable lead-free and low temperature (room temperature) processing as well as more environmental-friendly assembly.

Gecko-inspired synthetic adhesives have recently found their niche in biomedical applications as bandages [26, 27] where the researchers have fabricated adhesives sufficiently stiff and strong enough to withstand even the beating of heart. Hence, there is a huge potential of medical applications for these adhesives.

The characteristics of the gecko foot-hairs such as the hierarchical and fibrillar structure made up of stiff material known as  $\beta$ -keratin [28] and angled foot-hairs [22] provide functional and unique properties to gecko attachment system. Autumn identified several benchmark functional properties of gecko's adhesive system [14] derived exclusively from the topographic features of the gecko's foot. They are summarized in the following sub-sections.



### **1.1.1 Low Attachment Force (Preload) and Detachment Force**

Autumn's record of gecko's detachment force being only  $0.3 \mu\text{N}/\text{seta}$  ( $0.15 \text{ Ncm}^{-2}$ ) which is quite negligible compared to the achieved  $20 \mu\text{N}/\text{seta}$  ( $10 \text{ Ncm}^{-2}$ ) [20]. Such low detachment force is crucial to facilitate geckos' fast mobility. Geckos achieve a large shear adhesive force to stay on the walls but yet low enough attachment and detachment forces for quick and easy mobility.

### **1.1.2 Material Independence**

Geckos are known to have the ability to stick to virtually any material with a wide variety of different surface types at different orientations, albeit smooth or rough, vertically or overhanging, hydrophobic and hydrophilic surfaces [29], and under any environmental condition i.e., varied humidity [30-32], and vacuum [33].

### **1.1.3 Anti-fouling / self-cleaning**

Another unique characteristics derived from its fibrillar and hierarchical structures is the ability of geckos to retain its adhesiveness in between its molting cycles (shedding of the superficial layer of epidermal cells) [34]. Russell, in many of his studies on live geckos [35-38] observed that the feet of geckos captured in nature are usually clean.

### **1.1.4 Non-sticky by default state**

Observations reveal that geckos do not leave any residue marks behind its track. This is likely due to its material composition which is  $\beta$ -keratin, a stiff material with high elastic / Young's modulus ( $E \sim 1\text{-}15$  GPa). As such, if a finger is placed against a gecko toe-pad, it does not feel sticky.

### **1.1.5 Anti self-matting / adhering**

It is noteworthy that yet another interesting property is exhibited through the features displayed. With the right material, structures and geometries, gecko toe pads are not only self-cleaning and non-sticky, but it is also anti self-matting / adhering [14, 39]. From the many observations made, none has revealed matting phenomenon on the adjacent setal stalks and adhesion of arrays of gecko toe pads [40].

## **1.2 Gecko – Inspired Dry Adhesives**

Hence, the basic features of the gecko-inspired dry adhesive should meet the following criteria [22]:

- 1) High aspect ratio micrometer (1:10-30) and nanometer (1:20-50) scale hierarchical structures fabricated with diameters of 3-10  $\mu\text{m}$  and 50-500 nm respectively.
- 2) Material properties of synthetic hairs: Young's modulus between 1-15 GPa, hydrophobic and high tensile strength.

- 3) Maximize micro/nano-hair density (number of hairs in a given area) to increase the split contact effect for higher adhesion.

One of the first fabrication technique employed to mimic gecko foot-hairs was serial processing by nano-indentation of wax using atomic force microscope (AFM) tips as mold for polymer casting [39]. Other popular fabrication approaches are soft-molding of elastomeric polymers [41], infiltration of liquid polymer [42, 43], direct drawing of polymer fibers [44, 45] on various microfabricated templates such as silicon wafer [46, 47], photoresist-on-silicon [43], elastomeric [41] and polymeric molds. Microfabrication techniques such as optical lithography and etching processes are usually employed in the making of the molds. Expensive techniques such as electron-beam lithography have also been attempted for the fabrication of molds to produce micro-sized biomimetic polyimide foot-hairs [47].

The most common employed mold material is silicon (Si) due to its high rigidity for the preservation of the fine features and its ability to be reused several times without obvious degradation [48]. However, the drawback of using Si is the extremely high cost to produce high aspect ratio molds. Casting of polymers onto porous anodic alumina (PAA) has been attempted [39, 49, 50]. However, results reported from these methods were not quite satisfactory as the pillars produced tend to clump together.

Although various fabrication techniques have been employed to produce gecko mimetic adhesives, there has yet to be any reports on the fabricated structures fulfilling all these criteria stated in the earlier Section 1.2. In addition, most of these methods require expensive and time-consuming lithography techniques.

Hitherto only linear polypropylene (stiff polymer) fibrils fabricated by molding in polycarbonate templates have shown high adhesion values of approximately  $25 \text{ N/cm}^2$  for a preload of  $16.5 \text{ N/cm}^2$  [51]. However these types of structures still face problems with matting and clumping of the fibers.

### **1.3 Research Objective**

The main motivation of this investigation is to fabricate gecko inspired dry adhesives with improved performance by replicating as close as possible the topographic features in the gecko toe pads consisting of hierarchical, high density and high aspect ratio micro to nano-pillars. These adhesives should have self-cleaning property and reusability.

### **1.4 Thesis Scope**

The scope of the thesis comprises of three parts. The first part is to develop a simple and cost-effective mold fabrication technique which allows fast polymer replication through nano-imprinting.

The second part is to understand the capillary effects on the filling process of a cylindrical nano-cavity during the nano-imprint process. For this purpose, investigations were conducted with single tier nano-pores/nano-pillars. Hitherto, most of the polymer flow studies performed to-date for hot embossing process are on micrometer scale [1-10]. In such a length scale, surface tension or capillary effect has not been considered as it is

negligible. However, in nano-scale mold filling, capillary effect is one of the most important factors. Existing numerical models for nano-imprinting have not considered capillary effects.

The final part of the scope is to characterize the performance of the fabricated gecko inspired multi-tiered dry adhesives. The characterization is performed by shear adhesion force measurements in the macro- and micro- scales in order to determine the advantages of hierarchical structure versus linear structure dry adhesives, and to have an understanding of the underlying shear adhesion mechanism.

## **1.5 Thesis Outline**

Chapter 1 gives a brief introduction to the background of bio-mimetic dry adhesives, research motivation and objectives of the thesis.

Chapter 2 provides a comprehensive review of the dry adhesive, mechanisms of gecko adhesion, fabrication methods for gecko-inspired dry adhesives and characterizations of synthetic gecko-inspired adhesives.

Chapter 3 describes the controlled fabrication of self-assembled mold template, specifically hierarchically branched porous anodic alumina (PAA). Using the Design of Experiment (DoE) methodology, the relationship between the barrier layer thicknesses, anodizing duration and anodizing voltage were systematically investigated.

Chapter 4 performs material characterizations on the imprint material to obtain the necessary parameters for use in the formulated simulation model as discussed in Chapter 5.

Chapter 5 presents an analytical and numerical model to predict the role of capillary effects on the filling process of a cylindrical nano-cavity during the nano-imprint process. In verifying the model, nano-imprinting experiments using commercial nano-porous PAA membranes are employed.

Chapter 6 elucidates the experimental method to fabricate gecko-mimicking hierarchical topography of high-density, high-aspect ratio branched nano-pillars on a stiff polymer, combining the use of multi-tiered PAA template and capillary force assisted nano-imprinting. Demolding of the mold by wet-etching instead of peel-off is employed to characterize the recovery phenomenon observed on the pillars. It also discusses the two main challenges faced in the nano-imprinting process and how they were overcome.

Chapter 7 presents the macro-scale shear adhesion force analysis of the fabricated branched pillars adhesive as compared to the linear pillars adhesive and pristine polycarbonate (PC) film. A systematic analysis was performed to understand the two phenomena observed: 1) the progressively increasing shear adhesion forces as the samples were being repeatedly tested; 2) the 150 % improvement in the shear adhesion force of the hierarchical topography of branched pillars over the linear pillars.

Chapter 8 presents the quantitative frictional analyses in the micro – scale for the fabricated branched pillars adhesive. In this investigation, the branched pillars

adhesive was compared to linear pillars adhesive and pristine PC film. In addition, nano-indentations were performed to obtain the mechanical behavior of the adhesive such as effective stiffness on the surface of the adhesive, buckling of the pillars, creep and plastic deformations.

Chapter 9 summarizes the research work performed as well as provides recommendations for future work.

# Chapter 2 Literature Review

## 2.1 Overview

Gecko's dry attachment system has been acknowledged to be the most efficient among all the biological attachment systems. It can repeatedly adhere and detach itself to all kinds of surface topographies [22] at an approximate velocity of  $77 \text{ cm s}^{-1}$  (or 15 body lengths per second) by attaching and detaching its feet in approximately 5 ms and 15 ms respectively [52].

Figure 2.1a illustrates the impressive attachment of the Malaysian House gecko/ House lizard on an inverted and rough house ceiling. Figure 2.1b shows a Gekko gecko adhering on a single toe to a vertical glass slide (smooth) and gradually overturned for measuring the angle at which the gecko toe detach [53].

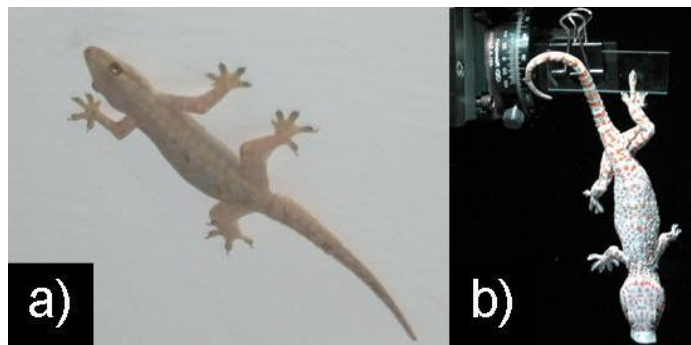


**Figure 2.1.** a) Malaysian House gecko/ House lizard or scientifically named, *Hemidactylus frenatus*. Also locally known as *chicak* (pr: chee chuck; said quickly) derived onomatopoeically from the sounds they make [54]. The gecko is attached to an inverted ceiling (rough). b) *Gekko* gecko is adhering on a single toe



to a vertical glass slide (smooth) and gradually overturned for measuring the angle at which the gecko toe detach [53].

Gecko is the heaviest animal that uses a *hairy* attachment system [18] whereby the terminal elements of its toe pads are split into thousands of self-similar structures to increase contact points. This is also known as *contact-splitting* whereby the total pull-off force,  $F'_c$  is increased by splitting up the contact into  $n$  sub-contacts (Eq. 2.1), each with radius  $R/\sqrt{n}$  [16].

$$F'_c = \sqrt{n} \cdot F_c \quad (\text{Eq. 2.1})$$

Through these finer contacts, the small asperities and minute distances between the contacting surfaces can be reached. The usually less prominent van der Waals attractions now act collectively [55] to be the main adhesion mechanism [20].

Figure 2.2 illustrates the detailed attachment system of *Gekko* gecko from the foot to its terminal elements. It can be seen that the attachment area is greatly enhanced by the *hierarchical* and *fibrillar* structures on their feet [21]. These two features, when combined, provide the necessary compliance to the gecko toe-pad to effectively engage a high percentage of the spatulae, at each step, to all kinds of surface topographies.

The fibrils begin with a lamellae with branches on 20 rows of setal arrays that are 1-2 mm in length [56] and each array consisting of thousands of primary setal stalks commonly known as setae [57]. They are typically 30-130  $\mu\text{m}$  in length and 5-10  $\mu\text{m}$  in diameter [56]. Schleich et al. [58] and Autumn et al. [59] approximated there are 14, 400 setae/ $\text{mm}^2$ , which is roughly 800, 000 setae per toe. It then branches out into secondary

setae that are about 20-30  $\mu\text{m}$  in length and 1-2  $\mu\text{m}$  in diameter. At the end of each secondary seta, 100-1,000 spatulae (being the look-alike to a spatula) with a diameter of 100-200 nm branch out and form the points of contact with the surface. The tips of the spatulae are approximately 500 nm in length, 200-300 nm in width [56], and 10 nm in thickness [60].

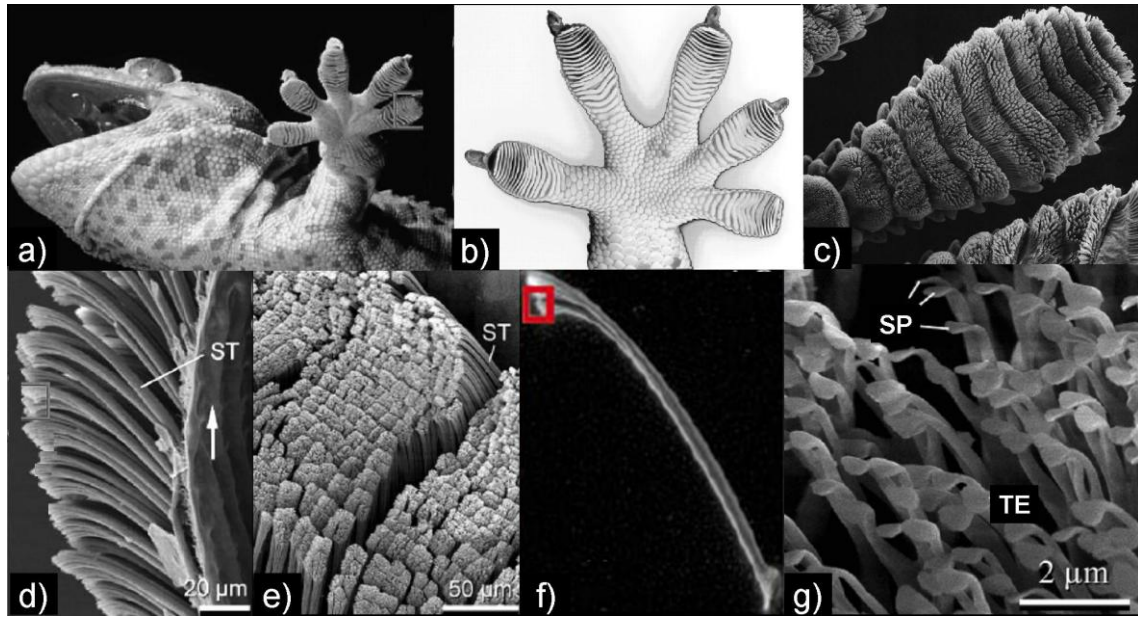


**Figure 2.2.** a) *Gekko gecko* looking bottom-up [20], b) a gecko foot [20] and c) a gecko toe [34]. Each toe contains hundreds of thousands of setae and each seta contains hundreds of spatulae (SP). d) and e) Scanning electron microscopy (SEM) micrographs of two (at different magnifications) of the setae (ST) [20] and f) single stalk of hierarchically branched seta [20] and g) the terminal elements (TE), and spatulae.

Table 2.1 lists the dimensions of the adhesion structures of each level of hierarchy. Referring to the table, the aspect ratio of each level is approximately 30. Without hierarchical structures, linear  $\beta$ -keratin setae would have to have a length of 160  $\mu\text{m}$  (AR 100-160) to have the same compliance and adhesion to a surface [14]. This would certainly cause the fibrils to bunch. Pillars bunching is undesirable as it reduces

contact points as well as increasing the stiffness of the fibrils thereby less compliance [39] . This demonstrates that the hierarchical structure confers additional and necessary mechanical stability to the gecko adhesive toe pads.

**Table 2.1.** Dimensions of the adhesion structures at each level of hierarchy [34].

	Name	Diameter	Height	Aspect Ratio
Level 1	Lamella	-	1-2 mm	-
Level 2	Seta	5-10 $\mu\text{m}$	30-130 $\mu\text{m}$	6-26 $\mu\text{m}$
Level 3	Branched Seta	1-2 $\mu\text{m}$	20-30 $\mu\text{m}$	10-30 $\mu\text{m}$
End of Level 3	Spatula	Width	Length	Thickness
		200 -300 nm	500 nm	10 nm

## 2.2 Current Fabrication Approaches for Developing Gecko Mimetic Adhesives

With the many promising applications for gecko-inspired dry adhesives as well as to gain a good understanding of the properties and characteristics of gecko foot-hairs, many research groups have delved into the fabrication of synthetic gecko-inspired dry adhesives. Wide varieties of materials, fabrication techniques as well as mold materials have been employed.

### 2.2.1 Materials Used

A wide range of elastomeric and polymeric materials have been tested; from low stiffness ( $E < 100$  MPa) to high stiffness ( $E > 1$  GPa). Generally, the lower stiffness materials used include silicone rubber [39], polyurethane (PU) [22, 33, 42, 48] and polydimethylsiloxane (PDMS) [46, 48, 61, 62].

Specialty polymers such as poly(vinylsiloxane) (PVS), an elastomer used in dentistry as impression material [63, 64] and most recently, conducting polymers such as polythiophene (PT) [65] as well as biodegradable and biocompatible poly (glycerol sebacate acrylate) (PGSA) [27] have also been explored. High stiffness materials; i.e., polyester (PE) [39], parylene [66], polyimide (PI) [39, 47, 67], epoxy [48, 67], poly(methyl methacrylate) (PMMA) [4, 50] and polypropylene (PP) [51] have also been tried.

Non-polymeric materials such as carbon nanotubes (CNTs) with  $E > 1$  GPa have provided very impressive surface adhesion [6, 68]. Yurdumakan et al. [69] fabricated multi-walled carbon nanotubes embedded in PMMA which has adhesion force (measured with atomic force microscope) 200 times higher than the natural gecko foot-hairs. In addition to strong adhesion force, Zhao et al. [70] constructed vertically aligned carbon nanotube surfaces whose adhesion and shear strength were in the same order of magnitude of a gecko foot. More recently, Ge et al. [6] demonstrated that patterned carbon nanotube surfaces could support shear loads of  $36 \text{ N/cm}^2$  which is four times as much as a natural gecko foot [71]. However, CNTs are not bio-compatible material and thus, not suitable for biomedical applications [72-74]. Moreover, CNTs is an expensive

material and hence not practical for large area applications. The materials that can potentially be employed in gecko-like adhesion are fabrication process and mechanical stability dependent.

## **2.2.2 Processing Approaches**

### **1) Nano-indentation and Nano-molding Techniques**

Fabrication of gecko mimetic adhesive started out with serial processing of nano-indentation of wax using AFM tips, with the wax subsequently acted as a mold for polymer casting [39]. Other popular fabrication approaches are soft-molding of elastomeric polymers [41], infiltration of liquid polymer [42, 43], direct drawing of polymer fibers [44, 45] on various microfabricated templates such as silicon wafer [46, 47], photoresist-on-silicon [43], elastomeric [41] and polymeric molds.

There are also reports of more unconventional fabrication methods. These include electrically-induced polymeric organo-rods by applying a bias between the sample coated with photoresist and plasma in the inductively coupled plasma (ICP) reactive ion etcher [75] (Figure 2.3a), and microfabrication involving embedding of multi-wall carbon nano-tubes (MWCNTs) into polymers [69, 76] (Figure 2.3b).

### **2) Colloidal Lithography**

Kustandi et al. [66] reported a novel approach combining colloidal lithography, silicon etching, and nano-molding. They successfully deposited parylene using vapor

deposition technique in a vacuum chamber yielding high aspect ratio (of 10) nano-fibrillar structured on flexible polymeric surfaces (Figure 2.3c).

### 3) **“Rigiflex Lithography”**

Jeong et al. [4] created high aspect ratio polymeric nano-structures using various capillary-driven “rigiflex” lithographic methods (Figure 2.3d). This method encompasses imprinting by soft lithography. This is to address the limitation of nano-imprint lithography in fabricating high aspect ratio structures due to the rigidity of silicon molds and the limited resolution of PDMS molds in creating sub-100 nm nano-structures due to its low stiffness.

An ultra-violet (UV)-curable polyurethane acrylate (PUA) was employed as mold and PMMA as the filling material. The Young’s modulus of this material is ~40 MPa which is higher than PDMS (~1.8 MPa) but lower than silicon molds of more than 100 GPa. The slight flexibility of the material allows easy removal of the nano-structures from the mold enabling it to achieve very high aspect ratio (~20) nano-fibrils.

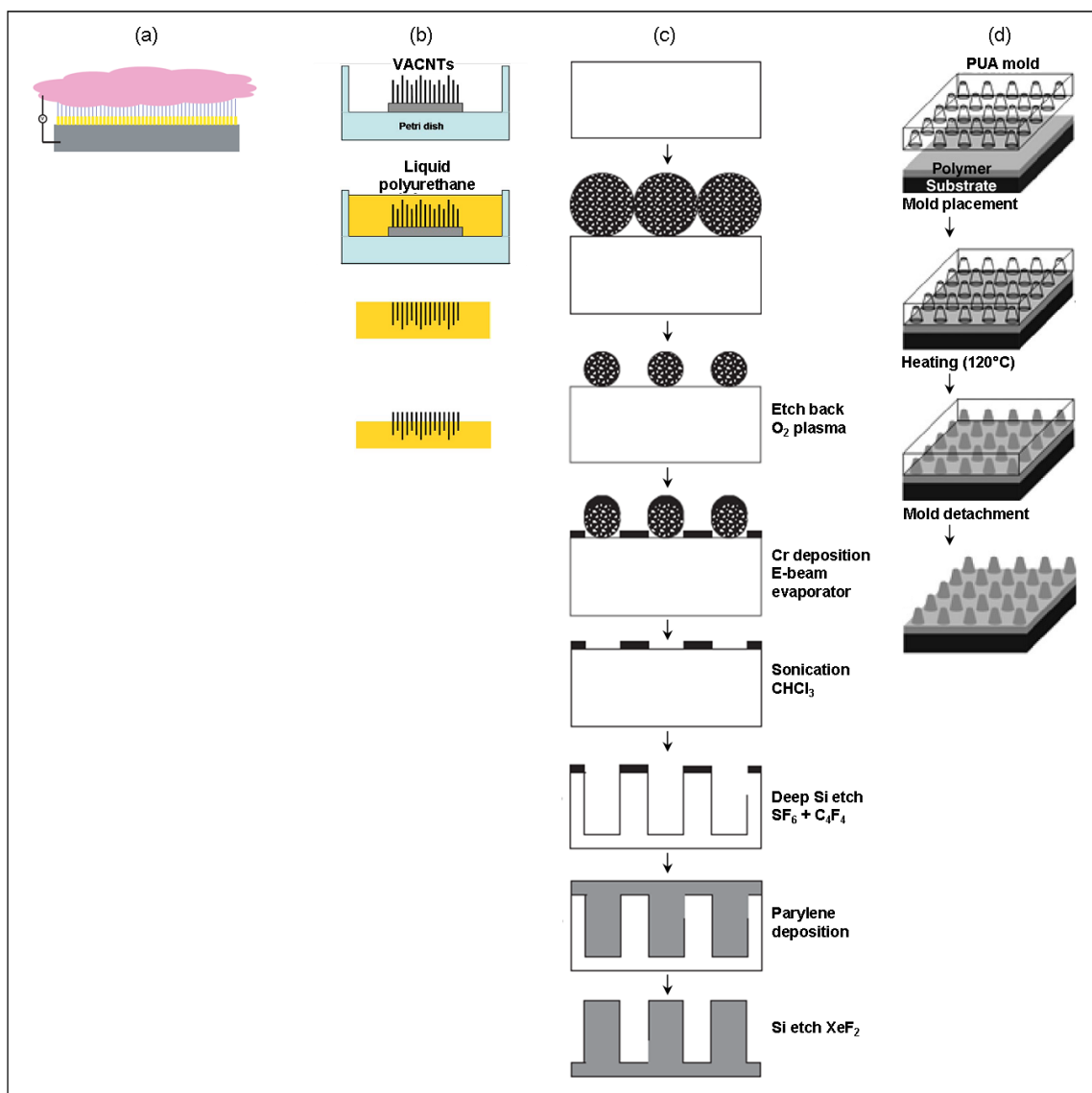


**Figure 2.3.** Schematics of unconventional fabrication methods for synthetic dry adhesives a) electrically induced polymeric organo-rods [77] b) PDMS with embedded vertically-aligned Carbon Nano-tubes (VACNTs) [76] c) colloidal lithography [66] d) “rigiflex” lithography [4].

### **2.2.3 Approaches to Various Shapes and Morphologies**

Numerous fabrication approaches, materials and geometries have been investigated to emulate the terminals of gecko foot-hairs. This is because the dimensions (fibril radius, aspect ratio and pitch) and shapes affect the adhesion properties of the fabricated nano-structures. More in-depth discussion on the effect of these factors will be provided in Section 2.3.2. In this section, discussion will be limited to the fabrication approaches and geometries obtained.

#### **1) Spatulate Tips**

Since a gecko foot hair has a spatula-shaped end, it was predicted that such shape would perform better than the spherical or flat tip. Kim et al. [42] devised a fabrication method to emulate the end of the physical gecko seta. The method was based on optical lithography and numerous etching. The schematic diagram in Figure 2.4a illustrates the fabrication steps involved. However, the drawback of this fabrication method is its complexity and requirement for costly fabrication tools. Although the structures obtained showed high adhesion forces of  $18 \text{ N/cm}^2$ , these structures also required high preloads of  $12 \text{ N/cm}^2$ . In addition, Gorb et al. [64] had also fabricated spatula-shaped end which he termed as mushroom-shaped fibrillar by casting of polyvinylsiloxane (PVS).



## 2) **Angled Fibrils and Directional Tips**

Attempts have also been made to match the directional orientation of actual gecko foot-hair in the hope that it will increase the contact area of the tips and facilitate the removal from a surface [33]. The angled micro-fibrils were fabricated using conventional optical lithography but varying the UV exposure angle by tilting the wafer during exposure (Figure 2.4b). The UV exposure angle has to be calculated to obtain the desired fibril angle by using Snell's law. An obvious advantage of this method is that the tip shape is flat and roughly parallel to the substrate thereby potentially increasing the contact area of the tips when brought to contact with a surface. The drawbacks of this method are that the UV diffraction and the SU-8 properties limit the resolution to approximately 2  $\mu\text{m}$  for high aspect ratio structures, and the reproducibility fabrication of the features is challenging. Yao et al. [78] created tilted film-terminated fibrillar surfaces on a spherical glass lens using conventional drilling on Teflon mold. Adhesion testings showed significant directional detachment and sliding resistance. Aksak et al. [23] have also reported fiber tip modifications to obtain angled spatula tips (Figure 2.4c). Figure 2.5 depicts the SEM images of the respective fabricated fibrils.

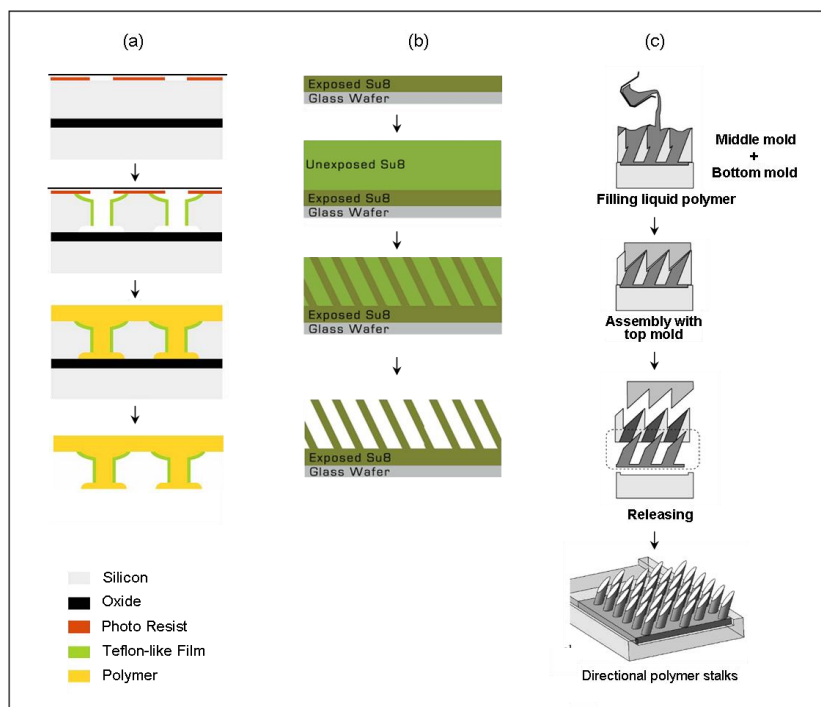


**Figure 2.4.** Schematics of fabrication methods for obtaining micro-structures with different shapes and orientation a) spatulate-tips [42] b) SU-8 polymeric high aspect ratio angled nano-pillars [33] c) directional polymer stalks [22].

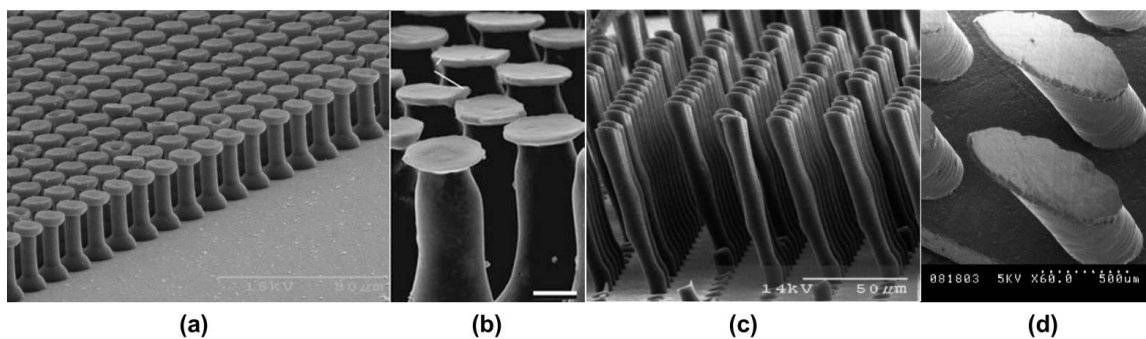


**Figure 2.5.** SEM images of structures with various shapes and orientations a and b) spatulate tips [42, 64] c) angled micro-fibrils [33] d) directional polymer stalks [22].

### 3) Hierarchical Terminals

Another feature of the gecko's foot hair researchers have tried to emulate is the hierarchical structure. This is the feature that provides the gecko's toe pad with the compliance and at the same time, sufficient mechanical stability needed for strong adhesion to a variety of terrains as well as self-cleaning properties. Such endeavor has been met only with a limited degree of success.

Gao *et al.* [19] have theoretically shown that the theoretical van der Waals adhesion strength between surfaces can be reached by having a hierarchical structure. This is further asserted when Kim *et al.* [79] showed in numerical modeling, that a hierarchical structure enables geckos with the adaptability to have a large effective area of contact with a rough surface. He also showed that a three-level hierarchical structure has an equivalent stiffness that is approximately 40 % lower than a one-level linear structure. This resulted in an enhancement in adhesion energy of more than 100 % [80].

In one approach, low aspect ratio hierarchical structures are produced first by sequential application of "rigiflex" lithography using a low-resolution PDMS mold to obtain the microstructures. Subsequently, a high resolution nano-patterned PUA mold was applied on top of the pre-formed polymer microstructures to mold the finer fibrils [3, 4]. The process is shown schematically in Figure 2.6a-i and the scanning electron microscope (SEM) image of the structure produced is shown in Figure 2.6a-ii.

Northen and Turner [75, 81] proposed multi-scale integrated compliant structures (MICS) by the standard lithography and multiple etch process.

Later, Greiner et al. [1] fabricated hierarchical gecko-like adhesives by sequential coating and exposing SU-8 by standard photolithography (Figure 2.6b-i). PDMS was used as the molding polymer. The diameter and height of the base pillars are 50  $\mu\text{m}$  and 200  $\mu\text{m}$  respectively. The top fibrils had a diameter of 5  $\mu\text{m}$  and heights ranging from 2.5 to 10  $\mu\text{m}$  as shown in Figure 2.6b-ii. Surprisingly, the pull-off test showed lower pull-off forces by an order of magnitude for these hierarchical structures. This was postulated to be due to the lower packing density of the hierarchical structure when compared to a linear structure.

Most recently, Murphy et al. [2] have developed modifications in micron-scale to the tips of the fiber arrays including the hierarchical spatula tips. They combined standard micro-molding technique to fabricate the base level fibrils and dip-transfer technique for the finer fibrils, see Figure 2.6c-i. This dip-transfer technique is to transfer the liquid polyurethane into the spatulate-tipped silicon molds [42] where curing of the polymer takes place. Etching of the silicon molds will reveal the terminal fibrils. Mean adhesion force of approximately 600 mN for a preload of 360 mN was reported. The two-level hierarchical structure has higher adhesion in comparison to the linear structures. The reason given was that the hierarchical structure enabled the reduction of the effective modulus of the material. This was inferred to lead to an increase in the contact area with the hemispherical indenter. Soft polymers (elastic modulus of 3 – 19.8 MPa) were typically used in these investigations. The SEM image of the structure produced is shown in Figure 2.6c-ii.

Another creative method of producing hierarchical structures engaged by Kustandi et al. [50] was by exploiting the parallel wafer-scale processing of conventional lithography and anisotropic chemical etching of the thick film of anodic alumina pores. The finer fibrils were acquired by bringing together the micro- and nano-porous alumina membranes into intimate contact and depositing a desired material into the pores (Figure 2.6d-i)

Kustandi *et al.*[50] reported the use of a stiff polymer (PMMA) to fabricate hierarchical structures by sequentially using two porous alumina templates. However, the densely packed pillars on the fabricated films were observed to have bunched. Consequently, accurate adhesion force of these structures could not be determined. Figure 2.6d-ii depicts the SEM image of the fabricated hierarchical fibrils.

Jeong *et al.*[5] fabricated a hierarchical structure with base-pillars of 5  $\mu\text{m}$  diameter with an aspect ratio of 5. The top pillars are slanted (with flat ends) with diameter and height of 600 nm and 3  $\mu\text{m}$  respectively. It was then compared with a slanted linear structure with the dimensions of the top pillars, in shear adhesion tests against a flat surface. Again, considerably lower shear adhesion was recorded for the hierarchical structure ( $\approx 9 \text{ N/cm}^2$ ) as opposed to the slanted linear structure ( $\approx 21 \text{ N/cm}^2$ ). These studies, with several structural variations however, were inconclusive in proving the advantages of a hierarchical structure. The above-mentioned background serves as a motivation for this present work.

Although much effort has been spent to mimic the gecko adhesive system, most of the methods produced hierarchical structures in the micrometer range [1, 2],

combination of micro- and nano-scale [3-5], low aspect ratio [3] or sparse packing structure density [1, 2]. Typically, sophisticated and expensive lithography and alignment tools are required and highly skilled personnel are needed for successful fabrication. Moreover, the current state of art is still unable to match the superb characteristics of the natural gecko's toe pad. Hitherto, there have yet to be any report that satisfies all the benchmarks set by Autumn et al. [14].

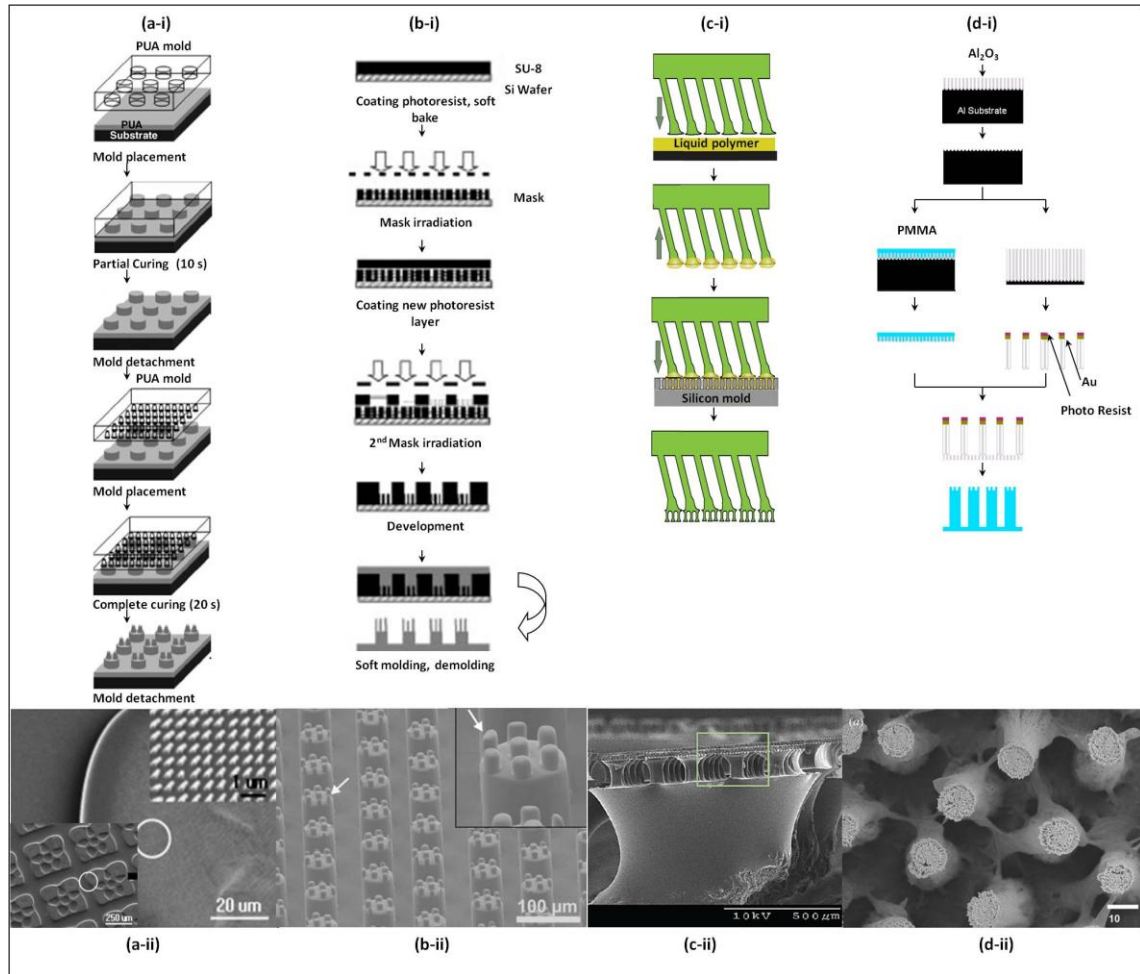


**Figure 2.6.** Schematics of fabrication methods for obtaining different shapes, orientation and hierarchical structures a) hierarchical micro- and nano-structures using “rigiflex” lithography [3] b) hierarchical micro-structures using SU-8 as mold [1] c) hierarchical micro-structure with spatulate-tips using dip-transfer technique [2] d) hierarchical micro- and nano-structures using PAA template [50].

#### 2.2.4 Mold Materials

Microfabrication techniques such as optical lithography and etching processes are usually employed in the making of the molds. There are other possibilities, for example, Geim et al. used electron-beam lithography and plasma etching to fabricate molds to produce micro-sized biomimetic polyimide foot-hairs [47]. However, this technique using e-beam is not only expensive but limited to very small areas.

The most commonly used mold material is silicon (Si) due to its high rigidity for the preservation of the fine features and its ability to be reused several times without obvious degradation [48]. However, the drawback of using Si is the extremely high cost to produce high aspect ratio molds.

Porous anodic alumina (PAA) membranes as mold material have also been employed by Sitti et al. [39] under vacuum condition. Other attempts of using nanoporous anodic alumina was carried out by Cho et al. [49] using h-PDMS. Low aspect ratio (~ 2 times) pillars were formed. This could be due to the low modulus of h-PDMS which being too soft and collapses under its own weight. Kustandi et al. [50] using PAA produced high aspect ratio PMMA pillars (~ 10 times). However, as the PAA in this work was removed by wet-etching and the pillars bunched due to capillary forces as the etchant was evaporated. Moreover, adhesion tests were not conducted to measure the effectiveness of the fabricated structures as dry adhesives.

Track-etched polycarbonate membranes [82] have been used to produce high-aspect ratio polymeric pillars that have shown impressive adhesion properties. However,

the pillars are linear structures and the true potential of hierarchical gecko foot-hairs has not been exploited.

## 2.3 Design Requirements for Gecko Mimetic Adhesives

To emulate gecko's attachment system, the synthetic adhesive tape must match closely the material properties and the surface morphology of a gecko toe pad. These parameters are shown in Table 2.2.

**Table 2.2.** Parameters influencing adhesion performance of split-contacts on surfaces [83].

Material Properties	Surface Morphology	
	Individual Contact	Array
Young's Modulus	Contact radius	Number of contacts
Tensile Strength	Contact shape	Density of contacts
Surface energy (Hydrophobicity)	Aspect ratio	Array Symmetry
Angle of orientation		

### 2.3.1 Material Properties

The material properties exhibited by  $\beta$ -keratin, which is a hard polymer with high stiffness  $E = 1\text{-}15$  GPa, seem counter-intuitive for good adhesion. This means that it is not tacky and would not be able to comply with surfaces as required for a good adhesive. However, if it were to have the same tacky properties as common adhesives, it



would not allow a low detachment force, the ability of self-cleaning, and reusability without any significant degradation. This is because soft sticky polymers have high surface energy and therefore easily accumulate dirt in the environment and are difficult to clean. They wear off quickly and would stick to each other, creating bunch. To reduce bunching, soft polymer fiber spacing has to be increased, which reduces density. However, a lower density fiber array compromises the overall adhesion.

The structural built-up was essential in compensating the shortcomings of conventional pressure-sensitive adhesives. Sitti et al. [39] gave a good analogy with a soft mattress made from hard material such as steel can still exhibit softness and compliance if it is fabricated in an array of coiled springs.

Hence, the required material properties to fabricate synthetically mimic gecko tapes are hard materials with high stiffness (at least in the same order of magnitude as  $\beta$ -keratin) for durability, with high tensile strength to dissipate the stored elastic energy during detachment and with low surface energy to remain clean.

### **2.3.2 Geometrical parameters – Individual Contact**

A good guide, which is summarized in this section, on the various geometrical parameters on adhesion force might be gained from the studies by Eduard Arzt's group of Max Planck Institut für Metallforschung. They had provided in-depth studies on the effects of geometry of an individual fibril on adhesion force. The geometrical parameters studied theoretical and experimentally include the effects of 1) fibril's radius [84], 2)

aspect ratio [84] and 3) its contact shape [85]. The adhesion force was measured as the pull-off force of the custom-made nano-indenter.

#### **1) Fibril's radius**

Varying the fibril's radius systematically, Greiner et al. [84] had shown that a decrease in the fibril radius causes a significant increase in pull-off force and strength. Patterns with smaller radii can be more densely packed to take advantage of a split contact surface as predicted by the contact splitting theory by Arzt et al [16].

#### **2) Aspect ratio**

Increasing fibril's height at a constant radius is more effective in enhancing compliance than a decrease in pillar radius at a constant height [86]. The increased adhesion of patterns with high aspect ratio has been attributed to a higher elastic energy dissipated at pull-off in analogy to the mechanism of crack propagation in rubber materials [86]. In addition, there is a decrease of the effective Young's Modulus when the aspect ratio increases as calculated by fitting the loading curves with the Hertzian indentation model [61, 84, 87] given in Eq. 2.2. The assumption of using Hertzian indentation model, when applied to a patterned surface, if the contact region is considerably larger than the pillar radius with the Young's modulus interpreted as an effective quantity [88].

$$P = \frac{4}{3} E^* \sqrt{R \delta^3} \quad (\text{Eq. 2.2})$$

Where  $P$ ,  $R$ ,  $\delta$ ,  $E^* = E / (1 - \nu^2)$  and  $\nu$  are the applied compressive preload, the radius of the indenting sphere, the indentation depth, effective Young's Modulus of the surface and the Poisson's ratio respectively.

### 3) **Contact shape at the terminal end**

Del Campo *et al* [85] showed that the contact shape exerts a stronger effect on adhesion than fibril's size. They obtained the different contact shapes by combining the inking and printing steps using elastomeric precursors with various viscosities and cross-linking kinetics. As shown in Figure 2.7, the different contact shapes obtained and tested were 1) flat, 2) spherical, 3) symmetric spatula, 4) asymmetric spatula, 5) concave tubes and 6) concave tips. Their results showed that although having the same overall dimensions, every contact shape exhibits different adhesion performance. The spatula-like surface has adhesion performance far better than all the other geometries with the symmetric spatulae being the best. This has reaffirmed the importance of the spatula-shaped at the end of each seta.

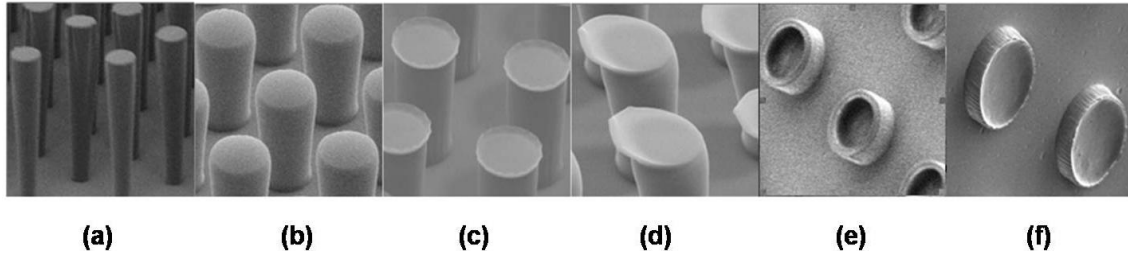


**Figure 2.7.** SEM images of the terminal structures fabricated in polymers a) flat tips, b) spherical tips, c) symmetric spatulae, d) asymmetric spatulae, e) concave tubes, f) concave tips [89].

### 2.3.3 Surface Morphology – Array Density

Arzt et al. [16] has pointed out the importance of array density of the fibrils in their observations of heavier insects possess denser attachment fibrils. They confirmed it using the theory of contact-splitting. Greiner et al. [1] pointed out that the disappointing performance of the fabricated hierarchical structures could be due to the lower packing density (5.15 %) as compared to the single-level structures (22.67 %). As such, this factor should also be taken into account when designing synthetic dry adhesives.

## 2.4 Potential Fabrication Techniques

### 2.4.1 Nano-imprinting Technique

Although numerous fabrication techniques (i.e. soft-molding [41], colloidal lithography [66], “rigiflex” lithography [4], etc.) have been reportedly, polymer replications were mainly performed by casting of polymers followed by curing by either thermally [41] or UV-irradiation [4]. Complete thermal curing of PDMS would normally

require 17 – 24 hours [41] while UV-irradiation technique is usually confined to UV-curable polymers. In the case of parylene deposition [66], it was performed using vapor deposition technique in vacuum conditions. Typically, a significant amount of time is required to reach the vacuum condition as compared to the actual deposition duration.

It is interesting to note that nano-imprinting technique has not been extensively employed as a polymer replication technique in the fabrication of gecko-inspired dry adhesives. This is despite the fact that nano-imprinting technique gained worldwide attention after being selected as one of the top ten emerging technologies [90] in the International Technology Roadmap for Semiconductors (ITRS) in 2003 [91].

Thermal nano-imprinting is a versatile micro-/ nano fabrication technique. This is attributed to its simple processing method which only requires the application of heat and pressure. Typically, the target solid polymer substrate is heated above its glass transition temperature ( $T_g$ ). It thus softens and becomes viscous. With suitable application of force and holding time, it readily fills into a mold cavity. When the polymer substrate is cooled to a temperature below its  $T_g$ , it solidifies and replicates the mold structure with high fidelity.

The nano-imprinting technique is capable of producing high-resolution nano-scale structures down to sub-10 nm [92] as well as high aspect ratio structures up to 50 [93]. Cycle time normally ranges in terms of minutes [94, 95], a vast advantage over thermal curing. Hence, it is a promising manufacturing technology to be adopted by the manufacturing industry [96, 97].

## **2.4.2 Multi-Tiered Porous Anodic Alumina**

As discussed in Section 2.2.4, there were attempts to use porous anodic alumina (PAA) as molds for the fabrication of their gecko-mimetic dry adhesives [49, 50]. However, only the use of linear PAA has been reported. In contrast, hierarchical nano-porous anodic alumina, obtained by a step-wise anodization process, has been employed for the creation of 3D nanostructures [98-100]. It has been used as a template for the production of branched carbon nanotubes [99], and gold nanotrees [100]. However, to produce gecko-inspired fibrillar structure for dry adhesive, the dimensions of the hierarchical nano-porous anodic alumina array structure needs to be easily controllable to achieve the desired dimensions with uniformity.

## **2.5 Summary**

With all the various reported fabricated structures and materials, there is still a lack of satisfactory adhesive performance in the fabricated gecko-inspired adhesives. In addition, these fabrication methods are also not catered for large production.

The important requirements for the successful fabrication of synthetic gecko hair dry adhesives [1] that have yet to be fulfilled include:

- 4) High aspect ratio micrometer (1:10-30) and/or nanometer (1:20-50) scale hierarchical structures fabricated with diameters of 3-10  $\mu\text{m}$  and 50-500 nm respectively.
- 5) Use of hydrophobic stiff materials with Young's modulus between 1-15 GPa, and with high tensile strength.

6) High density micro/nano hair structures for improved adhesion performance

To address these points, in this investigation, the use of multi-tiered porous anodic alumina (as a mold) combined with nano-imprinting technique (as a polymer replication technique) will be developed for the fabrication of synthetic gecko hair dry adhesives. The aim is to obtain hierarchical, high density and high aspect ratio pillars of nano structures made of stiff polymeric material.

In addition, the experimental studies on several structural variations of hierarchical architecture have been inconclusive. Thus, there is a need to demonstrate or otherwise determine the advantages of a hierarchical structure, which will form part of the present investigation.

# **Chapter 3    Mold Fabrication using Porous Anodic Alumina (PAA)**

## **3.1    Introduction**

Chapter 2 indicates that to emulate closely gecko's excellent adhesion, hierarchically structured high density, high aspect ratio, nano-pillars made from stiff polymers are required. However, to fabricate high aspect ratio hierarchical structures in nanometer scale is challenging for several reasons. The first road block is the unavailability of a mold substrate or fabrication process to generate such template. Consequently, up to date there are no reports of structures emulating closely the gecko topography.

Interestingly, one of the widely employed self-assembly methods – anodization of aluminum can produce high density nano-porous structures with tunable aspect ratio commonly known as porous anodic alumina (PAA). This structure can be used as a template or mold [101]. It is a cost-effective and simple technique not limited by diffraction and writing area capacity; hence, the pattern features achievable can go well below the micrometer range to sub-100 nm. In addition, as it is not limited in writing area capacity, this method is amenable to large scale production. Hierarchical nano-porous



anodic alumina with 3D nanostructures can be obtained by a step-wise anodizing process [98-100]. This hierarchical nano-porous alumina structure has been employed as a template to produce branched carbon nanotubes [99], and gold nanotrees [100].

However, for the production of gecko-inspired fibrillar structure dry adhesive, the dimensions of the hierarchical nano-porous structure needs to be controlled to form the desired regular array with good uniformity. Thus, this chapter focuses specifically on the fabrication of PAA with tunable dimensions. The methodology to achieve multi-tiered branched PAA is presented (i.e. two-tiered PAA on aluminum sheet, three-tiered PAA on Al-on-Si substrate and ordered two-tiered PAA on aluminum sheet).

A methodical study of the processing parameters in the fabrication of multi-tiered branched PAA consisting of an array of inter-connected network of pores within pores is presented. The tiered 3D structure was achieved by reducing the anodizing voltage in each successive step for a determined time period while etching or thinning of the barrier layer (also termed pore-widening) was performed after each anodizing step. The controllable process parameters such as the relationship between the barrier layer thicknesses, anodizing duration and anodizing voltage were investigated in detail.

### 3.2 Overview of Porous Anodic Alumina (PAA) Hole Arrays as Templates

PAA presents self-ordered pores as a closed-pack hexagonal lattice (Figure 3.1a) and exhibits a homogeneous morphology of parallel pores which grow perpendicular to the surface (Figure 3.1b). It has a narrow distribution of pore size and inter-pore spacing, the size of which can be controlled between 10 to 100 nm.

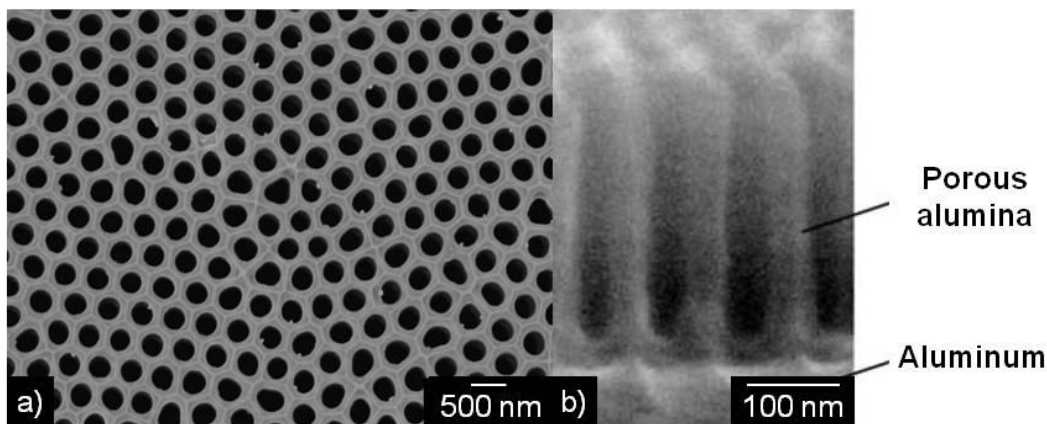


**Figure 3.1.** SEM micrograph of a) top and b) cross-sectional view of alumina nano-hole array [102].

The fabrication of PAA requires simple processing conditions for the self-ordering phenomena and pore size control [103-108]. Due to the ease of fabrication, [109] PAA has become a popular substrate as templating material in the fabrication of nanometer-scale electronics [110, 111], photo-electronic devices [112-114], magnetic data storage devices [115, 116], biological applications [117-122], organic light emitting devices [123], and humidity sensors [124, 125] etc. It has also been used as membranes for ultra filtration [126, 127]. The reason for the intense interest in this material as

template is because it allows low cost fabrication of nano-devices as compared to the conventional method of lithography.

### **3.3 Mechanism of Linear PAA Formation and Self-Ordering**

Pores grow in bulk aluminum when it is being subjected to an anodizing process in an acidic electrolyte, with aluminum being the anode and another inert metal being the cathode [128]. The electrochemical reactions taking place, together with the migration of ions, during the anodizing process when an electric field is applied are shown in Figure 3.2. Aluminum ions ( $\text{Al}^{3+}$ ) from the bulk aluminum travel through the barrier layer and subsequently react with water at the oxide/electrolyte interface to form aluminum oxide [128]. Simultaneously,  $\text{O}^{2-}/\text{OH}^-$  ions migrate from the electrolyte through the barrier layer to react with aluminum at the metal/oxide interface to form aluminum oxide [128]. The rates of the simultaneous field-enhanced chemical dissolution of alumina in acidic solution and the electrochemical reaction are such that the thickness of the walls remain constant.

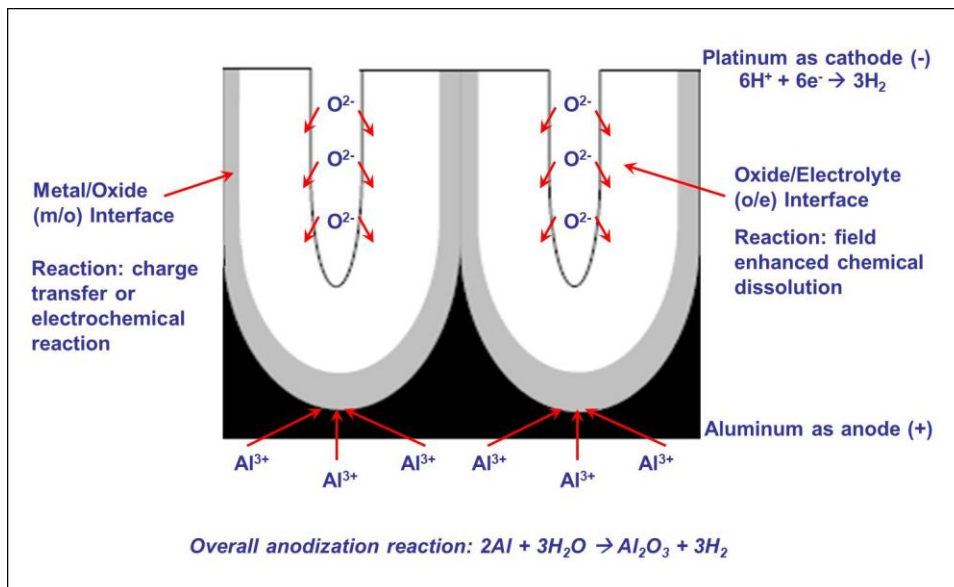


**Figure 3.2.** Migration of  $\text{Al}^{3+}$  and  $\text{O}^{2-}$  through the metal/oxide interface and oxide/electrolyte interface respectively.

The process of oxidizing aluminum to porous alumina causes the volume to expand [103]. This is because porous alumina has a lower atomic density than aluminum [103]. The volume expansion factor is defined as the ratio of the thickness of the alumina grown to the aluminum layer consumed [103]. Jessensky et al. [129] concluded that the volume of the alumina expansion depended on the voltage used.

The mechanism of self-ordering has been attributed to repulsive stresses caused by volume expansion during the alumina pores' growth [129]. These stresses were studied by examining the volume expansion ratio. It was observed that highly ordered porous alumina is obtained as long as the volume expansion factor is approximately 1.4. This ratio is independent of the anodizing parameters such as voltage, temperature, type of acidic electrolyte and its concentration [103]. For example, highly ordered porous

alumina can be obtained using 2.7 wt% oxalic acid at 40 V at 1 °C, 20 wt% sulfuric acid at 19 V at 1 °C, or 1.7 wt% sulfuric acid at 25 V at 10 °C. All these conditions result in a volume expansion ratio of approximately 1.4.

Shingubara et al. [102] attributed the regularity of the PAA array as a function of anodic voltage, acid concentration (depending on the type of acid used) and duration of anodization.

### **3.4 Fabrication of Multi-Tiered Branched PAA**

The method of producing multi-tiered branched porous anodic alumina is simple and inexpensive. The equipment used consists of a cold plate stirrer and a direct current (DC) power supply. As for apparatus, thermally insulated beaker filled with suitable acidic electrolyte (according to the target pore size and inter-pore spacing), magnetic stirrer, platinum or any inert metal as the counter electrode. Figure 3.3a, b and c show the schematic of the experiment setup, images of the actual set-up, and close up of the electrolytic bath respectively.

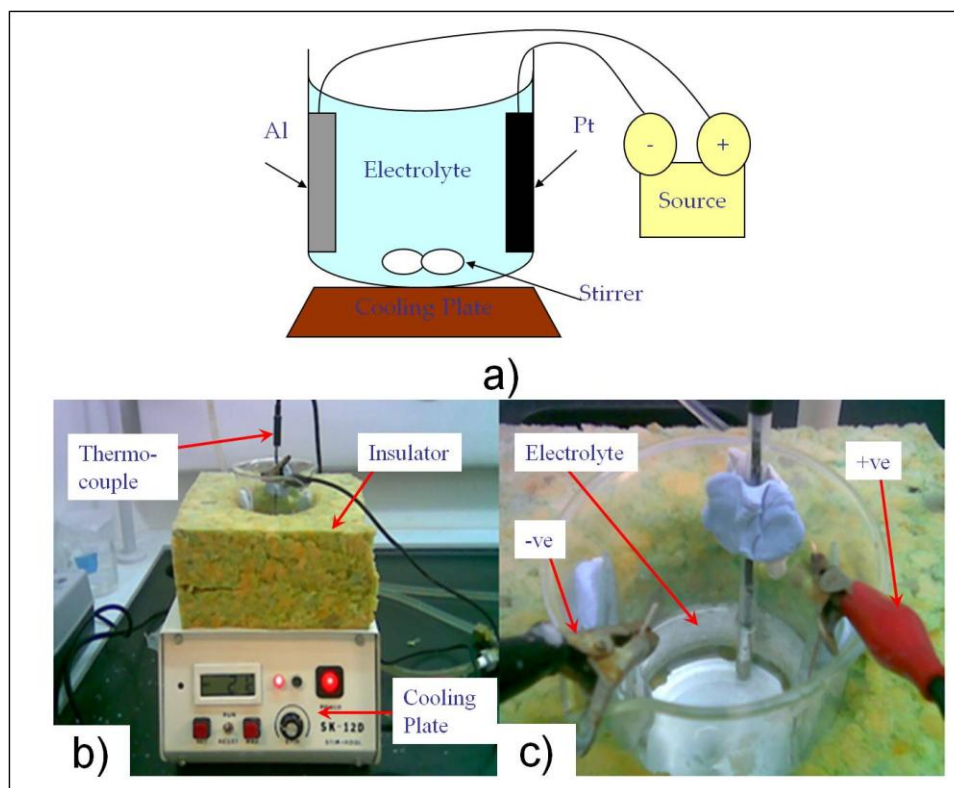


**Figure 3.3.** Set up apparatus for control production of porous alumina a) schematic of the experimental setup, b) actual experimental setup c) close-up of the electrolytic bath.

To obtain PAA, either an aluminum sheet or an aluminum thin film deposited on silicon substrate can be used as starting materials. By controlling the anodizing parameters, the depth of the pores, the number of tiers, as well as the number of branches can be controlled and tailored to the required application. Ordered pores can also be obtained by employing Masuda's method [101] of two-step anodization. Detailed experimental procedures for the fabrication of two-tiered PAA on aluminum film, three-tiered PAA on aluminum-on-Silicon substrate (Al-on-Si) as well as ordered two-tiered PAA are provided in the following sections.

Figure 3.4 depicts schematically the cross-sectional and top views of the step-by-step anodizing process for fabricating multi-tiered branched PAA. Prior to the first anodization, the aluminum free standing film was electro-polished to mirror finishing. This is to reduce surface roughness of the film that would cause non-uniform pore growth. Depending on applications, Al-on-Si substrates could also be used. The growth of the porous alumina layer was controlled by the anodizing duration which grew at a rate of  $\sim 33 \text{ nm min}^{-1}$ . The barrier layer ( $\text{Al}_2\text{O}_3$ ) inherently produced by the anodizing process, was thinned down to  $115 \pm 5 \text{ nm}$ . This is a crucial step to enable subsequent anodizing processes. The second-tier anodization was carried out at a reduced voltage and the sub-pores could be observed after pore-widening. Finally, the third-tier anodization was carried out at a further reduced voltage. The height of each of the pore tier could be controlled independently by controlling the duration of the anodizing process.

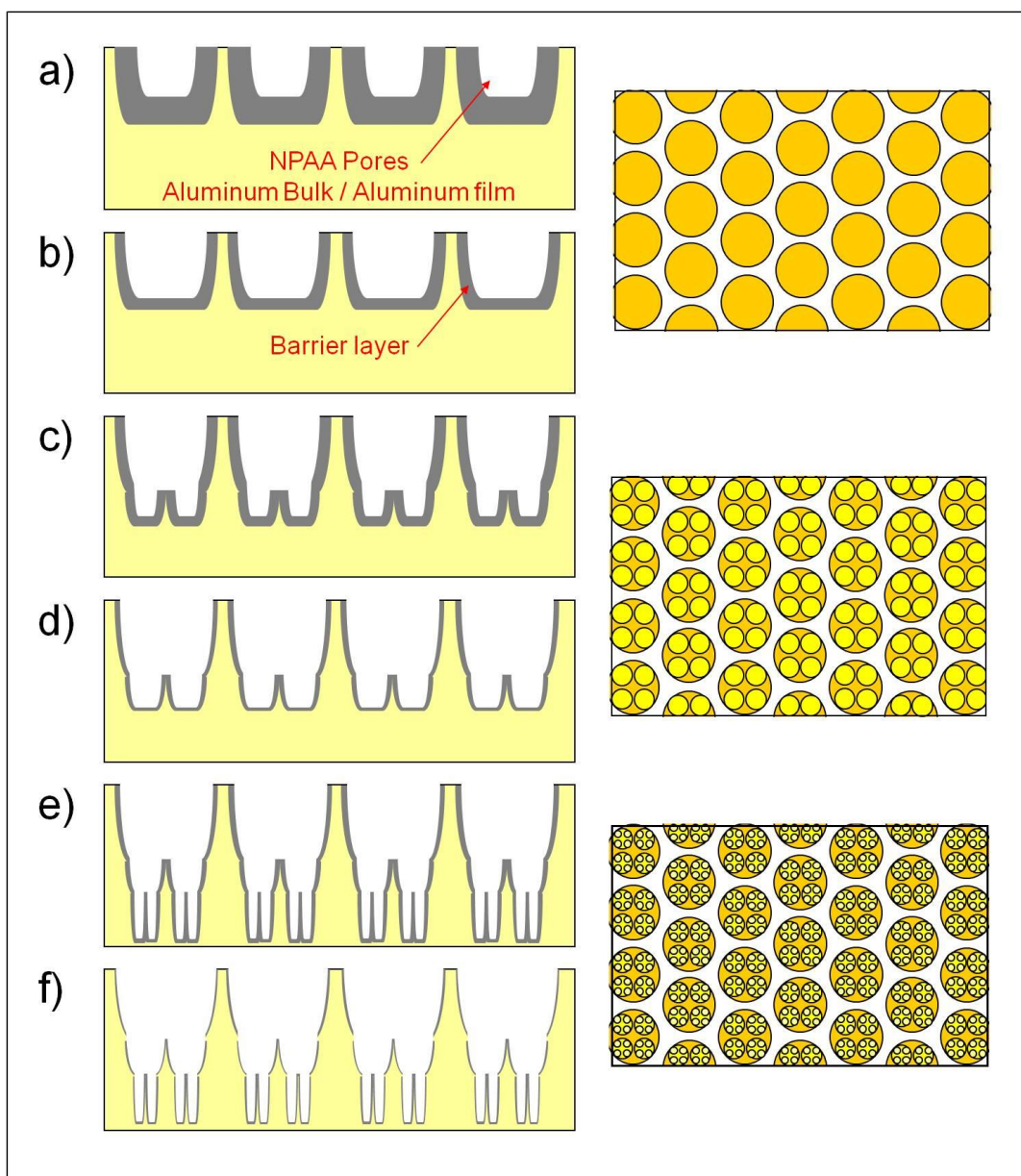


**Figure 3.4.** Schematic of the steps involved in the fabrication of 3-tiered branched NPAA. a) and b) 1<sup>st</sup> Tier - First tier anodization pores and thinning of barrier layer step. c) and d) 2<sup>nd</sup> Tier – Formation of sub-pores at reduced potential followed by barrier layer thinning. e) and f) 3<sup>rd</sup> Tier – Formation of third tiered pores at further reduced anodizing potential completed by barrier layer thinning.



Additional tiered pores could be produced by repeating the anodizing process at a step down voltage.

This voltage for a successive anodization ( $V_{i+1}$ ) should be at least 0.6 times of the preceding anodizing voltage ( $V_i$ ) as given in Eq. 3.1. Details of the experiments are given in Sections 3.4.1 to 3.4.3.

$$V_{i+1} = 0.6V_i \quad i = 1, 2, 3, \dots \quad (\text{Eq. 3.1})$$

### **3.4.1 Fabrication of Two-Tiered Branched PAA on Aluminum Sheet**

The experimental details to produce two tiers of branched pores are given below:

- 1) 100 mm x 100 mm aluminum sheet of 99.999 % purity and 0.25 mm thick were purchased from Goodfellow. These were then cut to size of 20 mm x 30 mm (hereon referred to as substrates).
- 2) Electro-polishing was then performed on the substrates using a 1:4 mixture of 60 % perchloric acid and ethanol with the following parameters: constant voltage of 25 V, at 5 °C and duration of 4 min. The electrolyte was vigorously stirred to maintain temperature uniformity throughout the process.
- 3) The substrate was fitted onto a glass slide. To avert the formation of excess charges at the edges, the edges were shielded (using Elmer's E949 Squeeze 'N Caulk 6-Ounce, Clear). This would ensure better anodization homogeneity of the substrate.
- 4) Subsequently, the substrates were immersed into a thermally insulated beaker containing electrolytic solution. To maintain constant temperature throughout the entire process, a cold plate was used.
- 5) A counter electrode (a platinum mesh) was then submerged into the electrolyte.
- 6) The positive terminal was connected to the aluminum substrate and the negative terminal was connected to the platinum mesh of a power supply.
- 7) Vigorous stirring during the anodizing process enhanced homogeneous diffusion of anions into the pore channel as well as prevent local heating of the surface.

- 8) To obtain the first tier of pores, the following anodizing conditions were used: 0.3 M phosphoric acid ( $\text{H}_3\text{PO}_4$ ) at constant voltage of 130 V at 0 °C for 50 min.
- 9) Etching of barrier layer was performed by submerging the substrate in 5 wt %  $\text{H}_3\text{PO}_4$  for 120 min at room temperature.
- 10) For the second anodizing step, the substrate was anodized at 80 ~100 V using 0.15 M oxalic acid ( $\text{C}_2\text{H}_2\text{O}_4$ ) at 0°C for 3 min. The current immediately dropped to approximately 1 mA (from a high current the moment the power supply was switched on). The formation of second-tier branched pores was signified when the current starts to increase. The process was then timed for 1 min.
- 11) This was followed by etching of the barrier layer for 90 min at the same conditions as (9).

### **3.4.2 Fabrication of Three-Tiered Branched PAA on Al-on-Si Substrate**

The experimental details to produce three tiers of branched pores are given below:

- 1) Al-on-Si substrate can be obtained by deposition of aluminum (99.999%) via electron beam (e-beam) or thermal evaporation. In this study, ~3  $\mu\text{m}$  thick aluminum layer was evaporated onto silicon substrates using e-beam evaporation.
- 2) The wafer was subsequently cleaved into ~20 mm x 15 mm and fixed onto a glass slides. Conductive Al tape was used to connect the top of the Al layer.
- 3) The rest of the preparation steps were the same as the two-tiered branched PAA on aluminum film.
- 4) To obtain the first tier pores, the following anodizing conditions were used: 0.3 M  $\text{H}_3\text{PO}_4$  at constant voltage of 130 V at 0 °C for 20 min. The rate of pore growth was approximately 25  $\text{nm min}^{-1}$ .
- 5) Etching of barrier layer was performed by submerging the substrate in 5 wt %  $\text{H}_3\text{PO}_4$  for 120 min at room temperature.
- 6) For the second anodizing step, the substrates were anodized at 80 ~100 V using 0.15 M  $\text{C}_2\text{H}_2\text{O}_4$  acid at 0°C for 3 min.
- 7) This was again followed by etching of the barrier layer under the same conditions as (5) for 90 min. The resultant barrier layer was approximately 60 nm.

- 8) The third tier was then created by anodizing at 50 ~ 60 V using 0.3 M  $C_2H_2O_4$  acid and subsequently pore-widened for 40 min.

### **3.4.3 Fabrication of Ordered Two-Tiered Branched PAA on Aluminum Sheet**

The experimental details to produce ordered two tiers of branched pores are as below:

- 1) Commercially available aluminum sheet (Goodfellow 99.999%, 0.25 mm thick) were cut to size, typically 20 mm x 30 mm.
- 2) The substrates were then electro-polished in a 1:4 mixture of 60 % perchloric acid and ethanol at the following conditions: constant voltage of 25 V, temperature of 5 °C and time of 4 min.
- 3) The first tier pores were obtained by anodizing the substrate in 0.3 M  $C_2H_2O_4$  at constant voltage of 40V at room temperature for 6 hrs with vigorous stirring.
- 4) An oxide layer of approximately 70  $\mu m$  was produced from the first tier anodization and was subsequently immersed into chromic acid to remove the first layer of aluminum oxide leaving dimples to guide the second step anodization. This would ensure the subsequent pore growth to be more ordered and straight into the aluminum film.
- 5) Second anodizing step was performed at the same condition using 0.3 M  $C_2H_2O_4$  at constant voltage of 40V at 2 °C for 4 min.
- 6) The barrier layer was thinned for 80 min.
- 7) Second tier anodization was carried out using 0.3 M sulfuric acid ( $H_2SO_4$ ) at 25 V for 1 hr and barrier layer thinned for 45 min.
- 8) Figure 3.5 illustrates the geometrical characteristics during the fabrication steps to obtain ordered pores.

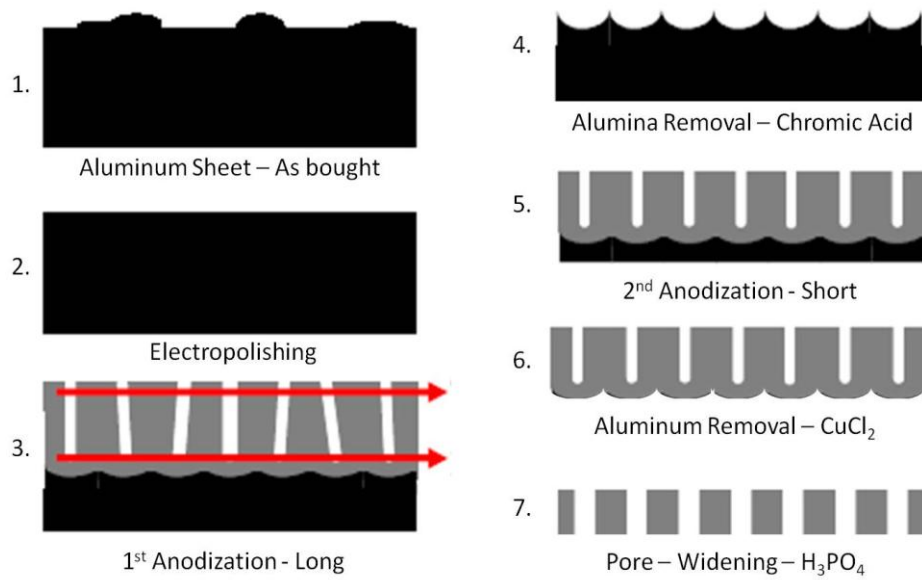


**Figure 3.5.** Schematic of the Masuda's two-step anodizing method to obtain ordered porous template [101].

Images of the tiered branched templates obtained with the process highlighted above are shown in Figure 3.6. Figure 3.6a shows the plane view of a two-tiered branched PAA while Figure 3.6b shows the side view. The sub-pores (the darkest shade) are prominently seen within the main pores in Figure 3.6a and shown to be branching out from the main pores in Figure 3.6b. The plane and side views of three-tiered branched PAA are shown in Figures 3.6c and Figures 3.6d respectively. Figure 3.6e shows the formation of tiered branches on ordered templates [130].

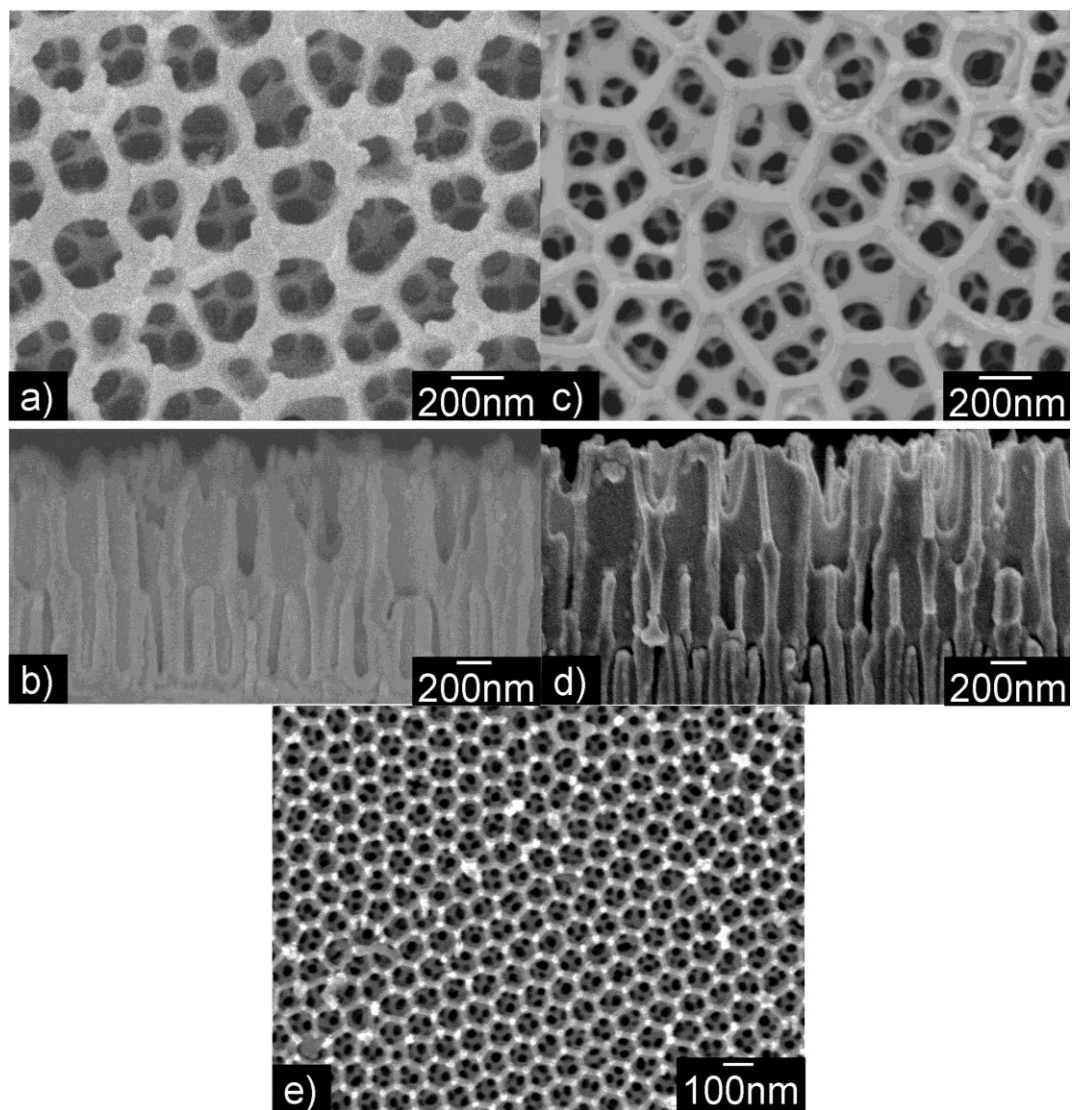


**Figure 3.6.** a) Plane and b) side views of a two-tiered branched PAA, c) plane and d) side views of a three-tiered branched PAA, e) top view of ordered two-tiered branched PAA employing Masuda's method of two-step anodization.

### 3.5 Parametric Study on the Processing Conditions of PAA

As explained earlier, during the anodizing process, ions migrate through the barrier layer to react either with water or the bulk aluminum. Therefore, to successfully form sub-pores in the 2<sup>nd</sup>, 3<sup>rd</sup> and subsequent tiers, the ability of  $\text{Al}^{3+}$  and  $\text{O}^{2-}/\text{OH}^-$  to move across the barrier layer is essential. The two main parameters affecting ion migration are the thickness of the barrier layer and the anodizing voltage. However, the range of anodizing voltage that can be employed is limited by the ionic conductivity of the employed medium (type and concentration of electrolyte, and pH) [131].

To successfully control the generation of sub-pores and to establish the optimum parameters, experiments were carried out systematically to determine the effect of the parameters on the formation of sub-pores. These parameters may have an individual effect as well as a combined effect on the creation of sub-pores. As such, Design of Experiment (DoE) methodology was employed for the investigation. Among the various types of DoE, factorial experimentation was found to be the most appropriate. Using this method, the main effect of a particular parameter and/or the interaction effect of two or more parameters could be effectively identified [132].

The three factors were: a) concentration of electrolyte, b) anodizing voltage and c) thickness of barrier layer. Since there are only three critical parameters (factors) to be investigated, a full factorial design (fully crossed design) could be employed. Hence, every combination of the test run was carried out experimentally. The simplest design is a  $2^k$  factorial design where 2 represents a high and low levels of each parameter and  $k$  is the

number of factors involved ( $k = 3$ ). As such, a complete set of experiments would require a total of eight test combinations ( $2^3$  permutations) to be performed. Table 3.1 shows the high and low levels chosen for each of these factors.

**Table 3.1.** Factors and “high” and “low” levels chosen.

	Factor		
	A Concentration (M)	B Applied Voltage	C Barrier Layer Thickness
Low (-)	0.15	80 V	110 nm
High (+)	0.30	100 V	170 nm

As the main objective of the experiment was to investigate the creation of sub-pores, fabrication of a two-tiered PAA on Al-on-Si substrates was sufficient for demonstration, the details of the fabrication steps can be found in Section 3.4.2. To minimize the variations inherent in the self-assembly anodizing process, a large Al-on-Si substrate was first anodized using 0.3 M  $\text{H}_3\text{PO}_4$  at 130 V for 15 min. The substrate was then cleaved into eight equal parts (sample *a* to *h*) and each was subjected to one of the test combinations listed in Table 3.2. Samples with successful generation of sub-pores were labeled as positive and vice versa. Sample *h* (with a thinned barrier layer), when anodized using the high level of electrolyte concentration and at the high voltage (0.3 M  $\text{C}_2\text{H}_2\text{O}_4$  at 100 V), experienced a high surge in current due to excessive local Joule heating. This led to burning of the porous alumina film. As such, it was also classified as a negative response (listed as breakdown in Table 3.2).

The samples were divided into two sets. For the first set of samples (Set A: samples *a* to *d*), barrier layer thinning was not performed. The barrier layer thickness was approximately  $183 \pm 7.5$  nm (Figure 3.7a). The second set (set B) was thinned down to approximately  $115 \pm 5$  nm (Figure 3.7b). These two sets of four samples were anodized with the following parameters a) 0.15 M  $C_2H_2O_4$  at 80 V, b) 0.3 M  $C_2H_2O_4$  at 80 V, c) 0.15 M  $C_2H_2O_4$  at 100 V and d) 0.3M  $C_2H_2O_4$  at 100 V. No sub-pores were observed after a 3 min anodization for all the four samples (*a* to *d*) in Set A. On the contrary, samples *e, f, g* from set B revealed sub-pores within the preceding pores despite the same corresponding conditions as the first set. The respective SEM images are shown in Figure 3.8.

From these experimental observations, it can be concluded that the main factor affecting the creation of sub-pores is the thickness of barrier layer.

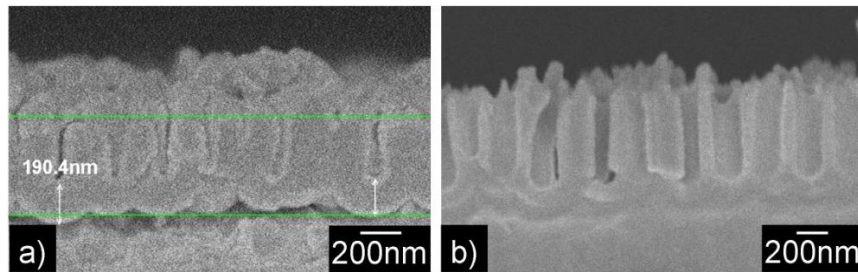


**Figure 3.7.** SEM images of cross-sectioned single-tier PAA on Al-on-Si substrate. a) Barrier layer thickness of samples for Set A  $183 \pm 7.5$  nm. b) Samples for Set B with barrier layer thinned to  $115 \pm 5$  nm using 5 wt %  $H_3PO_4$  at room temperature.



**Table 3.2.** List of full factorial  $2^k$  “Design of Experiment” with a total of eight test combinations ( $2^3$  permutations). “Positive” response denotes successful formation of sub-pores and negative otherwise. Breakdown denotes the substrate that was burnt due to localized Joule heating.

Label	Factor			Response
	Concentration (M)	Applied Voltage (V)	Barrier Layer Thickness (nm)	
a	0.15	80	$183 \pm 7.5$	Negative
b	0.30	80	$183 \pm 7.5$	Negative
c	0.15	100	$183 \pm 7.5$	Negative
d	0.30	100	$183 \pm 7.5$	Negative
e	0.15	80	$115 \pm 5$	Positive
f	0.30	80	$115 \pm 5$	Positive
g	0.15	100	$115 \pm 5$	Positive
h	0.30	100	$115 \pm 5$	Breakdown

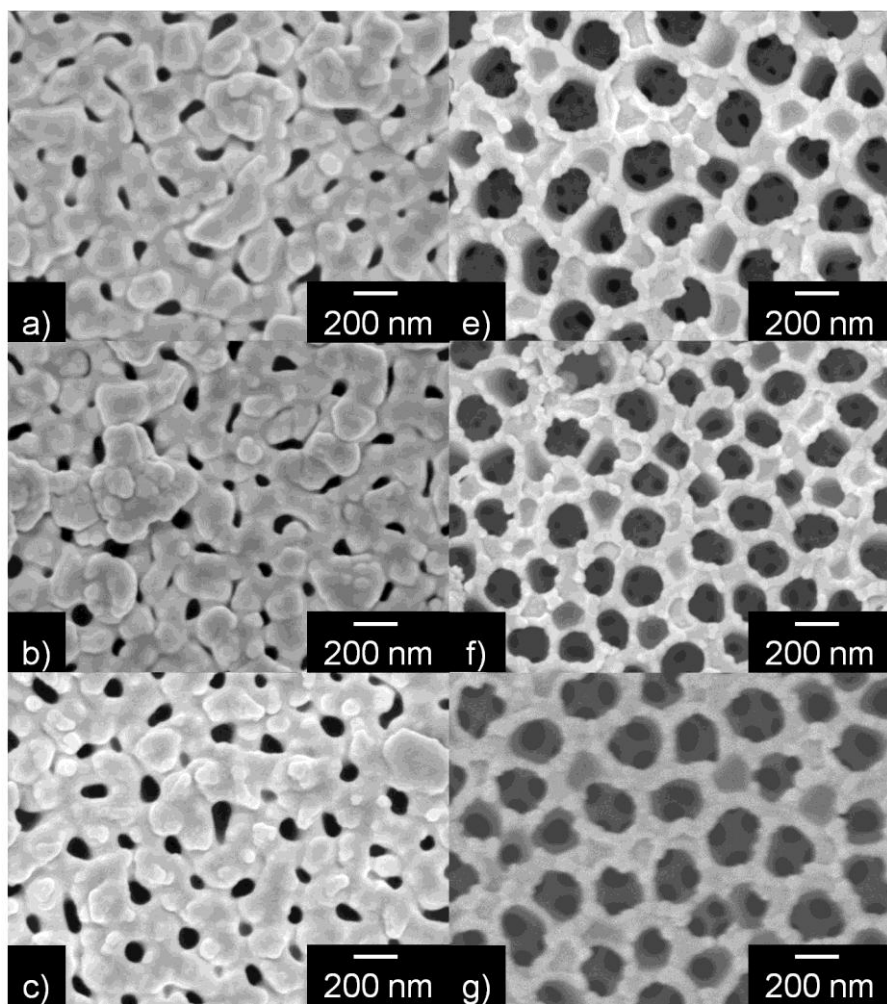


**Figure 3.8.** SEM images of the experimental results based on Design of Experiment on the formation of sub-pores under the respectively conditions. a) 0.15 M Oxalic acid; 80 V;  $BL-183 \pm 7.5$  nm b) 0.3 M Oxalic acid; 80 V;  $BL-183 \pm 7.5$  nm c) 0.15 M Oxalic acid; 100 V;  $BL-183 \pm 7.5$  nm e) 0.15M Oxalic acid; 80V;  $BL-115 \pm 5$  nm f) 0.3 M Oxalic acid; 80 V;  $BL-115 \pm 5$  nm g) 0.15M Oxalic acid; 100 V;  $BL-115 \pm 5$  nm.

### 3.5.1 Interpore Distance of Sub-Pores Within ( $d_w$ ) versus Between ( $d_b$ ) Preceding Pores

Figure 3.9a and b illustrate the center-to-center interpore distance of sub-pores located between different preceding pores,  $d_b$  and the interpore distance of sub-pores within their preceding pore,  $d_w$ . Figure 3.9b, shows that  $d_b$  and  $d_w$  are distinctly different. It is hypothesized that the reason for this difference is that the boundaries of the preceding formed pores define or constrain the arrangements of sub-pores in the second tier.

To test this hypothesis, statistical hypothesis testing was employed [133]. For this purpose, the interpore distance of sub-pores located between different preceding pores,  $d_b$  and the interpore distance of sub-pores within their preceding pores,  $d_w$ , were measured using *AnalySIS* software imaging system on the SEM images. As the pores are not perfect circles, the center of the pore is obtained by the intersections of the lines drawn across the pore as shown in Figure 3.9a. Center-to-center interpore distances are then measured by the software. The measurements are within an error of  $\pm 10$  nm. Figure 3.9b shows one of the SEM micrograph that was used for the measurements.

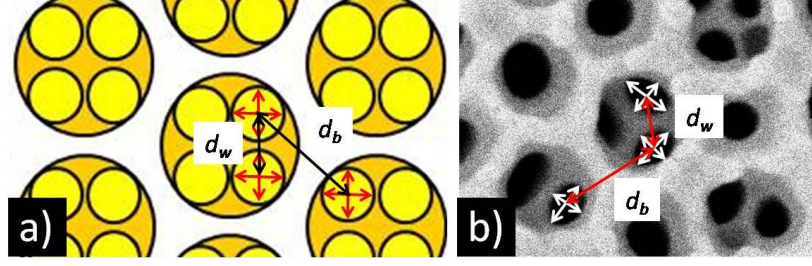


**Figure 3.9.** a) Schematic b) SEM micrograph illustrating the center-to-center inter-pore distance of sub-pores located between different preceding pores,  $d_b$  and the inter-pore distance of sub-pores within its preceding pores,  $d_w$

Measurements were conducted over a range of employed voltage ratio of 0.54 to 0.96. Voltage ratio is calculated by dividing the 2<sup>nd</sup> – tier anodizing voltage with the 1<sup>st</sup> – tier anodizing voltage. The 1<sup>st</sup> – tier anodizing voltage used was 130 V, while the range of 2<sup>nd</sup> –tier anodizing voltage used was 75 V to 125 V. 20 – 60 measurements of  $d_b$  and  $d_w$  were taken from each sample. Their mean values with their respective standard deviations are shown in Table 3.3.

The null hypothesis for this test is ( $H_0$ ) that there is no significant difference between  $d_b$  and  $d_w$ . The alternative hypothesis ( $H_1$ ) is that the difference is significant. This is a one-sided test where the alternative hypothesis states that  $d_b$  is significantly larger than  $d_w$ .

$$\text{Null hypothesis } (H_0) \quad : \overline{d_b} = \overline{d_w}$$

$$\text{Alternative hypothesis } (H_1) \quad : \overline{d_b} > \overline{d_w}$$

Since the objective is to compare the difference between mean of  $d_b$  and  $d_w$  (comparing two-paired groups) for each voltage ratio, the most appropriate statistical hypothesis testing method is the two-sample paired  $t$ -test, which is also known as paired difference test [134].  $t - stat$  for each voltage ratio is calculated as follows:

$$t - stat = \frac{\overline{d_b} - \overline{d_w}}{S_d / \sqrt{n}} \quad (\text{Eq. 3.2})$$

Where  $\overline{d_b}$  is the mean of  $d_b$ ,  $\overline{d_w}$  is the mean of  $d_w$ ,  $S_d$  is the standard deviation of the difference between each pair ( $d_{bi} - d_{wi}$ )  $i = 1, 2, \dots, n$  and  $n$  is the number of measurements. Table 3.3 also shows the respective  $t - stat$  for each voltage ratio.  $t - stat$  is then compared with the critical value  $t_{crit}$  obtained from  $t - table$  of row  $n-1$  degree of freedom and column for the respective confidence interval. The critical value indicate if the mean is accepted as insignificantly different and vice versa for the chosen confidence interval. A confidence interval of 95 % is commonly accepted for providing reasonable precision and confidence [135].

**Table 3.3.** Interpore distance of sub-pores between ( $d_b$ ) and within ( $d_w$ ) preceding pores with respective  $t$ -values. Results from the statistical hypothesis  $t$ -tests show that the two measures of interpore distances are significantly different.

Interpore Distance of Sub-pores Between Preceding Pores, $d_b$ (nm)											
Voltage Ratio	0.58	0.62	0.65	0.69	0.73	0.77	0.81	0.85	0.88	0.92	0.96
Mean	192.71	210.11	216.18	221.07	226.30	238.75	236.86	239.34	269.99	260.26	252.89
Std. Dev.	24.11	25.28	24.31	22.24	29.51	30.54	30.62	34.43	42.55	31.32	36.11
Interpore Distance of Sub-pores Within Preceding Pores, $d_w$ (nm)											
Voltage Ratio	0.58	0.62	0.65	0.69	0.73	0.77	0.81	0.85	0.88	0.92	0.96
Mean	121.65	127.39	127.87	129.84	122.30	130.87	137.84	143.52	149.47	153.91	156.90
Std. Dev.	20.78	14.33	14.97	22.17	26.56	19.86	13.15	21.53	19.89	15.56	22.21
t-stats	18.16	20.50	22.92	20.37	21.70	16.36	15.36	10.28	10.18	16.25	10.96

Figure 3.10 illustrates the t-distribution curve in which  $H_0$  is valid when  $t - stat$  is lower than  $t_{crit}$ . When  $t - stat$  is higher than  $t_{crit}$ ,  $H_0$  is rejected and  $H_1$  is valid. The  $t_{crit}$  for each of the voltage ratio ranges from 1.671 – 1.725. All the  $t - stat$  values in Table 3.3 are higher than  $t_{crit}$ . This means that  $H_0$  should be rejected and that indeed,  $d_b$  is significantly larger than  $d_w$ .

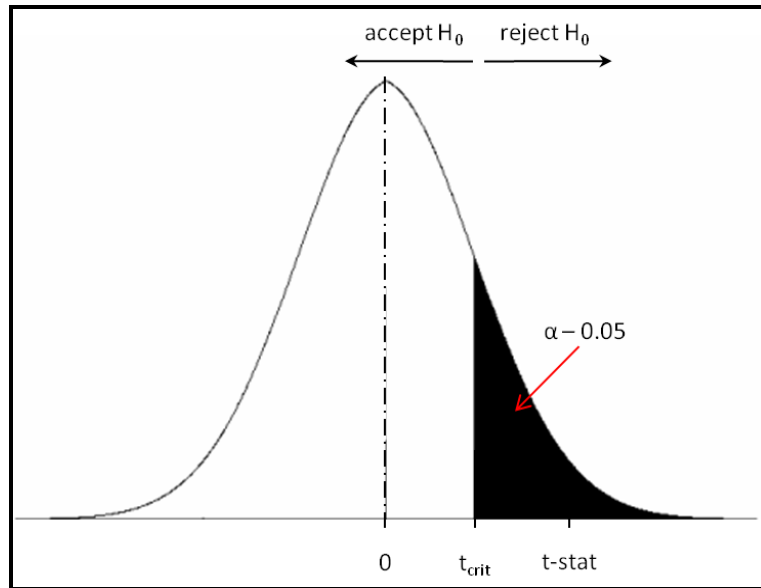


**Figure 3.10.** T-distribution curve

With a confidence level of 95 %, the results shown in Table 3.3 implies that, indeed, the boundaries of the preceding pores will constrict the distribution of sub-pores which otherwise would have had the same mean. In addition, the two types of interpore distance increased in tandem with the voltage ratio.

### 3.5.2 Interpore Distance of Sub-Pores *versus* 2<sup>nd</sup> – Tier Anodizing Voltage

In linear pores, the center-to-center interpore distance,  $D_{int}$  is usually linearly proportional to the applied voltage with a proportionality constant,  $k$  (2.5~2.8 nm/V) [136]. However, the constant for the interpore distance of sub-pores within their preceding pores appeared to vary in accordance with the 2<sup>nd</sup> – tier anodizing voltage.

For practical applications of these nanostructures as templates, characterization of center-to-center interpore distance ( $d_w$  in Figures 3.9a and b) and the number of sub-pores within their preceding pores are important parameters. This characterisation could be achieved by relating the ratio of center-to-center interpore distance of sub-pores to its 2<sup>nd</sup>-tier anodizing voltage, ( $d_w/V_a$ ) as a function of voltage ratio. Again, the 1<sup>st</sup>-tier anodizing voltage was fixed at 130 V for the investigation and the range of voltage ratios used was between 0.48 to 0.96 (65 V to 125 V). From the experimental data obtained, Figure 3.11 is constructed with a plot of  $d_w/V_a$  vs. voltage ratio. The curve follows an exponential decaying function with asymptotic value of 1.16 nm V<sup>-1</sup>. Thus, Figure 3.11 can be employed to estimate the  $d_w/V_a$  required for subsequent tier anodizations.

The constant for the interpore distance for the 3<sup>rd</sup> tier nanopore can be deduced from the curve presented in Figure 3.11. As an illustration, when the 2<sup>nd</sup> tier and 3<sup>rd</sup> tier anodizing voltages are 80 V and 50 V respectively, this corresponds to a voltage ratio of 0.625. From Figure 3.11, the predicted constant for the interpore distance of 3<sup>rd</sup>-tier PAA is  $d_w = 1.525 \text{ nm V}^{-1}$ . This matches the experimental measured value of  $d_w = 1.52 \pm 0.12$

nm V<sup>-1</sup>. This indicates that the relationship shown in Figure 3.11 is not limited to sub-pores of 2<sup>nd</sup> tier but could also be applied for subsequent tiered sub-pores.

Note that the results shown in Figure 3.11 are different with the typical reported value of 2.5~2.8 nm V<sup>-1</sup>[136] for center-to-center interpore distance for porous alumina films. This reaffirms the argument of Section 3.5.1 that, the reason for this difference is due to the boundary constriction of the preceding tier during the subsequent anodizing step.

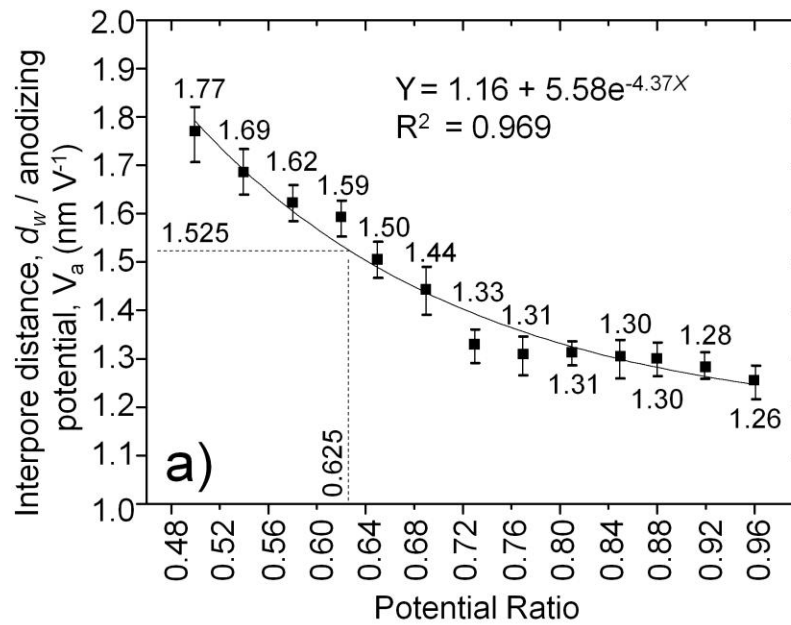


**Figure 3.11.** Relationship of ratio of sub-pores' interpore distance to anodizing voltage ( $d_w/V_a$ ) for 2<sup>nd</sup> tier anodization with its respective voltage ratio. Goodness of fit,  $R^2$  is shown in the figure and error bar indicates one standard deviation.



### 3.5.3 Number of Sub-Pores *versus* 2<sup>nd</sup> – Tier Anodizing Voltage

The number of sub-pores in each preceding pores can be tuned by varying the voltage ratio. With the same samples as discussed in Section 3.5.2, the trend of the number of sub-pores is mapped out. This can be used to predict the number of sub-pores. From the experimental data obtained, Figure 3.12 shows the average number of sub-pores plotted versus its respective voltage ratio. The average number of sub-pores generated at a specific voltage ratio is obtained by dividing the number of sub-pores by the number of preceding pores. The graph also shows an exponential decaying function, with the number of sub-pores reduces as the voltage ratio is increased.

However, from SEM images, there are variations in the number of sub-pores in each voltage ratio. For example, with the 1<sup>st</sup> tier anodizing voltage constant at 130V, for voltage ratio of 0.50 (65 V as the second tier anodizing voltage), the number of sub-pores in each preceding pore varied from 1 to 8, for voltage ratio of 0.54 to 0.65 (70 -85 V), it was between 1 to 7, for voltage ratio of 0.73 to 0.77 (95 – 100 V), it was between 1 to 5, and for voltage ratio of 0.77 (100 V), it was between 1 to 4 sub-pores. Despite the variability, there is a general trend that the number of sub-pores decreases with an increase in voltage ratio. It is postulated that the variability observed in each voltage ratio can be reduced by employing Masuda's method [101] of two-step anodization to obtain ordered preceding pores.

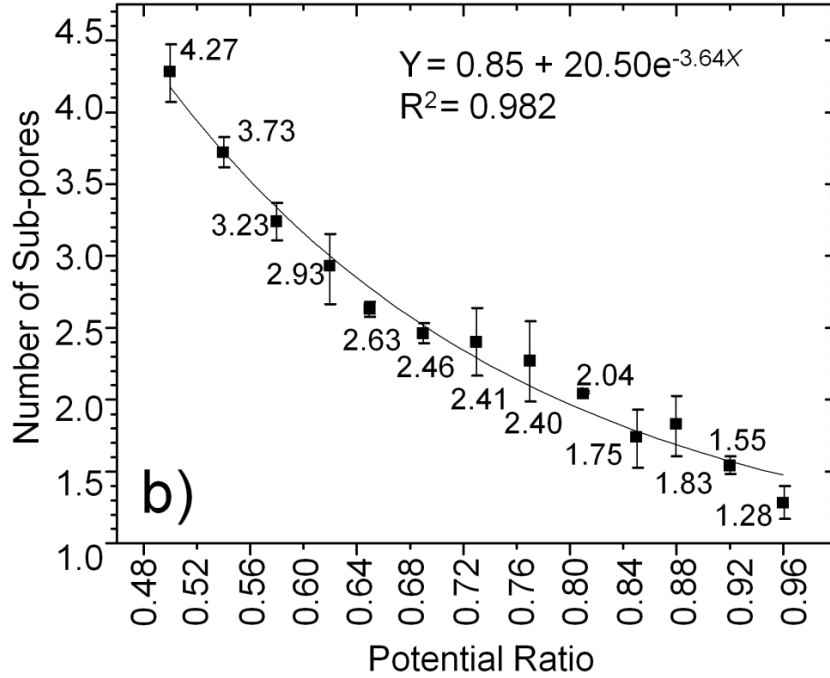


**Figure 3.12.** Number of sub-pores versus its respective 2<sup>nd</sup> tier voltage ratio. Goodness of fit,  $R^2$  is as shown in the figure and error bar indicates one standard deviation.

### 3.5.4 Anodizing Duration versus 2<sup>nd</sup> Tier Anodizing Voltage

Existing literature indicates that at least an electric field of 1 V is needed to drive the respective ions across 1 nm of the barrier layer [131] independent of the anodizing duration. This would imply that a 65 V anodizing voltage would not be sufficient to generate sub-pores through a 115 nm thick barrier layer. However, experimentally we observed that this is not valid in a 2<sup>nd</sup> tier anodization. As noted in Section 3.4.1 point 10, it was observed that at a certain point in time, the current surged and started to increase during the second-tier anodization (refer to Section 3.4.1 No. 10), Hence, it is inferred that at this point, ions have eventually been able to migrate across the

barrier layer and that it is possible to generate sub-pores if the anodizing duration is increased.

An experiment was carried out to confirm the above observation with the same anodizing voltage of 130 V for the first tier, and varying 2<sup>nd</sup> tier anodizing voltage from 65 V to 125 V. The anodizing duration required for the generation of sub-pores for each voltage ratio is shown in Figure 3.13. The barrier layer thickness in this study was  $115 \pm 5$  nm. The duration was timed from the moment the current stabilized at 1 mA (upon turning on the power supply) until the time when the current started to increase. This signals the generation of sub-pores. SEM images of PAA were taken at short intervals before and immediately after the current started to increase.

Figure 3.13 shows that the anodizing duration for the formation of sub-pores versus the anodizing voltage follows an exponential decaying function. It is worthwhile to note that there is only a small standard deviation for all the 2<sup>nd</sup> tier anodizing voltages indicating that these experiments are highly repeatable. This exponential decaying function implies the rate of generation of sub-pores, and can be used as a guide for experimental planning. For example, anodizing the sample with a voltage ratio less than 0.50 (65 V) though possible, will not be as efficient since the anodizing duration is expected to be excessively long. Vice versa, anodizing with a voltage ratio above 0.77 (100 V) is not advisable as the duration is too short to allow the process to be properly controlled.

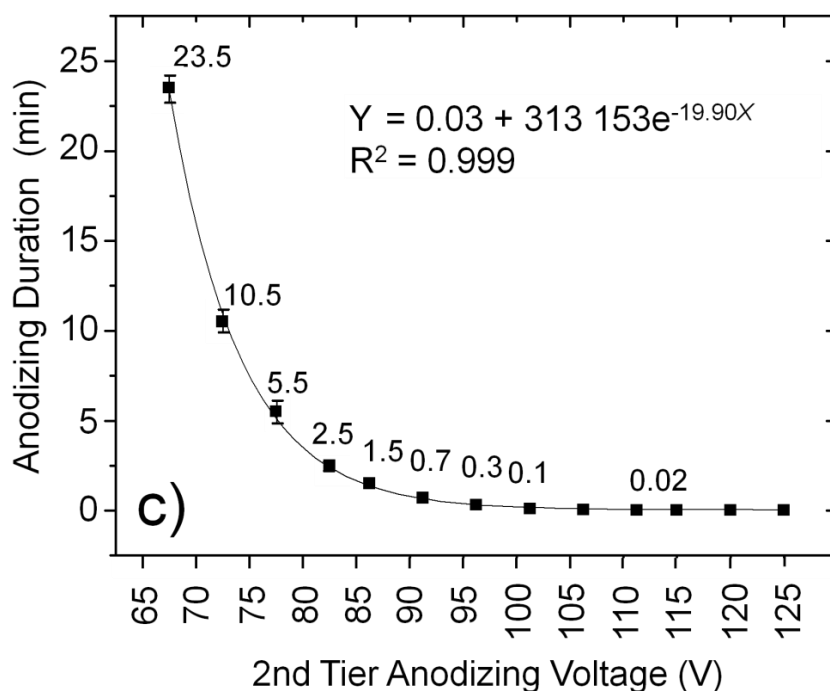


**Figure 3.13.** Anodizing duration vs. 2<sup>nd</sup> tier anodizing voltage for the formation of sub-pores through barrier layer thickness of  $115 \pm 5$  nm. Y- values of 0.02 are only approximate. Equation of fit for Y (vertical axis) versus X (horizontal axis, i.e. Anodizing Voltage) and goodness of fit,  $R^2$  for each curve are shown in the figure. Error bar indicates one standard deviation.

### 3.5.5 Effect of Electrolyte on the Formation of Sub-Pores

It was also observed that at a given anodizing voltage, different electrolytes would produce different effects on the formation of sub-pores. To investigate further, two substrates were first anodized and subsequently barrier layer thinned at the same anodizing and pore widening conditions (at 130 V using 0.3 M  $H_3PO_4$  for 30 min). The 2<sup>nd</sup>-tier anodization was carried out with anodizing voltage at 100 V using 0.15 M  $C_2H_2O_4$  or 0.3 M  $H_3PO_4$ . In both cases, the temperature and stirring conditions were kept constant.

Figure 3.14 shows the sub-pores produced with different electrolytes. The sub-pores produced by 0.15 M  $\text{C}_2\text{H}_2\text{O}_4$  (Figure 3.14a) were more distinct, more numerous, and achieved smaller diameters than those produced by 0.3 M  $\text{H}_3\text{PO}_4$  (Figure 3.14b). The sample anodized in  $\text{H}_3\text{PO}_4$  (Figure 3.14b) seemed to produce larger sub-pores. Since they were confined within the boundary of the preceding pores, the sub-pores were forced to merge. Figure 3.14a also shows the preceding pores with thinner pore walls than Figure 3.14b. This is postulated to be due to a higher rate of alumina dissolution in  $\text{C}_2\text{H}_2\text{O}_4$  since it is a stronger electrolyte than  $\text{H}_3\text{PO}_4$ .

This result is in agreement with the observations made by Jessensky et al. [137] and Krishnan et al. [98]. For functional applications, it is worth noting the effect of different electrolytes on the formation of tiered sub pores since it affects the number of pores and the pore size.

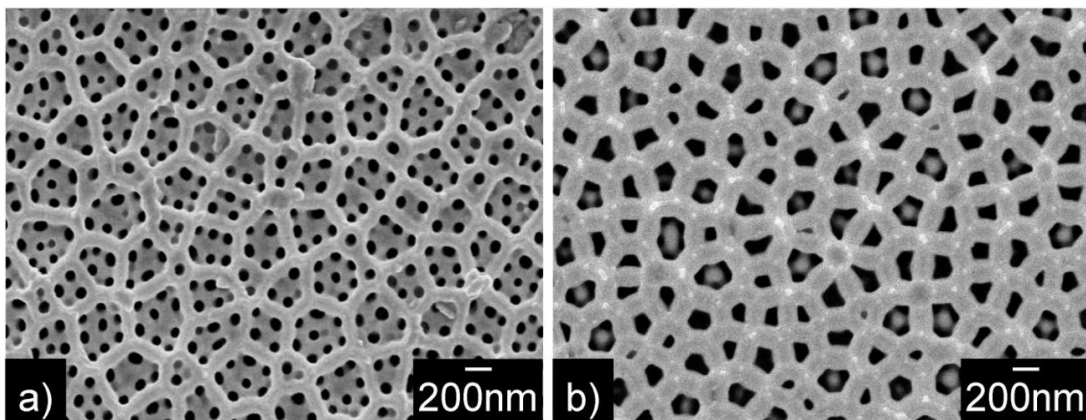


**Figure 3.14.** PAA films subjected to a second tier anodization at 100 V using two different electrolytes. a) 0.15 M  $\text{C}_2\text{H}_2\text{O}_4$  and b) 0.3 M  $\text{H}_3\text{PO}_4$ . Both were pore widened for 45 min. 1st-tier anodization was previously performed at 130 V using 0.3 M  $\text{H}_3\text{PO}_4$  for 30 min.

### 3.6 Wetting Properties of PAA

Hitherto, there have not been any reports on the wetting properties of multi-tiered PAA. However, the change of surface topography is expected to alter the wetting behavior of the film surface. Hence, the wetting characteristic of the PAA obtained was examined by measuring the water contact angles ( $\theta$ ).

Contact angle measurements were carried out using Ramé-Hart digital contact angle goniometer. Cleaned samples were placed on the stage of the equipment and leveled horizontally. A deionized water droplet of 1  $\mu$ L was gently released onto the substrate surface using an automatic pipette. The image of the droplet was immediately captured and the contact angle was measured by the software provided. Three readings of the contact angles were taken for each sample and averaged.

Water contact angles of Al-on-Si substrate, single tiered PAA on silicon substrate and shallow two-tiered branched PAA were compared. Figure 3.15 depicts the respective contact angles of, a) Al-on-Si substrate ( $\theta = 113.9^\circ \pm 0.8$ ), b) single tiered PAA on silicon substrate ( $\theta = 46.3^\circ \pm 1.8$ ) and c) shallow two-tiered branched PAA ( $\theta = 15.8^\circ \pm 2.1$ ). These values indicate that the wettability of aluminum films increases significantly with tiered anodizations. The low value of contact angle measured for 3D PAA shows that water spreads more and hence this surface is highly hydrophilic.

This finding could be understood based on the fact that increasing the thickness and porosity of the hydrophilic alumina layer increases the contact with the water droplet that wicks into the pores by capillarity. In fact, it has been shown in another

report that structuring topographically a hydrophilic material increases its hydrophilicity or wetting [138]. Similarly, as demonstrated here, the wettability of PAA templates can be modified by manipulating its topography through multi-tier anodizations. This finding has important implications on the use of PAA as templates in casting or nano-imprinting processes since surface energy and morphology would affect the filling of materials into the alumina pores.

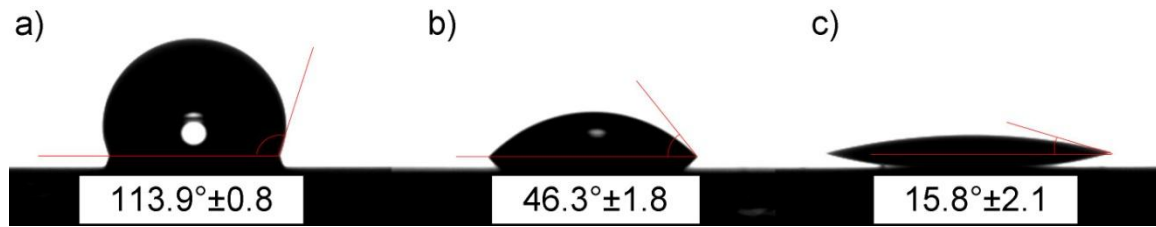


**Figure 3.15.** Contact angles of water on a) aluminum-on-Si; b) single tier PAA on Si substrate; and c) shallow two-tiered PAA on Si substrate.

### 3.7 Summary

In this chapter the fabrication of tiered branched PAA templates has been described. Through statistical and systematically designed experiments, the most significant parameter, which is the thickness of barrier layer, has been identified as the main factor controlling the creation of sub-pores. In addition, it has been shown that due to the constriction caused by the boundaries of the preceding pores, the center-to-center interpore distance,  $D_{int}$  is no longer linearly proportional to the applied voltage with a proportionality constant,  $k$  (2.5~2.8 nm/V). Instead, the constant for the interpore distance of sub-pores within their preceding pores varies in accordance with the 2<sup>nd</sup> – tier anodizing voltage. In addition, by increasing the tiers in a PAA substrate, an increase in

surface wettability is achieved and this could improve the filling of PAA when it is used as an embossing template.

The tiered branched PAA produced in this investigation could be employed to produce 2D and 3D structured surfaces . It can serve as a template for the fabrication of dendritic hydrogels as scaffolds in tissue engineering. The templates could also be used to produce inexpensively a wide variety of complex architectures such as branched nanotubes and nano-wires for complex nano-electronic circuits, photonic/optical devices or photovoltaic cells. These branched PAA when made free-standing can be used as nanomembranes for filtration or molecular separation in size-exclusion chromatography. In the context of biology and chemistry, the enhanced surface area enables a higher diffusion for biological and chemical substances on the surface, thus increasing reactivity.

In the present investigation, the tiered branched PAA template (two-tiered PAA on aluminum sheet) is applied specifically on the fabrication of synthetic gecko-inspired dry adhesives using polymer replication technique, specifically, via nano-imprinting. The methodology to produce topographical structures via nano-imprinting using PAA as a template will be discussed in Chapter 6.





# Chapter 4 Polymer Characterizations

## 4.1 Overview

The fabricated branched tiered PAA templates in Chapter 3 were employed to produce synthetic gecko-inspired dry adhesives using polymer replication technique, specifically, via nano-imprinting. Prior to this, it would be advantageous to gain some understanding of the mechanics of polymer mold filling during imprinting and the subsequent behavior of the polymer after imprinting. This would provide essential information for the choice of the nano-imprinting process parameters. This was in anticipation of the challenges encountered during imprinting for the polymer to completely fill into the high-density, high aspect ratio and specifically branched tiered nano-pores of the PAA templates.

For this purpose, experimental and numerical modeling were carried out. As a pre-requisite of establishing a numerical model, there are several polymer properties that need to be determined.

Hence, this chapter would discuss several material characterization methods used to obtain the required material parameters for the study. The model material chosen was polycarbonate (PC). Gel permeation chromatography (GPC) was employed to

determine the molecular weight distribution and the mechanical properties were characterized through rheological measurements.

## 4.2 Polycarbonate (PC)

Polycarbonate (PC) is amorphous, linear thermoplastic polymer. Figure 4.1 illustrates the molecular chain of PC consisting of phenyl groups, methyl groups ( $\text{CH}_3$ ) and carbonate groups ( $-\text{O}-(\text{C}=\text{O})-\text{O}-$ ) [139]. Polycarbonate owes its molecular stiffness to the phenyl and methyl side groups which constrict the mobility of the individual molecules. This provides PC the basis of good mechanical properties such as high impact strength and durability as well as high chemical resistance over a wide temperature range [140]. In addition, the rigidity of these two groups prevents the formation of crystalline structure. This results in PC having good light transmission characteristics due to its high transparency to visible light (a characteristic of an amorphous polymer). These superior properties rendered PC to be commonly classified as an engineering plastic for a wide variety of applications (e.g. optical lenses, bulletproof windows, compact disks (CDs) etc). The glass transition temperature ( $T_g$ ) and melting temperature ( $T_m$ ) of PC are approximately  $145 - 150^\circ\text{C}$  and of  $267^\circ\text{C}$  respectively [141].

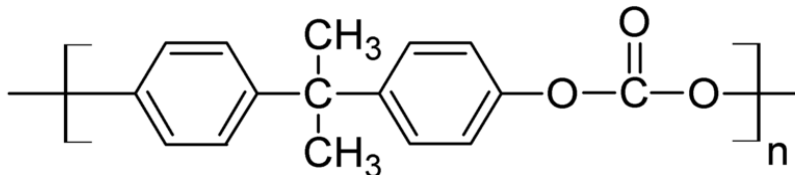


**Figure 4.1.** Chemical structure of polycarbonate [142].

### 4.3 Gel Permeation Chromatography (GPC)

The molecular weight distribution (MWD) (also known as polydispersity index (PI)) of commercial grade polymers varies from batch-to-batch in production [143]. This would intrinsically affect the physical properties. To determine the average molecular weight,  $M_w$ , the average molecular number,  $M_n$  and the molecular weight distribution, MWD of the commercial grade Lexan PC films (0.25 mm thick) used for nano-imprinting, GPC method was employed.

Process flow and steps as given by the equipment manual were followed [144]. A PC sample was dissolved in tetrahydrofurane (THF) (HPLC grade) to obtain a solution of approximately 0.5% by weight. It was then filtered with pore size 0.22 $\mu$ m filter. Polystyrene standard (PSS) was used for narrow standard calibration. Upon setting up of the system and software, 50  $\mu$ l of polymer solution was injected into the injection valve. The molecules that passed through the column were detected by the evaporative light scattering detector (ELSD). The peaks were recorded and the respective  $M_w$ ,  $M_n$  and MWD were subsequently calculated by the data acquisition software. Figure A1 (in Appendix A) illustrates the GPC flow path for PC solution. Table A1 (in Appendix A) summarizes the specifications of the equipment as well as the testing conditions.

Three tests were performed. Figure 4.2 shows the chromatogram of the three tests performed. The y-axis is the light scattering (LS) units captured by the detector as the molecules pass through the columns and the x-axis represents the retention time (RT) which is the duration the molecules took to go through the system. Data from Peak 1 at

RT of 22.5 min and the area under the peak were used to calculate the molecular weight averages of the PC molecules while Peak 2 shows the low  $M_w$  of a side product.

The results were averaged and tabulated in Table 4.1. The averaged  $M_w$  and  $M_n$  are  $49,965 \pm 1,880$  Daltons and  $34,218 \pm 1,297$  Daltons respectively. It has a medium range of polymeric distribution of  $1.46 \pm 0.03$ .

**Table 4.1.**  $M_w$  and  $M_n$  of commercial grade polycarbonate (Lexan).

Test No.	$M_w$	$M_n$	$PI = M_w / M_n$
1	48,509	32,914	1.50
2	52,088	35,507	1.47
3	49,299	34,235	1.44
Average	49,965	34,218	1.46
StdDev.	1,880	1,297	0.03

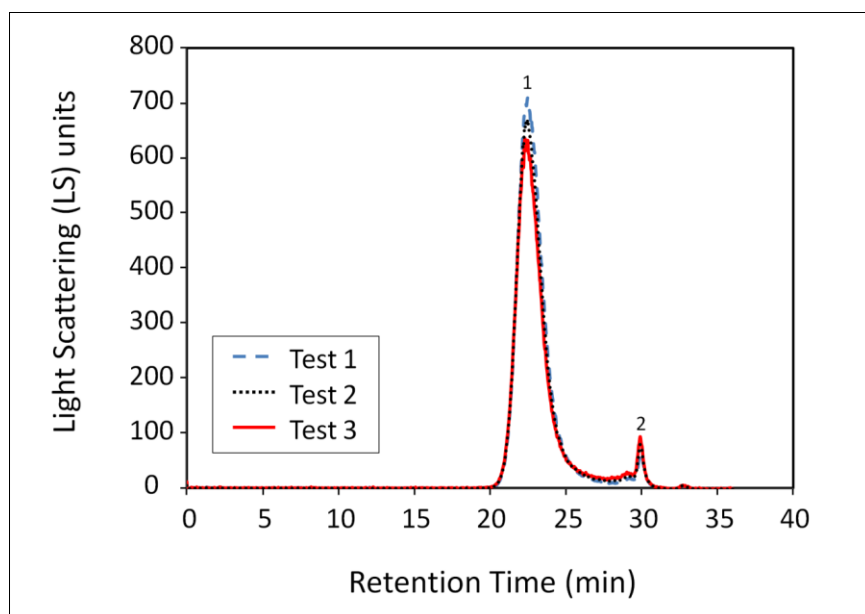


**Figure 4.2.** Chromatogram of PC (Peak 1) and a side product (Peak 2).

## 4.4 Dynamic Mechanical Thermal Analysis (DMTA)

For the simulation, it is necessary to know the actual creep or relaxation properties of the material. A mathematical representation for a given polymer for these properties over many decades of logarithmic time will be advantageous. This mathematical representation is commonly known as a time-temperature superposition (TTS) master curve.

A relatively straightforward approach is to use a generalized Maxwell model (GMM) with sufficient elements to span the spectrum of relaxation times represented by the transition behavior of the data. To construct this model, using an Anton Paar Physica MCR 301 rheometer, material characterizations via dynamic mechanical thermal analysis (DMTA) (based on dynamic loading) were performed to obtain the necessary parameters.

PC films of 10mm x 50mm x 0.25mm were cut to size and clamped to the solid rectangular fixture (SRF) and placed in a convection temperature device (CTD600) chamber with heating capability up to 600 °C. Figure 4.3a shows a typical SRF fixture for the torsional experiments conducted. Figure 4.3b shows the schematic of the clamp. The PC sample was placed with a slight tension under a normal force of 0.1 N to ensure that the film was taut. The sample height after clamping was around 45mm.

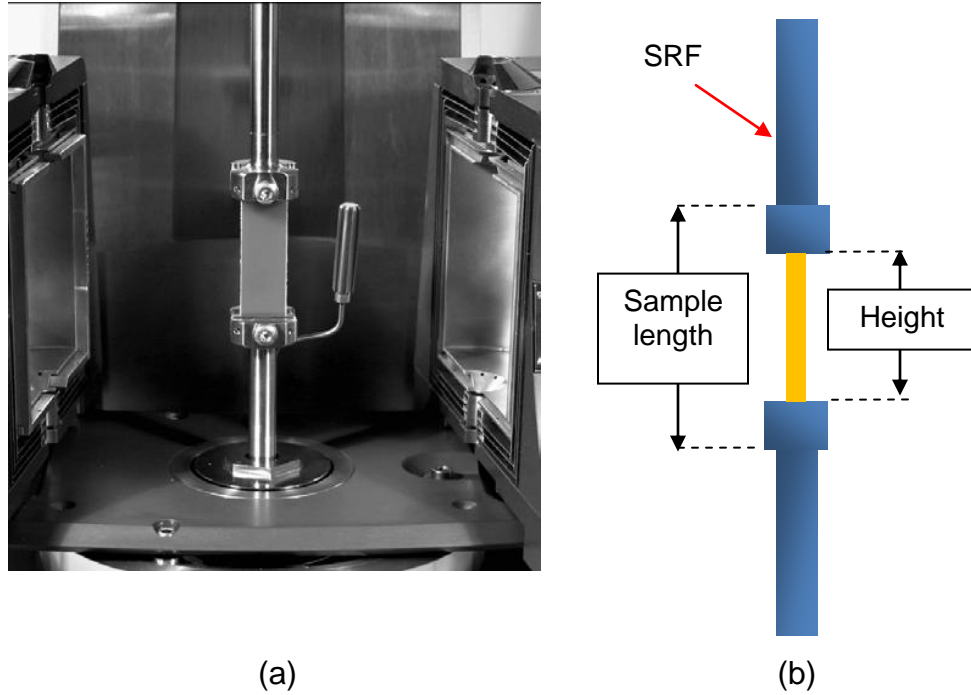


**Figure 4.3.** a) Typical SRF fixture in a CTD [145] b) schematic of clamp and sample dimension.

The glass transition temperature of PC was determined by the temperature sweep technique used to investigate the relaxation process of PC. Measurements commenced from room temperature ( $\sim 25\text{ }^{\circ}\text{C}$ ). The PC film was oscillated at a set frequency with increasing temperature up to  $195\text{ }^{\circ}\text{C}$ . The temperature was ramped at  $5\text{ }^{\circ}\text{C}/\text{min}$ . The set angular frequency was either  $10$  or  $50\text{ rads}^{-1}$  with a strain rate of  $0.1\%$ . This low strain rate was used such that it was within the linear viscoelastic range to prevent structural deformation of the polymer.

For analysis, a complex modulus ( $|G^*|$ ) over a wide range of temperature ( $25\text{ }^{\circ}\text{C} - 195\text{ }^{\circ}\text{C}$ ) was plotted to determine  $T_g$  as shown in Figure 4.4. The  $T_g$  in this experiment is defined as the onset of the drop in  $|G^*|$  where large segments of the PC

chain begins to move. It represents the transition of PC from a hard glassy state to a rubbery state. This transition state spans approximately 20 °C. At room temperature,  $|G^*|$  of PC was 2.45 GPa and 1.07 GPa at angular frequencies of 50 and 10  $\text{rads}^{-1}$  respectively. For a given angular frequency,  $|G^*|$  did not change significantly as long as it was below the  $T_g$ . The  $T_g$  of PC at the respective angular frequencies of 50 and 10  $\text{rads}^{-1}$  are 137 °C and 140 °C. This difference in  $T_g$  at different angular frequencies could be due to experimental variations since the difference is small and not significant [146]. It should be noted that the higher complex modulus of PC at 50  $\text{rads}^{-1}$  is due to the insufficient time for the polymer chains to respond to flow at the higher strain rate thus behaves more elastically.

At the rubbery state,  $|G^*|$  measured at 50  $\text{rads}^{-1}$  dropped to 0.93 GPa, while the measurement performed at 10  $\text{rads}^{-1}$  dropped to 70 MPa. This implies that the  $|G^*|$  measured at 50  $\text{rads}^{-1}$  is less sensitive to a change in temperature than at 10  $\text{rads}^{-1}$  for the same reason given previously. Since nano-imprinting is a process of low deformation rate [147], the viscosity above the  $T_g$  at 10  $\text{rads}^{-1}$  would be at a sufficiently low strain rate for a good representation for the polymer filling process.



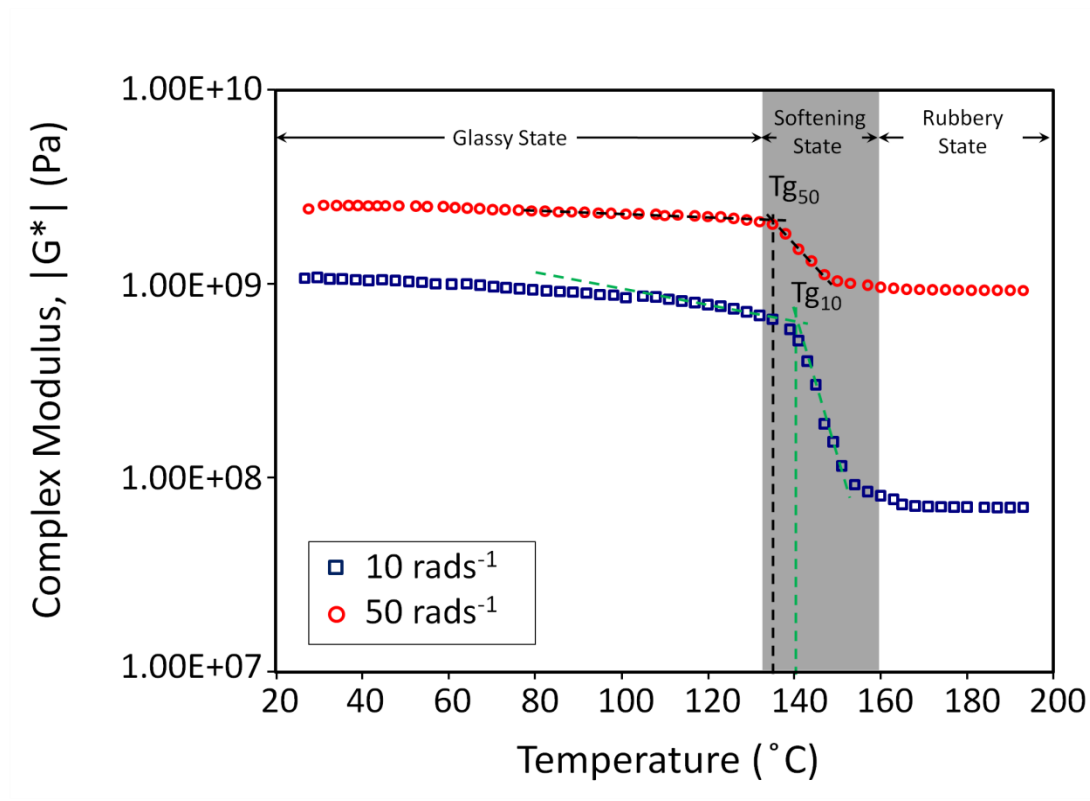


**Figure 4.4.** Complex modulus versus temperature at constant frequency of 10 rad/s and 50 rad/s.

Figure 4.5 shows that at constant angular frequency of  $10 \text{ rad/s}^{-1}$ , PC behaves more elastically at temperature below  $145^\circ\text{C}$  where the storage modulus ( $G'$ ) of PC is higher than the loss modulus ( $G''$ ). The onset of glass transition temperature brings about a sudden decrease of  $G'$  while at the same time,  $G''$  increases. Above  $145^\circ\text{C}$ ,  $G''$  is higher than  $G'$ . This means that PC begins to behave more liquid-like. Although the same trend was observed for angular frequency of  $50 \text{ rad/s}^{-1}$ , PC still behaves very much solid-like above  $145^\circ\text{C}$  as  $G''$  is still less than  $G'$ .

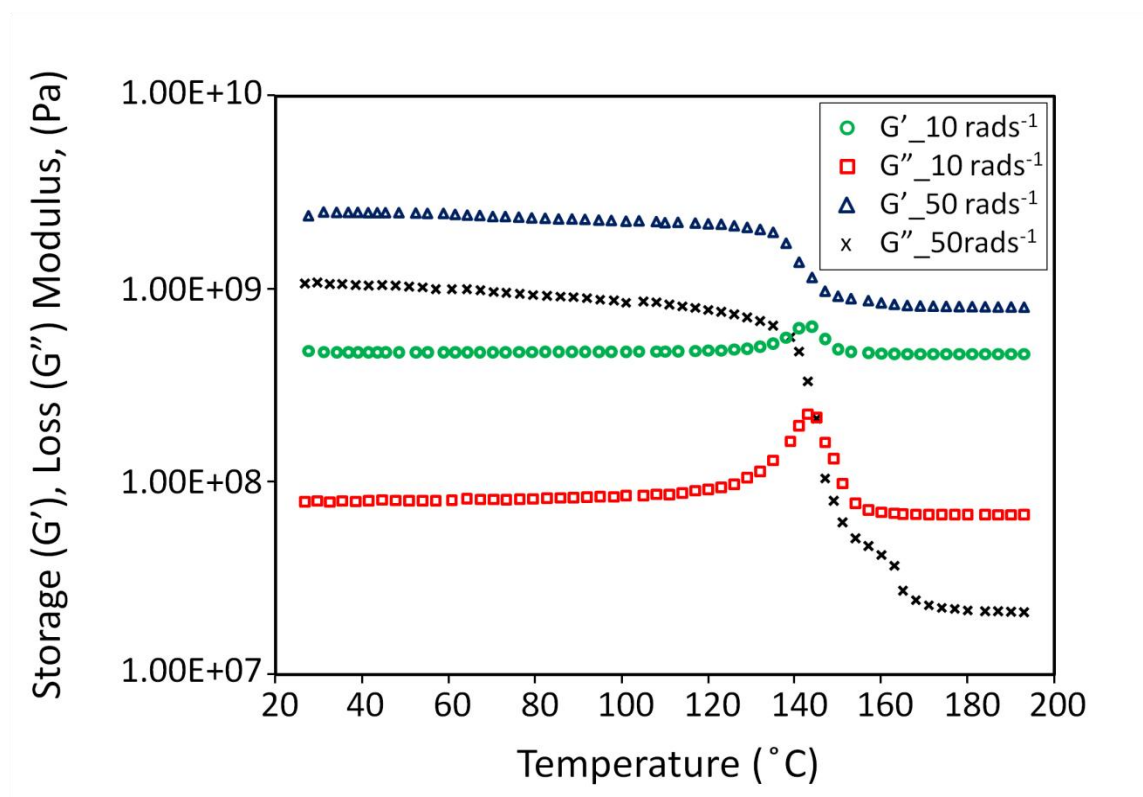


**Figure 4.5.** Storage and loss modulus versus temperature at constant frequency of 10  $\text{rad s}^{-1}$  and 50  $\text{rad s}^{-1}$ .

The same measurements were repeated, but instead of a temperature sweep, a frequency sweep at several constant temperatures (155°C, 170°C, 185°C) was performed on PC. In general, as temperature increased from 155 to 185°C, both the storage (Figure 4.6a) and loss modulus (Figure 4.6b) were found to decrease with increasing temperature.

For nano-imprinting, it can be expected that the polymer would flow at rather slow rates. Hence the data obtained below the angular frequency of 10  $\text{rad s}^{-1}$  would be sufficient to characterize the flow behavior meaningfully.

As shown in Figure 4.6a, at 155°C,  $G'$  was 0.17 GPa at the low angular frequency of 0.1  $\text{rad s}^{-1}$ . As the frequency increased,  $G'$  increased gradually to reach 1.5

GPa. At 170°C,  $G'$  was 5.6 MPa and increased to 0.54 GPa at 10  $\text{rads}^{-1}$ . The data obtained for 185°C from 0.1 – 0.3  $\text{rads}^{-1}$  were fluctuating but subsequently stabilized at 2.3 MPa and increased to 0.16 GPa.

The  $G''$  for 155°C was significantly higher than the other two temperatures. This was probably because it was still in the transition range when the polymer commenced to behave more fluid-like. The  $G''$  at 170°C was not significantly different from that at 185°C. This could be due to the polymer being in the rubbery state where the  $G''$  has stabilized and has a lower value than that at the transition stage, see Figure 4.5. However, the  $G''$  of all three temperatures increased as the angular frequency increased.

The data in Figures 4.6a and b were used to calculate the complex modulus ( $|G^*|$ ) in Figure 4.6c using Eq. 4.1, and complex viscosity ( $\eta^*$ ) in Figure 4.6d with Eq. 4.2.

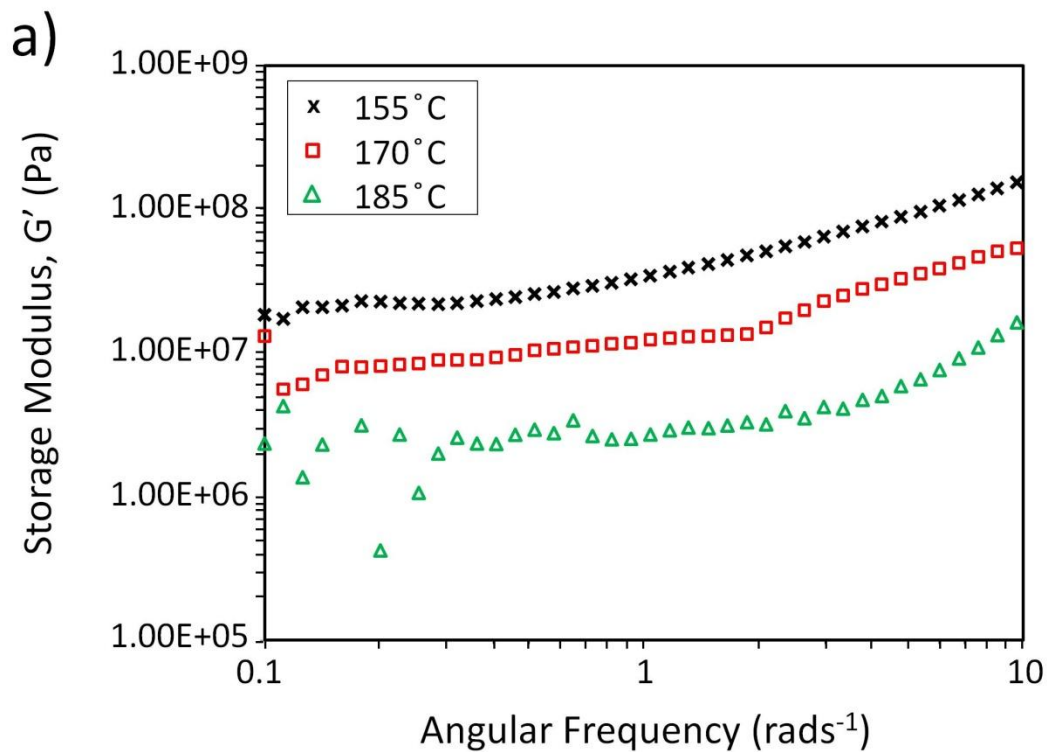
$$|G^*| = \sqrt{G'^2 + G''^2} \quad (\text{Eq. 4.1})$$

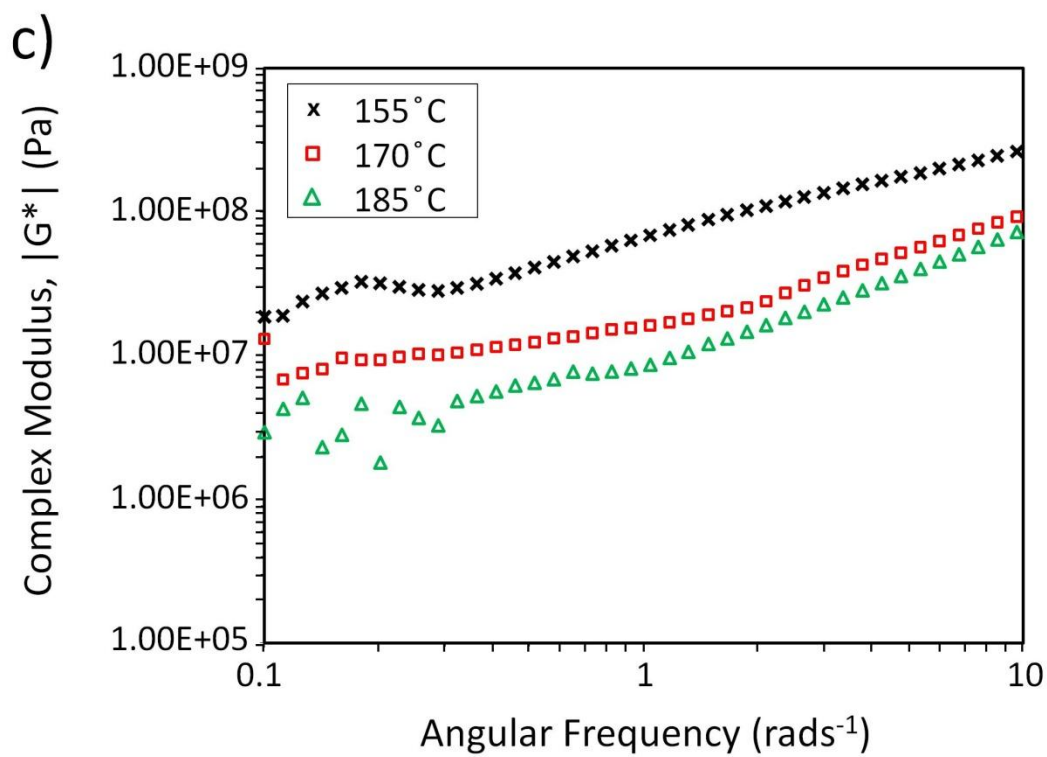
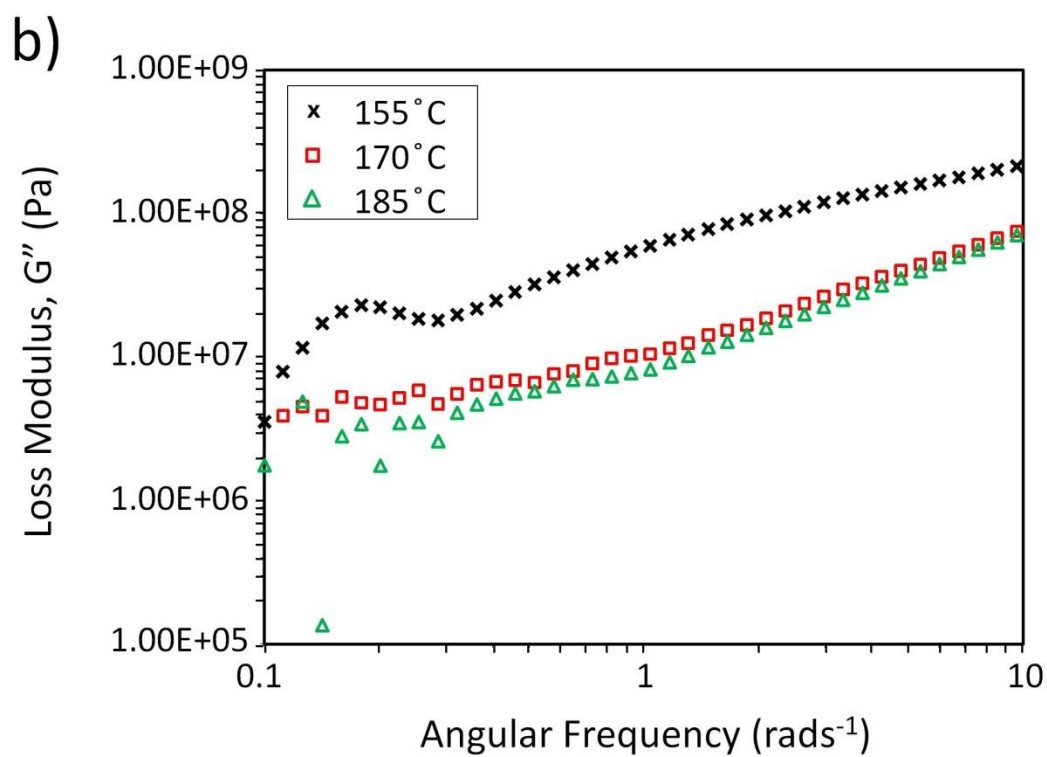
Where  $G'$  is the in-phase or real component of the complex shear modulus, is associated with energy storage in the periodic deformation and is therefore called the storage modulus. It provides information about the elasticity of the polymer.  $G''$ , the out-of-phase or imaginary component, is associated with the dissipation of energy as heat and is therefore called the loss modulus [148].

$$|\eta^*| = |G^*| / \omega \quad (\text{Eq. 4.2})$$

where  $\omega$  is the frequency of oscillation.

It is observed that  $\eta^*$  reduced significantly as temperature increased, with a decrease of viscosity approximately by an order of magnitude with every increase of 15 °C. The viscosity also decreased as shear rate increased, i.e. as the angular frequency increased, indicating that PC is a non-newtonian fluid experiences shear-thinning phenomenon.





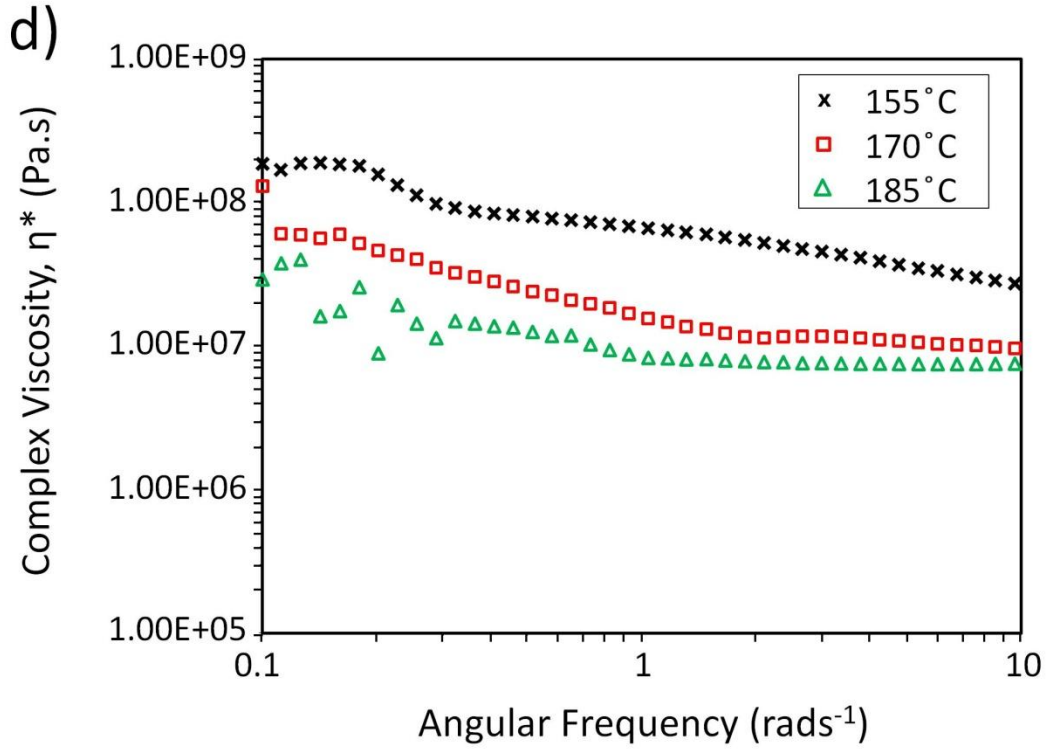


**Figure 4.6.** a) storage modulus b) loss modulus c) complex modulus and d) complex viscosity with respect to angular frequency.

These data for PC were used to construct the time-temperature superposition (TTS) master curve. To construct the master curve of complex modulus, the Williams, Lander, and Ferry (WLF) equation (Eq. 4.1) was used to obtain the shift factors for the superposition curve fitting of the experimental data. The WLF equation expresses a logarithmic relationship between time and temperature [149].

$$\log a_T = \frac{-C_1(T-T_0)}{C_2 + (T-T_0)} \quad (\text{Eq. 4.3})$$

Where  $a_T$  is the temperature shift factor,  $T_0$  is an arbitrary reference temperature,  $C_1$  and  $C_2$  are constants derived from curve fitting. These constants were

determined by minimizing the deviation between the superimposed frequency-complex modulus curves measured at various temperatures. For the polycarbonate employed, Table 4.2 shows the constants and shift factors at each temperature with respect to  $T_g$  (145°C) as the reference temperature for easy reference. Indeed, any temperature could be used as the reference temperature [149]. However, Table 4.2 indicates that in order for the data at different temperature to collapse into the same region,  $C_1$  and  $C_2$  of the polycarbonate used are not constant but temperature dependent. This temperature dependency of  $C_1$  and  $C_2$  has also been observed on different polymers, e.g. polystyrene, polyisobutylene [149].

**Table 4.2.** Values of constants, ( $C_1$  and  $C_2$ ) and shift factors,  $a_T$  at each temperature with respect to the reference temperature.

$C_1$	$C_2$	$T$	$T_0$	$\text{Log } a_T$	$a_T$
10.31	15.5	155	145	-4.04314	0.00009054
11.27	65.21	175	145	-3.55110	0.00028113
12.11	105.12	185	145	-3.33793	0.00045927

Figure 4.7 shows the single curve obtained of complex modulus established from experimental data with  $T_g$  (145°C) as the reference temperature for polycarbonate, and the fitted values of  $C_1$  and  $C_2$  and the corresponding value of  $a_T$  at the various temperatures. The complex modulus curves obtained at these three temperatures experimentally do show good superposition in the mid frequency range, and agree well with the fitted curves over this frequency range. The curves (starting with 185 °C) start to deviate only in the high angular frequency range as compared to the numerically fitted curves. This is because, at high temperature and frequencies, the polymer sample

softened and started to warp. This created slippage of the polymer from the tool fixture. Measurements were repeated but the phenomenon still recurred. It was due to the limitation of the SRF fixture that was used. However during the actual nano-imprinting experiment, it was expected that the polymer would flow at relatively low timescales, hence the curve obtained for the mid angular frequency was still deemed to be meaningful.

To use the data from the curves in subsequent numerical simulations, they must be represented in mathematical terms. The most frequent mathematical approach to represent these data is to employ the exponential (Prony) series.

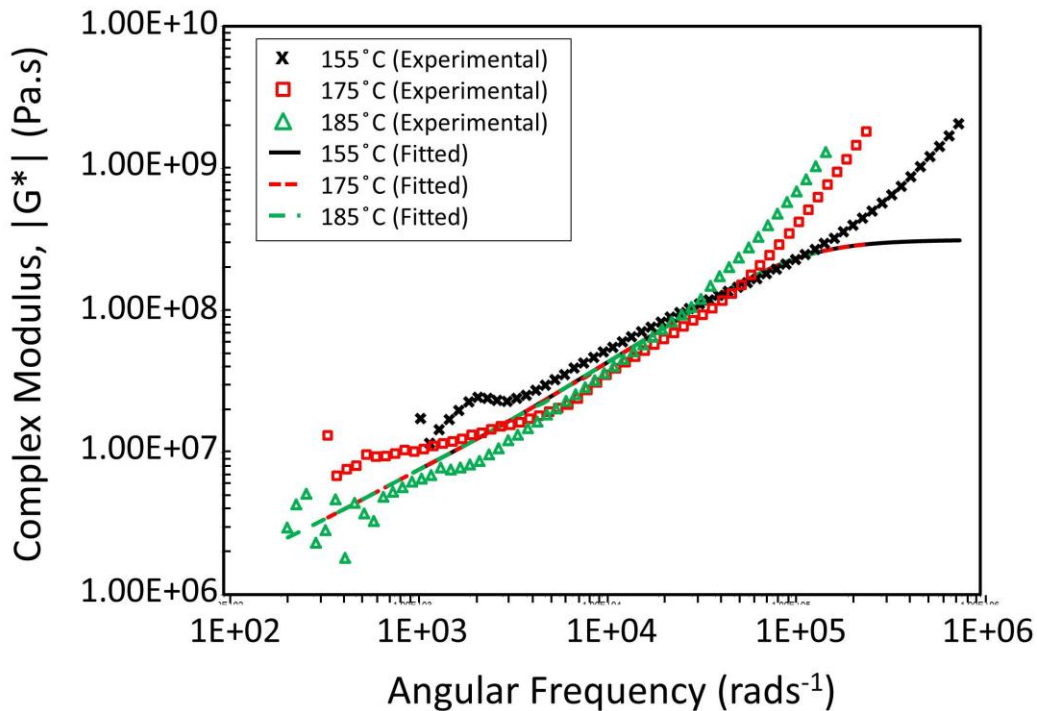


**Figure 4.7.** Master curve of complex modulus at 145 °C reference temperature for polycarbonate depicting the experimental and fitted curves.



Power law Ostwald-de Waele fluid as shown in Eq. 4.4 will be used in the analytical analysis and numerical simulations. Using Eq. 4.4, the constant values employed from experimental curve fitting are  $m = 31.2$  MPa.s,  $n = 0.715$  (Figure 4.8) as shown in Eq. 4.4

$$\eta = m\dot{\gamma}^{n-1} \quad (\text{Eq. 4.4})$$

where  $\dot{\gamma}$  is the shear rate,  $m$  is the material consistency constant,  $n$  is the flow index,  $T_a$  is a material constant associated with temperature sensitivity of the material and  $T$  is the temperature.

The surface tension value was also estimated from the curve fitting of measurement results (obtained from DMTA) to be  $\sigma = 0.00006$  N/mm. However, it should be noted that the power-law model is adequate only for those materials whose Newtonian viscosity is limited to very small shear rate.

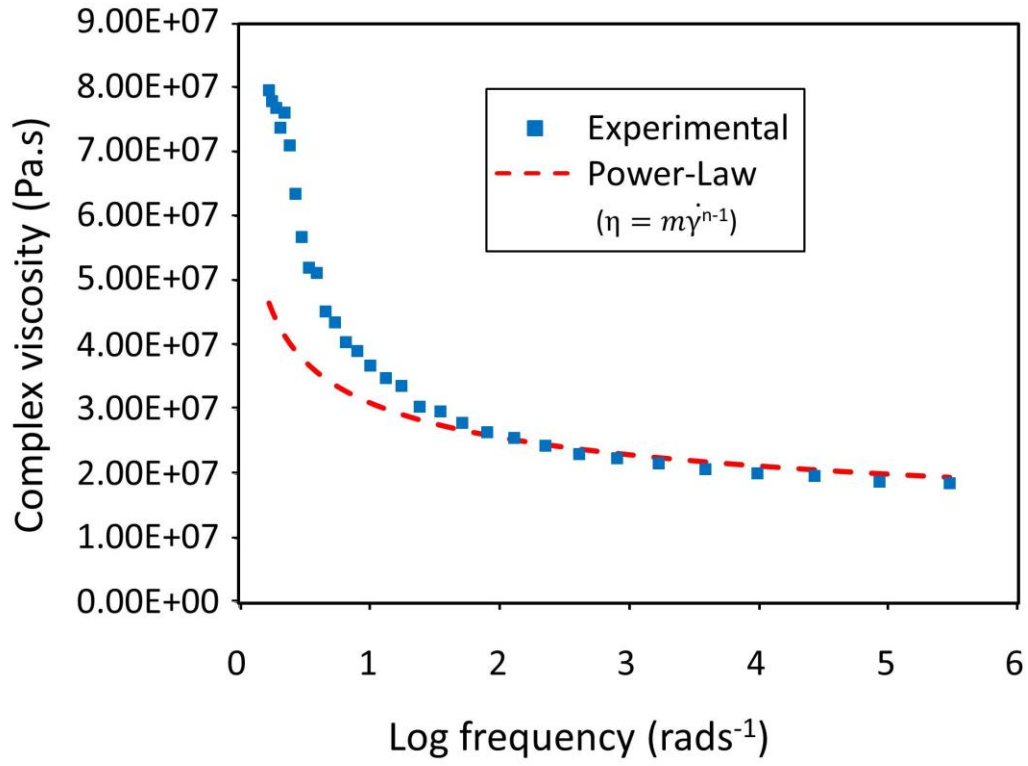


**Figure 4.8.** Fitting curves of viscosity at temperature 165°C according to Power-law model

To incorporate the Prony series, relaxation to the material using the available experimental data, the relaxation modulus in the GMM model was first examined. The relaxation modulus as a function of time  $G(t)$  can be divided into two components;  $G'$  (storage modulus) and  $G''$  (loss modulus). They can be expressed as a series of relaxation time  $\lambda_i$  and weight factors  $g_i$  (Table 4.3) [150].

**Table 4.3.** Summary of equations for relaxation modulus  $G'$  (storage modulus) and  $G''$  (loss modulus) by relaxation time  $\lambda_i$  and weight factors  $g_i$ .

$G(t) = \sum_{i=1}^N g_i \exp(-t/\lambda_i)$	
Storage modulus	Loss modulus
$\Rightarrow G' = \omega \int_0^{\infty} \sum_{i=1}^N g_i \exp(-s/\lambda_i) \sin \omega s ds$ <p style="text-align: right;">(Eq. 4.4)</p>	$\Rightarrow G'' = \omega \int_0^{\infty} \sum_{i=1}^N g_i \exp(-s/\lambda_i) \cos \omega s ds$ <p style="text-align: right;">(Eq. 4.7)</p>
$\Rightarrow -\sum_{i=1}^N g_i \left\{ -1 + \frac{1}{\omega \lambda_i^2} \int_0^{\infty} \sin \omega s \exp(-s/\lambda_i) ds \right\}$ $\therefore \int_0^{\infty} \sin \omega s \exp(-s/\lambda_i) ds = \frac{\omega^2 \lambda_i^2}{1 + \omega^2 \lambda_i^2}$ <p style="text-align: right;">(Eq. 4.5)</p>	$\Rightarrow \sum_{i=1}^N g_i \left\{ \frac{1}{\lambda_i} \int_0^{\infty} \cos \omega s \exp(-s/\lambda_i) ds \right\}$ $\therefore \int_0^{\infty} \cos \omega s \exp(-s/\lambda_i) ds = \frac{\omega \lambda_i}{1 + \omega^2 \lambda_i^2}$ <p style="text-align: right;">(Eq. 4.8)</p>
$\therefore G' = \sum_{i=1}^N g_i \frac{\omega^2 \lambda_i^2}{1 + \omega^2 \lambda_i^2}$ <p style="text-align: right;">(Eq. 4.6)</p>	$\therefore G'' = \sum_{i=1}^N g_i \frac{\omega \lambda_i}{1 + \omega^2 \lambda_i^2}$ <p style="text-align: right;">(Eq. 4.9)</p>

Figure 4.7 also depicts the fitted master curve of the complex modulus ( $|G^*|$ ) where Eqs. 4.6 and 4.9 were used to establish a mathematical relation between the angular frequency and the complex modulus. The curve fitting was performed as follow:

Let  $\rho_i = \ln G_i$ ,  $t_i = \ln \lambda_i$

$$G' = \sum_{i=1}^N G_i \frac{\omega^2 \lambda_i^2}{1 + \omega^2 \lambda_i^2} = \sum_{i=1}^N \frac{\omega^2 \exp(\rho_i + 2t_i)}{[1 + \omega^2 \exp(2t_i)]} \quad (\text{Eq. 4.5})$$

$$G'' = \sum_{i=1}^N G_i \frac{\omega \lambda_i}{1 + \omega^2 \lambda_i^2} = \sum_{i=1}^N \frac{\omega \exp(\rho_i + t_i)}{[1 + \omega^2 \exp(2t_i)]} \quad (\text{Eq. 4.6})$$

$$|G^*(\omega)| = \sqrt{G'^2(\omega) + G''^2(\omega)} \quad (\text{Eq. 4.7})$$

$$= \sqrt{\left[ \sum_{i=1}^N \frac{\omega^2 \exp(\rho_i + 2t_i)}{1 + \omega^2 \exp(2t_i)} \right]^2 + \left[ \sum_{i=1}^N \frac{\omega \exp(\rho_i + t_i)}{1 + \omega^2 \exp(2t_i)} \right]^2} \quad (\text{Eq. 4.8})$$

$$= \sum_{i=1}^N \frac{\omega \exp(\rho_i + t_i)}{1 + \omega^2 \exp(2t_i)} \sqrt{\omega^2 \exp(2t_i) + 1} \quad (\text{Eq. 4.9})$$

In this investigation, ten elements (see Figure 4.9) were used to span the spectrum of relaxation times represented by the transition behavior of the polymer. Table 4.4 shows the calculated values for the stiffness ( $G_i$ ) and Prony coefficients ( $\lambda_i$  and  $g_i$ ) of the respective Maxwell element. These values were calculated so as to minimize the sum of logarithmic square of the errors from the measured data. These values would be used to construct the model for polymer filling during nano-imprinting.

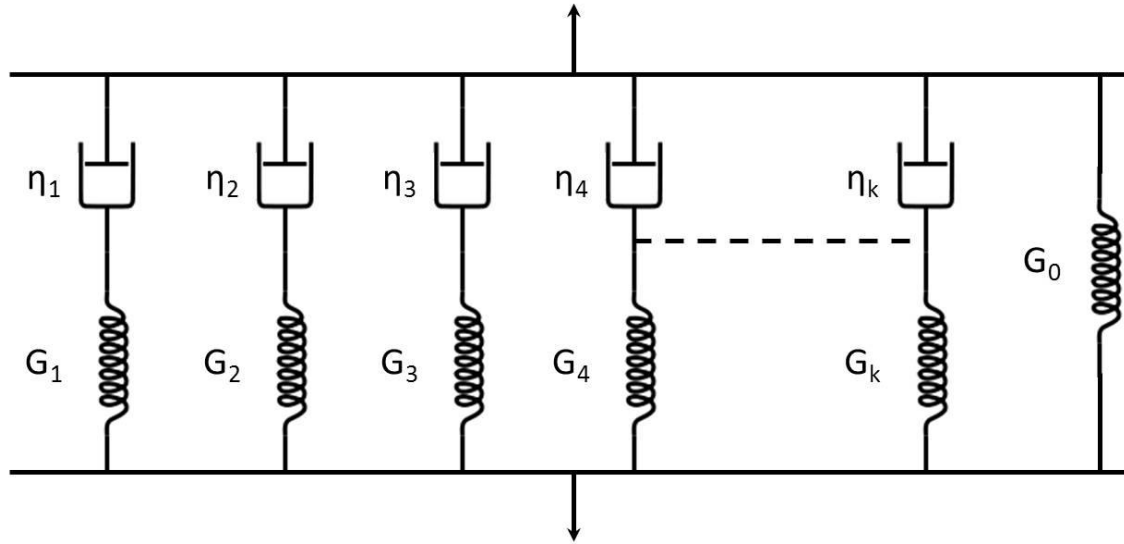


**Figure 4.9.** A Generalized Maxwell Model.

**Table 4.4.** Values calculated for the stiffness ( $G_i$ ) and Prony coefficients ( $\lambda_i$  and  $g_i$ ) of the respective Maxwell element.

$i$	$G_i$	$\lambda_i$	$g_i$
1	3.00E+08	1.00E-05	9.37E-01
2	5.00E+06	1.00E-04	1.56E-02
3	5.00E+06	1.00E-03	1.56E-02
4	3.00E+06	1.00E-02	9.37E-03
5	2.00E+06	1.00E-01	6.25E-03
6	5.00E+06	1.00E+00	1.56E-02
7	1.00E+00	1.00E+01	3.12E-09
8	1.00E+01	1.00E+02	3.12E-08
9	1.00E+02	1.00E+03	3.12E-07
10	1.00E+03	1.00E+04	3.12E-06
$G_0$	3.20E+08		

## 4.5 Summary

This chapter discusses several polymer characterization methods used to obtain the necessary material parameters. The model material used in this work was polycarbonate (PC). Gel permeation chromatography (GPC) was employed to determine the molecular weight distribution and the mechanical properties were characterized through rheological measurements.

From the data obtained, generalized Maxwell model (GMM) with ten elements to span the spectrum of relaxation times was used as a mathematical representation of the relaxation properties of PC.

These data would be employed to obtain the numerical models proposed in Chapter 5 where the mechanics of polymer mold filling during imprinting is examined.



# **Chapter 5   Polymer Flow Modeling during Nano- Imprinting**

## **5.1   Overview**

Several groups have previously studied mechanics of polymer mold filling during imprinting. Parameters such as the imprint temperature [151, 152], imprint pressure [153-155], substrate thickness [156] and molecular weight [152], pattern size [157], layout and density of the mold [158] were investigated.

Numerical simulation for the nano-imprinting process is valuable in several ways. Firstly, the mold-filling pattern can be predicted. Once the filling pattern is known, the polymeric molecular orientation (alignment to filling direction) can be estimated. This can influence the mechanical properties and structural behaviour of a part. Such information allows one to choose the appropriate polymeric materials and pattern layout as required by the application. Secondly, the cycle time of the imprint process can be optimized by optimizing the process parameters through simulating the process. A reasonable window of process conditions could be estimated with a model of residual stress and distortion to ensure acceptable product quality [2-3].



However, most of the polymer flow studies performed to-date for the nano-imprinting process are in the micrometer length scale [147, 156, 159-166]. In such length scales, surface tension or capillary effect has not been considered and are usually dismissed as negligible both in analytical as well as numerical calculations. Hitherto, numerical modeling of nano-imprinting has not considered capillary effects. Nevertheless, in nano-scale mold filling of high aspect ratio pores, the capillary effect is an important factor. When the aspect ratio of the mold pores is high, the filling or displacement of the softened polymer solely by pressure would require extremely high values that would result on the breakage of the mold [167]. Many of the polymers in softened state are able to wet the mold surface and the capillary effect then dominates over the pressure applied during the process of imprinting. .

Hence, this chapter aims to investigate the role of capillary effects on the filling process of a cylindrical nano-cavity during the nano-imprint process and to propose a new numerical model to predict the polymer heights. The material parameters obtained from Chapter 4 will be employed in the proposed numerical model.

For comparison of experimental results against the numerical simulations, single-tier instead of multi-tier imprinted PC pillars were used. Commercially available single tier (linear) PAA molds were used for the purpose since this study requires a number of repeated experiments. Experiments were performed to measure the actual height of the pillars and the results obtained were used to verify the proposed model. The multi-tiered PAA molds will only be used when the process parameters have been optimized.

## 5.2 Evidence of Capillary Effect

Figure 5.1 portrays the surface tension effect when imprinting at different temperatures. Figures 5.1a and b show atomic force micrograph (AFM) images taken with AFM Multimode-Digital Instruments of the imprint performed at 165°C and 175°C respectively and subsequently demolded by wet-etching with 5 wt% phosphoric acid. The PAA molds were removed via wet-etching to avoid any geometrical deformation due to demolding by peeling off. The higher contrast in Figure 5.1b indicates that there is a difference in pillar heights due to the non-uniformity in pore filling. This effect is believed to be caused by the slight difference in the diameter of the pores which is inherent in the anodization process. The variation in pore sizes have a significant effect on the capillary forces (see Eq. 5.38), and thus provides an explanation for the difference in pillar heights. As such, this observation suggests the existence of capillary effect on the filling of the pores in the mold, and the necessity in investigation its effects.

Figures 5.1c and d show the profiles of the respective features obtained. The distinct difference in the profiles shows the surface tension effect on polymer filling when the temperature is varied. At the higher imprinting temperature of 175°C, it is evident that polymer flow along the wall of the cylindrical cavity of AAO membrane was significantly more pronounced, resulting in an approximately 200 nm peak-valley difference (ref. Figure 5.1d) as compared to the small difference as observed in Figure 5.1c.

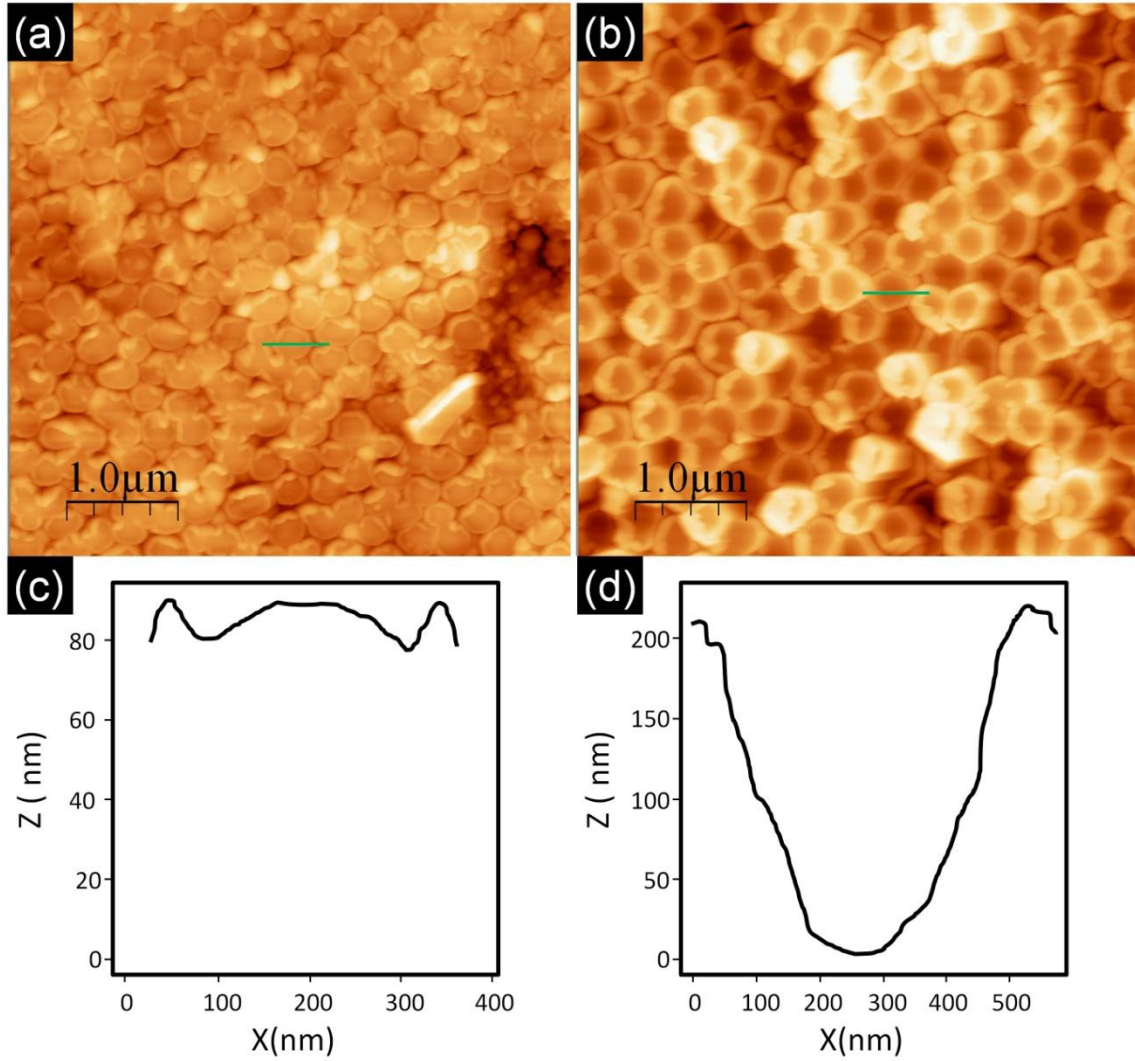


**Figure 5.1.** Atomic force micrograph (AFM) images of the imprint performed at a) 165°C and b) 175°C respectively and subsequently demolded by wet-etching. The profiles of the imprinted feature obtained at c) 165°C and d) 175°C respectively.

Hence, to understand the role of capillary force and surface tension on the filling process, the viscous polymer flow model using the lubrication approximation [168] is employed and will be elaborated in this section. The imprinting process is simulated with consideration of both the polymer displacement caused by pressure and

the capillary effects due to surface tension. The basic flow model constructed is used to establish the relationship between the flow parameters and the pillar height.

### 5.3 Experimental Details

Nano-imprint experiments were carried out to validate the proposed model. The model polymer material in this study was polycarbonate (PC) as characterized in Section 4.2. The geometrical thickness of the circular PC film is  $h_0 = 250 \mu\text{m}$ . The porous anodic alumina (PAA) mold employed was obtained commercially (Anodisc® from Whatman Inc). The specifications of the PAA mold are – thickness of the membrane:  $60 \mu\text{m}$ , pore density:  $10.7 \times 10^6 \text{ pores/mm}^2$ , pore wall thickness:  $80.4 \pm 33.34 \text{ nm}$ , average pore diameter:  $271.4 \pm 23.3 \text{ nm}$  (Figure 5.2).

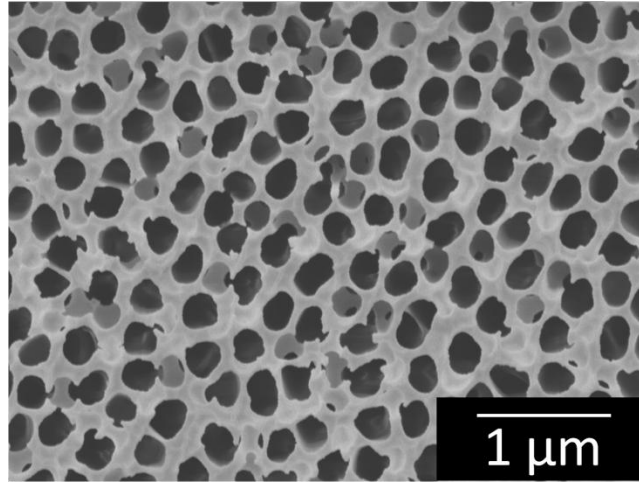


**Figure 5.2.** SEM image of the commercial PAA mold used for imprinting experiments. The specifications of the PAA mold are – thickness of the membrane:  $60 \mu\text{m}$ , pore density:  $10.7 \times 10^6 \text{ pores/mm}^2$ , pore wall thickness:  $80.4 \pm 33.34 \text{ nm}$ , average pore diameter:  $271.4 \pm 23.3 \text{ nm}$ .

Figure 5.3 schematically depicts the entire process flow. Nano-imprinting was conducted under an applied pressure of 1 MPa. The processing temperature used was 165 °C, which is well above the glass transition temperature of this material (approximately 145 °C). The imprinting process was varied between 60 s, 150 s, 300 s, 600 s and 1200 s. The imprinting pressure was removed at the end of the process without active cooling and the imprinted polymer with the mold was unloaded from the imprinter immediately. Figure 5.4a shows the temperature and pressure profile of the imprint process. The temperature of the imprinted polymer – mold was measured with a thermocouple with the cooling profile as shown in Figure 5.4b.

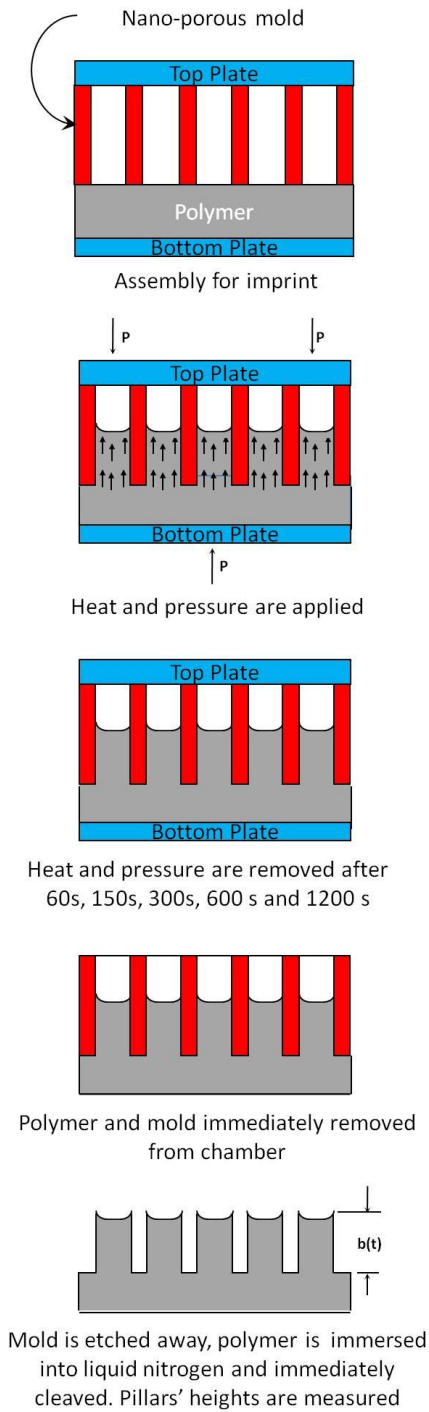


**Figure 5.3.** Schematic of the nano-imprint process for pillar height measurement.

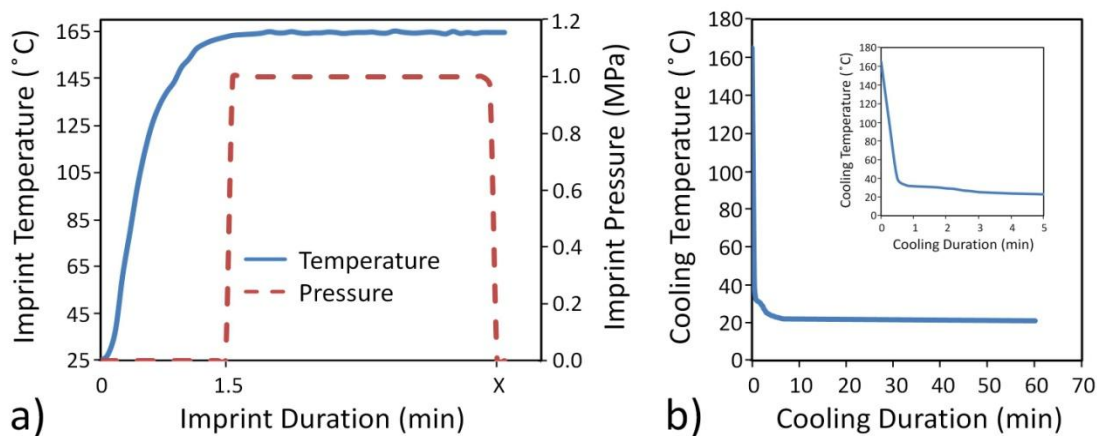


**Figure 5.4.** a) Temperature and pressure profiles during imprint. b) Temperature profile during cooling (inset showing initial 5 min of the cooling profile)

To measure the height of the pillars, the imprinted polymer – mold was cooled with liquid nitrogen and immediately cleaved. The PAA mold was then dissolved using 5 wt%  $\text{H}_3\text{PO}_4$  over a period of 12 hours. The cross-sections of the pillars were observed with scanning electron micrograph (SEM) JEOL 6700. Using an image processing software (ImageJ, version 1.41o), each image was calibrated with the scale-bar of the SEM image prior to the pillar height measurements as shown in Figure 5.5.

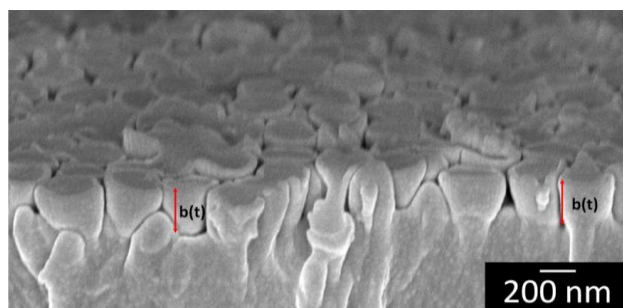


**Figure 5.5.** SEM image of cross-sectioned PC imprinted at 165 °C under pressure of 1 MPa for 150 s for pillars' heights measurements.

Thirty measurements of the pillars' heights and diameters were obtained from each SEM image and subsequently averaged. The respective mean and standard deviation values are tabulated in Table 5.1.

**Table 5.1.** Imprint parameters and pillar heights. Standard deviations are shown.

Temp (°C)	Pressure (MPa)	Imprint Duration (s)	Pillars' Height (nm)	Standard Deviation (nm)
165	0.6	10	91.5	20.7
165	1.0	60	183.1	26.9
165	1.0	150	276.9	45.2
165	1.0	300	358.2	69.4
165	1.0	600	507.8	45.5
165	1.0	1200	798.3	64.9

## 5.4 Flow Analysis of an Amorphous Polymer in Nano-imprinting

To understand and to predict the role of capillary effects on the filling process of a cylindrical nano-cavity during the nano-imprint process, the viscous polymer flow model using the lubrication approximation is employed to simulate the mold filling by considering the pressure exerted on the polymer by the press plates and the capillary effects due to surface tension under isothermal conditions. The axisymmetrical time-dependent squeeze flow field is studied. The simulated results show the evolution of polymer filling under these conditions.



### 5.4.1 Physical description

As the dimensions of the topographical structures decrease to nano-meter scale, surface-to-volume ratio increases significantly. As such, surface tension is no longer negligible in comparison with viscous stress. The polymer flow analysis performed in this investigation takes into account the capillary force exerted due to surface tension effect.

An efficient approach for modeling nano-structures of any size is to develop a sub-domain strategy, in which the entire structure can be approximated by these sub-domains. In this investigation, the randomly distributed nano structures in the PAA mold were approximated by many axisymmetric unit cells, with each axisymmetric unit cell contains one nano-hole, see Figure 5.6. Axisymmetrical constraint conditions were used at each cylindrical surface for reducing the computational domain to a single unit cell.

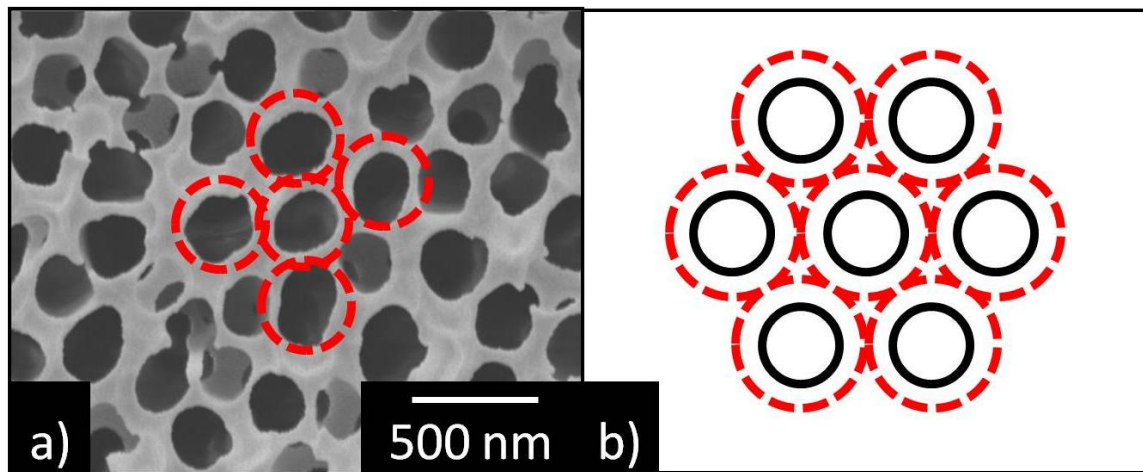


**Figure 5.6.** a) SEM image and b) schematic of axisymmetric unit cell as sub-domain on a PAA mold.

## 5.4.2 Mathematical formulation

The mold filling phenomena in nano-imprinting is assumed to be governed by the following physics and assumptions:

### 1) Continuum Assumption

The Knudsen number,  $Kn$ , represents the ratio of the molecular mean-free path to the characteristic length. It is well known that deviation from the continuum hypothesis for gas media is identified with the Knudsen number, which is defined as

$$K_n = l / L \quad (\text{Eq. 5.1})$$

where  $l$  is the mean-free-path of the molecules and  $L$  is a characteristic length scale of flow device [1]. The dimension of a polymer molecular-chain is usually characterized by the radius of gyration,  $R_g$ , defined as the square root of the average squared distance of all repeating units of the chain from the center of the mass of the chain, which can be estimated as follow [2]:

$$R_g = 0.012M^{0.583} \quad (\text{Eq. 5.2})$$

where  $M$  is the molecular weight.

A low Knudsen number is required for the validity of the continuum assumption. For most liquids, the mean-free path is in the order of few nanometers. From the above equation, for PC used with  $M = 34,218$  g/mol obtained from our GPC

experiments,  $R_g = 5.28$  nm. In addition, the minimum characteristic length of flow device (characterized as the height of a nano-pore) is  $L > 100$  nm. Thus Knudsen number is calculated to be  $K_n = R_g / L = 0.05 < 0.1$ .

## 2) **Lubrication Approximation**

In nano-imprinting, many parts are fabricated out of thin sheets, with the dimension  $a$  in the radial direction of the cylindrical cavity being much smaller than the other dimensions of the part, see schematic representation in Figure 5.7. The mold-filling model makes use of this simplifying feature. Several assumptions are made:

- The polymeric film is treated as an incompressible isotropic fluid and its flow is creeping.
- The dimension perpendicular to the flow direction is smaller than the dimension along the flow direction, eg.  $r$  vs.  $h(t)$ ;  $a$  vs.  $b(t)$
- The imprint velocity is time-independent (constant).
- No-slip boundary condition at the top and bottom surfaces of the plate and wall of cylindrical cavity.
- No junction effect (no velocity change, energy loss and second flow effect) as the polymer fills the cylindrical cavity from the film.
- $\theta_a$  is the dynamic contact angle between the polymer fluid and the pore wall.

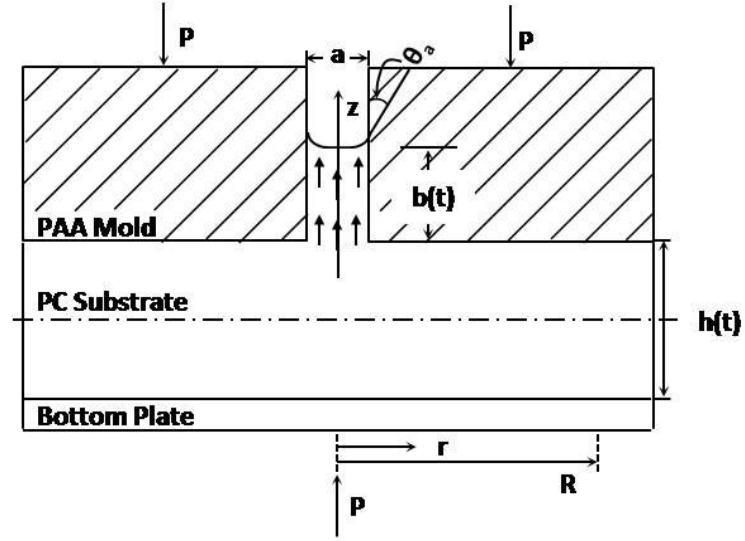


**Figure 5.7** Model domain, parameters and coordinate system used in theoretical simulation

### 3) Generalized-Newtonian Model

In general, the extra stress is assumed to be [168]:

$$\tau = -p\mathbf{I} + 2\eta\mathbf{E} \quad (\text{Eq. 5.3})$$

where  $p$  is the fluid phase hydrostatic pressure,  $I$  is the identity tensor,  $\eta$  the viscosity of fluid.  $E$  is the local rate of strain defined as [168]:

$$\mathbf{E} = \frac{1}{2} [\nabla \mathbf{u} + \nabla \mathbf{u}^T] \quad (\text{Eq. 5.4})$$

The most commonly used viscosity for a polymeric system is the power-law fluid model with Arrhenius-type temperature dependence [169]. In this model, the viscosity is expressed as

$$\eta = m_0 \exp\left(\frac{T_a}{T}\right) \dot{\gamma}^{n-1} \quad (\text{Eq. 5.5})$$

where  $\dot{\gamma}$  is the shear rate,  $m_0$  is the material consistency constant,  $n$  is the flow index,  $T_a$  is a material constant associated with temperature sensitivity of the material and  $T$  is the temperature.

It should be noted that the power-law model is adequate only for those materials whose Newtonian viscosity is limited to very small shear rate. The power-law model limits the fluid flow at higher shear rates and will present erroneous results when describing creep flows with lower shear rates. Therefore, for a wide range of shear rates experienced during nano-imprinting, the modified Cross model (WLF-Cross model) is more appropriate, as it can capture the Newtonian plateau at low shear rates, non-linear transition zone at moderate rates and strong shear thinning behaviors at high shear rates [170].

$$\eta = \frac{\eta_0}{1 + (\eta_0 \dot{\gamma} / \tau^*)^{1-n}} \quad (\text{Eq. 5.6})$$

where  $\eta_0$  is the Newtonian viscosity at zero shear-rate for a sufficient small shear rate  $\dot{\gamma}$ ,  $\eta_0 = B \exp(T_b / T)$ , and  $B$ ,  $T_b$ ,  $n$  and  $\tau^*$  are material constants. At high shear rate, Eq. 5.6 can be simplified to a power-law model

$$\eta = (\eta_0 \dot{\gamma}_0^{1-n}) \dot{\gamma}^{n-1} \quad (\text{Eq. 5.7})$$

$$\dot{\gamma}_0 = \tau^* / \eta_0$$

#### 4) Squeeze Effect

With the exception of the moving top plate, these assumptions are similar to those made by Kim [171]. The Hele-Shaw model is thus generalized for a description of the polymer flow in nano-imprinting but with the additional consideration of surface tension effect. Based on these assumptions, the pressure distribution for thin cavity and cylindrical tube satisfies the equations as follows:

For thin cavity

$$\frac{\partial}{\partial x} \left( S \frac{\partial p}{\partial x} \right) + \frac{\partial}{\partial y} \left( S \frac{\partial p}{\partial y} \right) = \dot{h} \quad (\text{Eq. 5.8})$$

where  $p$  is applied pressure,  $S = \int_0^h \frac{(z - h/2)^2}{\eta} dz$ ,  $\eta$  is the viscosity.

For cylindrical tube

$$Q = 2\pi \int_0^R r u_z(r) dr \quad (\text{Eq. 5.9})$$

where  $S = \int_0^R \frac{r^3}{\eta} dr$

For an isothermal power-law fluid,  $\eta = m\dot{\gamma}^{n-1}$ , with  $\dot{\gamma}$  the shear rate,  $m$  the material consistency constant, and  $n$  the non-Newtonian flow index:

$$S = \frac{\Lambda^{1/n-1} h^{\frac{1+2n}{n}}}{m^{1/n} 2^{\frac{1+n}{n}}} \left( \frac{n}{1+2n} \right) \quad (\text{Eq. 5.10})$$

where  $\Lambda = -\frac{\partial P}{\partial z}$

For a circular region, the approximated solution of the pressure distribution for a power-law fluid subjected to zero pressure on the free flow front is

$$P(r) = -m \left( \frac{2n+1}{2n} \frac{\dot{h}}{h^{2+1/n}} \right)^n \frac{R^{n+1}}{n+1} \left[ 1 - \left( \frac{r}{R} \right)^{n+1} \right] \quad (\text{Eq. 5.11})$$

and 
$$h(t) = h_0 \left\{ 1 - \frac{2(n+1)h_0^{1+1/n}t}{2n+1} \left[ -\frac{(n+3)F}{\pi n R^{n+3}} \right]^{1/n} \right\}^{-\frac{n}{n+1}} \quad (\text{Eq. 5.12})$$

where  $F$  can be a linear function of time at the initial stage ( $t_1 < t < t_2$ ) and then a constant load force ( $t > t_2$ ) as shown in Figure 5.8.

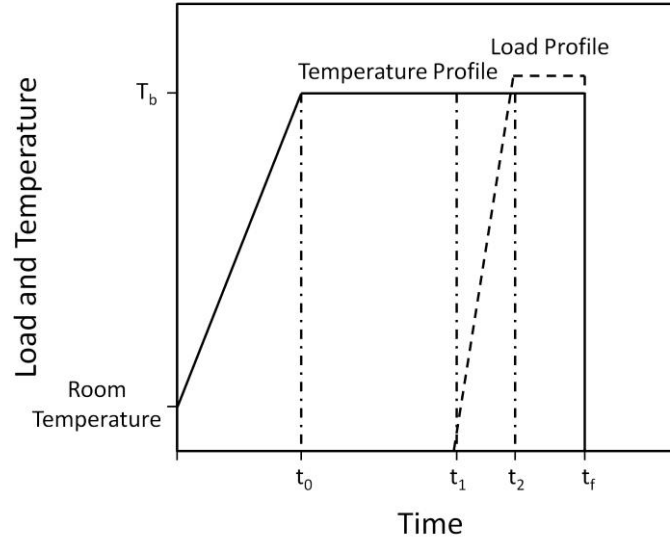


**Figure 5.8.** Schematic of load and temperature profiles.

## 5) Capillary Force

From an energy perspective, the effective surface tension force applied on the fluid in a nano-pore can be derived from the derivative of the surface energy of the whole mold system with the spatial coordinates in Figure 5.7. Figure 5.2 is a SEM image of the capillary nano-pores. The total energy  $S_E$  can be expressed as follows:

$$S_E = S_0 + 2\pi a(l-z)\gamma_{sa} + 2\pi az\gamma_{sl} \quad (\text{Eq. 5.13})$$

where  $S_0$  is the surface energy stored in the filling reservoir,  $2\pi a(l-z)\gamma_{sa}$  the surface energy generated by the void area, and  $2\pi az\gamma_{sl}$  the surface energy generated by the wetting area.



Taking the derivative of Eq. 5.13 with respect to  $z$ , the equivalent capillary force,  $F_s$  applied on the fluid column along the  $z$  direction is obtained:

$$F_s = -\frac{dS_E}{dz} = 2\pi a(\gamma_{sa} - \gamma_{sl}) = \Delta p_{la} \pi a^2 \quad (\text{Eq. 5.14})$$

The pressure drop  $\Delta p_{la}$  across the liquid-air interface can therefore be deduced as :

$$\Delta p_{la} = \frac{2(\gamma_{sa} - \gamma_{sl})}{a} = \frac{2\gamma_{la} \cos \theta_a}{a} \quad (\text{Eq. 5.15})$$

where  $\gamma_{la}$  is the surface tension force between the liquid and air, and  $\theta_a$  the contact angle.

## 6) Back Pressure in Nano-Imprint

It should be noted that the pressure caused by trapped air acting on the pillar front during filling of an imprinting process increases from the atmosphere pressure at the beginning. Assuming an ideal gas situation, it will theoretically reach an infinite value when the flow front reaches the end of the cavity. Hence, it is an important factor to assess if it would overcome the capillary effect.

The modeling of air back pressure assuming an ideal gas situation for capped end of nano-pore (closed, without venting) in isothermal system was assessed. This was assessed based on the ideal gas equation as well as from the volume ratio which is the

ratio of the volume of polymer fill to the initial volume of void cavity (pillar height) in the AAO mold (60 $\mu\text{m}$  height). The model for the assessment is given in Appendix B.

The volume ratio for the experiments conducted was not very high (less than 20%). Thus, pressure increased (0.118MPa) with capped effect is about 20% higher than that (0.1MPa) without capped effect. However, this capped effect on pressure is still negligible as compared to surface tension which is around 2.4 MPa as shown in Figure 5.9 comparing the nano-pillar height with and without the capped effect.

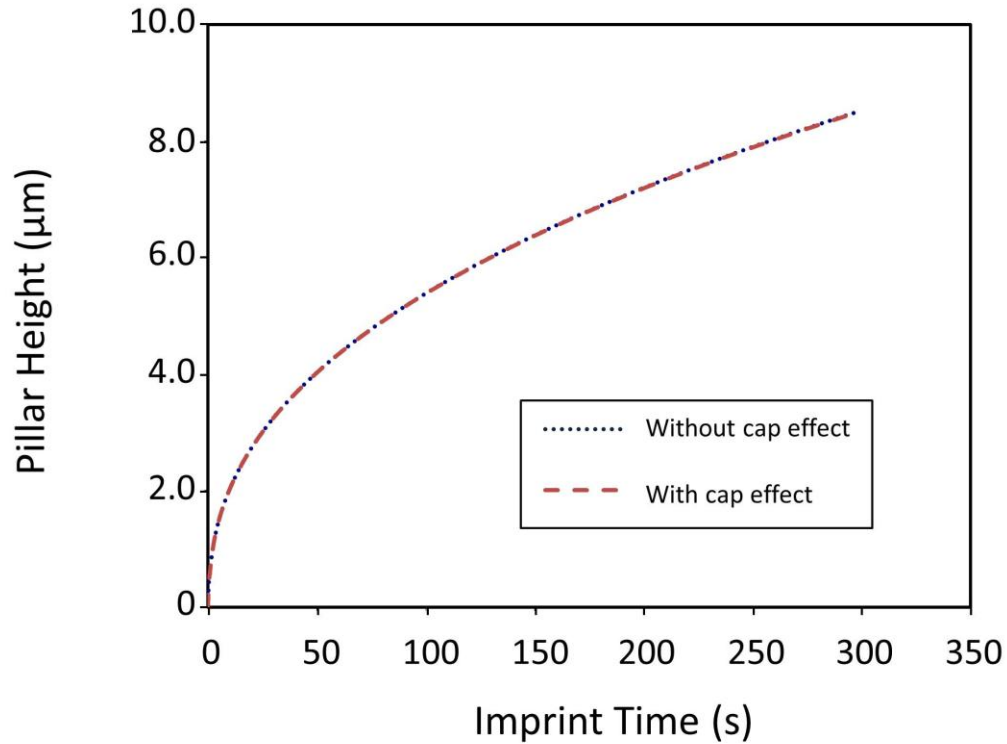


**Figure 5.9.** Comparison of pillar height achieved with and without capped effect.

## 7) Flow Motion Model Within Nano-Pore

Driven by the pressure, the flow motion of the polymer melt into a cylindrical nano-pore subjected to the surface tension force can be solved by using incompressible Navier-Stokes equation based on the lubrication approximation [171] for the problem depicted schematically in Figure 5.7. The governing momentum and mass balance equations [168] as:

$$\nabla \cdot \vec{u} = 0 \quad (\text{Eq. 5.16})$$

$$-\nabla P + \nabla \cdot \vec{\tau} = 0 \quad (\text{Eq. 5.17})$$

where:  $P$  = the hydrostatic pressure

$\vec{\tau}$  = the extra stress tensor

$\vec{u}$  = the velocity field

For a generalized Newtonian fluid, the extra stress tensor  $\vec{\tau}$  is given by:

$$\vec{\tau} = \eta(|\dot{\gamma}|, T, \phi) \dot{\gamma} \quad (\text{Eq. 5.18})$$

For an axisymmetric flow in the cylindrical coordinates  $(r, z, \theta)$  the magnitude of  $|\dot{\gamma}|$  for the shear rate tensor  $\dot{\gamma}$  can be written as:

$$|\dot{\gamma}| = \left[ \frac{1}{2} \{ \dot{\gamma} : \dot{\gamma} \} \right]^{1/2} = \left[ \frac{1}{2} \{ \dot{\gamma}_{rr}^2 + \dot{\gamma}_{\theta\theta}^2 + \dot{\gamma}_{zz}^2 + 2\dot{\gamma}_{rz}^2 \} \right]^{1/2} \quad (\text{Eq. 5.19})$$

The components in Eq. 5.19 are given by:

$$\dot{\gamma}_{rr} = 2 \frac{\partial u_r}{\partial r}, \dot{\gamma}_{\theta\theta} = 2 \frac{u_r}{r}, \dot{\gamma}_{zz} = 2 \frac{\partial u_z}{\partial z}, \dot{\gamma}_{rz} = \frac{\partial u_z}{\partial r} + \frac{\partial u_r}{\partial z} \quad (\text{Eq. 5.20})$$

Therefore, Eq. 5.16 and Eq. 5.17 can be written as:

$$\frac{\partial u_r}{\partial r} + \frac{u_r}{r} + \frac{\partial u_z}{\partial z} = 0 \quad (\text{Eq. 5.21})$$

$$-\frac{\partial p}{\partial r} + \frac{\partial \tau_{rr}}{\partial r} + \frac{\tau_{rr}}{r} + \frac{\partial \tau_{rz}}{\partial z} - \frac{\tau_{\theta\theta}}{r} = 0 \quad (\text{Eq. 5.22})$$

$$-\frac{\partial p}{\partial z} + \frac{\partial \tau_{rz}}{\partial r} + \frac{\tau_{rz}}{r} + \frac{\partial \tau_{zz}}{\partial z} = 0 \quad (\text{Eq. 5.23})$$

Due to axisymmetry,  $\tau_{rz} = \tau_{zr}$ . For a pressure-driven tube flow,  $\partial/\partial z \ll \partial/\partial r$ ,  $u_r \ll u_z$ ,  $u_z = u_z(r, z)$  and  $p = p(z)$ . Based on these assumptions, also known as the lubrication approximation theory [168], Eq. 5.22 and Eq. 5.23 can be simplified as [168]:

$$\frac{\partial p}{\partial z} - \frac{1}{r} \frac{\partial}{\partial r} (r \eta \frac{\partial u_z}{\partial r}) = 0 \quad (\text{Eq. 5.24})$$

The global continuity equation associated with the above equations is given by

$$Q = 2\pi \int_0^R r u_z(r) dr \quad (\text{Eq. 5.25})$$

where  $Q$  is the volumetric flow rate,  $R$  is the radius of the capillary tube. Consistent with above flow equations, appropriate boundary conditions in the  $r$  direction are given by

$$\frac{\partial u_z}{\partial r} = 0 \text{ at } r = 0 \quad (\text{Eq. 5.26})$$

$$u_z = 0 \text{ at } r = a \quad (\text{Eq. 5.27})$$

On the basis of hydrodynamic principles [172], Eq. 5.24 is averaged over the volume of the moving liquid

$$\overline{\frac{dp}{dz}} - \overline{\frac{1}{r} \frac{\partial}{\partial r} (r \eta \frac{\partial u_z}{\partial r})} = 0 \quad (\text{Eq. 5.28})$$

For a relative slow flow, the assumption of a power law liquid

$\eta = m \dot{\gamma}^{n-1} = m \left( \frac{\partial u_z}{\partial r} \right)^{n-1}$  can be employed. Thus, it can be assumed that the fully developed velocity profile in the cylindrical nano-pore follows a parabolic profile given by:

$$v_z(r, t) = \overline{v_z(t)} \frac{3n+1}{n+1} \left[ 1 - \left( \frac{r}{a} \right)^{1+1/n} \right] \quad (\text{Eq. 5.29})$$

where

$$\overline{v_z(t)} = \frac{2}{a^2} \int_0^a v_z(r, t) r dt \quad (\text{Eq. 5.30})$$

is the flow velocity averaged over the cross section of the cylindrical nano-pore.

The averaged pressure gradient term is obtained by taking into account that

$$p|_{z=0} = \bar{p} \text{ and}$$

$$p|_{z=h(t)} = -\frac{2\gamma \cos \theta_a}{a} \quad (\text{Eq. 5.31})$$

where  $\theta_a$  is the capillary contact angle. For simplicity but without loss of generality due to the slow flow rate, it is assumed that  $\theta_a \approx \theta_s$ , where  $\theta_s$  is the static contact angle. The average pressure gradient can now be written as:

$$\frac{\overline{dp}}{dz} = \frac{1}{b} \left\{ \frac{2\sigma \cos \theta_s}{a} + m \left( \frac{2n+1}{2n} \frac{\dot{h}}{h^{2+1/n}} \right)^n \frac{R^{n+1}}{n+1} \left( 1 - \frac{2}{n+3} \left( \frac{a}{R} \right)^{n+1} \right) \right\} \quad (\text{Eq. 5.32})$$

The viscous term may be averaged as:

$$\overline{\frac{m}{r} \frac{\partial}{\partial r} \left( r \left( -\frac{\partial u_z}{\partial r} \right)^n \right)} = \frac{2m}{a^{1+n}} \left( \frac{3n^2 + n}{n^2 + 2n + 1} \right)^n \overline{u_z(t)}^n \quad (\text{Eq. 5.33})$$

Together with the mass balance equation,  $\overline{u_z(t)} = \dot{b}$  and substituting Eq. 5.32 and Eq. 5.33 into Eq. 5.28, one obtains:

$$\frac{1}{b(t)} \left\{ \frac{2\sigma \cos \theta_a}{a} + m \left( \frac{2n+1}{2n} \frac{\dot{h}}{h^{2+1/n}} \right)^n \frac{R^{n+1}}{n+1} \left( 1 - \frac{2}{n+3} \left( \frac{a}{R} \right)^{n+1} \right) \right\}$$

$$+ \frac{2m}{a^{1+n}} \left( \frac{3n^2 + n}{n^2 + 2n + 1} \right)^n \dot{b}^n = 0 \quad (\text{Eq. 5.34})$$

The required force for a constant motion of the plates causing polymer melt flow can now be calculated as:

$$F = \int_0^{2\pi R} \int_a^R (\Delta p + \tau_{zz}) \Big|_{z=h} r dr d\theta = 2\pi R^2 \int_a^R \Delta p \left( \frac{r}{R} \right) d \left( \frac{r}{R} \right)$$

$$\left( \frac{\dot{h}}{h^{2+1/n}} \right) = \frac{2n}{2n+1} \left[ -\frac{(n+1)F}{\pi n R^{n+3}} \left[ \frac{n+1}{n+3} - \left( \frac{a}{R} \right)^2 + \frac{2}{n+3} \left( \frac{a}{R} \right)^{n+3} \right]^{-1} \right]^{1/n} \quad (\text{Eq. 5.35})$$

The analytical solution of a power-law fluid for a height of nano-pillar  $b(t)$  under loading conditions as shown in Figure 5.8 can be derived as:

$$b(t) = \left\{ -\frac{C_0}{C_5 C_1^{\frac{1}{n}}} \frac{n}{n+1} \left[ (C_1 - C_5 \Delta t)^{1+\frac{1}{n}} - C_1^{1+\frac{1}{n}} \right] + C_0 \left[ C_1 - \frac{F_w}{\pi R^2} C_3 C_4 \right]^{\frac{1}{n}} (t - t_2) \right\}^{\frac{n}{n+1}}$$

(Eq. 5.36)

where  $\Delta t = t_2 - t_1$

$$C_0 = \frac{(n+1)^3}{(3n+2)n^2} \left( \frac{a^{n+1}}{2m} \right)^{\frac{1}{n}},$$

$$C_1 = \frac{2\sigma \cos \theta_a}{a},$$

$$C_2 = \frac{F_w}{\pi R^2} \frac{1}{\Delta t},$$

$$C_3 = \left[ \frac{n+1}{n+3} - \left( \frac{a}{R} \right)^2 + \frac{2}{n+3} \left( \frac{a}{R} \right)^{n+3} \right]^{-1},$$

$$C_4 = \left( 1 - \frac{2}{n+3} \left( \frac{a}{R} \right)^{n+1} \right),$$

$$C_5 = C_2 C_3 C_4$$

where  $\sigma$  is the surface tension,  $a$  is the radius of the nano-pore,  $\theta_a$  the dynamic contact angle of polymer,  $n$  the non-Newtonian flow index. It should be noted that for slow flow, it is assumed that  $\theta_a \approx \theta_s$ , where  $\theta_s$  is the static contact angle.

## 8) Numerical implementation

Eq. 5.36 gives the approximated analytical solution of the height evolution of nano-pillar during nano-imprinting using the lubrication approximation. However, for more complex viscosity model, e.g. Herschel-Bulkley fluid, non-linear Eq. 5.8 has to be solved numerically, for example by employing the commonly used finite element method. Finite element formulation for a non-Newtonian isothermal filling flow is basically the same as the previous formulation of Hieber and Shen [169], Kim et al [171], Kennedy [173] and Lam et al [174] except for the inclusion of surface tension effect and moving top plate in this study.

Using the hybrid *Finite Element Method / Finite Difference Method* (FEM/FDM), thin shell triangular elements are employed to describe a three-dimensional



thin part. The triangular elements are further divided into three sub-volumes by connecting the midpoints of their three edges to their centroid, which are considered to be a network of control volume [169]. The control volume at each node is the union of all sub-volumes that are linked to that node, shown as the hatched area in Figure 5.10. The nodal control-volume formulation is derived from the Galerkin approach, as described by Hieber and Shen [169]. The numerical equation for the net mass flow of an element in a planar can be written as [174]:

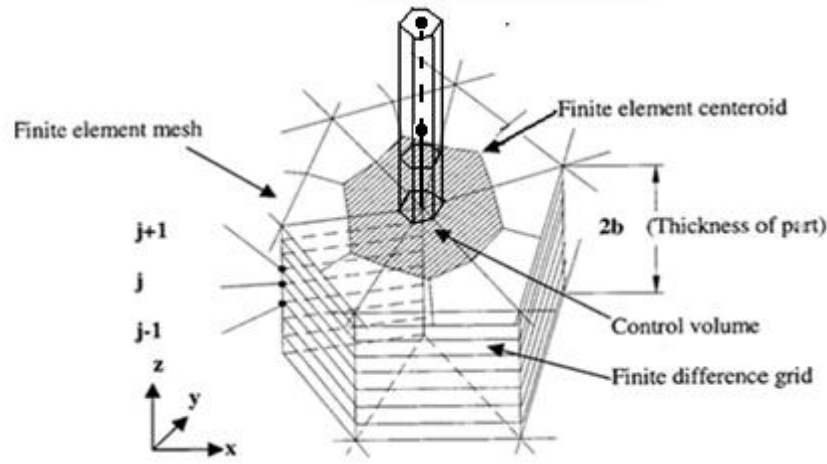


**Figure 5.10.** Control volume and finite difference grid [174]

$$\dot{m}_i^{(l)} = S^{(l)} \sum_{k=1}^3 D_{ik}^{(l)} P_N, \quad i = 1, 2 \text{ or } 3 \quad (\text{Eq. 5.37})$$

where  $S^{(l)}$  and  $D_{ik}^{(l)}$  are the flow conductance and the coefficient of the nodal pressure to the net flow in element respectively.  $l$  transverses all triangular elements of nodal  $N$ .

Mass conservation for the control volume at node  $N$  as shown in Figure 5.10 can be written as:

$$\sum_{l=1}^L S^{(l)} \sum_{k=1}^3 D_{ik}^{(l)} P_{N'} + \sum_{l'=1}^{L'} S^{(l')} \sum_{k=1}^2 R_{ik}^{(l')} P_{N'} = 0 \quad (\text{Eq. 5.38})$$

where  $S^{(l')}$  and  $R_{ik}^{(l')}$  are the flow conductance and the coefficient of the nodal pressure to the net flow in element  $l'$  respectively.  $l'$  transverses all one-dimensional elements of nodal  $N$ .

Nodal Eq. 5.38 can be solved for the nodal pressure.

A Flow Analysis of Network (FAN) approach [174] for which the rectangular cells are replaced by the control volumes is employed to track the flow front advancement as a function of time. To distinguish the filled nodes from the melt front nodes, a fill factor  $f_{ij}$ , having a value between 0 and 1, which is associated with each element to indicate the percentage of filling, is defined by [174]:

$$f_{ij} = \Delta V_{ij} / V_i \quad (\text{Eq. 5.39})$$

Where  $V_i$  and  $\Delta V_{ij}$  denote control volume and filled volume respectively of the  $i$ th vertex node at the  $j$  time step. Numerical calculation of the pressure field is based on mass conservation in each control volume which can be either empty ( $f_{ij} = 0$ ), partially filled ( $0 < f_{ij} < 1$ ) or completely filled ( $f_{ij} = 1$ ) with polymer melt. In each time step, the pressure field is calculated to obtain the velocity distribution in the flow domain.

A boundary condition for Eq. 5.39 is that the pressure is zero on the free flow front for the planar compression flow field. As such, there is no deformation of the liquid flow front. To account for the surface tension effect as a parameter for the evolution of the polymer flow front inside the nano-pores of the template, the Young-Laplace equation (given as  $C_1$  in Eq. 5.36) based on static contact angle is adopted:

$$\Delta p = \frac{2\sigma \cos \theta_a}{a} \quad (\text{Eq. 5.40})$$

### 5.4.3 Verification of Flow Model

Figure 5.11 shows the pillar height evolution with respect to imprint duration. The rate of increase of pillar height in the first minute of imprint is the highest and gradually decreases with imprint duration. To verify the flow model, comparisons between experimental measurements of pillar height and predictions with and without surface tension effect are made and are shown in Figure 5.11. Simulations predicted a higher pillar height with the presence of surface tension to that without surface tension. With the surface tension assumed to be  $\sigma = 0.00006$  N/mm (obtained from experimental curve fitting), the experimental results matches well with simulated results with surface tension included in the model, but not with predictions without surface tension, see Figure 5.11.

Thus, imprinted pillar heights can be predicted by the model taking into consideration of surface tension and that surface tension does affect the pillar heights rather significantly.

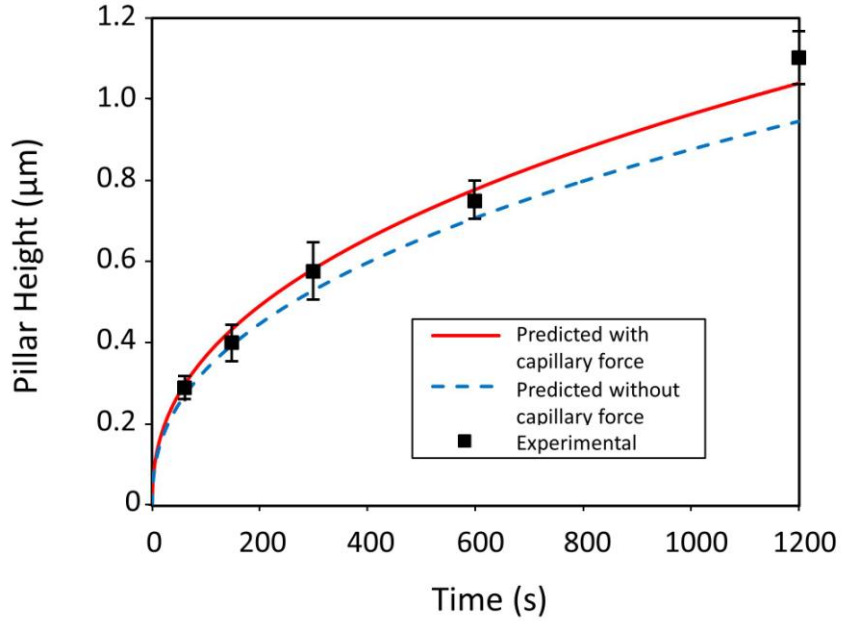


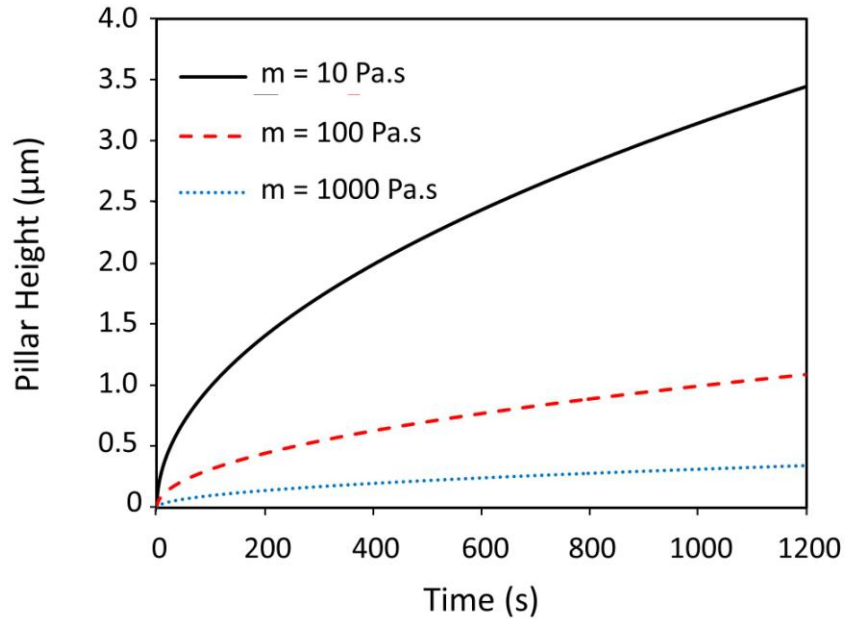
**Figure 5.11.** Comparison between experimental and predicted results with and without capillary force (surface tension).

#### 5.4.4 Effects of Material Flow Properties on Pillar Height

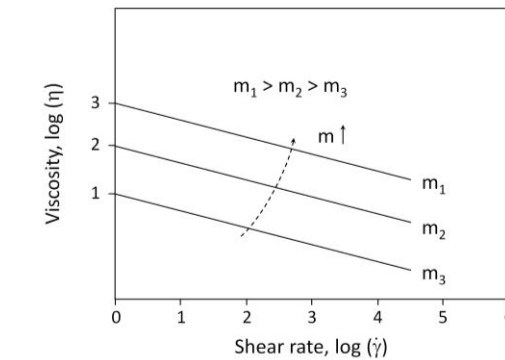
The analytical Eq. 5.36 can be employed conveniently to understand the effects of different polymers with different properties on nano-imprint, in particular the pillar height. As such, the evolutions of pillar height were predicted for different values of the flow consistency ( $m$ ) (Figure 5.12), and surface tension ( $\sigma$ ) (Figure 5.14). The effect of power-law index (flow behaviour index,  $n$ ) is not investigated as with slow flow rate within a small range, its effect will be negligible.

Figure 5.12 depicts the effect of flow consistency index on the pillar height. It shows that the pillar height is inversely proportional to the value of flow consistency ( $m$ ). As the index reduces by a factor of ten, the pillar height increases approximately 3 – 4

times (Figure 5.12). This can be understood from Figure 5.13, where it is shown that the higher the consistency index, the higher the viscosity (on a log scale),  $\log \eta$  at any shear rate (on a log scale),  $\log \dot{\gamma}$  [175]. Thus, the higher the consistency index, the more difficult for the polymer to flow and thus the lower the pillar height.



**Figure 5.12.** Pillar height evolution for three different values of material constants  $m = 10$  Pa.s, 100 Pa.s and 1000 Pa.s



**Figure 5.13.** Viscosity,  $\log \eta$  versus shear rate,  $\log \dot{\gamma}$  [175].

Figure 5.14 shows the impact of surface tension in pillar height. Low surface tension values do not have a significant effect on the pillar height. For example, when the value increased from  $1.e^{-6}$  N/mm to  $1.e^{-5}$  N/mm, the increase in pillar height was almost negligible. However, as the surface tension increased from  $1.e^{-5}$  N/mm to  $1.e^{-4}$  N/mm, there is a sharp increase in pillar height of approximately 14 %.

From Eq. 5.40, it can be deduced that the effect of surface tension is a function of material properties of the two contacting surfaces (contact angle of the polymer fluid on a substrate), imprint pressure as well as the pore radius. Imprint temperature would also come into play as it changes the viscosity of the polymer fluid (contact angle of the polymer on the pore wall). Thus, imprint pressure and imprint temperature, in addition to directly affecting the pillar height (refer to Eq. 5.36), they would also have effects on the surface tension and thus, indirectly affecting the pillar height as well.

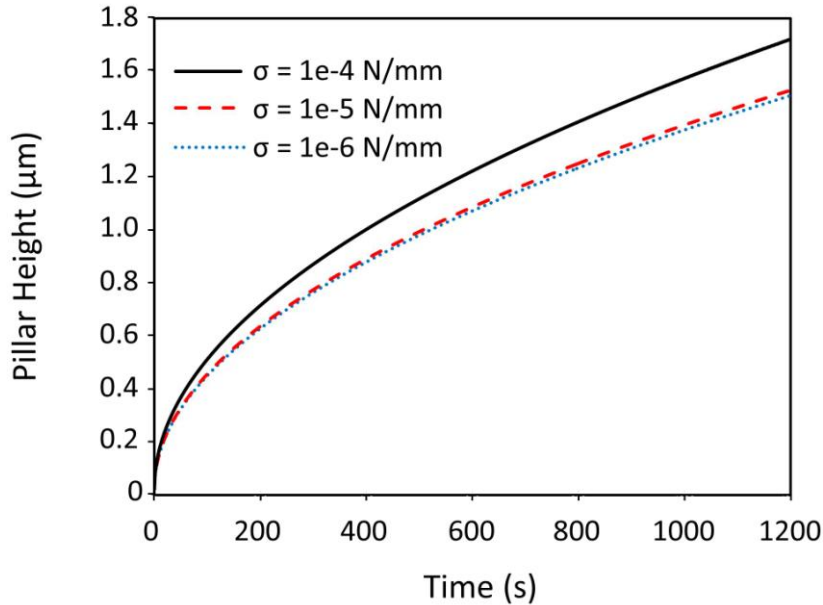


**Figure 5.14.** Pillar height evolution for three different values of surface tension  $\sigma = 1.e^{-4}$  N/mm,  $1.e^{-5}$  N/mm and  $1.e^{-6}$  N/mm.

### 5.4.5 Parametric Studies on Polymer Pillar Height

It would be advantageous to determine the process parameters prior to performing the imprint. A complete polymer filling yields high structure fidelity. Jaszewski et al. [176] noted from his experimental observations that the primary parameter in process control is temperature. The imprint pressure and duration can also be tuned to optimize cycle time. With such understanding, an appropriate choice of processing parameters can be made. The FEM numerical method for solving nonlinear pressure equation (5.38) together with WLF-Cross viscosity model in equation (5.6) were employed to obtain the theoretical predictions of pillar height.

Figure 5.15 elucidates the pillar heights at various imprint temperatures with imprint pressure and duration kept constant at 1 MPa and 300s respectively. The pillar height increases exponentially as the temperature increases. This would reduce the imprint duration. However, the trade-off with a longer cooling duration associated with a higher processing temperature has to be considered. To optimize the cycle time, the cooling system has to be extremely efficient.

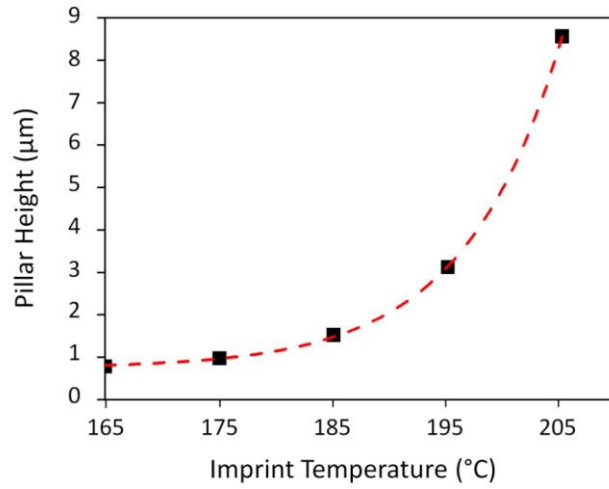


**Figure 5.15.** Numerical simulation of pillar height profile at various imprint temperature. Imprint pressure and duration are kept constant at 1 MPa and 300s respectively.

Figure 5.16 depicts the pillar heights at various imprint pressures with imprint temperature and duration kept constant at 165 °C and 300s respectively. Upon the slightest application of imprint pressure, when a conformal contact is established, there is a sudden increase of pillar height. In general, there are three force parameters on pillar height evolution which are capillary force, squeeze force and gravity force. At the initial stage, capillary force will play a more dominant role and then time-dependent squeeze action will dominate the pillar creep flow as seen in the near linear slope of pillar height. This will be finally balanced by the gravitational force. However, the gravitational force was ignored in the theoretical analysis due to the negligible Archimedes number.



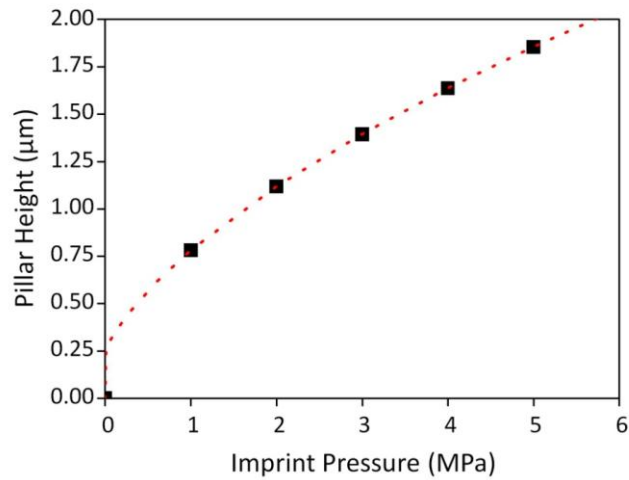


**Figure 5.16.** Numerical simulation of pillar height profile at various imprint pressures. Imprint temperature and duration are kept constant at 165 °C and 300s respectively.

Figure 5.17 illustrates the pillar heights at various imprint durations with imprint temperature and pressure kept constant at 165 °C and 1 MPa respectively. The rate of increase of pillar height in the first minute of imprint is the highest and gradually decreases with imprint duration. The same explanation as discussed previous is applicable here for explaining the rapid increase of pillar height during the initial imprint stage.

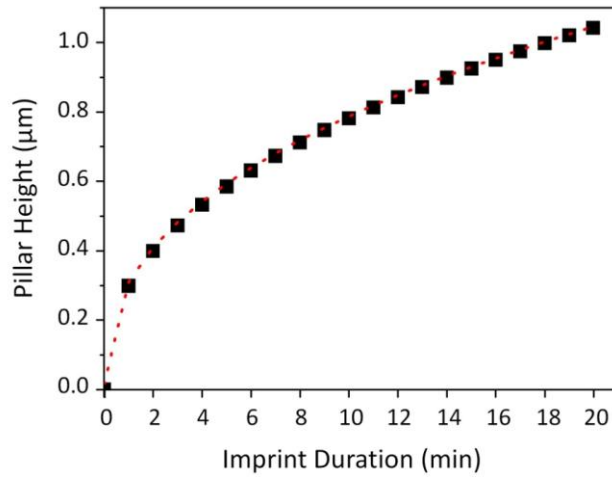


**Figure 5.17.** Numerical simulation of pillar height profile at various imprint duration. Imprint temperature and imprint pressure are kept constant at 165 °C and 1 MPa respectively.

From these plots, the imprint temperature was found to be most effective in increasing the pillar height. Imprint pressure and duration are observed to have the same trend where the rate of increase of pillar heights reduces with the increase of imprint pressure or imprint duration. As the maximum imprint pressure of the imprinter (Obducat Nanoimprinter System) is 6 MPa, imprinting at 165 °C at this pressure would be difficult to achieve the desired pillar height of approximately 6.5 μm (for the gecko-inspired dry adhesive used in this study). To increase the imprint duration to achieve the desired results at the same temperature of 165 °C is also not a viable option: it would take 161 min to achieve the required pillar height of 6.5 μm. Instead, Figure 5.15 indicates that the desired pillar height of approximately 6.5 μm can be achieved at 200 °C with a duration of 5 min at 1 MPa imprint pressure, which are acceptable processing parameters.

## 5.5 Summary

Capillary force has been found the main driving mechanism for filling high aspect ratio nanometer pores. The material properties and process parameters are key to the filling process during nano-imprinting. To describe the complex interactions between these considerations, a viscous polymer flow model based on lubrication approximation with consideration of surface tension effect was developed. The model was verified with experimental results of nano-imprint of polycarbonate, a typical thermoplastic polymer.

The mold-filling process of nano-size cavity during imprinting was investigated experimentally, analytically and numerically for a non-Newtonian fluid. The basic flow model constructed was used to predict the pillar height of the imprints as well as to establish the relationship between the flow parameters (i.e. flow consistency index and surface tension values) and the predicted pillar height. Results obtained experimentally and by simulations were comparable (within 8.4 %) indicating that the model can be used to predict imprinted pillar heights. It also indicates that surface tension does affect the pillar heights.

It was found that a higher material flow constant increases the viscosity and thus results in lower pillar height. Conversely, the higher the flow index, the higher the pillar height is obtained. The simulated results indicate that surface tension has an effect on the filling of the cavity, namely the higher the surface tension, the higher the pillars.

For a specific material, the imprint temperature was found to be most effective in increasing the pillar height. Imprint pressure and duration are observed to have the

same trend, but have a less dominant effect. Since longer imprint duration lengthens the cycle time, it is the least desired controlling parameter for increasing pillar height. As such, the imprint temperature of approximately 200 °C was used to imprint nano-pores of approximately 6.5  $\mu\text{m}$  depth for the fabrication of high aspect ratio gecko structures in PC.



# Chapter 6    Fabrication of Gecko-Inspired Dry Adhesives

## 6.1    Overview

In Chapter 5, preliminary studies were conducted on understanding the mechanics of polymer mold filling during imprinting. These studies provide guidance on the selection of the important process parameters for the production of gecko-inspired dry adhesives by nano-imprinting.

This chapter discusses the fabrication of gecko-inspired hierarchical topography of branched nano-pillars on a stiff polymer. The topographical features involve high aspect ratio nano size pillar structures. Their fabrication of such structures has hitherto posed numerous challenges and they have only been produced with very limited success. One of the main limitations has been the availability of a mold, and indeed such mold hitherto has not been produced. Additional issues are the structuring of polymer with high stiffness to have high aspect ratio and sufficient mechanical stability. Another challenging step is the demolding or release of the structures without damage, collapse or clumping.

In this chapter, these fabrication challenges are addressed and the fabrication of gecko-inspired hierarchical structures is achieved by combining the use of multi-tiered

branched PAA templates and capillary force assisted nano-imprinting. The fabrication of multi-tiered PAA templates has been previously described in Chapter 3. The demolding process in releasing the structures has also been studied by either direct peeling off the PAA template or dissolution in etchants. Another important process parameter in the fabrication of high aspect ratio structures to minimize recovery of polymer is the holding pressure (pressure applied during the cooling cycle). These initial results are elaborated in the following sections.

## **6.2 Fabrication of High-Aspect-Ratio (HAR) Polymeric Pillars**

In this investigation, single tier high-aspect-ratio (HAR) polymeric pillars were termed as linear pillars. They were fabricated using PAA as template. The PAA mold was fabricated in the same manner as the multi-tiered branched PAA as discussed in Chapter 3 but in a single anodization step.

Positive replicates were obtained using the capillary force assisted nano-imprinting method [177]. The PAA mold has high surface energy and allows the wetting and filling of the polymer. Commercial grade Lexan polycarbonate (PC) was used as the substrate. With an elastic modulus of  $2.19 \pm 0.09$  GPa, the stiffness is comparable to the reported stiffness of  $\beta$ -keratin of gecko foot-hairs, which is approximately 2 GPa [14].

Figures 6.1a, b and c show the schematic cross-sectional and top views of the linear PAA as well as its SEM image respectively. The following abbreviations were

used for the dimensions of the templates, namely  $D$  – Diameter of the linear PAA and  $H$  – Height of the template. The fabricated template was placed on top of a commercial polycarbonate (PC) film.

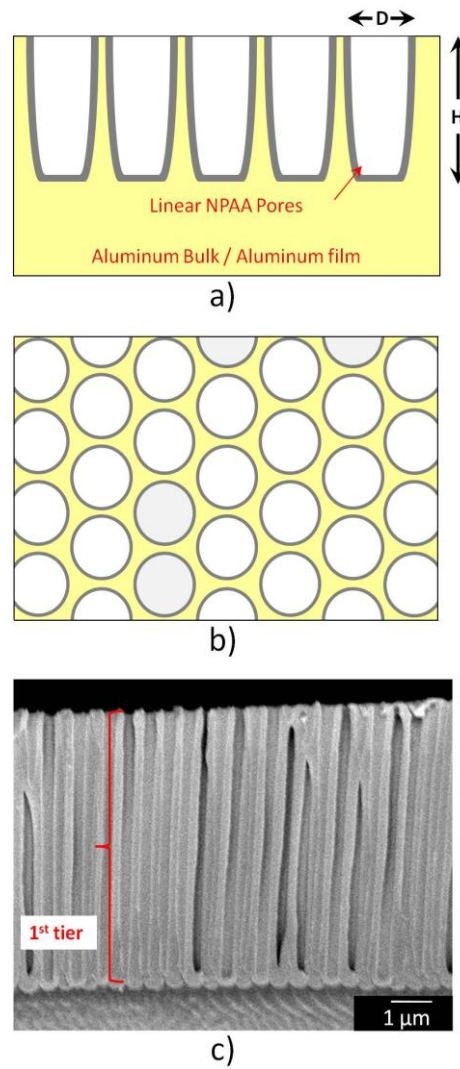


**Figure 6.1.** Linear PAA templates a), cross-sectional view b) top view and c) SEM image of the PAA template.



The dimensions of the linear pillars were  $280 \pm 20$  nm in diameter and  $6.5 \pm 0.5$   $\mu\text{m}$  in height with a pillar density of  $6.2 \times 10^6$  pillars /  $\text{mm}^2$ . The height of the pillars can be controlled by the anodizing duration. The pillars' height was controlled to match those of the branched pillars as the main objective of this investigation was to determine if a hierarchical structure indeed does improve shear adhesion compared to the linear one. Hence, ambiguous results which may arise from the difference in bending stiffness caused by dissimilar pillar heights could be dismissed.

To obtain positive replicates of the templates, the  $1 \times 1 \text{ cm}^2$  of the fabricated PAA template was placed on top of the polycarbonate (PC) film of thickness 250  $\mu\text{m}$ . Subsequently, it was loaded into an Obducat Nanoimprinter system (NIL 4"). The processing parameters were 200 °C (55 °C above  $T_g$  of PC) at a pressure of 1 MPa. These conditions were applied for 5 minutes under vacuum. The schematic nano-imprint process is described in Figure 6.2.

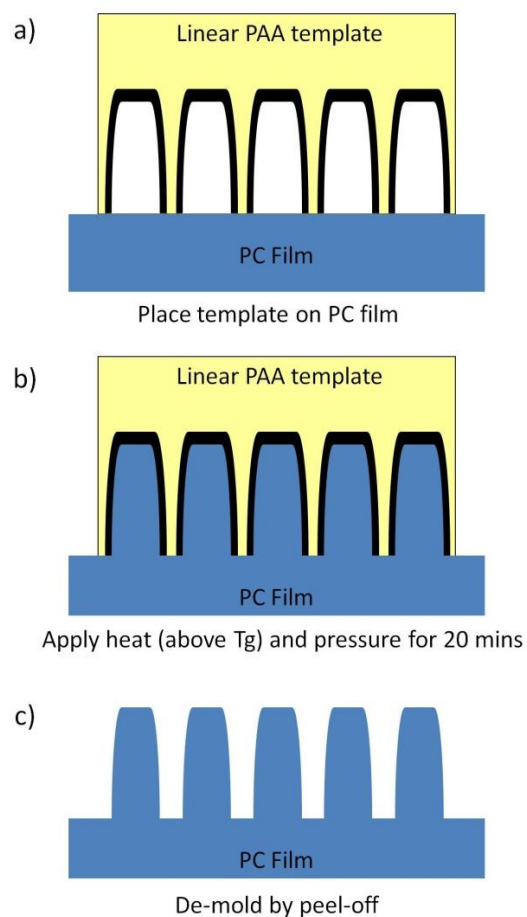


**Figure 6.2.** Fabrication process of linear polymeric topographic structures.

The imprinted sample was then cooled to room-temperature before demolding by manually peeling off the PAA template. Demolding by this method would prevent the clumping of the high-aspect ratio pillars as observed by other authors when wet etching with solvents were used to dissolve the template [50].

### 6.3 Fabrication of Polymeric Hierarchical Nano-structure

High aspect ratio, hierarchical nano-structured polymer films were obtained using multi-tiered branched PAA as mold [178]. The pillar density of  $10.7 \times 10^6$  pillars /  $\text{mm}^2$  obtained was in the same order of magnitude as a natural gecko foot-hair which is approximately  $25 \times 10^6$  pillars /  $\text{mm}^2$  [79].

The fabrication of multi-tiered branched PAA molds has been described in Chapter 3. For this investigation, only a two-level hierarchical structure was fabricated. Here, the duration of anodizations and barrier layer thinning have been optimized to obtain the required dimensions close to those of gecko foot-hairs. Figures 6.3a and b illustrate the cross-sectional and top views of a two-tiered branched PAA template. Figure 6.3c shows the SEM image of the template. For the two-tiered templates,  $D$  denotes the diameter of the 1st-tiered PAA and  $H$  is the overall height of the template. In addition,  $d$  and  $h$  represent the diameter and height respectively of the 2nd-tiered PAA template.

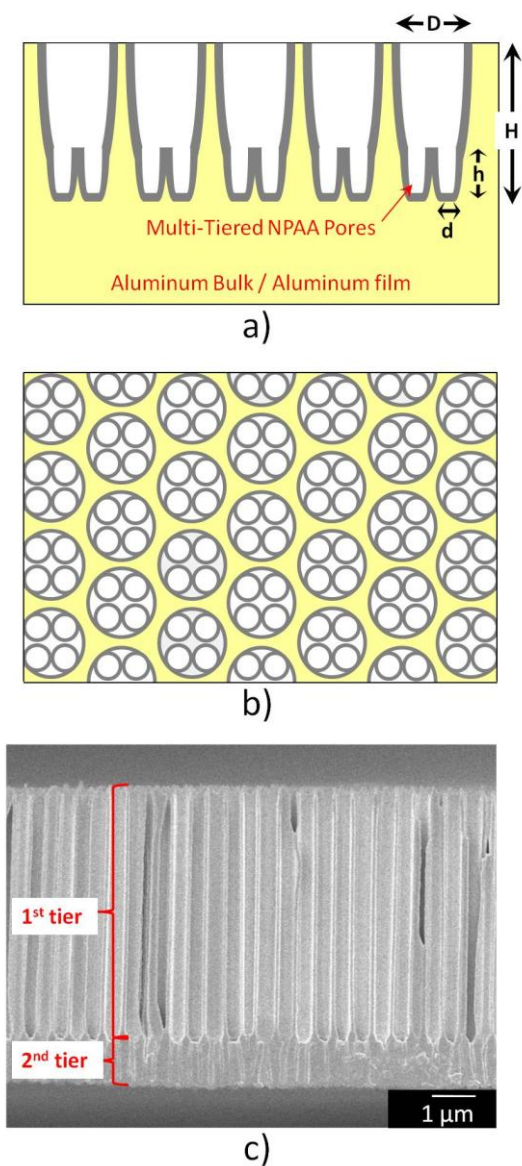


**Figure 6.3.** Multi-tiered PAA templates a), cross-sectional view b) top view and c) SEM image of the PAA template.

The same method as in obtaining the linear pillars was used to obtain the positive replicates of the branched pillars. Figure 6.4 illustrates the schematic process to obtain the positive replicates of the two-tiered branched PAA in PC.

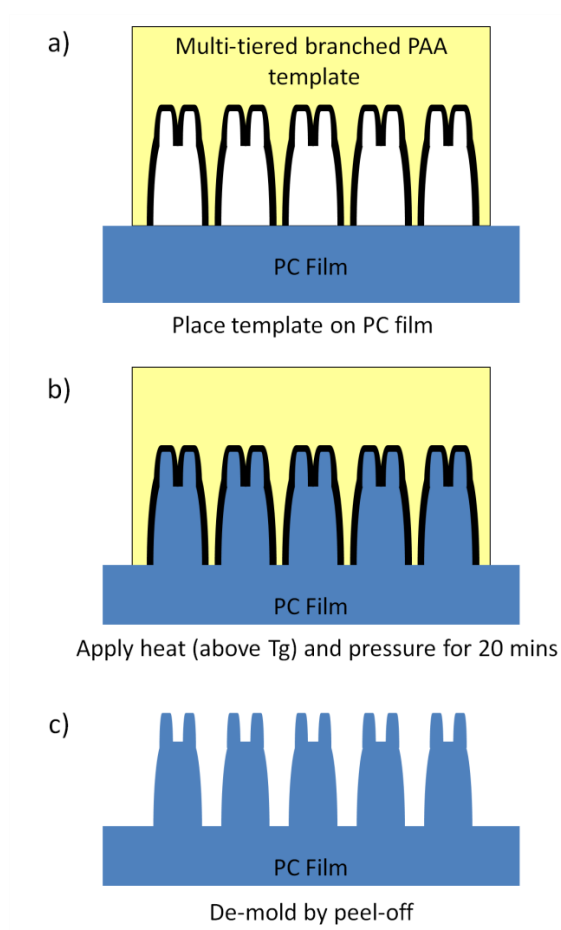


**Figure 6.4.** Fabrication process of hierarchically branched polymeric topographic structures.

Figures 6.5a and b show the SEM images of imprinted polymer hierarchical pillars obtained by PAA templates fabricated with varying the anodizing conditions. The base pillars' dimensions in Figure 6.5a are  $280 \pm 20$  nm in diameter with an aspect ratio of 8-10; the top pillars had a diameter and aspect ratio of  $90 \pm 10$  nm and 5-6 respectively. The branched pillars in Figure 6.5b had base pillars with diameter and height of  $280 \pm 20$  nm and  $6.5 \pm 0.5$   $\mu\text{m}$  respectively; and the top pillars had diameter and aspect ratio of  $110 \pm 10$  nm and 5-6 respectively. There is a 10-15 % standard deviation in the pillar dimensions and this is caused by the variation in the PAA template

dimensions. This variation is due to the inherent property in the self-assembly processes of the alumina template [179].

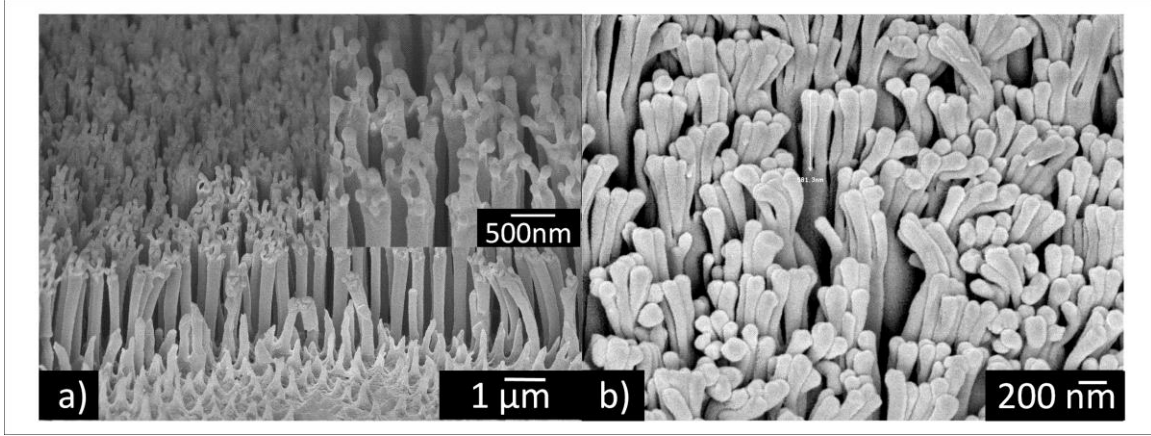


**Figure 6.5.** SEM images of imprinted hierarchically branched pillared substrates. a) Four branches (Insert shows magnified view of pillars). The base pillars' dimensions are  $280 \pm 20$  nm in diameter with aspect ratio of 8-10, and a diameter and aspect ratio of  $90 \pm 10$  nm and 5-6 respectively for the top pillars. b) Five branches. The dimensions of the hierarchical pillars are  $280 \pm 20$  nm and  $6.5 \pm 0.5$  μm for the diameter and height of the base pillars respectively; and a diameter and aspect ratio of  $110 \pm 10$  nm and 5-6 respectively for the top pillars.

## 6.4 Nano-imprint Processing Conditions for Hierarchical Nano-Structure

Temperature is the most important process parameter in nano-imprinting of hierarchical nanostructures [151, 152]. It greatly influences the height of the structures that are obtained. The optimized parameters obtained for polycarbonate are depicted in Table 6.1, showing that the pillar height is sensitive to the processing temperature. The processing temperature has to be high enough to allow the polymer to soften sufficiently to flow into the mold. By increasing the processing temperature, the polymer becomes

less viscous and allows complete filling of the template cavities. Typically the high aspect ratio pillars can be achieved with high processing temperature. The contact pressure required could generally be kept constant.

**Table 6.1.** Processing conditions to obtain various linear pillar heights of polycarbonate.

<b>Fibril Heights [<math>\mu\text{m}</math>]</b>	<b>Aspect Ratio</b>	<b>Process Temp. [<math>^{\circ}\text{C}</math>]</b>	<b>Pressure [bar]</b>	<b>Duration [min]</b>	<b>Template Removal Method</b>
~ 2.5	~ 8	180	10	5	Peel Off
~ 5.5	~ 18	200	10	5	Peel Off
~ 10	~ 33	220	10	5	Etched Off

Demolding was carried out by peeling off the template when the polymer had cooled to approximately 50  $^{\circ}\text{C}$  for fibrillar structures with heights of ~ 2.5 – 5.5  $\mu\text{m}$  (aspect ratio ~10-20). Demolding without wet-etching was performed by gripping one end of the aluminum of the imprinted substrate and peeling it off at 90 $^{\circ}$  from the PC substrate. For higher aspect ratios i.e. (aspect ratio > 20), the template had to be etched as the mechanical strength of the small pillars is insufficient to withstand the adhesion force during peel off.

The success of demolding by peel-off depends on the followings: :

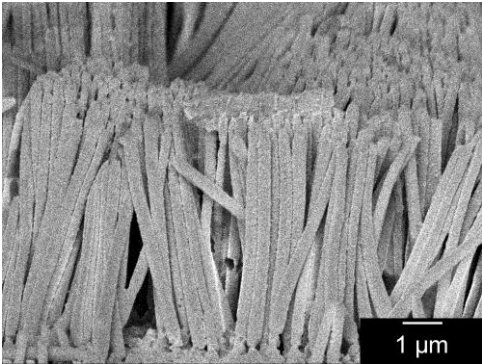
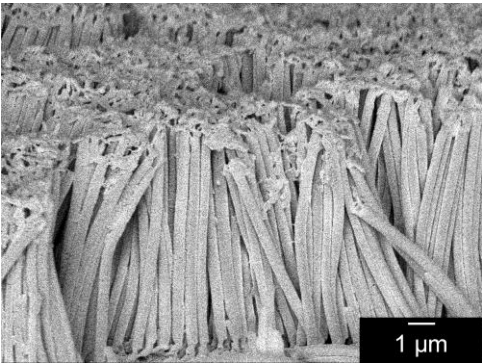
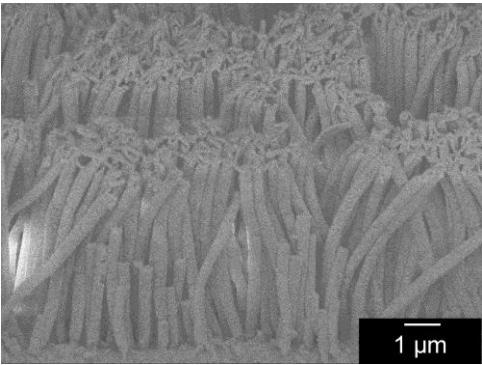
1. The height of the pillars was optimized to 6.5  $\mu\text{m}$  ( AR of 25). For higher aspect ratio, the adhesion force could be too large to cause elongation or breakage of the pillars.

2. The base of the pillars were widened to allow the pillars to withstand a large peel-off force without breakage.
3. PC was the chosen material due to its toughness when compared with other polymers such as PVC, PS, and PMMA which are more brittle [180].

For demonstration purpose, this process was also applied to other stiff thermoplastic polymers such as polyvinyl chloride (PVC) with Young's modulus of 2.9 – 3.3 GPa [181] and Poly(methyl methacrylate) (PMMA) with Young's modulus of 2.8 GPa [182]. Table 6.2 presents the parameters used for replicating high aspect ratio branched fibrillar structures in various stiff polymeric materials, i.e., PC, PMMA and PVC. Note that only the processing temperature was being varied. The SEM image for each of the patterned polymer is attached for ease of reference. Imprinting temperature was approximately 60 – 80 °C above its respective  $T_g$ . This may be the general rule of thumb to obtain high aspect ratio pillars (> 20) of stiff thermoplastic polymers as it enables the polymer to fill into the cavity assisted by capillary force (a function of temperature) as discussed in Chapter 5.



**Table 6.2.** Processing conditions for the fabrication of tiered branched polymer pillars in various polymeric materials.

Polymer	SEM Image	Pillars dimensions	Temp [°C]	Tool Pressure [bar]	Duration [mins]
PC $T_g = 146^\circ\text{C}$ (measured)		1st tier: H: ~ 5 μm D: ~ 300 nm AR: ~ 16  2nd tier: H: ~ 300 nm D: ~ 90 nm AR: ~ 3	200	10	5
PMMA $T_g = 91^\circ\text{C}$ [182]		1st tier: H: ~ 5 μm D: ~ 300 nm AR: ~ 16  2nd tier: H: ~ 300 nm D: ~ 90 nm AR: ~ 3	170	10	5
PVC $T_g = 82^\circ\text{C}$ [181]		1st tier: H: ~ 5 μm D: ~ 300 nm AR: ~ 16  2nd tier: H: ~ 300 nm D: ~ 90 nm AR: ~ 3	160	10	5

## **6.5 Challenges for Achieving High Aspect Ratio Polymeric Pillars**

There are a number of process issues for obtaining high aspect ratio and high density polymeric structures. These issues are investigated in this section.

### **6.5.1 Polymer Relaxation**

For a good understanding of the polymer flow during nano-imprinting, it is necessary to avoid the possibility of permanent nano-pillar deformation caused by demolding stresses. A way to achieve this is demolding by etching of the mold after nano-imprint. This will not introduce any applied stress on the nano-pillars, thus avoided any permanent deformation.

Upon demolding by wet-etching (using 5 wt%  $\text{H}_3\text{PO}_4$  for 24 hrs), polymer pattern relaxation was observed. Polymer pattern relaxation is a phenomenon that causes the diameter of the polymer pillars after mold release to become larger than the diameter of the nano-pores of the mold. This is believed to be caused by the inherent relaxation of the elastic stresses stored in the polymer during imprint resulting in partial restore of the initial shape [183].

Additional reasons that may cause the pillars' enlargement were also considered. First, the polymer could swell during the chemical etching of the PAA mold. To eliminate this possibility, the imprinted polymer (at 165°C under imprinting pressure of 1 MPa for 300 s with cooling profile as shown in Figure 5.4) was demolded by

mechanical force (peel-off). The polymer substrate with the imprinted nano-pillars was then cut into two halves. One half was examined with SEM and the second half was immersed into the etching solution (5 wt%  $\text{H}_3\text{PO}_4$ ) for twenty-four hours at room temperature before being examined with SEM. Three SEM images of the polymer imprint were taken. Thirty measurements of the pillars' diameter were obtained from each SEM image and subsequently averaged. The results are tabulated in Table 6.3, indicating that there is no significant difference between the two samples. As such, swelling of the pillars was ruled out as the caused for the pillars' enlargement.

**Table 6.3.** Average diameter of imprinted polymeric pillars after 1) mechanical force demolding and 2) mechanical force demolding coupled with immersion into chemical etching solution.

	Peel Off	Peel Off 5wt% $\text{H}_3\text{PO}_4$ -24hrs
Average Diameter	327.23	323.94
Standard Deviation (StdDev)	28.15	26.75
% StdDev	8.35	8.01

Second, the pillars' enlargement could be caused by deformation of the PAA during imprint. To rule out this possibility, measurements of the pores' diameter before and after imprint were carried out. Three SEM images of the mold were taken before imprint. Thirty measurements of the pores' diameter were obtained from each SEM image and subsequently averaged. After the imprint with PC (at 165°C under imprinting pressure of 1 MPa for 300 s with cooling profile as shown in Figure 5.4), the polymer –

mold sample was immersed in dichloromethane to dissolve the PC. The same pores' diameter measurements were obtained. The pores of the PAA mold before and after imprint were  $271.4 \pm 23.3$  nm and  $269.5 \pm 21.5$  nm respectively. This shows that the PAA mold (Young's modulus of 344.83 – 395.01 GPa at 500 °C and compressive strength of 1.476 GPa at 400 °C) [184] did not undergo deformation due to compression. The observed diameter of the pillars at different imprinting times are tabulated in Table 6.4 , it can be seen that for all the measurements the diameter is larger than the template pore size.

**Table 6.4.** Imprint parameters with the respective diameter (top, mid and bottom) of the pillars obtained. Standard deviations are shown. PAA pore diameters are approximately 270 nm

Temp (°C)	Pressure (MPa)	Imprint Duration (s)	Top Pillars' Diameter	Standard Deviation	Mid Pillars' Diameter	Standard Deviation	Bottom Pillars' Diameter	Standard Deviation
165	0.6	10	297.9	31.19	N.M	N.M	291.9	32.31
165	1.0	60	316.6	24.37	N.M	N.M	296.7	33.74
165	1.0	150	343.0	26.32	334.8	43.36	294.2	11.98
165	1.0	300	360.3	34.53	347.7	30.03	301.3	30.27
165	1.0	600	348.2	30.31	325.4	26.84	273.4	22.03
165	1.0	1200	351.9	35.90	349.1	46.85	287.0	25.76

Note: N.M - Not measurable as a result of blocked view by another pillar

From these two experiments, it was concluded that the enlargement of the polymeric pillars was due to the relaxation of the residual stresses stored in the polymer during imprint.

Another observation to corroborate the polymer relaxation phenomenon finding is that the top of the pillar expands more than the base of the pillar (see Table 6.4). This could be understood from the perspective of the Poisson's ratio effect. Poisson's ratio  $\nu$  is the ratio of transverse contraction strain to longitudinal extension strain of a stretched body [185]:

$$\nu = -\frac{\epsilon_{transverse}}{\epsilon_{longitudinal}} \quad (\text{Eq. 6.1})$$

The negative sign in Eq. 6.1 is included to yield a positive value [185]. This is because most common materials become thinner in cross section when stretched [185].

The Poisson's ratio of alumina decreases as the porosity increases [186]. This implies that PAA mold, with porosity of approximately 19 % (calculated from Figure 5.2) would have Poisson's ratio,  $\nu$  of less than 0.22 (for porosity of 6 %). This means that there is less transverse contraction or expansion strain as a result of either tension or compression that causes a longitudinal strain.

For polycarbonate, PC, the Poisson's ratio is 0.37 measured with Instron 5569 Universal Testing Machine using non-contacting video extensometer. As such, given the same tension or compressive stress, PC will experience more transverse strain. Figure 6.6 illustrates the change in transverse strain according to Poisson's ratio during a) tension and b) compressive stress.

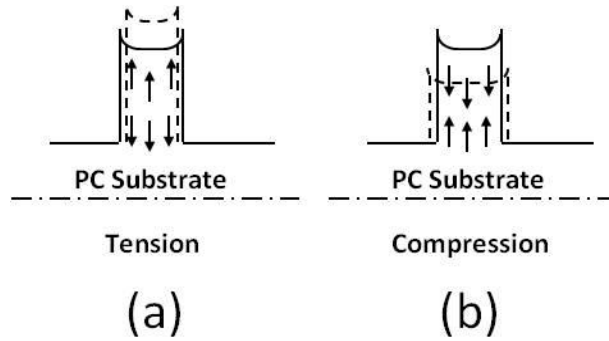
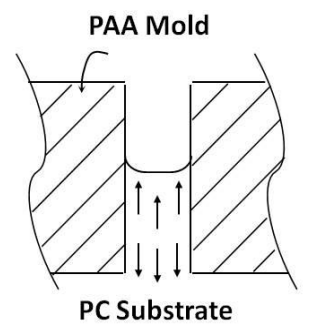


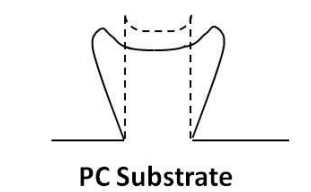
**Figure 6.6.** Schematic of Poisson's ratio effect a) in tension and b) in compressive stress.

In addition, PAA mold has a thermal expansion coefficient of approximately  $8.6 \times 10^{-6} \text{ cm/cm/}^{\circ}\text{C}$  [187], and PC a thermal expansion coefficient of  $6.5 \times 10^{-5} \text{ cm/cm/}^{\circ}\text{C}$  [187]. Thus, after imprint and cooling from the raised imprinting temperature to room temperature, PC will tend to contract much more than the PAA mold. However, PC could not contract freely as it is being constrained by the mold. As such, the pillar is held in tension (see Figure 6.7a). With a rapid cooling profile (temperature below its  $T_g$ ), there is insufficient time for the polymer to relax during cooling. Upon etching of the mold, the excess tensile stress is released and this causes a change in the longitudinal strain. Consequently, this leads to a transverse strain to the pillar resulting in the expansion of the pillar diameter. The top of the pillar is free to expand while the base of the pillar is being constrained by the thick substrate and thus could not expand freely. This results in the inverted cone shape of the pillar shown schematically in Figure 6.7b while Figure 6.7c shows the SEM image of the said PC pillar.



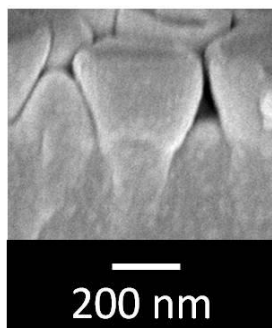
After imprint

(a)



PAA mold etched

(b)



(c)

**Figure 6.7.** Schematic of PC pillar a) under tension after imprint with PAA mold still intact, b) relaxed after the removal of PAA mold by wet-etching and c) SEM image of pillar after mold removal by wet-etching.

One way to minimize the pillar recovery is to maintain the imprint pressure during the cooling cycle (approximately 180 s), also known as the holding pressure. Table 6.5 presents the imprint parameters incorporating holding pressure with the respective pillars' diameter. The diameter of the pillars is smaller than those without holding pressure and matches the diameter of the PAA pores. This additional holding pressure might cause additional flow of the polymer during cooling. This would result in less residual stress after cooling, and therefore less transverse expansion upon demolding.

**Table 6.5.** Imprint parameters with holding pressure and its respective diameter of the pillars. Standard deviations are shown.

Temp (°C)	Pressure (MPa)	Imprint Duration (s)	Pillars' Diameter (nm)	Standard Deviation (nm)
165	1.0	60	275.04	20.50
165	1.0	150	281.27	25.78
165	1.0	300	272.21	20.18
165	1.0	600	285.34	34.72

The constraint of the substrate to the base of the pillars results in high stress concentration at the base of the pillar. This high stress concentration is a potential site of failure, which is discussed in the next section.



### **6.5.2 Demolding of Patterned Polymeric Pillars**

Generally, two methods are used to release the structures from the mold. They are 1) peel-off and 2) wet etching. For structures with aspect ratio below 10, the peel off method was adopted. This method is practical and in some cases allows the re-use of the template.

Since ordered PAA templates are high in pores density and aspect ratio, with large surface to volume ratio, the adhesion force is very large between the filled pillars and the template. Peeling off with such a great force would break the pillars at the base which has high stress concentration around it. Therefore, these structures are released from the mold by wet etching. However, this method promotes bunching / clumping of the high aspect ratio pillars ( $> 10$ ), which is highly undesirable. In addition, the etched mold can no longer be used.

The bunching / clumping of the pillars (Figure 6.8) is due to the capillary effect of the etchant as it evaporates from the patterned surface. Pillars bunching adversely affects the performance of the synthetic dry adhesive as discussed in Chapter 1.1.5.

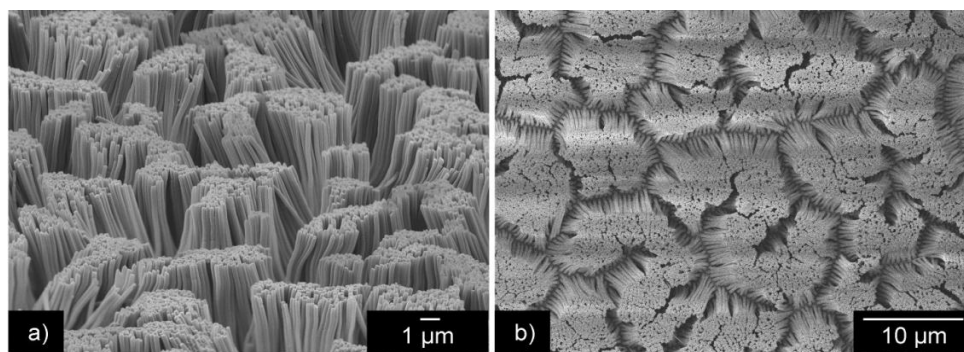


**Figure 6.8.** SEM images showing a) oblique view and b) planar view of the bunched pillars.

To circumvent these difficulties, the PAA template was designed and processed to provide a wider base for the replicated pillars. This would minimize the high stress concentration around the base allowing the pillars to be strengthened. As such, the patterned polymer could be peeled off the template without breakage at the base. Wet etching is then not necessary and can be omitted.

To obtain such templates, the aluminum film was anodized for a short duration to achieve approximately 300 – 500 nm pore depth. After that, the PAA template was barrier thinned for 90 min. Then the template was subjected to further anodization to grow the pores. When the desired pore height was achieved and subsequently barrier layer thinned for 5 hrs, a PAA template with slightly larger pores at the top of the film was obtained. With a larger base (see Figure 6.9a), the replicated pillars were able to withstand the large peel-off force without the necessity of etching away the template. Demolding by peel-off was performed by gripping one end of the aluminum of the imprinted substrate and peeling it off at 90° from the PC substrate.

Therefore, the problem of bunching/clumping associated with etching was avoided, and the template was reusable. Interestingly, it should be noted that besides geckos, insects like beetles too have fibrillar attachment systems with broad bases as shown in Figure 6.9b.

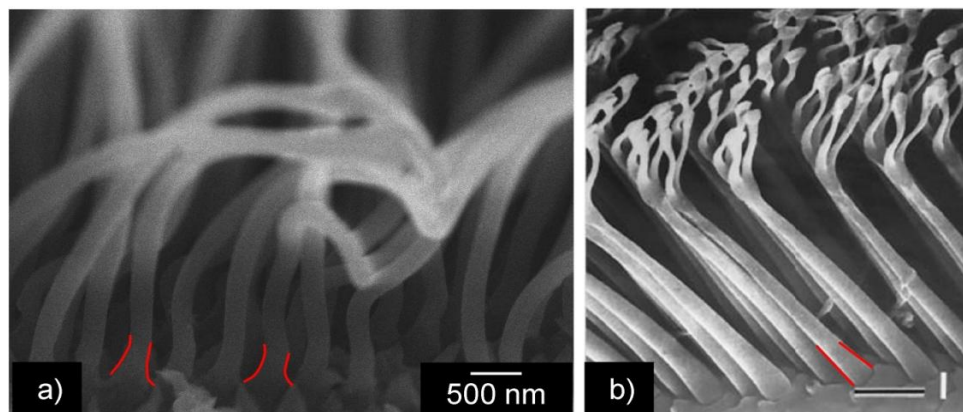


**Figure 6.9.** SEM image a) peel-off of high aspect ratio PC pillars with a broader base, b) fibrillar attachment system of a beetle (*Hemisphaerota cyanea*) showing its broad bases [18].

### 6.5.3 Density of Patterned Polymeric Pillars

Initially, randomly ordered PAA templates obtained by one step anodization were used. It was observed that not only were the pores randomly ordered but some have ceased to grow (possibly after some stress equilibrium of the film was achieved [188]). The dashed red circles in Figure 6.10a show some of the pores that had ceased to grow. In addition, the pores did not grow straight down into the aluminum bulk as shown in Figure 6.10b and some of the pores had narrower openings during the initial stage of pore growth (indicated by dashed circles). These two phenomena resulted in a lower density of polymer pillars as well as pillars with limited strength at the base causing breakage during peel-off (Figure 6.10c).

To address these difficulties, Masuda's two-step anodization method for producing the PAA template was employed, which has been described in Chapter 3.4.3 [101]. This anodization method yielded better pore density as well as uniformity across the anodized area (Figure 6.10d). The pore density achieved was  $10.7 \times 10^6$  pores/mm<sup>2</sup>.

The pore growth was also more uniform resulting in straighter channels perpendicular to the aluminum substrate (Figure 6.10e). This improved the result of polymer patterning, which can be clearly observed in Figure 6.10f.

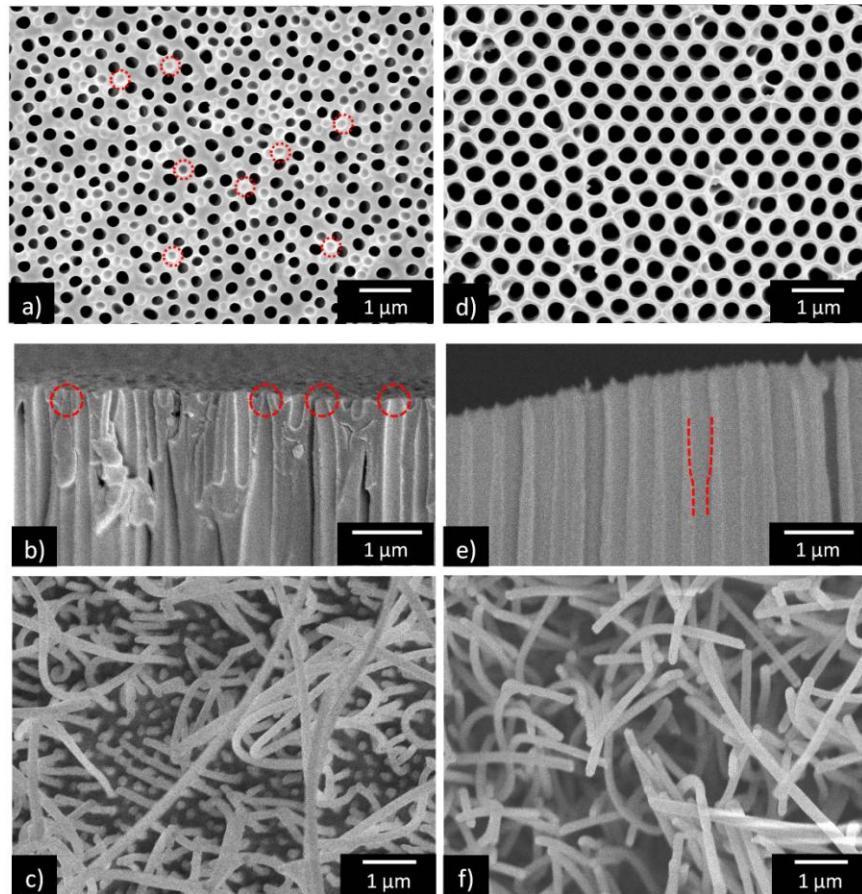


**Figure 6.10.** SEM images of a) planar view and b) cross-sectional view of random AAO template, c) imprinted polymer using random AAO template, d) planar view and e) cross-sectional view of ordered AAO template, f) patterned polymer with ordered AAO template.

## 6.6 Summary

High density, high aspect ratio gecko-mimicking hierarchical structure on a stiff polymer has been successfully fabricated by capillary force assisted nano-imprinting using a multi-tiered porous anodic alumina template.

Experiments have shown that the high aspect ratio pillars can be imprinted when the temperature is well increase above the  $T_g$ . An imprint temperature of 70 – 80 °C above  $T_g$  is a general rule of thumb that high aspect ratio pillars greater than 20 can be obtained for the three stiff thermoplastic polymers (PC, PMMA and PVC). This imprint temperature allows the polymer to fill completely the template cavity.

Polymer pattern recovery was observed, namely the PC pillar diameter with an inverted cone shape was larger than the PAA nano-pore diameter. This is ascribed to the inherent relaxation of the residual elastic stresses stored in the polymer after etching of the mold. This residual stress was a result of the coefficient of thermal expansion mismatch between the polymer and the mold. It was demonstrated that with a holding pressure during cooling, this phenomenon could be minimized.

For structures with aspect ratio greater than 10, the peel off method results on breakage of the pillar at the base of the pillar. This is caused by stress concentration at the base of the pillar. However, demolding by wet etching would cause the pillars to bunch, and the non-reusability of the mold. These difficulties were overcome by producing PAA with wider base pore diameters to minimize the stress concentration. This was achieved by intermediate barrier thinning of the PAA template after a short anodization duration.

With this method, it was found that for aspect ratio  $< 20$ , it is possible to produce structurally stable polymer replicates by simple peel-off and thus avoiding the bunching issues.

In addition, Masuda's two-step anodization was deemed important to achieve regular and straight-through pores to yield high density, high aspect ratio polymeric structures.

Characterizations and analyses of the shear adhesion forces of the nanostructure dry adhesive produced will be performed and discussed in the next chapters.



# **Chapter 7   Macro-Scale Shear Adhesion Force Analysis of Gecko- Inspired Dry Adhesives**

## **7.1   Overview**

The gecko-inspired dry adhesives were fabricated with fabrication methods discussed in Chapter 3 (PAA mold fabrication) and Chapter 6 (capillary force assisted nano-imprinting). In this chapter, the adhesive force of the dry adhesive tapes is characterized.

Furthermore, brief explanations on the mechanism of gecko adhesion (dry friction) are presented. Preliminary adhesive force measurements were obtained to demonstrate that the samples fabricated with polymeric nano-fibrils indeed have better adhesion than unstructured samples.

This is followed by a more rigorous quantitative macro-scale measurements to further characterize the gecko mimetic adhesives. The sample size used for macro-scale measurements is  $1 \text{ cm}^2$ .



A systematic analysis is performed to understand the two phenomena observed: 1) the progressively increasing shear adhesion forces as the samples were being repeatedly tested and 2) the 150 % improvement in the shear adhesion force of the hierarchical topography of hierarchical pillars over the linear pillars.

## **7.2 Mechanisms of Gecko Adhesion**

Hitherto, scientists have failed to unanimously agree on the underlying mechanism(s) of gecko's adhesion. Initially, there were several theories on the cause of the gecko adhesion such as glandular secretion [189], suction and electrostatic attraction [56] as well as micro-interlocking [190]. However, with the advent of the Scanning Electron Microscopy (SEM), these proposals were ruled-out. Capillary attractions too were implicated as the main mechanism of gecko adhesion in the studies performed by Huber et al. [30] and Sun et al. [191].

However, lately, among the many possibilities, the most accepted mechanism for adhesion is based on the inter-molecular attractions (van der Waals forces). This was first proposed by Hiller et al. [192, 193] and later reaffirmed by Autumn and co-workers [20, 29]. Although van der Waals forces are classified as weak forces, at atomic distances, strong adhesion is created when they act collectively.

Recently, Autumn et al. [53] further supported the claim adding that the large adhesion force generated from van der Waals attractions increases the friction force between the geckos' toe pads and the contacting surface. This is because the adhesive

force is one of the mechanisms of dry friction [194]. The coupling of adhesion and friction force was then termed as “frictional adhesion”.

This concept also provides an explanation to how a gecko can hang itself on an inverted surface. Even if gravity cannot provide the normal preload for the generation friction, the gecko would pull their toes inward (gripping motion) as it comes down on a surface to attach, which gives rise to strong adhesion and thus, friction forces. These friction forces would reduce to almost zero during detachment by recurling, peeling or bending outward to eliminate adhesion.

### **7.3 Frictional Adhesion in Gecko Attachment System**

Friction is a reaction force of a body that resists any externally applied force to it [195]. It is in a way similar to the adhesion force between two contacting bodies, which is only experienced when one attempts to separate the bodies from contact.

The most basic law of friction was given by Amontons which states that the friction (lateral) force,  $F_f$  for any two contacting surfaces is directly proportional to the normal applied load,  $L_N$  given a constant proportionality known as Amontons’ friction coefficient or Amontons’ coefficient of friction,  $\mu$  [196] as given in Eq. 7.1. It is independent of the contact area, the surface roughness, and the sliding velocity.

$$F_f = \mu L_N \quad (\text{Eq. 7.1})$$

In most cases,  $\mu$  is lesser than 1 [197]. However, this quantity is a condition-specific constant, which means that it is dependent on the type of contacting materials and the conditions of the sliding surfaces (e.g. humidity, temperature, smooth or rough morphologies) [196].

There are instances where Amontons' law is deviated and Eq. 7.1 no longer applies, for example, in situations where there is friction even at zero or negative normal force, such as gecko's frictional adhesion [197].

In such instances, it has been established, for two adhering surfaces, there are two separate but additive terms contributing to lateral friction forces, i.e. 1) the normal load (external) which is also known as load-controlled and 2) adhesion energy (internal) which is adhesion-controlled [196, 198, 199]. Thus, the modified version of Amontons's equation can be written as [196] : ,.

$$F_{Sad} = \mu(L_0 + L_N) = F_0 + \mu L_N \quad (\text{Eq. 7.2})$$

where  $F_{Sad}$  can be termed as the shear adhesion force,  $L_0$  is the “internal” load accounting for intermolecular adhesive forces due to van der Waals attractions and  $L_N$  is the external load applied normally. This means that it is possible to have friction force at zero normal load as long as there are contacting surfaces over a finite area.

Eq. 7.2 could also be written as [200]

$$F_{Sad} = \mu L_N + S_c A \quad (\text{Eq. 7.3})$$

where  $\mu$  is the Amontons' coefficient of friction of pristine PC on glass surface,  $L_N$  is the applied preload normal to sliding,  $A$  is the area of contact and  $S_c$  is the shear strength accounting for the intermolecular adhesive force also known as Van der Waals force [201].  $S_c$  itself is a function of adhesion energy hysteresis,  $\Delta\gamma$  (materials dependent), which can be expressed as [20] :

$$S_c = \varepsilon \Delta\gamma / \delta \quad (\text{Eq. 7.4})$$

where  $\varepsilon$  is the factor accounting for the less-than-full transfer of energy and  $\delta$  is the atomic gap between the two contacting surfaces for effective Van der Waals attraction ( $\approx 0.3$  nm). As such, at very low loads where  $L_N$  approaches zero, the adhesion-controlled term ( $S_c A$ ) in Eq. 7.3 is dominating while at very high loads, the load-controlled term would dominate even for adhesive systems [196].

## 7.4 Morphology of Test Substrates

Three types of substrates were used for all the shear adhesion tests (preliminary, quantitatively, micro- and macro-scale). The morphology of the substrates tested are shown in Figure 7.1, namely a) pristine film, b) linear pillars and c) branched.

The dimensions of the linear pillars were  $280 \pm 20$  nm in diameter and  $6.5 \pm 0.5$   $\mu\text{m}$  in height. The dimensions of the hierarchical pillars fabricated for shear adhesion tests were: base pillars:  $280 \pm 20$  nm and  $5.5 \pm 0.5$   $\mu\text{m}$  in diameter and height

respectively; top pillars: diameter and height of  $90 \pm 10$  nm and 800 – 900 nm respectively.

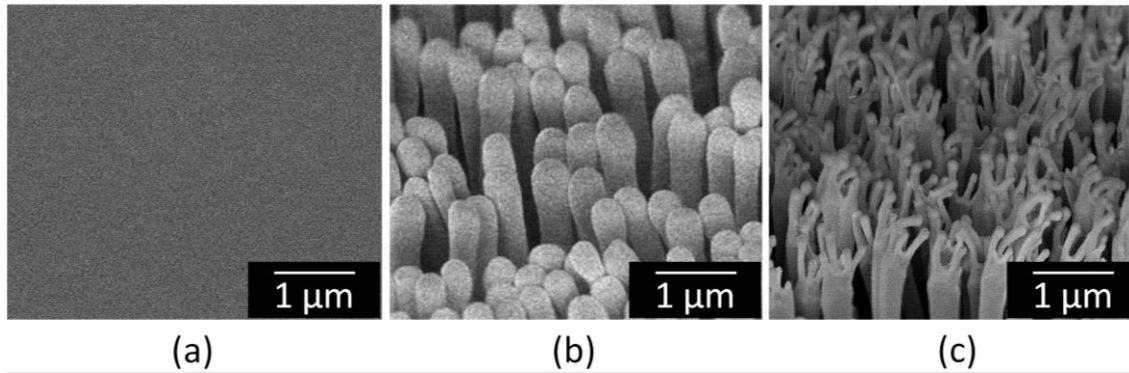


**Figure 7.1.** SEM images of shear adhesion test substrates a) pristine PC, b) linear pillars and c) hierarchical pillars imprinted on PC.

## 7.5 Shear Adhesion Analysis

### 7.5.1 Preliminary Shear Adhesion Force Measurements

#### 1) **Adhesive force comparison between polycarbonate with linear pillars and pristine polycarbonate**

A preliminary adhesive force measurement was conducted to demonstrate that the samples fabricated with polymeric linear nano-pillars indeed have higher adhesion than unstructured samples. For direct comparison, both hierarchical nano-pillars and pristine PC samples were glued to a 5 cents coin (1.41 g).

The size of the pristine PC was cut to match the sample size of the nano-pillars sample. The samples were then placed with the pillars facing against a cleaned glass slide (Figure 7.2a). When the glass-slide was tilted (Figure 7.2b), the coin with PC nano-pillars adhered to the substrate while the coin with PC without nano-pillars slipped off.

This preliminary measurement is based on friction measurement with the weight of the coin acting as a preload. It can be deduced from this experiment that the polycarbonate nano-pillars have sufficient contact and friction forces with the glass-slide to keep it from sliding off.

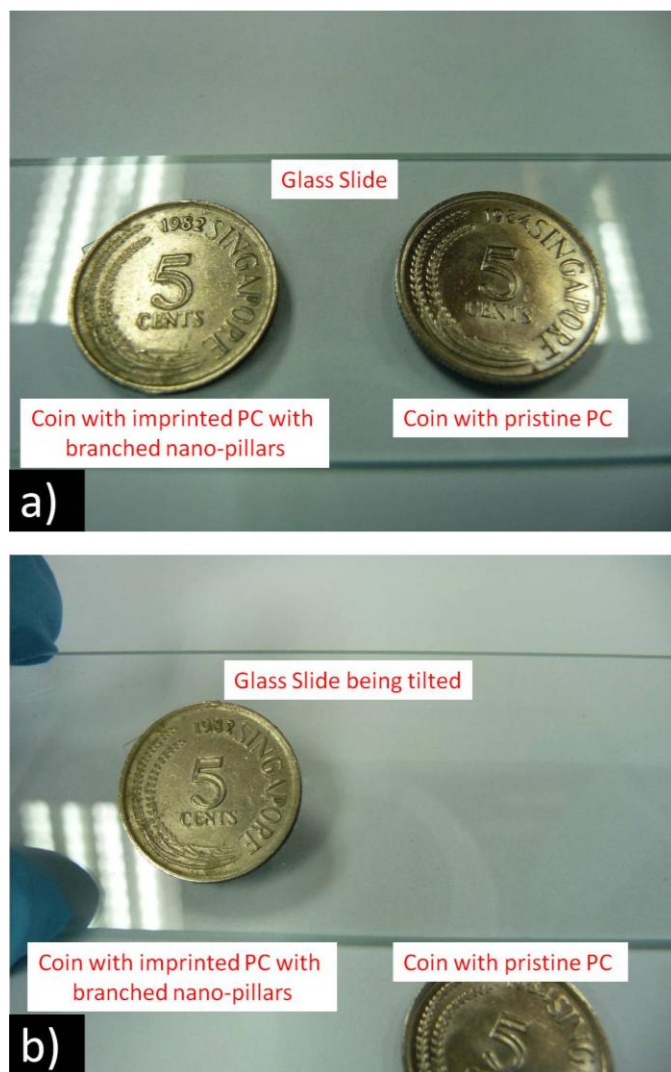


**Figure 7.2 .** a) Polycarbonate (PC) nano-pillars sample (left) and unstructured PC sample (right) each being glued to a 5 cents coin were placed onto an ethanol cleaned glass-slide with the nano-pillars facing the glass-slide, b) Glass-slide was tilted and the coin with PC nano-pillars remain adhered to the glass-slide while the unstructured PC slipped off.

## 2) Adhesive force comparison between polycarbonate with hierarchical pillars linear pillars

To determine the importance of the hierarchical geometry, comparison between with linear and hierarchical pillars was carried out. New batches of samples were fabricated for the tests. For these tests, the sample was cut into 1 x 1 cm<sup>2</sup> size. The back of the sample was glued using superglue (cyanoacrylate adhesive) to a metal disc (weighing 1.41 g and 16.26 mm in diameter and 1.02 mm in thickness). The sample was then placed with the pillars facing against a cleaned glass slide. With one end of the glass slide fixed acting as a pivot, the other end was raised. The angle at which the coin started to slide was measured.

The shear adhesion force of linear and hierarchical pillars is illustrated respectively in Figures 7.3a and b. The sample with linear pillars slid off at 64° tilt angle while the hierarchical nano-pillars sample remained adhered to the glass-slide at 90° tilt angle. This shows that the hierarchical pillar tape indeed has enhanced adhesion over the linear one.

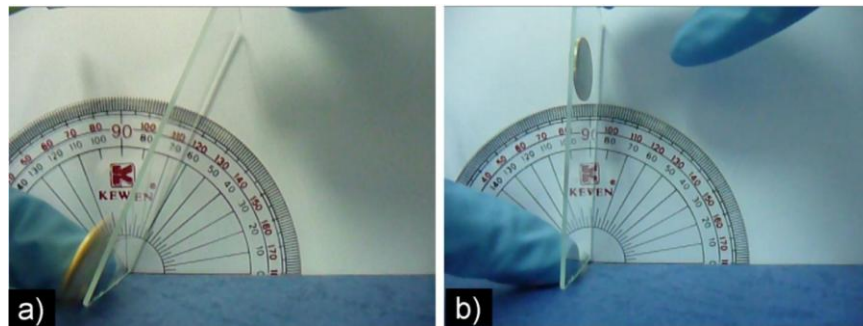


**Figure 7.3.** Preliminary shear adhesion force tests. a) linear pillared tape sliding off at 64° tilt c) hierarchical pillared tape still remaining on the glass slide at 90° tilt.



A series of experiments were conducted whereby weights were added to determine the angle at which the coin started to slide so as to provide an estimate of the adhesive friction force (Figure 7.4a). Figure 7.4a depicts the schematics of the test performed, with the back of a hierarchical nano-pillars sample glued to the coin and subsequently placed facing down on the glass-slide and tilted. From this diagram, a free body diagram was generated (Figure 7.4b) to resolve the force to its components for the calculation of the adhesive friction force and normal force (Figure 7.4c).

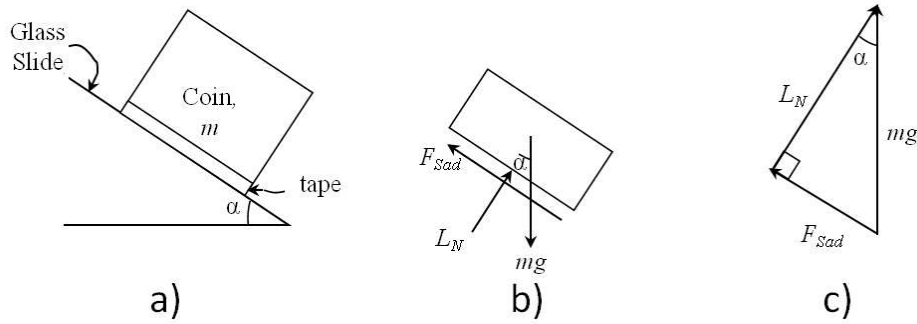


**Figure 7.4** a) Schematic of coin on glass-slide being tilted, b) free body diagram of the forces acting on the tape c) closed diagram to calculate shear adhesion friction force,  $F_{Sad}$ .

As stated in Eq. 7.3, shear adhesion force has two components: the Amontons' frictional force component ( $\mu L_N$ ) and van der waals force component ( $S_c A$ ).

$$F_{Sad} = \mu L_N + S_c A \quad (\text{Eq. 7.3})$$

By normalizing the adhesive friction force by the normal external load applied:

$$\frac{F_{Sad}}{L_N} = \mu + \frac{S_c A}{L_N} \quad (\text{Eq. 7.5})$$

The shear adhesion force in this case is the force applied parallel to the inclined surface to cause the movement of the object by overcoming the static friction,  $F_{Sad}$ .  $L_N$  is the normal force acting on the sliding sample.

From Figures 7.4b and 7.4c, the forces are resolved to obtain:

$$F_{Sad} = mg \sin \alpha \quad (\text{Eq. 7.6})$$

$$L_N = mg \cos \alpha \quad (\text{Eq. 7.7})$$

Table 7.1 contains the experimental data obtained with increasing weights and its corresponding slipping angles, frictional forces and normal forces.

**Table 7.1.** Data from adhesive friction measurements and calculated adhesive friction force for hierarchical pillars.

Total Weight, m (g)	Slip angle, $\alpha$ (°)	$F_{Sad} = mg \sin \alpha$ (mN)	$L_N = mg \cos \alpha$ (mN)	$\frac{F_{Sad}}{L_N}$	$\frac{1}{L_N}$
1.41	90	13.83	0.00	$\infty$	$\infty$
4.01	75	38.00	10.18	3.73	0.098
5.91	60	50.21	28.99	1.73	0.034
8.70	45	60.34	60.34	1	0.017

Based on  $\frac{1}{L_N}$ ,  $\frac{F_{Sad}}{L_N}$  vs.  $\frac{1}{L_N}$  is plotted in Figure 7.5 to show the relationship

of  $\mu$  and  $S_c.A$ . When the slip angle is at  $90^\circ$ ,  $\cos \alpha$  is zero, therefore the value of  $\frac{F_{Sad}}{L_N}$  and  $\frac{1}{L_N}$  for weight of 1.41 g approaches infinity. This data point whereby  $\frac{F_{Sad}}{L_N}$  and  $\frac{1}{L_N}$  approach infinity when the slip angle is at  $90^\circ$  is not plotted. This is because both this point would extend infinitely from the adjacent data point of 10.18 N and the trend in between these two points could not be determined accurately. The corresponding values of  $L_N$  are highlighted in parenthesis at each data point for easy reference.

For  $L_N$  tend to infinity,  $\frac{1}{L_N}$  tend to zero, and the term  $\frac{S_c.A}{L_N}$  tends to zero.

According to Eq. 7.3, it means that  $\mu$  is the intercept, with  $0 < \mu < 1$ . The term  $S_c.A$  is represented by the gradient of the non-linear curve. Due to the nano-pillared structure of

the PC film, it appears that when  $L_N$  is small,  $\frac{F_{Sad}}{L_N}$  is large due to the existence of high van der Waals forces. This corresponds well with the dominance of the adhesion-

controlled term  $\frac{S_c.A}{L_N}$  as stated in Eq. 7.3. However, when  $L_N$  is large, the effect (or

proportion) of van der Waals forces decreases and  $\frac{F_{Sad}}{L_N}$  becomes small and the

contribution of  $\mu$  in the load controlled term as given in Eq. 7.3 tends to become more significant. This phenomenon serves as a precursor for further investigations.

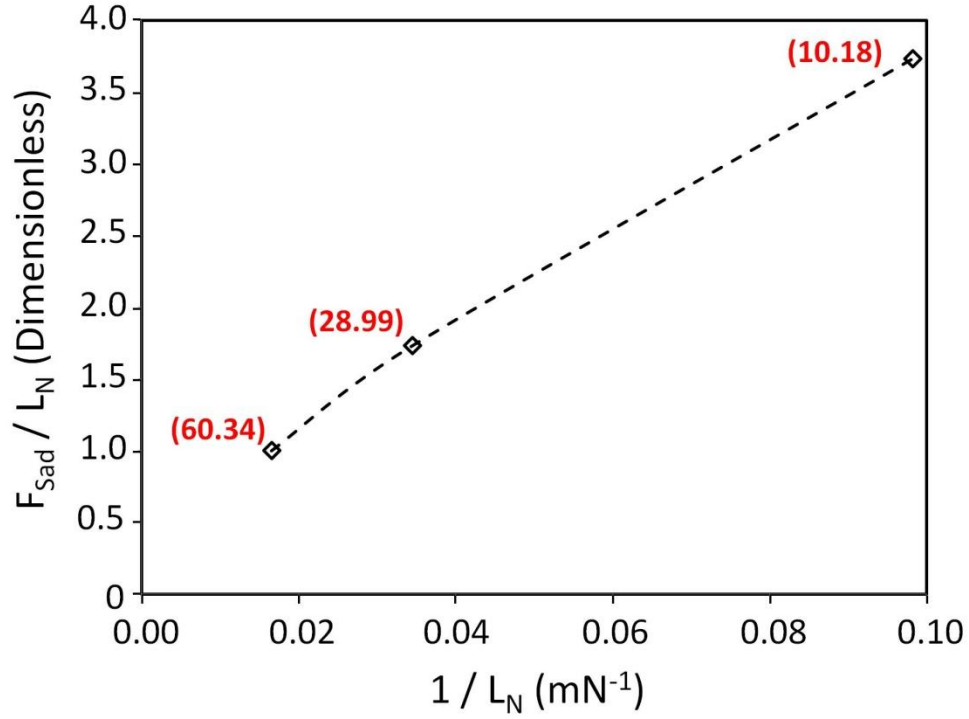


**Figure 7.5.** Plot of  $(\frac{F_{Sad}}{L_N})$  vs.  $(\frac{1}{L_N})$ .

By considering that  $S_c$  is a material constant, we assume that  $A$  is a function of  $L_N$ .

$$A = f(L_N) \quad (\text{Eq. 7.8})$$

Intuitively, it is expected that the contact area  $A$  is a function of normal force and will increase non-linearly with normal force. This is expected as with increasing normal force applied to the branched-pillar PC substrate, the pillars will undergo more deformation with the branched-pillars first being in contact with the glass slide surface followed by the base pillars. Figure 7.5 indicates that when  $L_N$  increases, the gradient of the curve becomes steeper, implying a corresponding increase in  $A$ .

However, this experimental investigation, although provides a useful preliminary indication on the relationship between frictional adhesion force, Amontons' frictional force and van der Waals force components, could not provide a quantitative assessment on contact area and related adhesion force. To have a quantitative assessment on the relationship of the contact area with respect to normal loads, more rigorous shear adhesion tests were carried out systematically as detailed in Section 7.6.

## **7.6 Quantitative Adhesive Force Measurements**

### **7.6.1 Shear Adhesion Testing Setup**

For macro-scale shear adhesion measurements, a Universal Testing Machine (UTM) Instron 5543 was employed to conduct the measurements. A tape with size of 1 cm<sup>2</sup> was used. Shear adhesion tests were performed at room temperature (~23°C) and humidity of ~70 %. A 2.5 N load cell was fixed to the machine's crosshead. A ball-bearing teflon pulley aligned directly under the load cell was used to translate the vertical movement to a lateral displacement for the shear tests. To connect the load cell to the test sample, a thin copper wire with diameter of 30 µm was employed. The sample was then placed with the pillars facing a glass slide. To prevent the sample from twisting during pulling when conducting the shear test, Teflon-taped side guides each with 0.5 mm clearance were fixed onto the glass slide on both sides of the sample.

A preload in the form of dead weights (45 mN) was placed on the sample and then the copper wire was pulled to just taut. The sample weight is negligible in the

analysis has each sample weighs averagely  $0.0225 \pm 0.001$  g (0.22 mN). This is approximately 130 times lighter than the initial preload of 30 mN. Hence, the sample weight is negligible in the analysis.

As the sample slid on the glass surface when the crosshead was extended upward, the shear force was registered. A constant speed of 5 cm/min was used to pull the sample over a total displacement of 5 cm. Figures 7.6a and b depict the schematic as well as the actual test setup respectively.

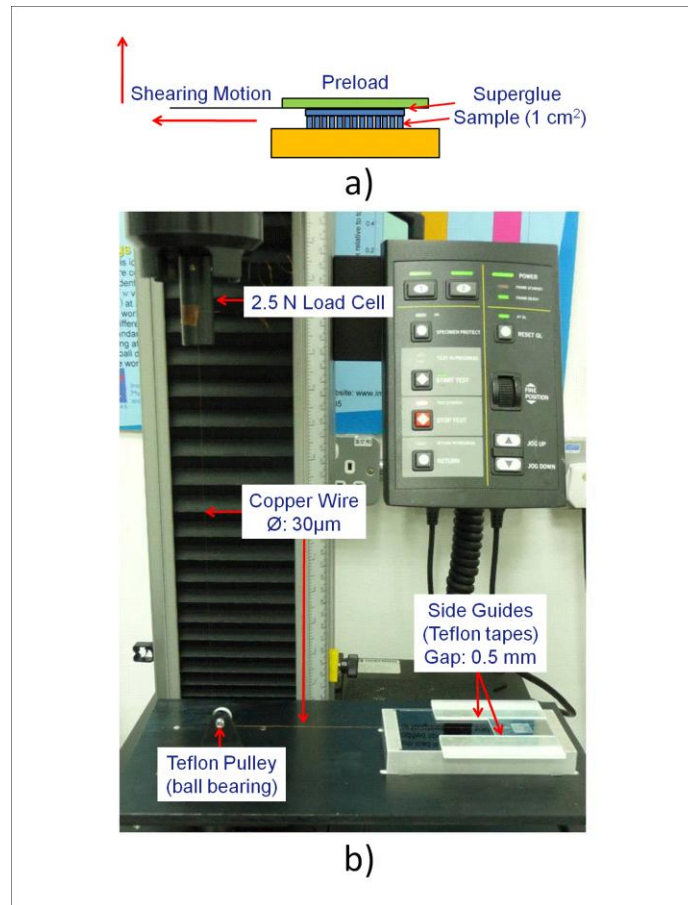


**Figure 7.6.** a) Schematic and b) actual shear adhesion force measurement setup.

Figure 7.7 shows the shear adhesion force versus the extension curve registered for the test conducted using preload of 45 mN. The shear adhesion force increased rapidly in the first 0.7 cm and peaked at 21.9 mN. The maximum shear adhesion force is considered as the static friction force, just before the substrate starts to slide on the glass surface is used. Stick-slip phenomenon was observed as a result of overcoming the apexes of asperities of the glass substrate [202, 203].

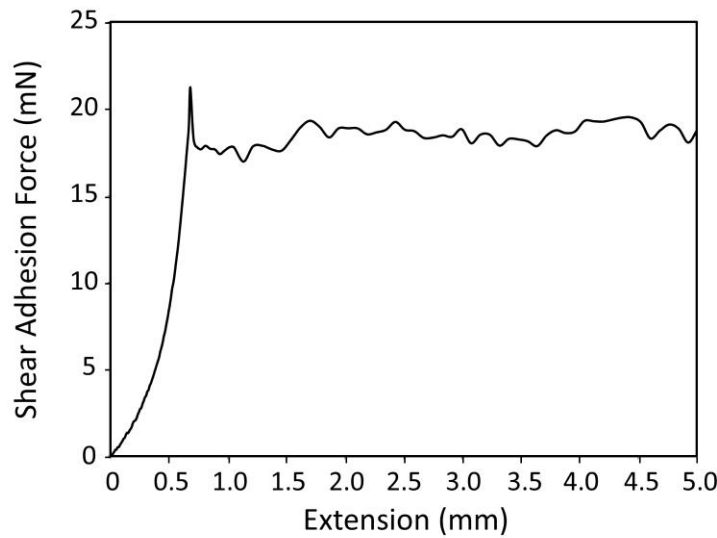


**Figure 7.7.** Shear adhesion force versus the extension curve for the test conducted using preload of 45 mN

After the shear tests, the tape surface was imaged by SEM. It was consistently observed that the pillars after the shear adhesion experiments remained deformed. This was ascribed to plastic deformation of the structures during the tests and thus experiences incomplete recovery upon load removal. Lee et al. [82] also reported the same observation. To obtain quantitative information of the effect of residual plastic deformation on the contact area, after each measurement, the samples' surface were taken

for observations under an optical microscope to capture the images of the areas of residual deformation. The areas of residual deformation are the areas where the pillars had been in contact with the glass surface. This method of contact area observation differs from those previously reported in the literature whereby in situ video recording of the contact area was employed during the shearing [82] or pulling-off [204] the samples. The in situ observation of surface would not provide any indication on the effect of residual deformation caused by plastic deformation of the pillars.

The substrates were consecutively tested with increased preloads. The same test procedure was repeated for step-increments of 25 mN of preload. Three measurement repetitions were carried out for each preload.

A control image for each sample was first captured using an optical microscope prior to the shear test. One obstacle faced was that the microscope was limited by its field of view, thus, it was not possible to capture the entire area of the sample. This was solved by taking the images in parts and subsequently stitched together before analyzing them with image processing software (ImageJ, version 1.41o). For the software to analyze the stitched image, it first has to be quantized to a 8-bit grayscale format from its original RGB format. Figure 7.8a illustrates the stitched and quantized control image.

The percentage of area with light contrast of the control image was estimated based on the percentage of pixels of the light contrast (area fraction) of the grayscale image, (Figure 7.8c). The reason that light contrast is observed even in the control image is due to the contrast from the adhesion layer between the sample and the preload. In



addition, handling of a sample caused minor scratches on top of the surface. The same procedure was repeated after each shear force measurement. Figures 7.8b and d elucidate the optical images after a typical shear adhesion test.

To obtain the area of residual deformation, the area fraction of each image after each shear force measurement was subtracted from the area fraction of the control image. This is on the basis that the increase of area fraction was due to the pillars being in actual contact with the glass slide. Thus, the increased of area fraction was assumed to be the area of residual deformation of the pillars with the glass slide. The basis of this assumption will be discussed in Section 7.6.2.

To account for the ambiguous spots due to focusing difficulty and errors arising caused by stitching of the images, three sets of images of the same sample after each test were carefully taken. The scatter of measurements is reflected by the standard deviations in the graphs.

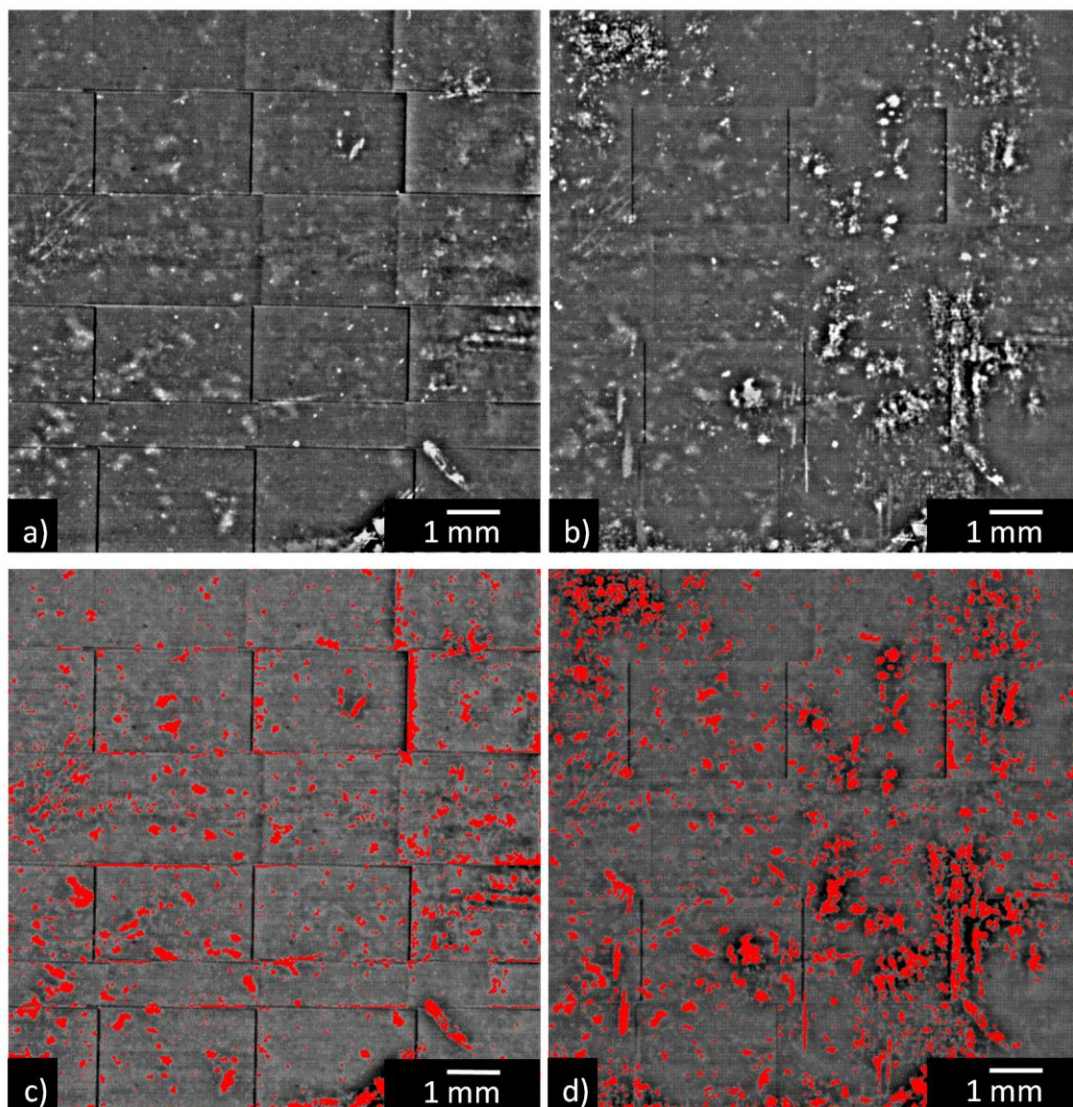


**Figure 7.8.** Stitched images of adhesive tapes taken with optical microscope. a) control images (prior to shear adhesion test). b) images taken after a typical shear force measurement. The light contrast differences between a) and b) corresponds to contact area of pillars with the glass slide. Images of a) and b) were analyzed using image processing software (ImageJ, v1.41o) and are shown in c) and d) respectively.

### 7.6.2 Shear Adhesion Force in Repetitive Measurements

Figure 7.9 shows that there is a linear increase of shear adhesion force for all the substrates when shear adhesion tests were repeated with the same preload (30 mN). The mean and its respective standard deviation values are shown in Table D1 (Appendix D). Such observation has previously been reported [82]. Though pristine PC films (without any pillar structures) did show increase of shear adhesion force during repeated tests, the increase was minimal ( $1.60 \pm 0.07$  mN/test). This was followed by the increase in adhesion force for linear pillars ( $4.88 \pm 0.23$  mN/test). The hierarchical pillars showed the highest increase in consecutive measurements ( $15.85 \pm 0.44$  mN/test).

The reason for this observation could be that shearing under a preload caused the pillars to deform plastically to the same height during each test. This resulted in side contact of the pillars (outer surface area along the pillar in contact with the shearing surface), see Figure 7.10a. The assumption of plastically deformed pillars is made based on the SEM image in Figure 7.10a which shows the hierarchical pillars remained in a deformed state. This indicated incomplete recovery upon the removal of preload.

To clarify further, due to the inherent non-uniformity of the self-assembled fabrication processes of the PAA template used, there was a small variation in pillar height as schematically shown in Figure 7.10b(i). Thus, it is probable that, during the first shear adhesion measurement, the taller pillars would first come into point contacts with the glass surface Figure 7.10b(ii). As the pillars were being sheared, the pillars would be bent along the shear direction [205]. Consequently, this decreases the overall height of

the pillared topography conceding the shorter pillars to come into contact with the glass surface. As a result, more pillars made side contact to the test surface (Figure 7.10b(iii)). As this occurred in each consecutive test, there was a proportional increase in the area of residual deformation resulting in higher shear adhesion force. This observation further confirms that the pillars were not completely recovered after each test. Hence, the area of residual deformation could be used as an indirect indication of the effective area of contact.

Hypothetically, this increase would prevail until all the pillars came into full contact with the glass slide. However, since the samples were inherently not completely flat coupled with the stiff polymer backing layer of the substrates ( $\sim 150\text{ }\mu\text{m}$ ), full contact of all pillars could not be achieved.

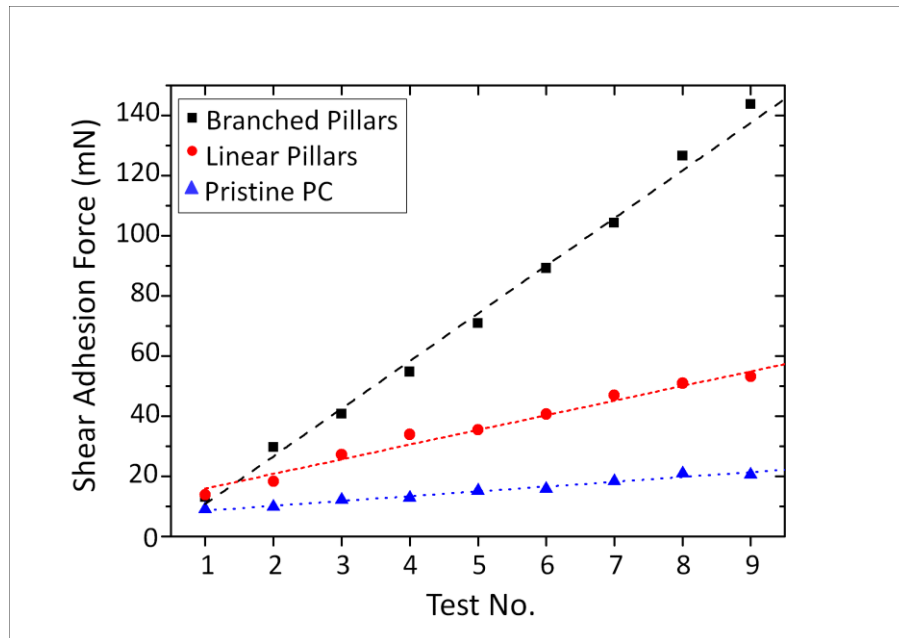


**Figure 7.9** Shear adhesion force of branched, linear pillars and pristine polycarbonate with repeated measurements using same preload of 30 mN.

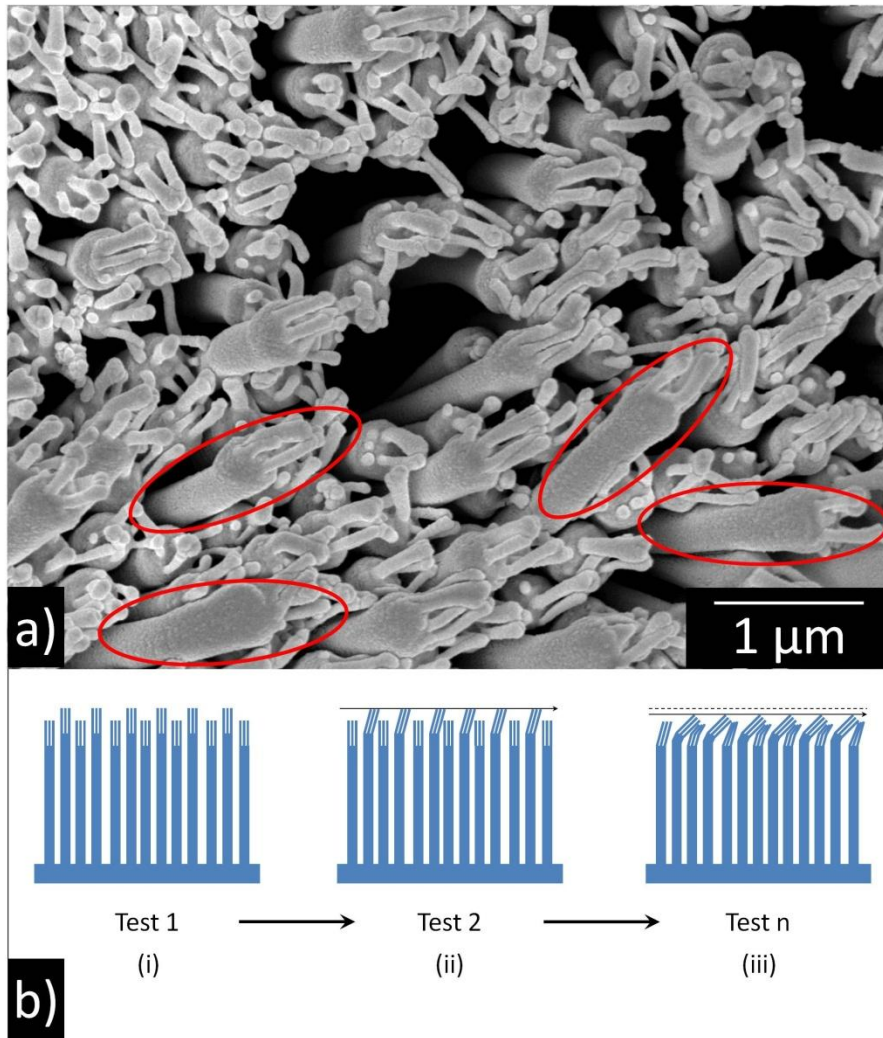


**Figure 7.10.** a) SEM image depicting the plastically deformed hierarchical pillars after a shear adhesion measurement. Circles highlight some of the side contacts of the pillars. b) Schematic illustration of pillars conditioning for consecutive shear adhesion measurements.

### 7.6.3 Shear Adhesion Force versus Applied Preloads

Figure 7.11a depicts the shear adhesion force measurements of substrates with hierarchical and linear pillars at different preloads. To plot the graphs, the maximum shear adhesion force, considered as the static friction force, just before the substrate starts

to slide on the glass surface is used. The hierarchical pillars exhibited higher shear adhesion force than the linear pillars for all preloads higher than 65 mN. Linear fitting of the data points produces a slope of  $1.39 \pm 0.08$  ( $R^2$  of 0.98) for hierarchical pillars and  $0.55 \pm 0.04$  (dimensionless) ( $R^2$  of 0.96) for linear pillars. These slopes indicate the adhesiveness of the two samples against the smooth glass surface. This translates to the hierarchical pillars outperforming the linear pillars in shear adhesion measurements by 150% or 2.5 times (for the same overall pillars' height and base pillars' diameter (ref. Figures 6.1 and 6.3)).

Figure 7.11b shows the estimated area of residual deformation of the test substrates obtained from image analysis as a function of different preloads. Excluding the very low preload, higher area of residual deformation was recorded between the hierarchical pillars and the glass surface as compared to the linear pillars. This proffers the reason for the higher effective shear adhesion force of the hierarchical pillars as shown in Figure 7.11a. At the very low preload region in Figure 7.11b, no significant difference was observed in the area of residual deformation between the hierarchical and linear pillars. Therefore, at these low preloads, the shear adhesion force registered similar values for both the hierarchical and linear pillars substrates as shown in Figure 7.11a. This further affirms the role of the contact area in shear adhesion and is in agreement to Yoon et al.'s observation [41]. The observation in Figure 7.11a is in line with our observation in Figure 7.5.

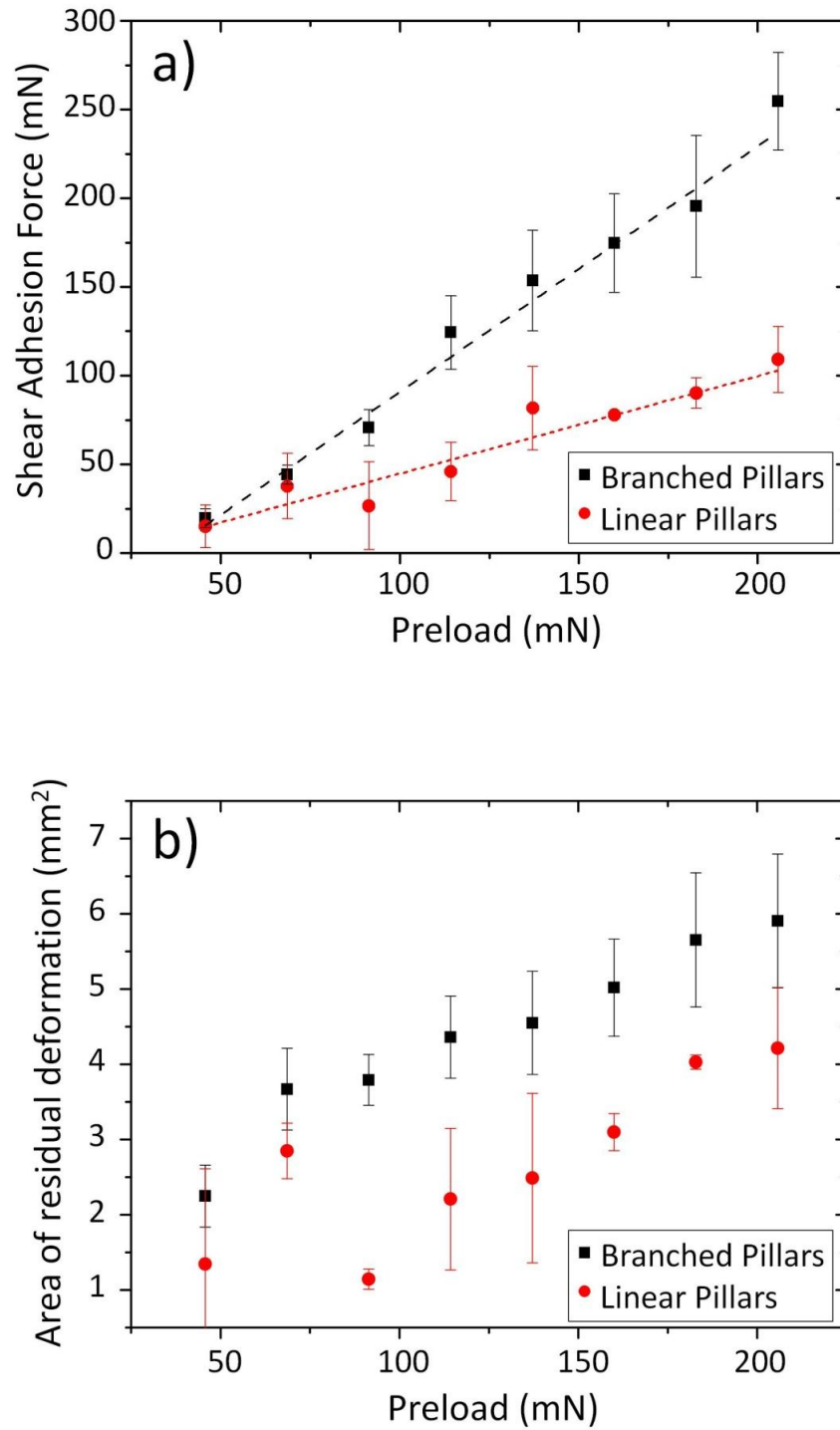


**Figure 7.11** a) Shear adhesion force as a function of preload for branch and linear pillars, b) Area of residual deformation (effective contact area after the removal of preload) of pillars against glass slide as a function of preload.

The classical beam theory [206] can be used to explain qualitatively the superior shear adhesion force displayed by the hierarchical pillar topography over the linear pillar topography. According to the theory, the deformation of a beam may be described by:

$$M = EI\kappa \quad (\text{Eq. 7.9})$$

where  $M$  is the applied bending moment,  $E$  is the Young's modulus,  $I$  is the moment of inertia of the beam's cross section and  $\kappa$  is the curvature. The product of  $EI$  is referred as the flexural rigidity of the beam, and it governs the ease of deformation of the beam. To have a flexible beam, the value of  $EI$  has to be a small value. If the two different beams are of the same material, the  $E$  will be the same, and hence, to have high flexibility, moment of inertia  $I$  has to be small.

The  $I$  of the linear pillar (circular cross-section) is given as [207]

$$I = \frac{\pi D^4}{64} \quad (\text{Eq. 7.10})$$

where  $D$  is the diameter of the linear pillar as shown in Figure 7.12a.

As the diameter of the branched pillars of the hierarchical pillar,  $d$ , is  $\sim \frac{1}{3}$  of the diameter of the base pillar,  $D$ , the  $I$  of a single branched pillar is (see Figure 7.12b)



$$I = \frac{1}{3^4} \left( \frac{\pi D^4}{64} \right) \quad (\text{Eq. 7.11})$$

Thus, the  $I$  of a single branched pillar is a significant 81 times less than that of a linear pillar. Every single base pillar has four branched pillars. As shown in Figure 7.12b, due to dissimilar planes of contact, only two out of four of the branched pillars are assumed to act in unison during shearing. As such, the equation for  $I_b$  is written as  $2 \left( \frac{\pi d^4}{64} \right)$ . The effective moment of inertia for two branched pillars will be  $\frac{2}{3^4} \left( \frac{\pi D^4}{64} \right)$ .

This is approximately 40 times less than that of a single linear pillar.

This analysis provides the explanation of the significant improvement in the flexibility of the hierarchical pillar configuration over the linear pillar configuration. Consequently, this increase in flexibility enhances the effective area in contact (through side contact) [205] to a test surface as shown in Figure 7.13a and b.

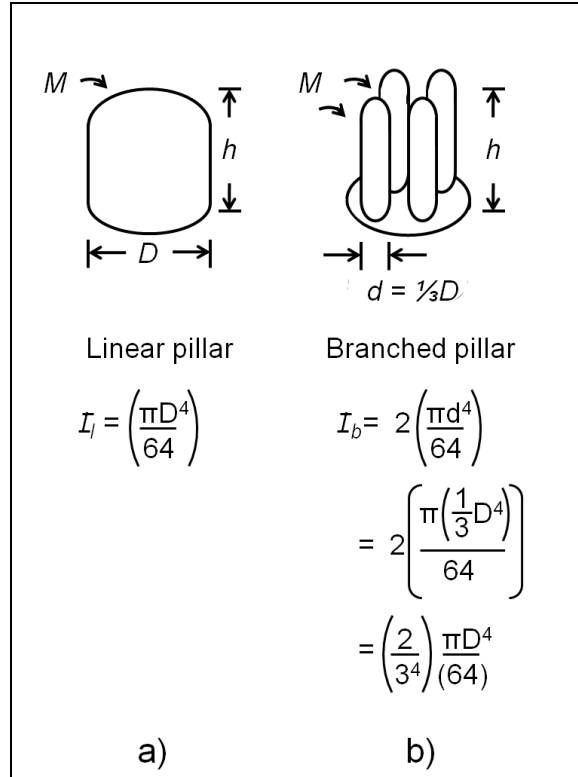


**Figure 7.12.** Illustration of the  $I$  for a) linear and b) hierarchical pillar respectively.

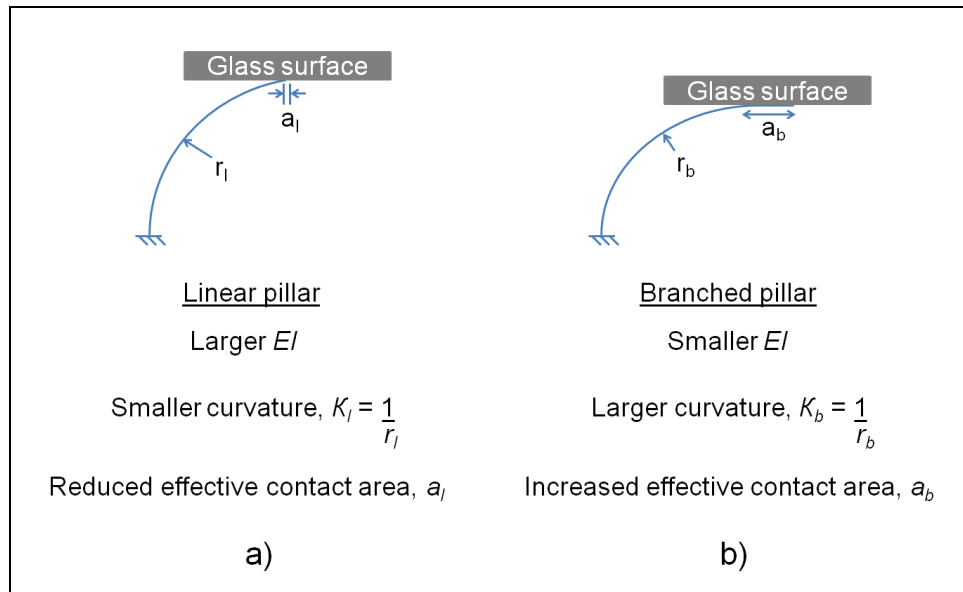


**Figure 7.13.** Illustration of the effective contact area of the a) linear pillar and b) hierarchical pillar respectively.

To verify this explanation, the SEM images in Figures 7.14a and b were taken for linear pillars and hierarchical pillars respectively after the same shear adhesion test was conducted. As seen from these images, there were more hierarchical pillars bent in the direction of shear, thus indicating higher area of residual deformation with the glass surface.

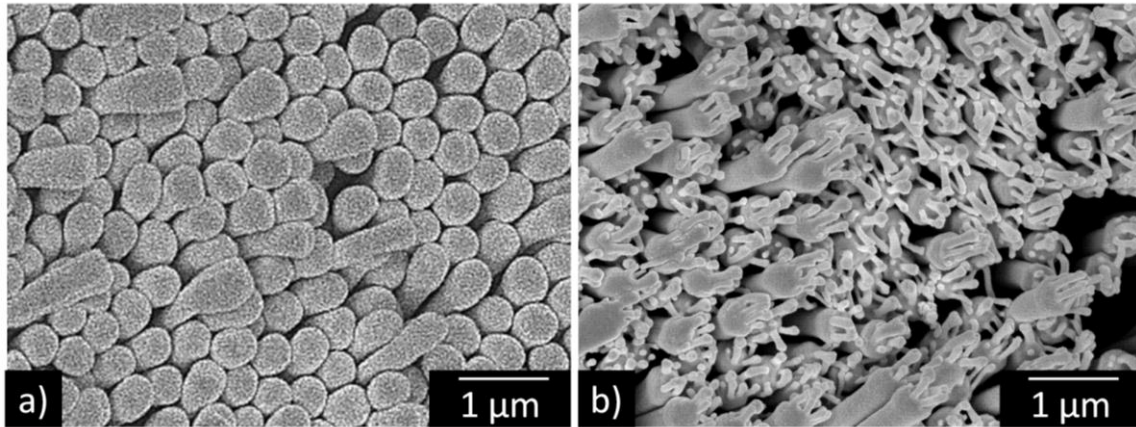


**Figure 7.14.** SEM images of samples after shear adhesive tests were performed a) linear pillars and b) branched pillars. More branched pillars bent in the direction of shear indicating more area of contact.

#### 7.6.4 Shear Adhesion Force versus Area of Residual Deformation

Analysis of the relationship between shear adhesion force and area of residual deformation for both branched and linear pillars is performed as shown in Figure 7.15. The linear fitted slope for hierarchical pillars and linear pillars are respectively  $65.2 \pm 8.2$  mN/mm<sup>2</sup> and  $26.6 \pm 5.6$  mN/mm<sup>2</sup>. Thus, for every unit of increased area, the shear adhesion force will increase by 65.2 mN and 26.6 mN respectively for hierarchical and linear pillars.

This significant difference between the hierarchical and linear pillars could be due to the ability of the branched pillars of the hierarchical pillars to reach into the finer asperities of the glass surface and approaches the atomic gap of 0.3 nm [20]. Hence, there is an increase of Van der Waals attraction between the surfaces.

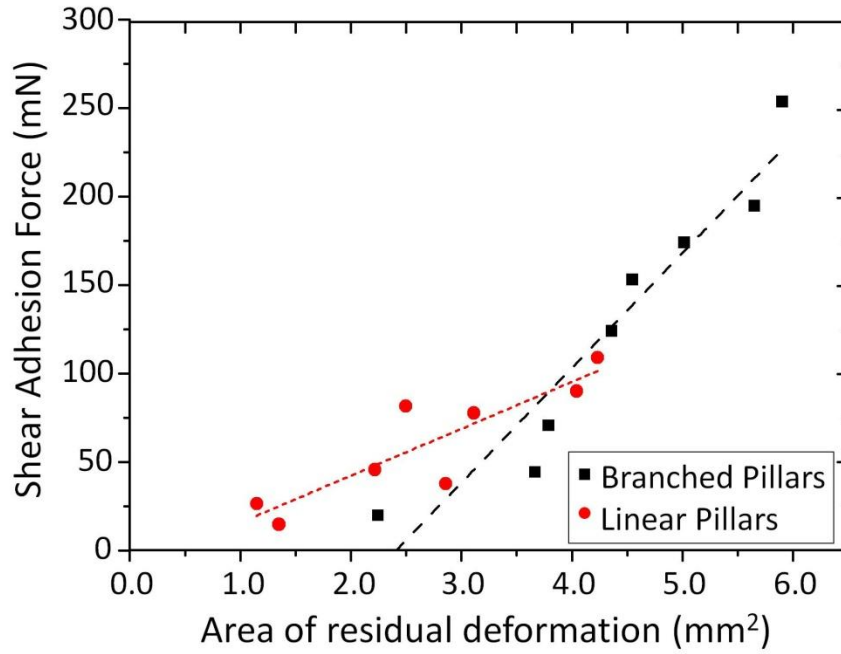


**Figure 7.15.** Shear adhesion force of hierarchical and linear pillars as a function of area of residual deformation.

These results are in agreement with description by the general equation for shear adhesion force (friction force),  $F_{Sad}$  of two sliding surfaces (of molecular smoothness) [200] given by Eq. 7.3

$$F_{Sad} = \mu L_N + S_c A \quad (\text{Eq. 7.3})$$

Eq. 7.3 indicates that an increase in effective contact area will result in an enhancement of shear adhesion force.

It may be arguable that the role of contact area in Eq. 7.3 is not well portrayed in Figure 7.11b, as the effective contact area may be induced by the externally applied normal load as discussed by Gao *et al* [196]. However, the results in Figure 7.9 showed increasing shear adhesion force for the same preload when repeatedly tested. This implies that the effective contact area is not only a function of the preload, but also the actual structural state of the pillars, which is exhibited by the residual deformation.

### **7.6.5 Shear Adhesion Force per unit Area versus Preloads**

Another perspective to evaluate the performance of hierarchical pillars is to examine the shear adhesion force per unit contact area as a function of applied preloads. Figure 7.16 is derived from dividing the shear adhesion force by the area of residual deformation, of the two types of pillars, and plotted as a function of its respective preloads. In the lower range of preload, it shows that both the hierarchical and linear pillars show similar values of shear adhesion force per unit area. As the preloads increase, the difference becomes more prominent, inferring that the hierarchical pillars have superior adhesive performance.

Figure 7.16 also shows that the shear adhesion force per unit area for linear pillars approaches saturation after a preload of 90 mN. In contrast, the hierarchical pillars

did not show any saturation for the maximum preload investigated even though the rate of increase of shear adhesion force per unit area decreased.

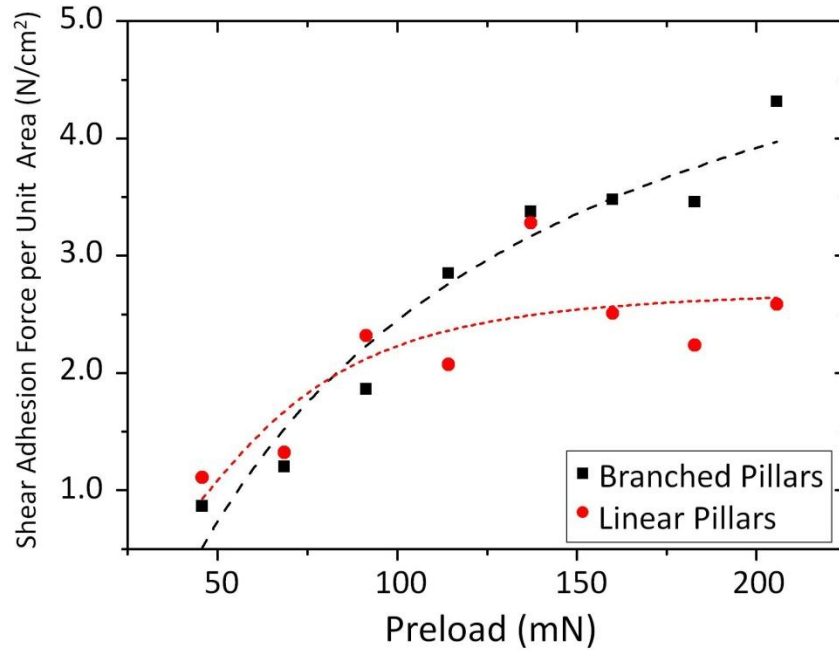


**Figure 7.16.** Shear adhesion force per unit effective contact area of hierarchical and linear pillars versus preload.

This could be comprehended from the context of collective stiffness of the linear and hierarchical pillars. The linear pillars seemingly reached its maximum collective stiffness. This is analogous to a compact film and therefore there is no improvement in shear adhesion strength irrespective of preload increments. However, the reason that the adhesion strength of the hierarchical pillars did not reach saturation is that the collective stiffness of the hierarchical pillars is lower than the linear pillars.

It is noteworthy that the area of residual deformation for the linear pillars was initially 1-3 mm<sup>2</sup> but gradually increased to 3.5-5 mm<sup>2</sup>. The same happened to the hierarchical pillars which was originally 1-3 mm<sup>2</sup> and increased to 5-7 mm<sup>2</sup> after the application of 210 mN preload. As the samples' sizes were 1 x 1 cm<sup>2</sup>, the area of residual deformation in correspondence to the area that had been in contact had only reach 7 % of the total sample area.

One rationale for this low value is that the unevenness of the thick polymer backing film of ~150 µm was too rigid to allow most of the topographic structures to reach the test surface. Thus, it is undesirable to have a thick backing layer in dry adhesion tests. This could be resolved by fabricating adhesive structures on a more flexible and thinner substrate [47].

Nonetheless, it can be seen from Table 7.2 that the shear adhesion force of the hierarchical structures produced in this work reached a value of 6.5 N/cm<sup>2</sup> which is 35 % less in force than the shear adhesion force of the natural gecko foot-hair (β-keratin) (10 N/cm<sup>2</sup>).<sup>7</sup> This could be due to the synergy of micro- and nano-scale features of the natural gecko-foot hair when used in unison as optimized by nature as well as the special muscles and joint design used for locomotion [19]. Table 7.2 also shows the comparison of hierarchically structured tapes fabricated in this work with those reported by other authors. However, direct comparisons of shear adhesion performance of the various reported synthetic gecko inspired adhesives are difficult as there are variations in terms of the type of polymeric materials used, the range of feature sizes as well as the type of measurements conducted.

**Table 7.2.** Summary of shear adhesion forces for reported natural gecko foot-hair and fabricated hierarchical structures

Material Type	Material (modulus)	Feature size	Type of measurement	Normal adhesion force	Shear adhesion force	Ref
<b>Hard</b>	B-keratin (1-15 GPa)	Micro & Nano	Macroscopic	1 N/cm <sup>2</sup>	10 N/cm <sup>2</sup>	[20]
	PMMA (2.4 GPa)	Micro & nano		Not available		[50]
	PC (2 GPa)	Nano	Macroscopic	Not available	6.5 N/cm <sup>2</sup>	This work
<b>Soft</b>	PDMS (1.8 MPa)	Micro	Microscopic	~ 4 N/m <sup>2</sup>	Not available	[1]
	PU (3 MPa)	Micro	Microscopic	~ 5.3 kN/m <sup>2</sup>	Not available	[2]
	PUA (19.8 MPa)	Micro	Macroscopic	Not available	9 N/cm <sup>2</sup>	[5]

### 7.6.6 Resolving Shear Adhesion Force into Components

As proposed by Zeng et al. [200] where gecko's adhesion is described by Eq. 7.3, it would be beneficial to resolve the shear adhesion force of the fabricated structures into its respective adhesion mechanism. This would provide greater understanding of adhesion mechanisms of the fibrillar structure as well as the hierarchical structure. With such understanding, the transition from one mechanism to another and its limiting normal load could also be determined.

For this purpose, the shear adhesion force,  $F_{Sad}$  is normalized with its respective area of residual deformation,  $A$  as given in Eq. 7.12 to determine  $\mu$  and  $S_c$



$$F_{Sad} = \mu L_N + S_c A \quad (\text{Eq. 7.3})$$

Normalizing the equation by  $A$

$$\frac{F_{Sad}}{A} = \mu \left( \frac{L_N}{A} \right) + S_c \quad (\text{Eq. 7.12})$$

Due to the large scatter of the experimental results obtained for shear adhesion force and area of residual deformation, a series of graphs spanning from +1 to -1 of the standard deviations for  $F_{Sad}$  and  $A$  were compared.  $L_N$  had no standard deviation since specific weights were used. In this analysis,  $\mu$  would be represented by the gradient of the curve with  $S_c$  as the intercept at  $(L_N / A)$  at zero. Constraints to be satisfied are  $1 > \mu > 0$  and  $S_c > 0$ .

In general, for a similar material of PC employed, a constant  $\mu$  is to be expected. However, for linear and hierarchical pillar samples, due to inherent variance in polymer material, and more importantly due to changes induced by the different processing for hierarchical and linear pillar, it is reasonable to expect a slightly different  $\mu$  between the linear and hierarchical pillar samples.

For the shear strength constant,  $S_c$ , it is also expected that for a similar material used, it would be a constant value. However, due to the different geometrical profiles of the linear and hierarchical pillars and processing histories, and the difficulty in obtaining accurate contact area values,  $S_c$  measured could be rather different for both samples.

Based on these analyses, for linear pillars,  $\mu$  is estimated to range from 0.24 to 0.48 and that  $S_c$  ranges from 0.16 to 1.24  $\text{Ncm}^{-2}$ . For hierarchical pillars,  $\mu$  ranges from 0.46 to 0.90 and  $S_c$  ranges from 0.18 to 1.05  $\text{Ncm}^{-2}$ . With the large scatter of experimental results, it is not possible to provide better estimates of the values for  $\mu$  and  $S_c$ . Figure 7.17 shows the various plots for linear and hierarchical pillars. Note the variations in both  $\mu$  and  $S_c$ .

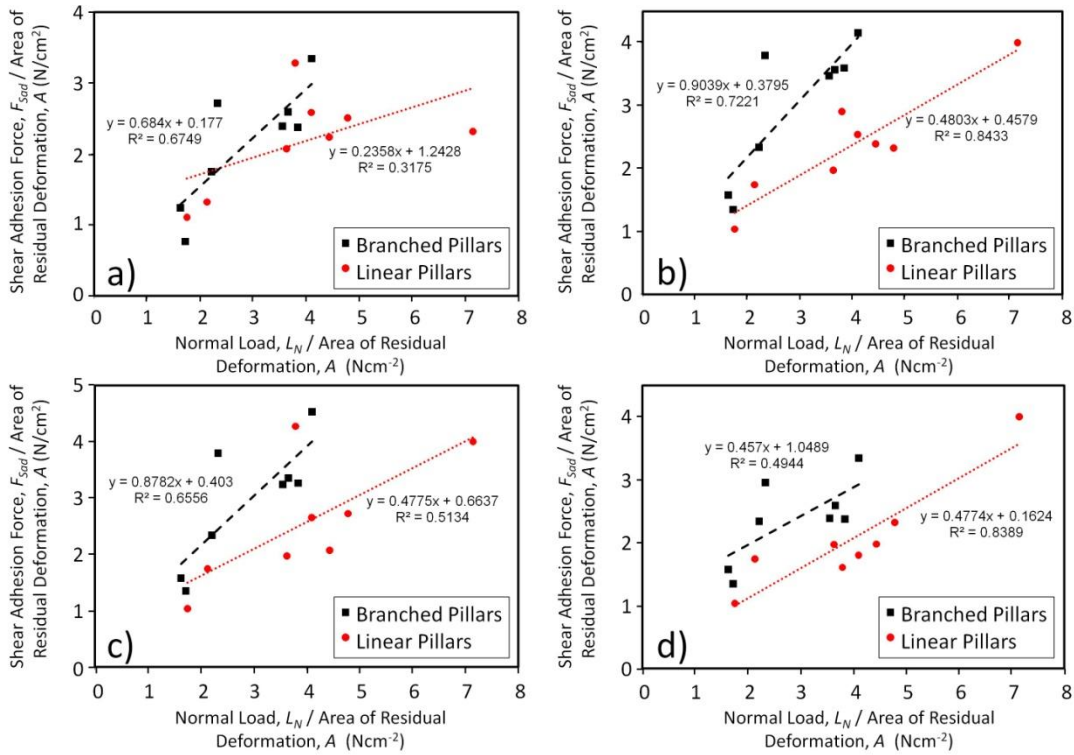


**Figure 7.17.** Various plots of  $\frac{F_{sad}}{A}$  versus  $\frac{L_N}{A}$ . Fitting equations depicting  $Y = mX + C$  where  $Y$

$= \frac{F_{sad}}{A}$ ,  $X = \frac{L_N}{A}$ ,  $m$  = slope of curve,  $\mu$  and  $C$  = intercept at Y-axis,  $S_c$ . The adjusted  $R^2$  values for

fitted equations are as shown.

### 7.6.7 Contact Angle Study

One of the advantages of hierarchical structures is the change in its wetting properties. The water contact angle of natural gecko setae  $160.9 \pm 1.4^\circ$  as determined by Autumn et al. [29]. As reported by Kustandi et al [50] and Jeong et al [3], there was a noticeable increase of water contact angle in a hierarchical topography. This increase in water contact angle was similarly observed in the hierarchical pillar topography fabricated in this investigation.

Using the Ramé-Hart digital contact angle goniometer, the water contact angle was measured when an automatic pipette drops a deionized water droplet of 3  $\mu\text{L}$  gently on to the substrate surface. The image was captured immediately and the water contact angle was measured by the software provided. Three readings of the contact angles were taken and averaged for each sample.

The water contact angle on a pristine PC surface was  $68.9 \pm 2.7^\circ$ , it increased to  $113.9 \pm 2.1^\circ$  for linear pillars and  $145.4 \pm 3.9^\circ$  for hierarchical pillars. Figure 7.18 illustrates the snapshots of the water contact angles on pristine PC, linear pillars and hierarchical pillars substrates. It is imperative to have high hydrophobicity in gecko mimetic adhesives. This is to have good self-cleaning ability for repeated usage of the adhesives. Hence, the hierarchical pillars fabricated could match the hydrophobicity of the natural gecko foot hairs [208].

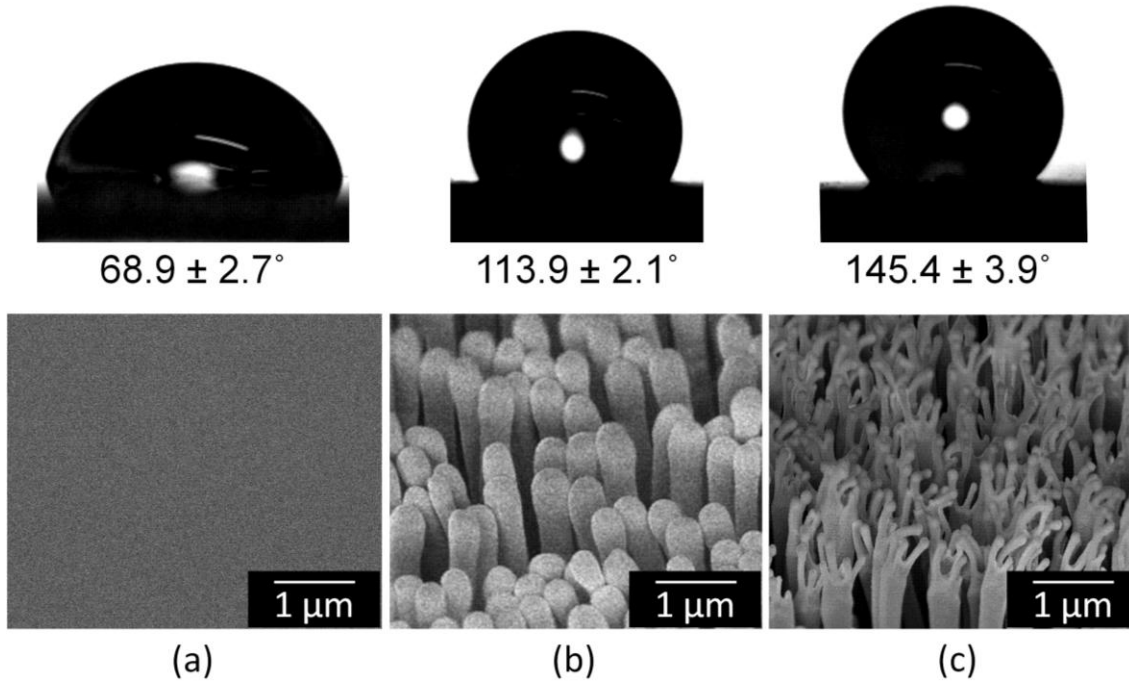


**Figure 7.18.** Water contact angles and corresponding SEM images of a) pristine polycarbonate b) linear polycarbonate pillars, and c) hierarchical polycarbonate pillars.

## 7.7 Summary

In summary, shear adhesion measurements in the macro-scale regime were carried out for the linear and hierarchical pillared gecko-inspired tapes and comparatively analyzed. The results conclusively show that the hierarchical structure improves the shear adhesion force over the corresponding linear structure by 150 %. Previous literature had hypothesized that hierarchical structures are superior to linear structures but has yet been able to establish some empirical results to prove this hypothesis. [1, 5, 50]. This is the first comparative study that establishes through a systematic evaluation the impact of the lower effective stiffness of a hierarchical structure to enhance shear adhesion.

This is achieved by carrying out optical microscopic examination to determine the contact area of residual deformation of the tape structures that had been in contact with the glass surface after the removal of preload. It was shown that the hierarchical pillars films had higher residual contact area than films with linear pillars due to their lower effective stiffness.

In addition, analysis by SEM revealed that upon contact with a surface, the increase in the area of residual deformation of the films, was greater for the hierarchical pillar structure than for the linear pillar structure. This was due to enhanced side contacts through bending of the pillars. These observations clearly exemplify the effect of a hierarchical structure in lowering the effective stiffness.

The reduction in effective stiffness favored a more efficient bending of the hierarchical topography and a better compliance to a test surface, hence resulting in a higher effective contact area. As the effective contact area increased, the shear adhesion force improved. Thus, through thorough investigation, the mechanism of the enhanced adhesion provided by hierarchical structure was successfully identified. The hierarchical pillar structures also showed a distinct increased in hydrophobicity, an important characteristic for the reusability of the dry adhesive tapes in practical applications.

# **Chapter 8   Micro –scale Shear Adhesion Force Analysis of Gecko- Inspired Dry Adhesives**

## **8.1   Overview**

Numerous experiments have shown that frictional force is scale-dependent as Amontons' friction coefficient ( $\mu$ ) of two contacting surfaces differ when measured at different length scales, i.e. micro/nano-scale versus macro-scale [209-211]. The different frictional behaviors can occur due to the dominance of different friction mechanisms (adhesion, plowing, plastic deformation, ratchet or “cobblestone mechanism” and “third body” mechanism) over different length scales [194].

Typically, friction force measurements in the nano-scale range are performed using friction force microscope (FFM) [212] while scanning force microscope (SFM) operates in the micro-scale regime [210]. Surface force apparatus (SFA) [199, 213, 214] were first developed to measure van der Waals attractions between two surfaces as a function of their separation either in vacuum or air.

To complement the macro-scale shear adhesion force analyses performed in Chapter 7, further investigations in the micro-scale regime are studied in this chapter. Micro-scale shear adhesion measurements were conducted using a dynamic nano-mechanical probe, namely the Nano Indenter® XP (MTS, Nano Instruments Innovation Center, USA).

Niederberger et al. reported that the ratio  $\frac{F_f}{L_N}$  which is Amontons' friction coefficient  $\mu$  (always less than 1) increased with normal loads [210], see Eq. 7.1. However, there are deviations to Amontons' law, for example it is possible to have friction force even at zero normal load as long as there are contacting surfaces over a finite area. This has been shown and discussed in Chapter 7 where the modified version of Amontons' equation (Eq. 7.3) is used [196]. For ease of reference, Eq. 7.3 is repeated here:

$$F_{Sad} = \mu L_N + S_c A \quad (\text{Eq. 7.3})$$

It can be rewritten as Eq. 7.5:

$$\frac{F_{Sad}}{L_N} = \mu + \frac{S_c A}{L_N} \quad (\text{Eq. 7.5})$$

The present investigation discovered that in the micro-scale regime, the ratio  $\frac{F_{Sad}}{L_N}$  for pillar structures and glass substrate increases with a decrease of the normal load, e.g. the coin-sliding experiments as discussed in Section 7.5.1. This will be further

elaborated from the perspective of different friction mechanisms acting on the sliding surfaces.

In addition, the hardness and elastic modulus of the surfaces of the respective samples were determined using load-penetration depth experiments. The elastic modulus of the hierarchical pillars was found to be lower in comparison to the linear pillars. This explains the higher contact area with the indenter and thus higher frictional forces as originally proposed by Bowden and Tabor [195].

## 8.2 Micro-scale Shear Adhesion Force Measurements

Initial reports on adhesion force measurements on gecko-mimetic adhesives were performed using atomic force microscopes (AFM). The probes used were usually tipless cantilevers [39, 50] as shown in Figure 8.1. The drawback of this method is that accurate contact area could not be determined. Other attempts to characterize the shear adhesive forces were carried out by using various custom-made setups [76, 215, 216]. As such, comparisons of shear adhesive performance among the reported fabricated gecko-mimetic adhesives could not be made easily or directly.

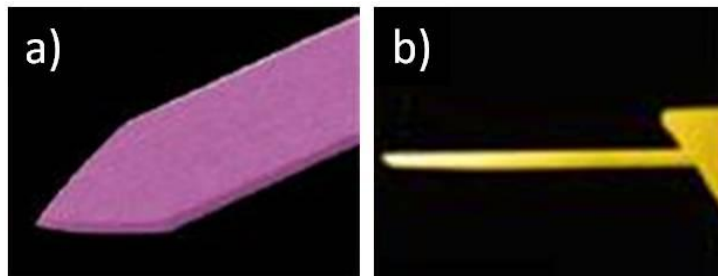


**Figure 8.1.** a) and b) Images of tipless AFM cantilevers



Micro-scale shear adhesion force measurements were conducted using a dynamic nano-mechanical probe, namely the Nano Indenter® XP (MTS, Nano Instruments Innovation Center, USA), (Figure 8.2). This equipment is hosted in a vibration isolation cabinet and rests on an air table to prevent external disturbances. Figure E1 (in Appendix E) illustrates the assembly of the primary functional components of the equipment. It is load-controlled with depth-sensing apparatus to continuously monitor the load and displacement of the indenter in relation to the sample surface [217]. The load is applied and controlled by modulating the current in the coil through the magnetic field strength of the permanent magnet as shown in the coil / magnet assembly in Figure E1. This type of load application is preferred for its simplicity and linear calibration [217]. Measurement of the indenter displacement is precisely performed by the capacitance gauge [218]. There are two slide methods which can be used; 1) progressive-force slide in which the applied load increases linearly with slide distance and 2) constant-applied force slide where the applied load remains constant throughout the slide. The contact area is in the range of tens of micrometer square.

Tangential force (friction force) experienced by the indenter during the sliding motion with the pillars can be measured using the slide mode. The slide and residual depths, friction coefficient, and residual roughness during slide testing could also be measured and output via equipment software (TestWorks™). Table E1 (in Appendix E) and Table E2 (in Appendix E) show the specifications of the equipment for nano-indentation and scratch mode.



**Figure 8.2.** Image of Nano Indenter® XP (MTS, Nano Instruments Innovation Center, USA).

### 8.2.1 Sample Preparation

The samples were mounted onto a 1.25” diameter sample holder using a very thin layer of instant cure superglue (cyanoacrylate adhesive). To ensure the sample surface to be perpendicularly flat to the tip of the indenter, the sample was cut to a smaller size to minimize the effect of any curvature of the sample. In addition, only a thin layer of glue was applied on the mount where the sample was adhered to.

Upon curing of the glue, a rigid bond is formed between the sample and the sample holder. As such, it is reasonable to assume that the superglue would not affect the measurements. To obtain reliable data, the sample surface was ensured to be perpendicularly flat to the tip of the indenter. The sample holder was then placed into the holes of the sample tray. The top of the sample was flushed with (at the same height as) the protruding edges of the sample tray. It was subsequently screw tightened. Figure 8.3a

shows the samples that had been glued to the holder and subsequently secured into the sample tray. The sample tray was finally loaded into the equipment as shown in Figure 8.3b.



Sample Tray

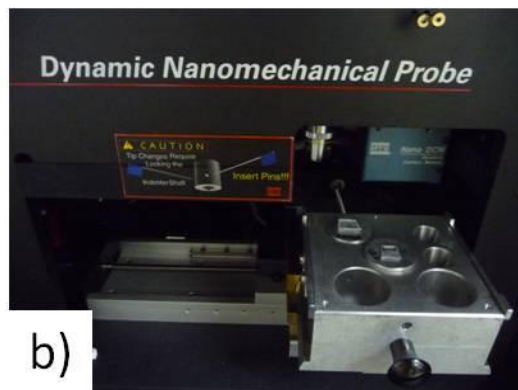


**Figure 8.3.** Images of a) samples glued to holder and subsequently secured into the sample tray, b) sample tray loaded into the equipment.

### 8.2.2 Experimental Procedure

The measurements were made using MTS Nano Indenter® XP with lateral-force (friction force) measurement module. Measurements were performed at room temperature (23°C) with a relative humidity of 70 %. The indenter tip (spherical, 5  $\mu\text{m}$  radius) was brought into contact with the pillars. Once contact had been detected, the stage would move laterally in the X- direction. The slide method used was constant-applied force slide.

Each measurement followed a pre-determined protocol. The protocol consisted of three horizontal sliding motions. The first slide was for profiling purpose, known as pre-slide. The load used was 10  $\mu\text{N}$ . The second slide was the actual slide where the lateral force and slide depth were registered. The final slide (post-slide) was to measure the residual depth / recovery on the surface of the polymer.

In the actual slide measurement, a line segment of 100  $\mu\text{m}$  was first profiled under an applied load of 10  $\mu\text{N}$ . This was followed by a 500  $\mu\text{m}$  line segment in which the normal load applied was varied (10  $\mu\text{N}$ , 25  $\mu\text{N}$ , 50  $\mu\text{N}$ , 100  $\mu\text{N}$ , 250  $\mu\text{N}$ , 500  $\mu\text{N}$ , 1 mN and 2 mN). The minimum load chosen was 10  $\mu\text{N}$ , which is at the lowest limit of the equipment. This capability of the equipment at this lowest limit was verified by observing that the system could maintain a stable 10  $\mu\text{N}$  during the slide, see Figure 8.4. The maximum slide force was chosen to be 2 mN as the pillars appeared to have plastic deformed along the slide direction as shown in Figure 8.5.

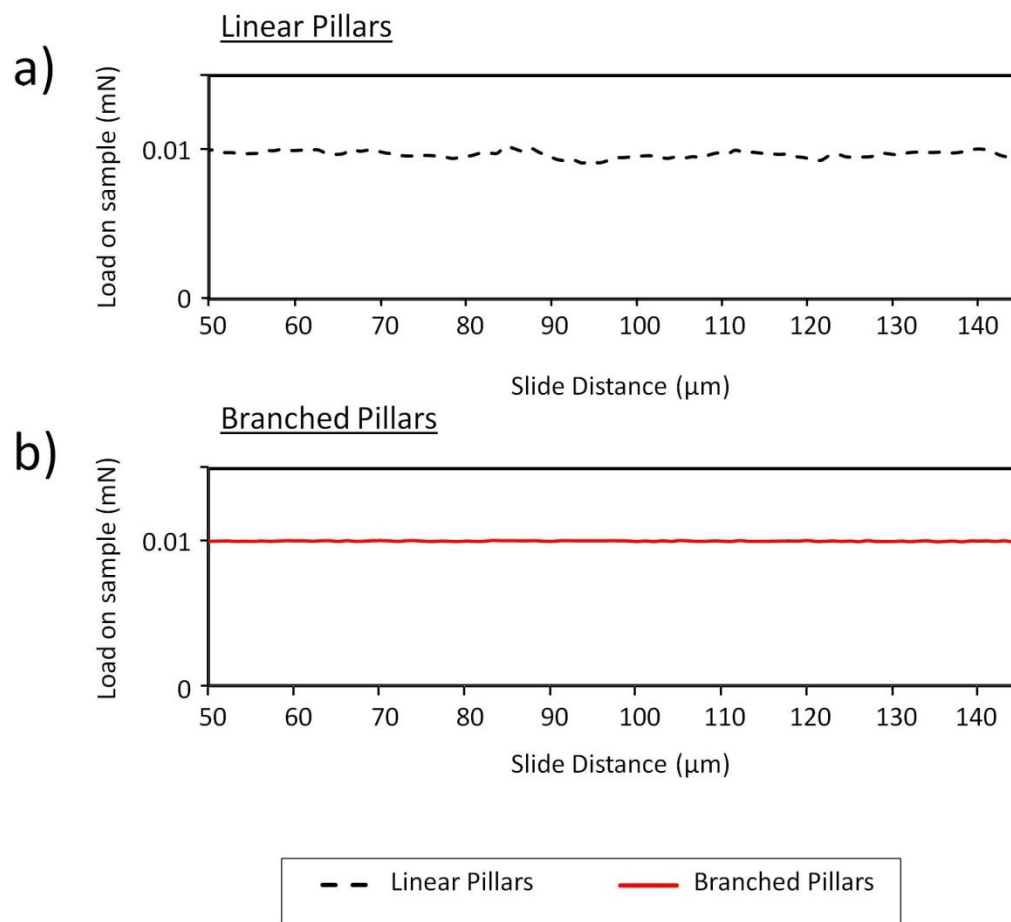


**Figure 8.4.** 10  $\mu\text{N}$  load on a) linear pillars and b) hierarchical pillars against representative slide distance

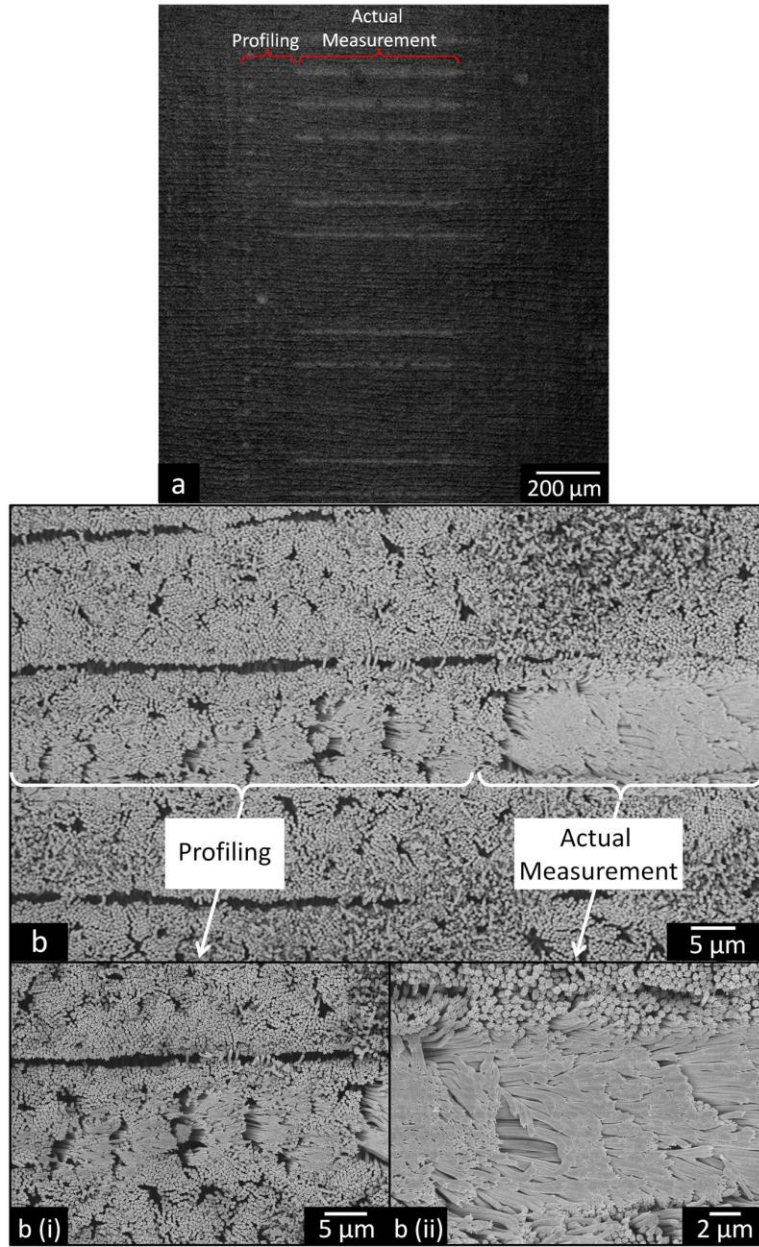


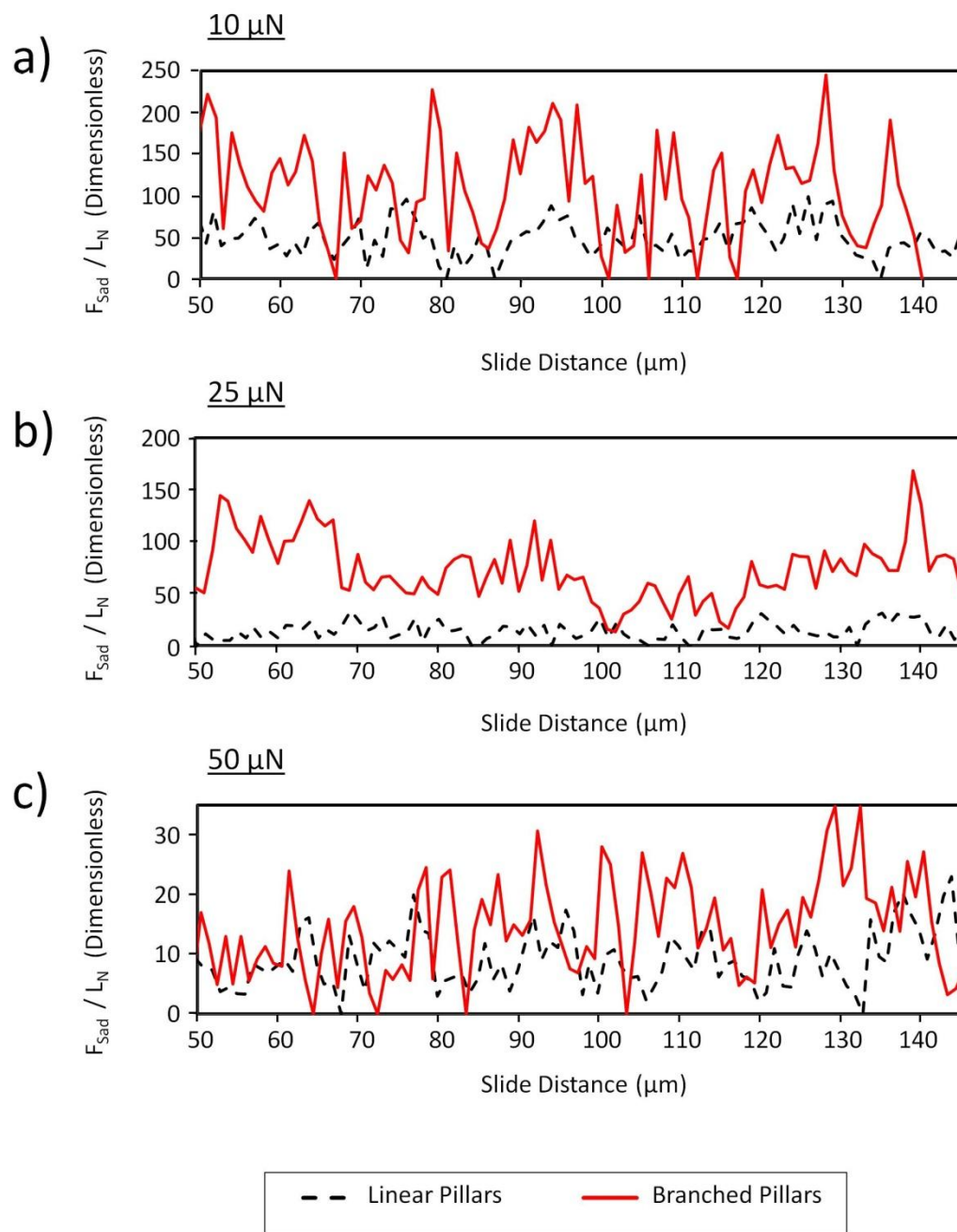
**Figure 8.5.** a) SEM images of a series of slides made by varying the applied loads, b) trail made by 2 mN normal load during sliding depicting the profiling and actual measurement section, bi) close-up of the profiling section, bii) close-up of the actual measurement section depicting the plastically deformed pillars.

Information such as normal and lateral displacements of the indenter as well as normal load on the indenter were recorded simultaneously. This information was only available during the actual slide measurement. Tangential force sensor was mounted on

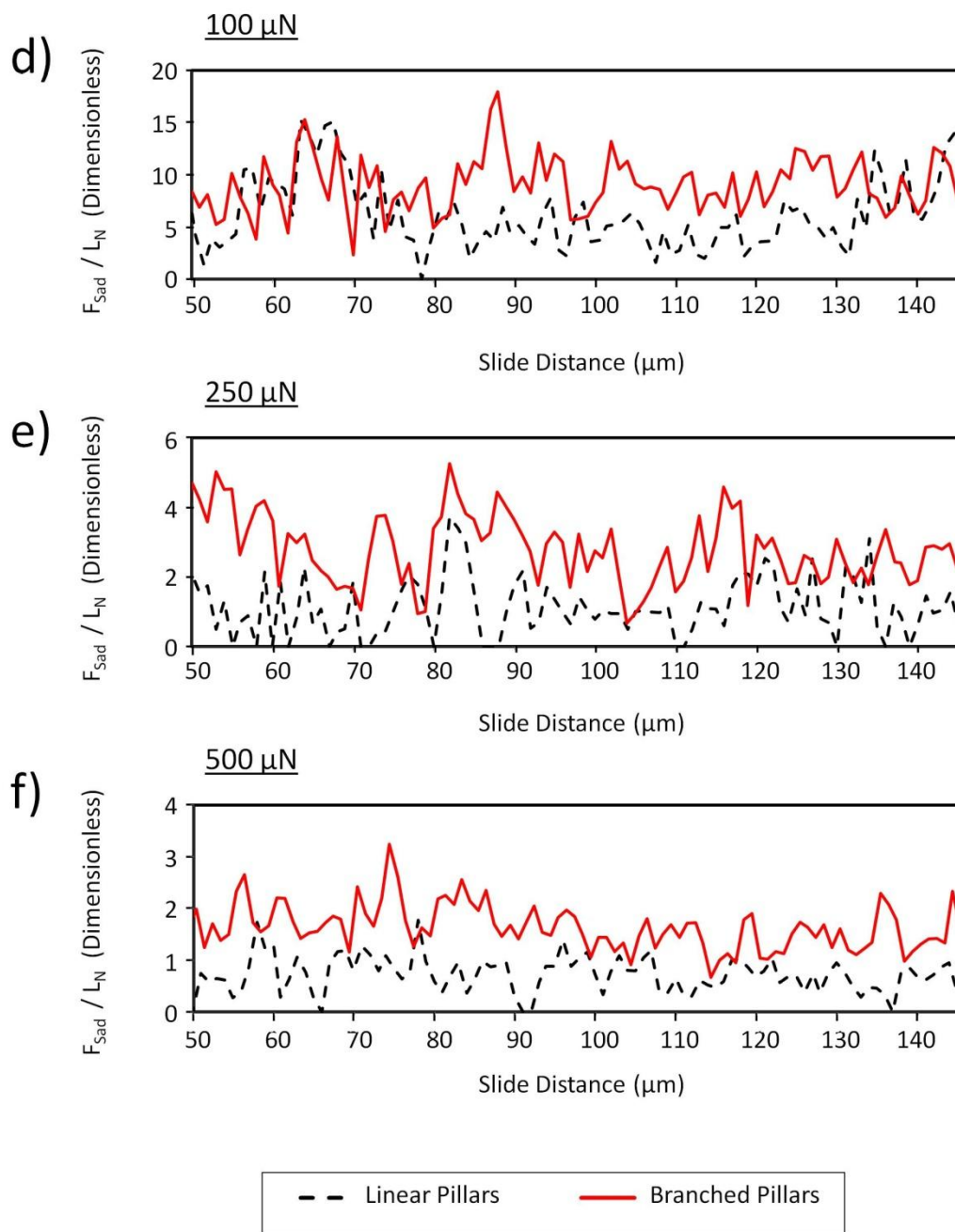
the slide collar to measure the tangential force and it was accorded as the friction force [219]. As the main objective of the measurements performed were to compare the shear adhesion forces between linear-pillars and branched-pillars samples, the input parameters were kept constant. Details of other variable input parameters are shown in Table E3 (in Appendix E).

### 8.2.3 Results

The ratio  $\frac{F_{Sad}}{L_N}$  was automatically computed by the software. This is graphically represented in Figure 8.6 against the slide distance. The friction forces that were measured were in the range of hundreds of micro Newtons. As such, it is well above the minimal measurable load of 10  $\mu\text{N}$  (refer to Table E2 in Appendix E) and is well within the capability of the equipment. Since it was a constant-force slide, the ratio  $\frac{F_{Sad}}{L_N}$  should be independent of the slide distance. Hence, only a representative 100  $\mu\text{m}$  distance of the 500  $\mu\text{m}$  slide distance (second slide) is shown. Figure 8.6a – h depict the ratio of  $\frac{F_{Sad}}{L_N}$  for linear pillars and hierarchical pillars for normal loads of 10  $\mu\text{N}$ , 25  $\mu\text{N}$ , 50  $\mu\text{N}$ , 100  $\mu\text{N}$ , 250  $\mu\text{N}$ , 500  $\mu\text{N}$ , 1 mN and 2 mN respectively.







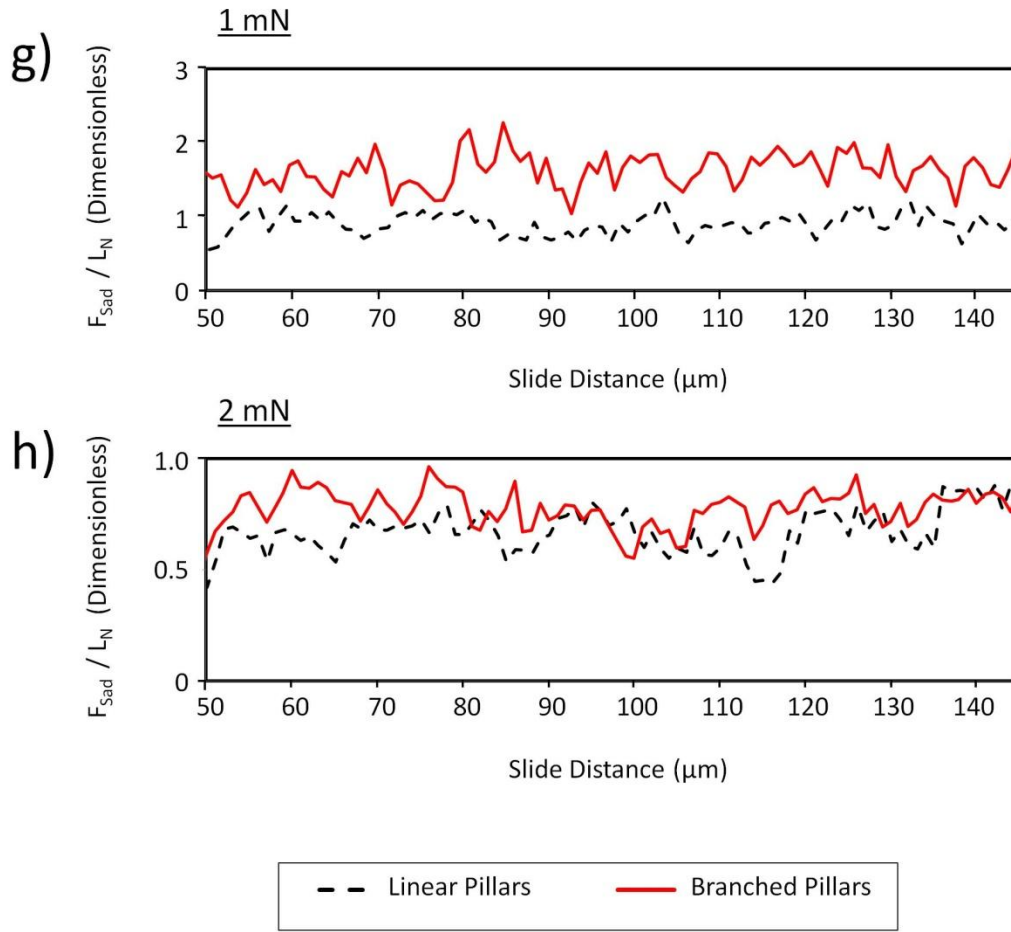


**Figure 8.6.** Ratio of shear adhesion force to applied normal load ( $\frac{F_{Sad}}{L_N}$ ) of linear pillars and hierarchical pillars as a function of representative slide distance with respect to its applied normal loads a) 10  $\mu N$ , b) 25  $\mu N$ , c) 50  $\mu N$ , d) 100  $\mu N$ , e) 250  $\mu N$ , f) 500  $\mu N$ , g) 1 mN and h) 2 mN. Each set of data represents average value of three measurements.

The variations in the ratio  $\frac{F_{Sad}}{L_N}$  are commonly known as stick-slip tribological phenomenon [202]. Stick-slip phenomenon is usually observed in the atomic – micro-scale frictional measurements. It was reported to be a result of overcoming certain critical friction force values when moving across apexes of asperities [202, 203]. This is

observed in both types of samples. The variations are more prominent in the hierarchical pillars and this is probably due to the topographical differences of the samples. Figure 7.1 shows that there are more topographical differences or asperities (the maximum versus the minimum of a peak) in hierarchical pillars as compared to linear pillars. However, the topographical differences appeared to be on a decreasing trend to match that of the linear pillars as the loads increase. This may be due to the plastic deformations of the asperities [194]. Yet, the average ratio  $\frac{F_{Sad}}{L_N}$  remains stable throughout the slide for all the applied loads indicating that there is no plowing (pile-ups) of material along the slide front.

The amplitudes (of variation) of the hierarchical pillars' plot are distinctively higher than the other two plots especially in the low load range as shown in Figure 8.6. This may be due to the greater variations in the topography of hierarchical pillars when engaging and disengaging from the indenter tip. It could be deduced that the ratio  $\frac{F_{Sad}}{L_N}$  for hierarchical pillars are higher than linear pillars.

Figure 8.7 shows the averaged ratio  $\frac{F_{Sad}}{L_N}$  for the two types of samples against its respective applied loads. It shows that the hierarchical pillars exhibit higher values of  $\frac{F_{Sad}}{L_N}$  in all the load conditions. Note that the ratio  $\frac{F_{Sad}}{L_N}$  reduced in an exponential decay function as the applied load increased. The change in the ratio  $\frac{F_{Sad}}{L_N}$  suggests that there was a change in the friction mechanism [210]. The exponential decay function indicates

that the change was gradual. Indeed, this decrease of ratio  $\frac{F_{Sad}}{L_N}$  is also exhibited in the preliminary tests described in Section 7.5.1 where Table 7.1 showed the ratio  $\frac{F_{Sad}}{L_N}$  reduced as the preload increased.

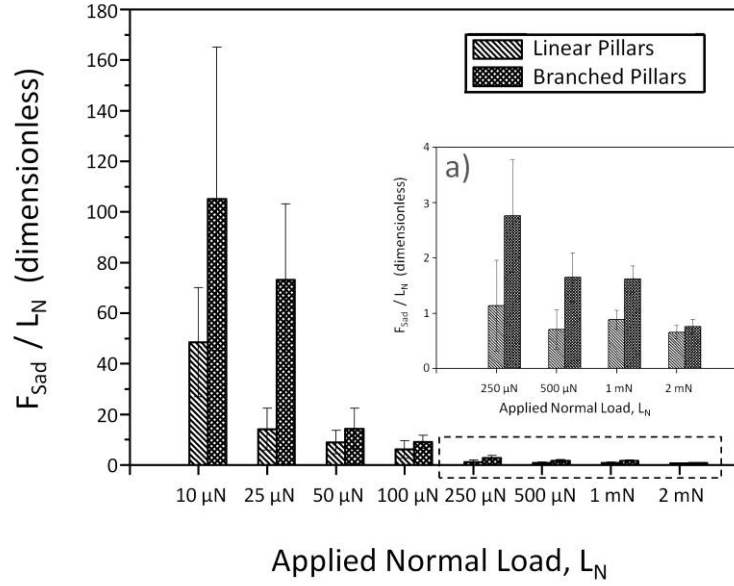


**Figure 8.7.** Averaged ratio  $\frac{F_{Sad}}{L_N}$  for linear pillars and hierarchical pillars with its respective applied normal loads during sliding. Each set of data is an average value of three measurements. Inset a) shows the close-up values of friction coefficients for 250  $\mu$ N, 500  $\mu$ N, 1 mN and 2 mN. Error bars indicate one standard deviation.

This observation is in agreement with those reported by Shooter and Tabor [220] and Gralen [221]. One possible explanation given is due to the nature of the deformation process. When a heavier normal load is applied, more plastic deformation is resulted. As discussed by Bowden and Tabor [213], surfaces undergoing plastic

deformation during sliding would yield area of contact,  $A$ , which is proportional to the normal load,  $L_N$  ( $A \propto L_N$ ). This indicates that the load-controlled term,  $\mu L_N$  of Eq. 7.3 is the dominating mechanism.

In contrast, at very light loads, where elastic deformation is dominant, the Hertzian theory where  $A \propto L_N^{2/3}$  is more applicable. This means that the area of contact is reduced with a reduction of an applied load. Thus, according to Eq. 7.3

( $F_{Sad} = \mu L + S_c A$ ),  $F_{Sad}$  would also decrease and result in a reduction of the ratio  $\frac{F_{Sad}}{L_N}$ .

However, Müser et al. [222] in his analytical solution and Sørensen et al. [203] in his molecular dynamics simulation showed that this only holds true for ideal cases. They noted that even a sub-monolayer of mobile atoms i.e. hydrocarbon, water and other small airborne molecules (as shown in Figure 8.8) [222] would lead to a finite ratio  $\frac{F_{Sad}}{L_N}$ . At

very low normal load  $L_N$ , even with a small friction force  $F_{Sad}$ , the resultant ratio  $\frac{F_{Sad}}{L_N}$

can be rather high (as seen in the low loads of Figure 8.7).

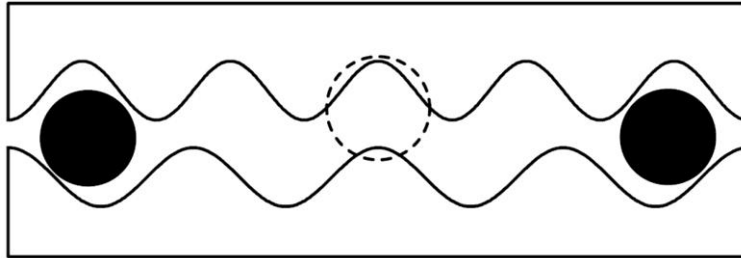


**Figure 8.8.** Sketch of two contacting surfaces separated by a sub-monolayer of mobile atoms [222].

The higher value of the ratio  $\frac{F_{Sad}}{L_N}$  observed in the hierarchical pillars than the linear pillars regardless of the normal loads can be inferred from Figure 8.9. Figure 8.9 illustrates the displacement of the indenter into the surface during sliding. The displacements were higher in hierarchical pillars for all the loads.

One possible reason for this observation is that the hierarchical pillars had a lower effective stiffness, which are validated by nano-indentation tests in Section 8.3. Figure 8.10 shows a deeper displacement of the indenter into the hierarchical pillars and causatively, higher contact area between the indenter and the pillars. A larger area of contact as originally proposed by Bowden and Tabor [195] would result in a higher  $F_{Sad}$  as shown in Eq. 7.3. This explains the higher ratio  $\frac{F_{Sad}}{L_N}$  registered by the hierarchical pillars for the same applied load on the same polymeric material.

As for the higher ratio  $\frac{F_{Sad}}{L_N}$  of the hierarchical pillars at the lower loads, it could be due to the topography resulting in more adhesion forces through van der Waals attractions or that the topography trapping more mobile atoms between the contacting surfaces as shown in Figure 8.8. This was evidenced by not observing any deformations of the pillars at the low loads of 10  $\mu\text{N}$  and 25  $\mu\text{N}$  during imaging with SEM. This also implies that the elastic limit of the fibers had not been exceeded.

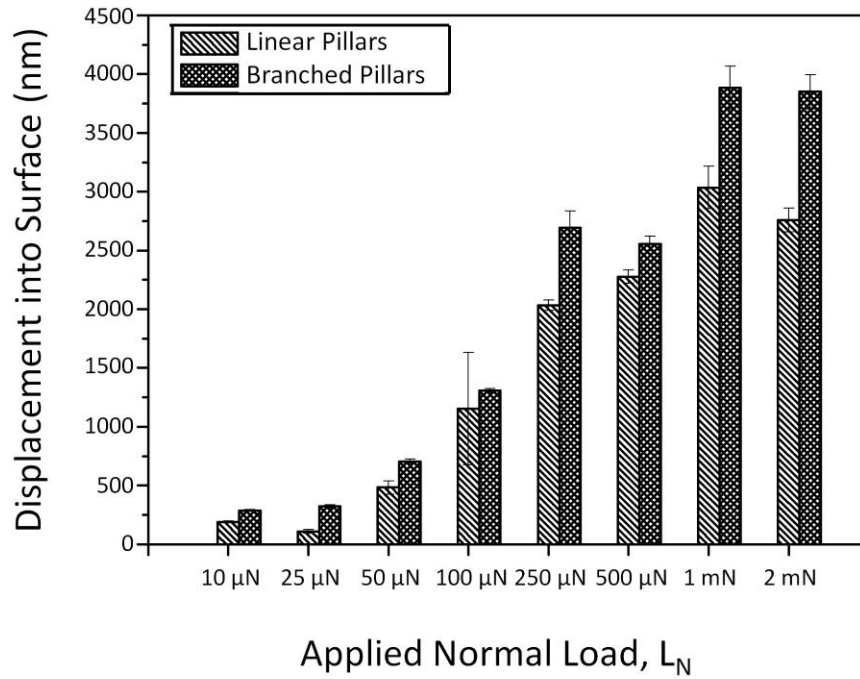


**Figure 8.9.** Displacement into surface for linear pillars and hierarchical pillars with its respective applied normal loads during sliding. Each set of data is an average value of three measurements. Error bars indicate one standard deviation.

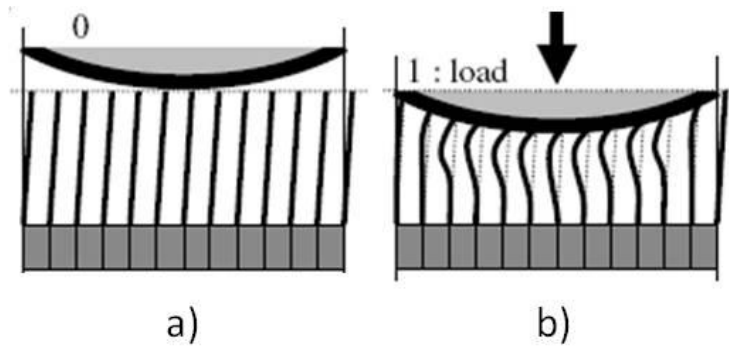


**Figure 8.10.** Area of contact between indenter and pillars a) prior to loading b) upon loading [223].

### 8.3 Nano-indentation

With the advent of simultaneous load-depth sensing instrument, hardness and elastic modulus ( $E$ ) of a sample can be determined [224]. Hardness of a sample is determined from the penetration depth which directly corresponds to the contact area of the indenter and the sample. Elastic modulus can be derived from the slope of the unloading curve (contact stiffness) and penetration depth. A fully defined pyramidal indenter (Berkovich) which is a three sided, self similar pyramid is used as shown in Figure 8.11. It has the same projected area to depth ratio as a Vickers indenter and is typically used for nano-indentation measurements [224].

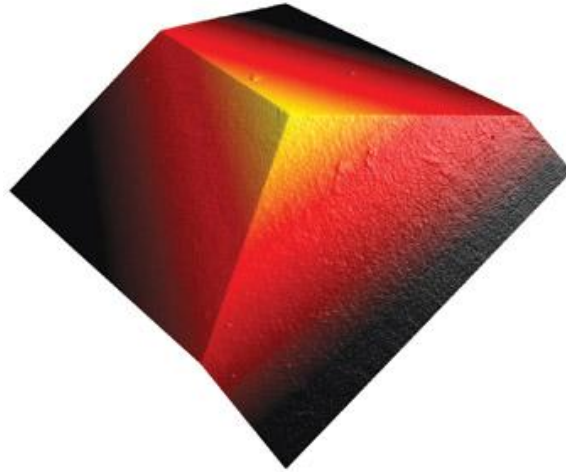


**Figure 8.11.** Image of a typical Berkovich tip used for nano-indentation tests [225].

Hardness ( $H$ ) is defined by the maximum indentation load ( $L_{\max}$ ) divided by the projected area ( $A$ ) of the impression :

$$H = \frac{L_{\max}}{A} \quad (\text{Eq. 8.1})$$



where

$$A = 24.5h_p^2 \quad (\text{Eq. 8.2})$$

and  $h_p$  is the sensed penetration depth as shown in Figure 8.12.

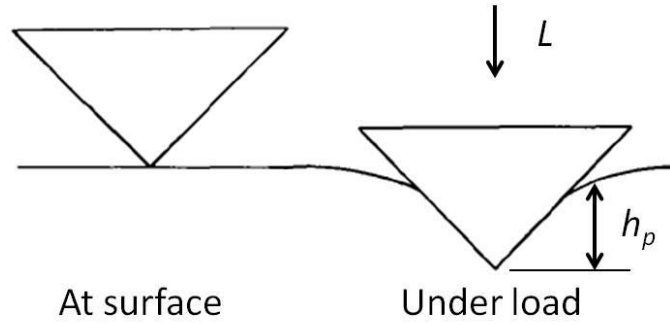


**Figure 8.12.** Schematic of indentation process illustrating penetration depth  $h_p$  [226].

To calculate the elastic modulus of a sample, the reduced modulus,  $E_r$  of the system must first be obtained from the following relationship [226]:

$$\frac{dh}{dL} = \frac{1}{2h_p} \left( \frac{\pi}{24.5} \right)^{1/2} \frac{1}{E_r} \quad (\text{Eq. 8.3})$$

where  $dh/dL$  is the reciprocal of the initial unloading slope as defined in Figure 8.13 (in general, the initial  $\frac{1}{3}$  of the unloading curve is employed). Subsequently, the elastic modulus of the sample can be calculated from the following relationship [226] :

$$\frac{1}{E_r} = \frac{1-\nu^2}{E} + \frac{1-\nu_0^2}{E_0} \quad (\text{Eq. 8.4})$$

where  $E$  and  $\nu$  are the elastic modulus and Poisson's ratio of the sample, and  $E_0$  and  $\nu_0$  are the elastic modulus and Poisson's ratio of the indenter.

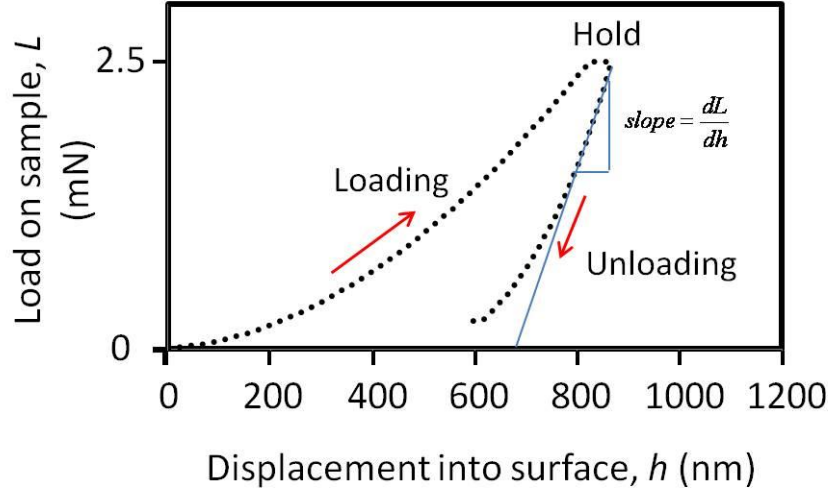


**Figure 8.13.** Load-displacement curve of pristine PC obtained with MTS Nano-indenter.

The same test setup could be used to perform nano-indentations to the sample. In this case, the penetration depth corresponding to the applied normal load was obtained. For the calculation of the hardness of the sample, one major assumption is that the contact area of the sample with the tip is assumed to be continuous. As for the calculation of the elastic modulus, the indentations were made such that they did not exceed the height of the pillars (6.5  $\mu\text{m}$ ). As such, elastic modulus of the surface of the sample could be obtained instead of the elastic modulus of the bulk [227].

The measurement protocol was to bring the indenter in contact with the surface of the sample, to load the surface of the sample in 30 s, and to hold the load for 20 s. Subsequently the indenter is to unload 90 % from the surface of the sample. The reason

for partial unloading to 10% of maximum load and then hold is for thermal drift correction [228]. Table E4 (in Appendix E) shows the input parameters for the nano-indentation tests.

Indentations using 100  $\mu\text{N}$ , 250  $\mu\text{N}$ , 1 mN and 2.5 mN were performed on each of the three types of samples. Five indentations were made for each load. Figure 8.14 depicts the SEM images of some of the indentations performed on linear pillars. It can be observed that the triangular projected areas are different for the two sets of indentations with different applied loads. A heavier load would incur more penetration depth thus larger projected area.

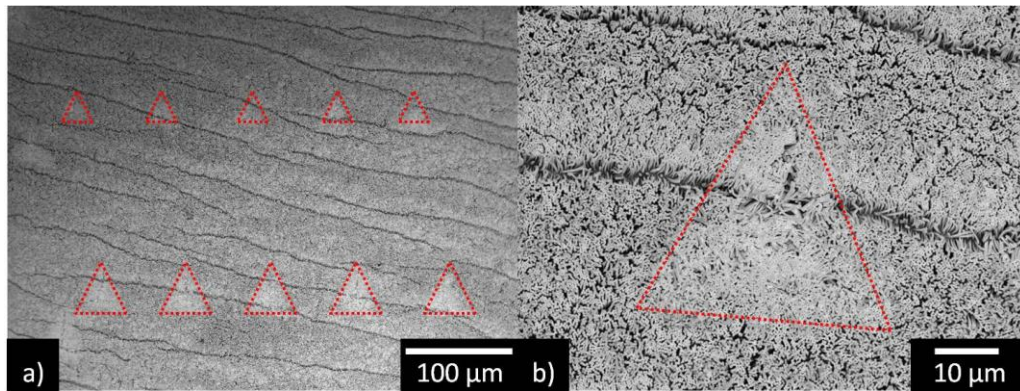


**Figure 8.14.** a) SEM image of some indentations performed on linear pillars. Five indentations were performed on each load. B) Close-up image of one of the indentations.

Figure 8.15 depicts the overall penetration depths of the respective applied loads for pristine PC, linear pillars and hierarchical pillars. Hierarchical pillars show the highest penetration depths for all the applied loads followed by linear pillars and pristine PC. The individual load-penetration depth for each type of the sample is illustrated in Figure 8.16.

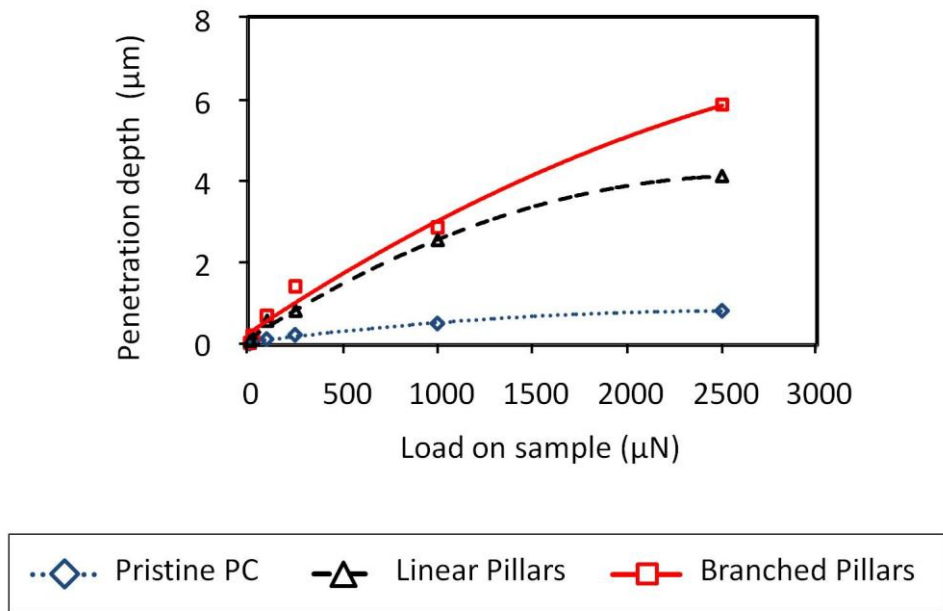


**Figure 8.15.** Overall penetration depths of the respective applied loads (100  $\mu\text{N}$ , 250  $\mu\text{N}$ , 1 mN and 2.5 mN) for pristine PC, linear pillars and hierarchical pillars.

In Figure 8.16, kinks (red circles) are observed on the loading curve of the linear and hierarchical pillars. This is probably due to buckling of the pillars of the respective samples [229]. Both the linear pillars' and branched pillars' loading curves had two kinks. However, the first kink of the linear pillars' loading curve is quite smooth and gradual. On the contrary, the second kink of the linear pillars' loading curve shows a more abrupt change than the branched pillars'. This might be attributed to the lower stiffness of the linear pillars due to its higher aspect ratio when compared to the shorter main pillars of the hierarchical pillars.

The first kink of the hierarchical pillars is likely due to the buckling of the branches and the second may be due to the buckling of the main pillars. The initial slope

of the loading curve (before the first kink) of the hierarchical pillars is small, showing that the penetration rate was high. This is likely due to the lower stiffness of the branches than the main pillar.

At peak load, the pristine PC had the least penetration depth of approximately 520 nm, this was followed by the linear pillars (approximately 2,400 nm), while the hierarchical pillars had the deepest penetration depth (approximately 3,800 nm). Note that these had not exceeded the height of the overall pillars of approximately 6.5  $\mu\text{m}$ . As a shallower displacement indicates smaller contact area between the indenter and the sample, this means that the pristine PC is harder than the linear and hierarchical pillars. The hardness of pristine PC, linear and hierarchical pillars measured by the indenter are  $173 \pm 2$  MPa,  $6.4 \pm 1.0$  MPa and  $4.4 \pm 1.3$  MPa respectively. However, it must be highlighted here that the hardness referred here is the “effective hardness” of the surface, and not the hardness of the PC material itself (especially for the linear and the hierarchical pillars).

During the holding period of 20 s, there was no further penetration for pristine PC. In contrast, approximately 100 nm and 300 nm were further displaced into the surface of the linear pillars and hierarchical pillars respectively during the holding period. These additional displacements can be attributed to the creep deformation [230] which is closely connected to plastic deformation. It is noted that there was a slight reduction of the applied load during the holding period. During holding at the peak load, if the creep was very large, the load on the sample was not compensated with further displacement

into the surface. Therefore, the load on the sample would be reduced. However, this would not affect the calculation of the hardness and modulus [228].

At close examination, there was a small difference in the slope of each of the unloading curve. The differences in penetration depth between the onset of unloading and the final depth of the indent were 158 nm, 135 nm and 102 nm for pristine PC, linear pillars and hierarchical pillars respectively. This implies that there was more plastic deformation experienced by the hierarchical pillars.

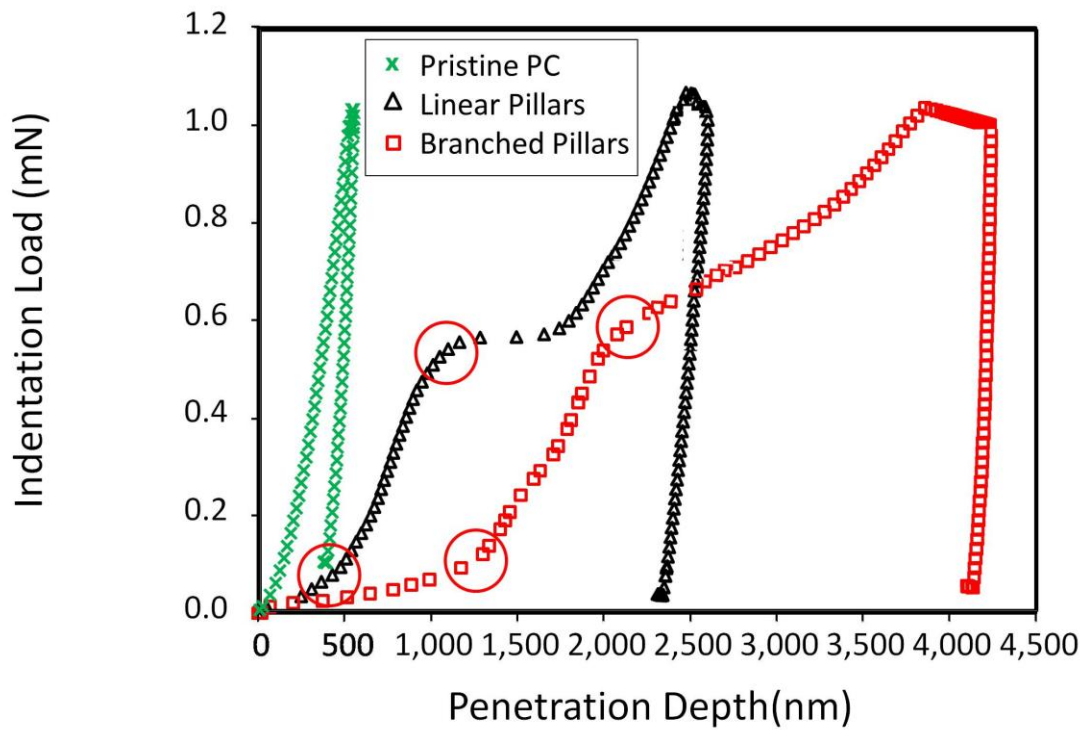


**Figure 8.16.** Penetration depth for pristine PC, linear pillars and hierarchical pillars with applied normal load of 1 mN during indentation. Each set of data is an average value of five measurements.

Since the indentation depths were still within the height of the pillars and had not extended into the bulk material, it is reasonable to assume that the elastic modulus measured is the elastic modulus of the surface topography. (Note: the elastic modulus here referred to the “effective elastic modulus” of the surface with the particular topography, and it is not the modulus of the PC material.)

Table 8.1 lists the elastic modulus computed by the equipment’s software from the initial  $\frac{1}{3}$  of the unloading curve. of the respective surface topography of the samples [227] for loads of 100  $\mu\text{N}$ , 250  $\mu\text{N}$ , 1 mN and 2.5 mN based on Eq. 8.3 and 8.4. Note that the modulus calculated should be the same regardless of the applied load. The high standard deviations for hierarchical pillars at 250  $\mu\text{N}$  and linear pillars at 1 mN may be due to the non-uniformity of some of the sample area. Pristine PC records the highest elastic modulus which is  $3.31 \pm 0.123$  GPa, followed by the linear pillars with  $1.34 \pm 0.098$  GPa. The hierarchical pillars has the lowest elastic modulus of  $0.67 \pm 0.028$  GPa

**Table 8.1.** Elastic modulus of pristine PC, linear pillars and hierarchical pillars at various applied loads.

	100 $\mu\text{N}$		250 $\mu\text{N}$		1 mN		2.5 mN		$E$ (GPa)	StdDev
	$E$ (GPa)	StdDev	$E$ (GPa)	StdDev	$E$ (GPa)	StdDev	$E$ (GPa)	StdDev		
Pristine PC	3.49	0.097	3.30	0.097	3.23	0.038	3.24	0.031	<b>3.31</b>	<b>0.123</b>
Linear Pillars	1.43	0.221	1.40	0.263	1.21	0.400	1.32	0.159	<b>1.34</b>	<b>0.098</b>
Hierarchical Pillars	0.67	0.18	0.68	0.331	0.63	0.140	0.69	0.090	<b>0.67</b>	<b>0.028</b>

## 8.4 Summary

This chapter has described, from Amonton's equation (Eq. 7.5), the experimental observation that in the micro-scale regime, the ratio  $\frac{F_{Sad}}{L_N}$  decreased exponentially with an increase of the normal load. This provides insights of the competition between adhesion-controlled (van der Waals forces) and load-controlled friction. At low loads,  $\frac{F_{Sad}}{L_N}$  shows a high value. This is possible due to large van der Waals component. This also correlated to the experimental results from Table 7.1.

Vice versa, when at high loads,  $\frac{F_{Sad}}{L_N}$  is generally low since VDW component decreases and only the frictional component is present. This can be observed from Figure 8.7 whereby at loads above 250  $\mu\text{N}$  for branched samples, there is little variation in  $\frac{F_{Sad}}{L_N}$ .

This observation is highly beneficial as, at low loads, it allows repeated usage of the sample without much wear as well as the adhesive being residue free on the contact surface. In-depth investigation found that this phenomenon could be explained by the different friction mechanisms as loads were increased indicated by the gradual change of the ratio  $\frac{F_{Sad}}{L_N}$ .



The high values of the ratio  $\frac{F_{Sad}}{L_N}$  at low loads were attributed to the adhesion forces due to van der Waals attractions or trapped mobile atoms (i.e. hydrocarbon, water and other small airborne molecules) between the contacting surfaces. This happens within the elastic limits of the pillars as evidenced by the lack of residual deformations observed by SEM imaging.

As the loads were increased, the ratio  $\frac{F_{Sad}}{L_N}$  reduced due to plastic deformation of asperities. This reduction also indicating the increased dominance of the load-controlled term,  $\mu L_N$  in Eq. 7.3 [194].

In addition, the inherent characteristics of the hierarchical and linear pillars were deduced from a different perspective. Nano-indentation measurements used to characterize the mechanical properties (i.e. hardness and elastic modulus) of pristine PC, linear pillars and hierarchical pillars. This further substantiated the enhanced shear adhesion by hierarchical pillars. This was made possible by determining the hardness and elastic moduli of the surfaces of the respective samples using load-penetration depth experiments. The elastic modulus of the hierarchical pillars was found to be the lowest in comparison to linear pillars and pristine PC. This explains the higher contact area with the indenter and thus higher friction forces as originally proposed by Bowden and Tabor [195].

The load-penetration depth curves from the nano-indentation tests could also be used to observe the various deformation phenomena such as creep observed in linear

and hierarchical pillars during the holding period. This observation as well as the penetration depth recovery during unloading explicates plastic deformation of the pillars. Buckling of the pillars could be implied by the kinks in the loading curve.



# Chapter 9 Conclusions and Future Work

## 9.1 Conclusions

In this thesis, a novel methodology has been developed to fabricate gecko-inspired dry adhesives. This mimetic dry adhesives consisted of high density, high aspect ratio, hierarchical nano-pillars made on a stiff polymeric material. This is far superior than most of the produced hierarchical structures that are either in the micrometer range [1, 2], a combination of micro- and nano-scales [3-5], low aspect ratio [3] or with sparse packing structure density [1, 2].

In addition, the proposed methodology employs an inexpensive and direct approach for mold fabrication. Hitherto, this process is the only known methodology that allows the fabrication of the features closely resemble the topographical gecko toe pads in a practical and low cost manner. This is an improvement against current technique where molds are fabricated with sophisticated and expensive lithography and alignment tools as well as the requirement of highly skilled personnel.

Through statistical and systematically designed experiments, the most significant parameter, which is the thickness of the barrier layer, was identified as the main experimental factor for controlling the creation of branching sub-pores. The study

also revealed that the number of sub-pores and interpore distance of the sub-pores varies in accordance with the 2<sup>nd</sup> – tier anodizing voltage. Such relationship is important for executing controlled fabrication of multi-tiered PAA according to application. In addition, with the increase in the tiers of a PAA substrate, an increase in surface wettability is achieved and this improved the filling of PAA when it is used as an embossing template.

Experimentally, hitherto, there is yet any conclusive evidence either on the advantages of hierarchical structure in aiding adhesion or in-depth shear adhesion force characterizations. Hence, with rigorous and systematic analyses, the shear adhesion properties of the adhesive films prepared were characterized. From these analyses, possible explanations was put forth to the two distinct phenomena observed. They are, 1) the shear adhesion force of the polymeric structured films increased progressively as the films were repeatedly tested, 2) the hierarchically-structured films of branched pillars indeed outperformed the linear pillars in experimental shear adhesion tests. These provided a basis for a better understanding of the underlying shear adhesion mechanisms.

Numerically, this thesis has performed analytical and numerical analyses of the polymer flow in nano-imprinting taking into consideration surface tension effects. The model developed highlighted the important contribution of the surface tension effect in the filling process exacerbated by capillary flow in nano-scale, which hitherto, has not been taken into account. This model allows an accurate prediction of flow behavior in high aspect ratio nano-pores, and thus the accurate prediction of the height of polymer filling in various operating parameters.

The models provided essential information for the choice of nano-imprinting process parameters to completely fill the high-density, high aspect ratio nano-pores of the PAA templates. The results obtained experimentally and by simulation were comparable (~8.4 % difference), indicating that the model can be used to predict imprinted pillar heights. The model also serves to provide evidence of the contribution of surface tension effecting the filling process, as ignoring it would result disagreement between predicted and experimental results in pillar heights.

From the numerical analysis, it was found that, for a given imprint material (PC), the imprint temperature is the most significant parameter in controlling the pillar height for optimization of a cycle time. As such, for the fabrication of gecko-inspired dry adhesives, the imprinting temperature of approximately 200 °C was used to imprint nano-pores of approximately 6.5  $\mu\text{m}$  depth with an imprint pressure of 1 MPa for 300 s.

In producing positive replicates of the multi-tiered nano-pores during experimentation, this work has successfully resolved numerous challenges faced such as the demolding of the sample and polymer recovery after demolding. It was found that, demolding by peel-off would avoid the polymer bunching issue when demolding is performed by wet etching in solvents. A specific process optimization performed to avoid pillar breakage during peel-off was to enlarge the base diameters of the pillars. This was achieved by pore widening of the templates which corresponds to the base region of the pillar. In addition, applying holding pressure during the cooling cycle was found to be effective in minimizing polymer recovery in the lateral dimensions.

Through macro-scale shear adhesion force measurements it was found that hierarchical structure experiments a reduction in effective stiffness of a result in ease of bending as compared to a linear structure. This renders a better compliance to a test surface, hence resulting in a higher effective contact area. As the effective contact area increased, the shear adhesion force emulated. It was determined that a hierarchical structure improves the shear adhesion force over the corresponding linear structure by approximately 150 %.

In the micro-scale regime, the ratio  $\frac{F_{Sad}}{L_N}$  increased with a decrease of the applied normal loads. This is due to the different friction mechanisms acting on the sliding surfaces. The high value of the ratio  $\frac{F_{Sad}}{L_N}$  at low loads (less than 50  $\mu\text{N}$ ) were attributed mainly to the contribution of van der Waals attractions or trapped mobile atoms between the contacting surfaces. This is typical when the deformation is within the elastic limits of the pillars as evidenced by no visible plastic deformations observed during SEM imaging. When a heavier normal load (more than 50  $\mu\text{N}$ ) was applied, more plastic deformation was observed from SEM imaging, indicating the dominance of the Amontons' load-controlled friction mechanism,  $\mu L_N$ .

In addition, nano-indentation measurements were used to characterize the hardness and elastic moduli of the surfaces of the respective samples (pristine, linear and hierarchical structure). The elastic modulus of the branched pillars was found to be the lowest ( $0.67 \pm 0.028$  GPa) in comparison to the linear pillars ( $1.34 \pm 0.098$  GPa) and pristine PC ( $3.31 \pm 0.123$  GPa).

The load-penetration depth curves from the nano-indentation tests could also be used to observe deformation phenomena, such as creep, in linear and branched pillars during the load holding period. The observation of creep as well as the penetration depth recovery during unloading explicates plastic deformation of the pillars. Buckling of the pillars could be implied by the kinks in the loading curve.

Last but not least, the branched pillar structures also showed a distinct increased in hydrophobicity, an important characteristic for reusable dry adhesives.

## **9.2 Future Work**

Further investigations are required, both experimental and numerical, for more rigorous analyses. Figure 9.1 shows a summary of the possible research areas.

For experimental work, new geometrical parameters could be studied for their effects on shear adhesion, which include the changes in pillar geometries such as base and branch diameters, aspect ratios, number of sub-tiers, number of branches and a combination of micro- and nano- structures. Such studies would yield optimized configurations for maximum shear adhesion strength.

Also, pore-widening duration should be lessened to reduce the pillars' diameter but yet retain the pillar density. This is to avoid the effect that, in close-packed pillars, the bending taller pillars (above the average height) would push away the shorter pillars (below the average height) during the contact motion against the counterpart surface, thus reducing the efficiency of contact.



For numerical simulation, a numerical model could be developed to determine the polymer recovery in 2D or 3D. This should be taken into account during the mold design stage especially when the critical dimensions (CD) of the feature affect its functionality.

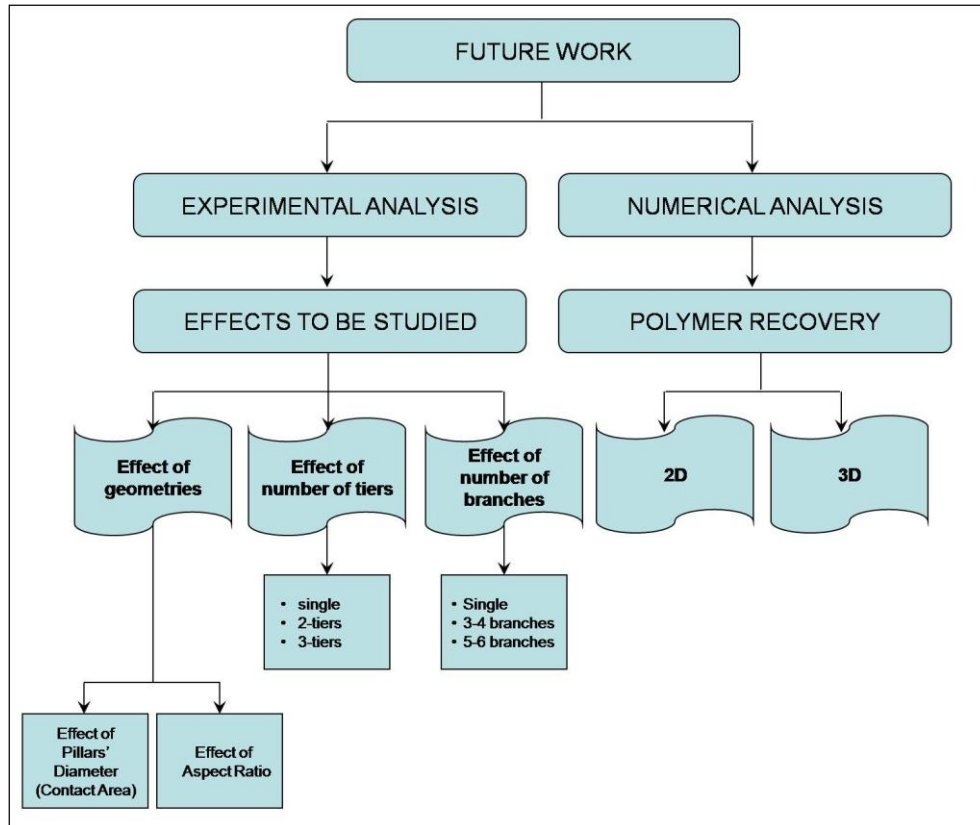


**Figure 9.1.** Variations of samples according to the types of effects to be studied.

In addition, systematic robust testing of the dry adhesives produced should be conducted. The limitations of the structures could be determined upon testing on different surface conditions (i.e. roughness) as well as under different environmental conditions (i.e. humidity and vacuum conditions). Durability of the dry adhesives could also be investigated.

# Appendix A

Figure A1 illustrates the GPC flow path for PC solution. Table A1 summarizes the specifications of the equipment as well as the testing conditions.

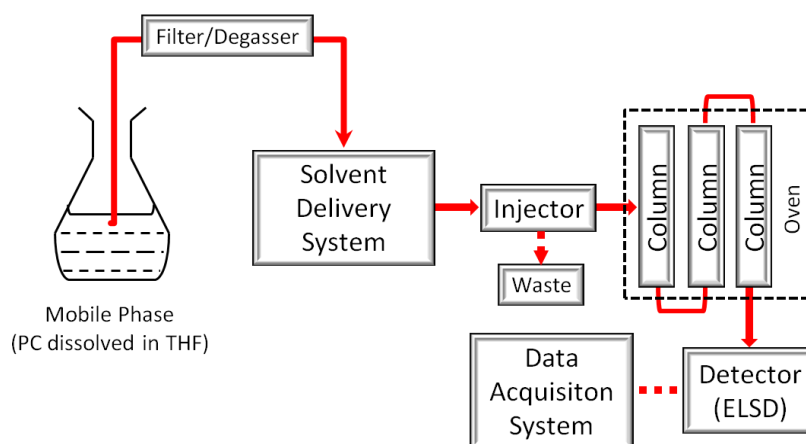


**Figure A1.** Process flow of gel permeation chromatography for PC [231].

**Table A1.** Specifications of the GPC equipment and testing conditions

<b>Brand</b>	Waters
<b>Model</b>	2690 Separation module; 2420 ELS detector
<b>Column</b>	Phenomenex (brand) columns; 300 x 7.8mm; 5 $\mu$ m; $10^6$ , $10^4$ , 500 Å
<b>Detector</b>	Evaporative Light Scattering Detector (ELSD)
<b>Mobile Phase</b>	Tetrahydrofuran (THF)
<b>Flow Rate</b>	0.8 mL/min
<b>Oven Temperature</b>	30 °C
<b>Injection Volume</b>	50 $\mu$ l
<b>Method Performance</b>	Precision of weight: average molecular weight (rsd of $M_w$ ) = < 1 % Precision of number weight: average molecular weight (rsd of $M_n$ ) = < 1 %

# Appendix B

## Modeling of air back pressure in nano-imprint

### Theoretical fundamentals

(1) ideal gas equation

$$PV = nRT \quad (1)$$

P-pressure, V- volume, n- gas mole number, R- gas constant, T-temperature

(2) gas evolution equation

$$\frac{\partial n}{\partial t} = -\rho_g Q_v \quad (2)$$

n- mass mole number, t- time,  $\rho_g$  - gas density,  $Q_v$  - flow rate of air through venting;

During a discrete time step  $\Delta t$ , the change in the number of gas moles becomes

$$\Delta n = -\Delta t \rho_g Q_v \quad (3)$$

Substitute (3) into the equation (1)

$$PV = \left( n^* - \Delta t \frac{n^*}{V} Q_v \right) RT \quad (4)$$

That (\*) is the value in last time step. P can be written as

$$P = \left( 1 - \Delta t \frac{Q_v}{V} \right) \frac{P^* V^* T}{V T^*} \quad (5)$$

For ideal sealed cap (closed, without venting) isothermal system,  $Q_v=0$  and  $T=T^*$  and then we have a simple relationship between old and new values of the pressure and volume of void cavity can be written as

$$P = \frac{P^* V^*}{V}$$

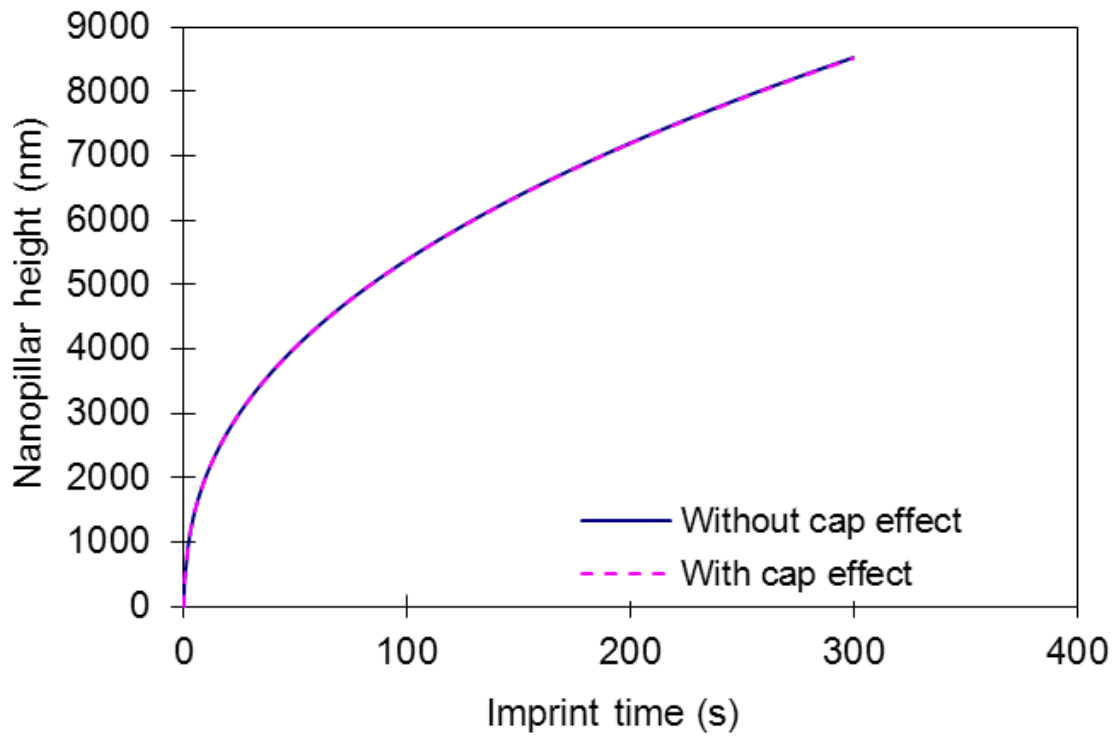


**Figure B1.** Comparison of nanopillar height with and without cap effect.

# Appendix C

## The Compression simulation for Nanoimprint

### C.1 Governing equations

At the stage of compression, the thickness of die cavity will change. The compressive velocity is given as

$$w = -\frac{d(2h)}{dt} = \dot{h} \text{ (constant)} \quad (\text{C.1})$$

Considering the assumptions and simplifications assumed as mentioned. The continuity equation can be simplified as:

$$\frac{\partial(h\bar{u})}{\partial x} + \frac{\partial(h\bar{v})}{\partial y} + \frac{\partial(h\bar{w})}{\partial z} = 0 \quad (\text{C.2})$$

$$\frac{\partial P}{\partial x} = \frac{\partial}{\partial z} \left( \eta \frac{\partial u}{\partial z} \right) \quad (\text{C.3})$$

$$\frac{\partial P}{\partial y} = \frac{\partial}{\partial z} \left( \eta \frac{\partial v}{\partial z} \right) \quad (\text{C.4})$$

$$\frac{\partial P}{\partial z} = \frac{\partial}{\partial z} \left( \eta \frac{\partial w}{\partial z} \right) \quad (\text{C.5})$$

where  $\bar{u}$  ,  $\bar{v}$  are averaged velocity of u and v respectively.

$$\text{Let } \Lambda_x = -\frac{\partial P}{\partial x}, \Lambda_y = -\frac{\partial P}{\partial y}, \quad (\text{C.6})$$

The velocity boundary condition at the wall is  $u = 0$

Integrating (C.3) across the gap direction,

$$\frac{\partial u}{\partial z} = -\frac{\Lambda_x}{\eta} \int dz = -\Lambda_x \frac{z}{\eta} + C$$

When  $z=h$ ,  $\frac{\partial u}{\partial z} = 0$

$$\frac{\partial u}{\partial z} = -\frac{\Lambda_x}{\eta} (z-h), \quad \frac{\partial v}{\partial z} = -\frac{\Lambda_y}{\eta} (z-h) \quad (\text{C.7})$$

Integrating (C.6) across the gap direction with respect to  $z$  again,

$$u(z) = -\Lambda_x \int_0^z \frac{z-h}{\eta} dz, \quad v(z) = -\Lambda_y \int_0^z \frac{z-h}{\eta} dz \quad (\text{C.8})$$

Applying Leibniz integral rule

$$\bar{u} = \frac{\Lambda_x S}{h}, \quad \bar{v} = \frac{\Lambda_y S}{h} \quad (\text{C.9})$$

$$\text{where } S = \int_0^h \frac{(z-h)^2}{\eta} dz \quad (\text{C.10})$$

Also, we can obtain

$$\bar{v} = \frac{\Lambda_y S}{h} \quad (\text{C.11})$$

$$\therefore \frac{\partial P}{\partial z} = \frac{\partial}{\partial z} \left( \eta \frac{\partial w}{\partial z} \right) = 0$$

$$\therefore \frac{\partial(h\bar{w})}{\partial z} = \frac{w_0}{2} \quad (\text{C.12})$$

substitute equation (C.9) and (C.7) into equation (C.2)

$$\frac{\partial(h\bar{u})}{\partial x} + \frac{\partial(h\bar{v})}{\partial y} + \frac{w_0}{2} = 0 \quad (\text{C.13})$$

Thus,

$$\frac{\partial}{\partial x}(\Lambda_x S) + \frac{\partial}{\partial y}(\Lambda_y S) = -\frac{w_0}{2} \quad (\text{C.14})$$

the tensor form of equation (C.13) was given as

$$\nabla \cdot (S \nabla p) = -\frac{w_0}{2} \quad (\text{C.15})$$

## C.2 Numerical Solution of Pressure field

The linear interpolation function used to discrete the pressure equation (C.14) was given as

$$P^{(e)} = \sum_{i=1}^3 N_i p_i$$

where  $N_i$  is the shape function,  $p_i$  is a value of the nodal pressure. In term of properties of Kronecker delta[] of shape function:

$$N_i(x_j, y_j) = \delta_{ij} = \begin{cases} 1 & i = j \\ 0 & i \neq j \end{cases} \quad (\text{C.16})$$



In this investigation, area coordinates was employed for a triangular element to construct shape function  $N_i$ . Let  $N_i$  is equal to the ratio of area  $A_i$  to the total area of the triangle  $A$ , that is

$$N_1 = \frac{A_1}{A}; N_2 = \frac{A_2}{A}; N_3 = \frac{A_3}{A} \quad (C.17)$$

where  $N_1 + N_2 + N_3 = 1$

$$\begin{Bmatrix} N_1 \\ N_2 \\ N_3 \end{Bmatrix} = \frac{1}{2A} \begin{bmatrix} x_2 y_3 - x_3 y_2 & y_2 - y_3 & x_3 - x_2 \\ x_3 y_1 - x_1 y_3 & y_3 - y_1 & x_1 - x_3 \\ x_1 y_2 - x_2 y_1 & y_1 - y_2 & x_2 - x_1 \end{bmatrix} \begin{Bmatrix} 1 \\ x \\ y \end{Bmatrix} \quad (C.18)$$

The derivative of equation (C.15), we have

$$\nabla P^{(e)} = \sum_{i=1}^3 \nabla N_i p_i \quad (C.19)$$

Using Galerkin approach on equation (C.14), The residual

$$R(p) = (\nabla \cdot \nabla S p) - b \quad (C.20)$$

$$0 = \int_A N_i R(p) dA = \int_A N_i (\nabla \cdot \nabla S p) dA - \int_A N_i b dA \quad (C.21)$$

$$\begin{aligned} \therefore \int_A N_i (\nabla \cdot \nabla S p) dA &= \int_A \nabla \cdot (N_i S \nabla p) dA - \int_A S (\nabla p \cdot \nabla N_i) dA \\ &= \int_{\Sigma} N_i S \nabla p \cdot \bar{n} d\Sigma - \int_A S (\nabla p \cdot \nabla N_i) dA \end{aligned} \quad (C.22)$$

where  $\Sigma$  the boundary of the domain.

$$\int_{\Sigma} N_i S \nabla p \cdot \vec{n} d\Sigma = \{Q\} = \begin{Bmatrix} Q_1 \\ Q_2 \\ Q_3 \end{Bmatrix} \quad (C.23)$$

$$\int_A S (\nabla p \cdot \nabla N_i) dA = \{K\}^{(e)} \{P\} = \begin{Bmatrix} k_{11} & k_{12} & k_{13} \\ k_{21} & k_{22} & k_{23} \\ k_{31} & k_{32} & k_{33} \end{Bmatrix}^{(e)} \begin{Bmatrix} P_1 \\ P_2 \\ P_3 \end{Bmatrix} \quad (C.24)$$

$$\{B\} = \left\{ \int_A N_i b dA \right\}$$

$$\therefore \int_A N_i^l N_i^m N_i^n dA = 2A \frac{l!m!n!}{(2+l+m+n)!}$$

$$\{B\} = b \begin{Bmatrix} \int_A N_1 dA \\ \int_A N_2 dA \\ \int_A N_3 dA \end{Bmatrix} = \frac{Ab}{3} \begin{Bmatrix} 1 \\ 1 \\ 1 \end{Bmatrix} \quad (C.25)$$

Substitute equation (C.2.8), (C.2.9) and (C.2.10) into equation (C.2.13), we have

$$\{K\}^{(e)} \{P\} - \{Q\} + \{B\} = 0 \quad (C.26)$$

The element equations can be assembled to create a global stiffness matrix and force vector. After modifying the components to ensure that the boundary condition at the flow front is met, one has a set of equations to be solved for the nodal pressures.

## C.3 Mass Conservation

Due to that the mass flow rate at flow front is equal to the volume change caused by compressing the mold, the mass conservation can be written as:

$$Q_c = \int_L \vec{V} \cdot \vec{n} dl = - \sum_{k=1}^m \frac{\dot{h}}{3} \Delta_k \quad (\text{C.27})$$

where  $\Delta$  is the area of a triangular element,  $\dot{h}$  is the compression velocity and  $m$  is the total numbers of filled melt control volume. The variation of substrate thickness is given as

$$h^{i+1} = h^i - \frac{\dot{h}}{h^i} \Delta t_{i+1} \quad (\text{C.28})$$

where  $\Delta t$  is the time step and  $h$  is the residual compression height of substrate.

## C.4 Computational Procedure

The main numerical step employed for flow analysis of nano-imprinting can be summarized as:

- (a) The viscosity of amorphous polymer PC at specific temperature is calculated using equation (5.4) for each element.
- (b) Global stiffness matrix equation from flow conductance obtained using equation (B.9);
- (c) At each instant we have a boundary value problem with normal gradients specified along boundary. The pressure field equation (C.26), which is quasi-

linear in pressure  $P$  if the temperature is known, is solved iteratively as flow conductance  $S$  is dependent on  $\bar{u}, \bar{v}$  and also the temperature  $T$ . On the first iteration of the first time step, the Newtonian problem is solved. The resulting pressure distribution is used to calculate flow conductivity at each centroid of the element. These values are used to modify the stiffness matrix, and the equations can be solved again for an improved guess at the pressure distribution. The convergence of the solution is achieved using a relaxation scheme at each time step by the finite element method.

- (d) Subsequent to the convergence of pressure, the melt front is updated by calculating the flux at each frontal control volume.

This procedure is carried out until the cavity is completely filled.



# Appendix D

**Table D1.** Mean and standard deviation values of branched pillars, linear pillars and pristine PC in 10 repeated measurements using preload of 30 mN..

Test No.	Branched Pillars		Linear Pillars		Pristine PC	
	Mean (mN)	StdDev (mN)	Mean (mN)	StdDev (mN)	Mean (mN)	StdDev (mN)
1	21.98	2.64	22.83	3.65	15.64	1.88
2	38.67	5.03	27.30	4.10	16.47	1.81
3	49.81	7.97	36.28	4.72	18.77	2.44
4	63.70	8.92	42.89	6.00	19.40	2.13
5	79.90	9.59	44.54	5.34	21.80	3.05
6	98.22	15.72	49.73	10.94	22.40	2.91
7	113.25	19.25	55.99	10.64	25.00	3.75
8	135.62	20.34	59.98	10.20	27.50	3.30
9	152.76	19.86	62.25	9.96	27.20	2.99
10	157.60	25.22	66.92	14.05	29.80	4.77



# Appendix E

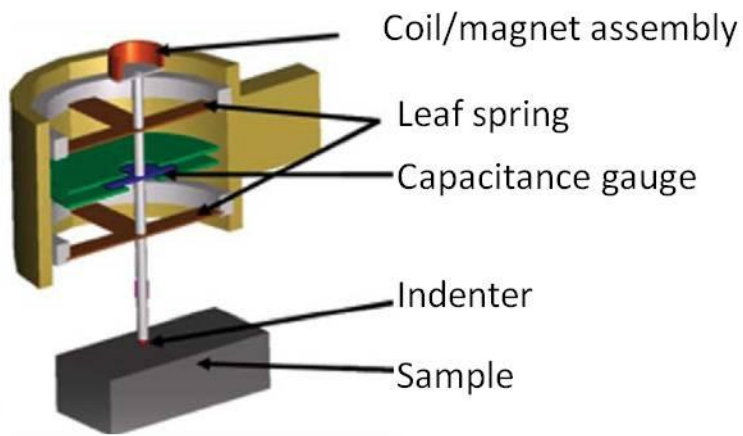


**Figure E1.** Schematic assembly of the indenter [219].

**Table E1.** Technical specifications of MTS Nano Indenter® XP for nano-indentation [232]

Displacement resolution	< 0.01 nm
Load resolution	50 nN
Total indenter travel	2 mm
Load application	Coil / magnet assembly
Displacement measurement	Capacitance gauge
Min. depth	15 nm
Max. depth	500 $\mu$ m
Min. load	0.1 $\mu$ N
Max. load	500 mN



**Table E2.** Technical specifications of MTS Nano Indenter® XP for scratch and tangential option [217]

Slide velocity	Max. 100 $\mu\text{ms}^{-1}$
Tangential displacement range	2 mm
Tangential displacement resolution	100 nm
Tangential load resolution	10 $\mu\text{N}$
Minimum measurable tangential load	10 $\mu\text{N}$

**Table E3.** Input parameters for the scratch test.

Slide Length	( $\mu\text{m}$ )	500
Surface Approach Velocity	(nm/s)	100
Slide Velocity	( $\mu\text{m/s}$ )	10
Slide Orientation (0 to scratch down)	(deg)	90
Allowable Drift Rate	(nm/s)	5
Profiling Acquisition Rate	(Hz)	5
Slide Acquisition Rate	(Hz)	5
Profiling Velocity	( $\mu\text{m/s}$ )	10

**Table E4.** Input parameters for the nano-indentation test.

Surface Approach Velocity	nm/s	10
Data Acquisition Rate	Hz	5
Allowable Drift Rate	nm/s	0.2
Peak Hold Time	s	20
Time To Load	s	30
Surface Approach Distance	nm	1000
Surface Approach Sensitivity	%	25

# List of Publications

## Journal Papers:

- 1) Ho, A.Y.Y., Gao, H., Lam, Y.C, Rodriguez, I. “Controlled Fabrication of Multi-Tiered Three-Dimensional Nanostructures in Porous Alumina”. *Adv. Funct. Mater.*, 2008, 18, 2057-2063.
- 2) Ho, A.Y.Y., Yeo, L.P., Lam, Y.C., Rodriguez, I. “Fabrication and Analysis of Gecko Inspired Hierarchical Polymer Nano-Setae”. *ACS Nano.*, 2011, 5 (3), 1897–1906.

## Conferences:

- 1) Ho, A.Y.Y., Yeo, L.P., Lam, Y.C., Rodriguez, I., “*Enhanced Shear Adhesion of Gecko Inspired Polymer Nano-Setae*”, 6<sup>th</sup> International Conference on Materials for Advanced Technologies (2011)  
[Oral, Jun-July 2011, Singapore]
- 2) Chen, X., Lam, Y.C., Ho, A.Y.Y., Yeo L.P., Rodriguez, I. and Yue C.Y., “*Flow Analysis of an Amorphous Polymer in Nanoimprinting*”, Singapore-MIT Alliance Annual Symposium (2011).  
[Poster, Jan 2011, Singapore]
- 3) Ho, A.Y.Y., Yeo, L.P., Lam, Y.C., Rodriguez, I., “*Fabrication and Analysis of Gecko Mimetic Adhesives*”, International Conference on Big Ideas in Molecular Materials (2011).  
[Poster, Jan 2011, Singapore]
- 4) Ho. A.Y.Y., Rodriguez, I., Lam, Y.C., “*Hierarchically Branched Gecko Tapes Imprinted using Porous Alumina Templates*”, 2<sup>nd</sup> Asian Symposium on Nano Imprint Lithography (ASNIL2009).  
[Oral, 07-08 Oct 2009, Taiwan]

- 5) Ho. A.Y.Y., Rodriguez, I., Lam, Y.C., “*Synthetic Nano-pillared Gecko Tapes Fabricated with Porous Alumina Templates with Tuned Geometrical Parameters*”, 4<sup>th</sup> International Conference on Materials for Advanced Technologies (2009)

[Oral, Jun-July 2009, Singapore]

- 6) Ho. A.Y.Y., Gao, H., Lam, Y.C., Rodriguez, I., “*Fabrication of Multi-Tiered Branched Three-Dimensional Nanoporous Alumina*”, Asian Conference on Nanoscience and Nanotechnology (AsiaNANO2008).

[Oral, 03-07 Nov 2008, Singapore]

- 7) Ho. A.Y.Y., Lam, Y.C., Ansari, K., Rodriguez, I., “*Mass Preparation of Long-Range-Ordered Nanoporous Anodic Alumina by Dynamic Nanoindentation*”, 4<sup>th</sup> International Conference on Materials for Advanced Technologies (ICMAT2007).

[Poster, Jun-July 2007, Singapore]

# References

1. Greiner, C., E. Arzt, and A. del Campo, *Hierarchical gecko-like adhesives*. Advanced Materials, 2009. **21**(4): p. 479-482.
2. Murphy, M.P., S. Kim, and M. Sitti, *Enhanced adhesion by gecko-inspired hierarchical fibrillar adhesives*. ACS Applied Materials & Interfaces, 2009. **1**(4): p. 849-855.
3. Jeong, H.E., et al., *Nanoengineered multiscale hierarchical structures with tailored wetting properties*. Langmuir, 2006. **22**(4): p. 1640-1645.
4. Jeong, H.E., et al., *High aspect-ratio polymer nanostructures by tailored capillarity and adhesive force*. Colloids and Surfaces A: Physicochemical and Engineering Aspects, 2008. **313-314**: p. 359-364.
5. Jeong, H.E., et al., *A nontransferring dry adhesive with hierarchical polymer nanohairs*. Proceedings of the National Academy of Sciences, 2009. **106**(14): p. 5639-5644.
6. Ge, L., et al., *Carbon nanotube-based synthetic gecko tapes* Proc. Natl. Acad. Sci. U.S.A., 2007. **104**: p. 10792.
7. *The friction product & materials market*, 2009, BCC Research: Market Research Report.
8. Gay, C. and L. Leibler, *Theory of tackiness*. Physical Review Letters, 1999. **82**(5): p. 936.
9. Silver, S.F., *Acrylate copolymer microspheres*, in *USPTO1970*: United States.
10. Dave, T. [cited 2012 February 02]; Available from: <http://www.thisisthat.com/faq/post-it.shtml>, Office Supplies Division of 3M.
11. Unver, O. and M. Sitti, *Flat Dry Elastomer Adhesives as Attachment Materials for Climbing Robots*. Robotics, IEEE Transactions on, 2010. **26**(1): p. 131-141.
12. Jeong, H.E., et al., *A nontransferring dry adhesive with hierarchical polymer nanohairs*. Proc. Natl Acad. Sci. USA, 2009. **106**(14): p. 5639-5644.
13. Sameoto, D. and C. Menon, *Direct molding of dry adhesives with anisotropic peel strength using an offset lift-off photoresist mold*. Journal of Micromechanics and Microengineering, 2009. **19**(11): p. 115026.

14. Autumn, K., *Properties, principles and parameters of the gecko adhesive system*. Biological Adhesives, ed. A. Smith and J. Callow 2006, Berlin Heidelberg: Springer-Verlag. 225-255.
15. Spolenak, R., S. Gorb, and E. Arzt, *Adhesion design maps for bio-inspired attachment systems*. Acta Biomaterialia, 2005. **1**(1): p. 5-13.
16. Arzt, E., S. Gorb, and R. Spolenak, *From micro to nano contacts in biological attachment devices*. Proceedings of the National Academy of Sciences of the United States of America, 2003. **100**(19): p. 10603-10606.
17. Stork, N.E., *Experimental analysis of adhesion of Chrysolina Polita (Chrysomelidae: Coleoptera) on a variety of surfaces*. J Exp Biol, 1980. **88**(1): p. 91-108.
18. Eisner, T. and J. Aneshansley, *Defense by foot adhesion in a beetle (Hemisphaerota cyanea)*. Proc. Natl Acad. Sci. USA, 2000. **91**(12): p. 6568-6573.
19. Gao, H.J., et al., *Mechanics of hierarchical adhesion structures of geckos*. Mechanics of Materials, 2005. **37**(2-3): p. 275-285.
20. Autumn, K., et al., *Adhesive force of a single gecko foot-hair*. Nature, 2000. **405**(6787): p. 681-685.
21. Duncan J. Irschick, et al., *A comparative analysis of clinging ability among pad-bearing lizards*. Biological Journal of the Linnean Society, 1996. **59**(1): p. 21-35.
22. Santos, D., et al., *Directional adhesion for climbing: theoretical and practical considerations*. Journal of Adhesion Science & Technology, 2007. **21**(12/13): p. 1317-1341.
23. Aksak, B., M.P. Murphy, and M. Sitti. *Gecko inspired micro-fibrillar adhesives for wall climbing robots on micro/nanoscale rough surfaces*. in *Robotics and Automation, 2008. ICRA 2008. IEEE International Conference on*. 2008.
24. Sangbae, K., et al., *Smooth vertical surface climbing with directional adhesion*. Robotics, IEEE Transactions on, 2008. **24**(1): p. 65-74.
25. Chik, H., *Nano-attach project*, in *iNEMI Technology Forum* May 15, 2007, International Electronics Manufacturing Initiative.
26. Yanik, M.F., *Towards gecko-feet-inspired bandages*. Trends in Biotechnology, 2009. **27**(1): p. 1-2.
27. Mahdavi, A., et al., *A biodegradable and biocompatible gecko-inspired tissue adhesive*. Proceedings of the National Academy of Sciences, 2008. **105**(7): p. 2307-2312.

28. Maderson, P.F.A., *Keratinized epidermal derivatives as an aid to climbing in Gekkonid lizards*. Nature, 1964. **203**(4946): p. 780-781.
29. Autumn, K., et al., *Evidence for van der Waals adhesion in gecko setae*. Proc. Natl Acad. Sci. USA, 2002. **99**: p. 12252-12256.
30. Huber, G., et al., *Evidence for capillarity contributions to gecko adhesion from single spatula nanomechanical measurements*. Proceedings of the National Academy of Sciences of the United States of America, 2005. **102**(45): p. 16293-16296.
31. Feiler, A.A., et al., *Effect of capillary condensation on friction force and adhesion*. Langmuir, 2007. **23**(2): p. 517-522.
32. Niewiarowski, P.H., et al., *Sticky gecko feet: The role of temperature and humidity*. PLoS ONE, 2008. **3**(5): p. e2192.
33. Aksak, B., M.P. Murphy, and M. Sitti, *Adhesion of biologically inspired vertical and angled polymer microfiber arrays*. Langmuir, 2007. **23**(6): p. 3322-3332.
34. Bhushan, B., *Adhesion of multi-level hierarchical attachment systems in gecko feet*. Journal of Adhesion Science & Technology, 2007. **21**(12/13): p. 1213-1258.
35. Russell, A.P., *Some comments concerning the interrelationships amongst gekkonine geckos*. Morphology and biology of reptiles, ed. A.d.A. Bellairs and C.B. Cox 1976, London: Academic Press.
36. Russell, A.P., *The foot of gekkonid lizards: A study in comparative and functional anatomy*, 1972, University of London.
37. Russell, A.P., *A contribution to the functional morphology of the foot of the tokay, Gekko gecko (Reptilia, Gekkonidae)*. Journal of Zoology London, 1975. **176**: p. 437-476.
38. Russell, A.P., *Parallelism and integrated design in the foot structure of gekkonine and diplodactyline geckos*. Copeia, 1979: p. 1-21.
39. Sitti, M. and R.S. Fearing, *Synthetic gecko foot-hair micro/nano-structures as dry adhesives*. Journal of Adhesion Science and Technology, 2003. **17**(8): p. 1055-1073.
40. Hansen, W.R. and K. Autumn, *Evidence for self-cleaning in gecko setae*. Proceedings of the National Academy of Sciences of the United States of America, 2005. **102**(2): p. 385-389.
41. Yoon, E.S., et al., *Tribological properties of bio-mimetic nano-patterned polymeric surfaces on silicon wafer*. Tribology Letters, 2006. **21**(1): p. 31-37.

42. Kim, S. and M. Sitti, *Biologically inspired polymer microfibers with spatulate tips as repeatable fibrillar adhesives*. Applied Physics Letters, 2006. **89**(26): p. 261911-3.
43. Crosby, A.J., M. Hageman, and A. Duncan, *Controlling polymer adhesion with "pancakes"*. Langmuir, 2005. **21**(25): p. 11738-11743.
44. Harfenist, S.A., et al., *Direct drawing of suspended filamentary micro- and nanostructures from liquid polymers*. Nano Letters, 2004. **4**(10): p. 1931-1937.
45. Jeong, H.E., et al., *Stretched polymer nanohairs by nanodrawing*. Nano Letters, 2006. **6**(7): p. 1508-1513.
46. Shan, J., et al. *Fabrication and adhesive force analysis of biomimetic gecko foot-hair array*. in *Nano/Micro Engineered and Molecular Systems, 2006. NEMS '06. 1st IEEE International Conference on*. 2006.
47. Geim, A.K., et al., *Microfabricated adhesive mimicking gecko foot-hair*. Nature Materials, 2003. **2**(7): p. 461-463.
48. Zhang, Y., et al., *Replica molding of high-aspect-ratio polymeric nanopillar arrays with high fidelity*. Langmuir, 2006. **22**: p. 8595-8601.
49. Cho, W.K. and I.S. Choi, *Fabrication of hairy polymeric films Inspired by geckos: wetting and high adhesion properties*. Advanced Functional Materials, 2008. **18**(7): p. 1089-1096.
50. Kustandi, T.S., et al., *Fabrication of a gecko-like hierarchical fibril array using a bonded porous alumina template*. Journal of Micromechanics and Microengineering, 2007. **17**(10): p. N75-N81.
51. Majidi, C., et al., *High friction from a stiff polymer using microfiber arrays*. Physical Review Letters, 2006. **97**(7): p. 076103-4.
52. Autumn, K., et al., *Dynamics of geckos running vertically*. J Exp Biol, 2006. **209**(2): p. 260-272.
53. Autumn, K., et al., *Frictional adhesion: a new angle on gecko attachment*. Journal of Experimental Biology, 2006. **209**(18): p. 3569-3579.
54. Marcellini, D., *Acoustic and visual display behavior of Gekkonid lizards*. Integrative and Comparative Biology 1977. **17**: p. 251-260.
55. Parsegian, V.A., *Van der Waals forces: A handbook for biologists, chemists, engineers and physicists* 2006, Cambridge and New York: Cambridge University Press.

56. Rodolfo Ruibal and V. Ernst, *The structure of the digital setae of lizards*. Journal of Morphology, 1965. **117**(3): p. 271-293.
57. Zhao, B., et al., *Adhesion and friction force coupling of gecko setal arrays: Implications for structured adhesive surfaces*. Langmuir, 2008. **24**(4): p. 1517-1524.
58. Schleich, H.H. and W. Kästle, *Ultrastrukturen an Gecko-Zehen (Reptilia: Sauria: Gekkonidae)*. Amphibia-Reptilia, 1986. **7**: p. 141-166.
59. Autumn, K. and A.M. Peattie, *Mechanisms of adhesion in geckos*. Integr. Comp. Biol., 2002. **42**(6): p. 1081-1090.
60. Person, B.N.J. and S. Gorb, *The effect of surface roughness on the adhesion of elastic plates with application to biological systems*. Journal of Chemical Physics, 2003. **119**(21): p. 11437.
61. Aranzazu del Campo, I. C. Greiner, and E. Arzt, *Contact shape controls adhesion of bioinspired fibrillar surfaces*. Langmuir, 2007. **23**: p. 10235.
62. Lee, H., B.P. Lee, and P.B. Messersmith, *A reversible wet/dry adhesive inspired by mussels and geckos*. Nature, 2007. **448**(7151): p. 338-341.
63. Bhushan, B. and R. Sayer, *Surface characterization and friction of a bio-inspired reversible adhesive tape*. Microsystem Technologies, 2007. **13**(1): p. 71-78.
64. Gorb, S., et al., *Biomimetic mushroom-shaped fibrillar adhesive microstructure*. J. R. Soc. Interface, 2007. **4**: p. 271.
65. Lu, G., et al., *Drying enhanced adhesion of polythiophene nanotubule arrays on smooth surfaces*. ACS Nano, 2008. **2**(11): p. 2342-2348.
66. Kustandi, T.S., et al., *Self-assembled nanoparticles based fabrication of gecko foot-hair-inspired polymer nanofibers*. Advanced Functional Materials, 2007. **17**(13): p. 2211-2218.
67. Majidi, C., R. Groff, and R. Fearing. *Clumping and packing of hair arrays manufactured by nanocasting*. in *2004 ASME International Mechanical Engineering Congress & Exposition*. November 13-19, 2004. Anaheim, California, USA.
68. Qu, L., et al., *Carbon Nanotube Arrays with Strong Shear Binding-On and Easy Normal Lifting-Off*. Science, 2008. **322**(5899): p. 238-242.
69. Yurdumakan, B., et al., *Synthetic gecko foot-hairs from multiwalled carbon nanotubes*. Chemical Communications, 2005(30): p. 3799-3801.



70. Zhao, Y., et al., *Interfacial energy and strength of multiwalled-carbon-nanotube-based dry adhesive*. Journal of Vacuum Science & Technology B: Microelectronics and Nanometer Structures, 2006. **24**(1): p. 331-335.
71. Qu, L. and L. Dai, *Gecko-foot-mimetic aligned single-walled carbon nanotube dry adhesives with unique electrical and thermal properties*. Advanced Materials, 2007. **19**(22): p. 3844-3849.
72. Zumwalde, R.a. and L. Hodson, *Approaches to Safe Nanotechnology: Managing the Health and Safety Concerns Associated with Engineered Nanomaterials*. National Institute for Occupational Safety and Health. NIOSH (DHHS) March 2009. **Publication 2009-125**.
73. Lam, C., et al., *A review of carbon nanotube toxicity and assessment of potential occupational and environmental health risks*. Crit Rev Toxicol, 2006. **36**(3): p. 189-217.
74. Poland, C., et al., *Carbon nanotubes introduced into the abdominal cavity of mice show asbestos-like pathogenicity in a pilot study*. Nature Nanotechnology 2008. **3** (7): p. 423.
75. Northen, M.T. and K.L. Turner, *A batch fabricated biomimetic dry adhesive*. Nanotechnology, 2005. **16**(8): p. 1159-1166.
76. Aksak, B., et al., *Friction of partially embedded vertically aligned carbon nanofibers inside elastomers*. Applied Physics Letters, 2007. **91**(6): p. 061906.
77. Northen, M.T. and K.L. Turner, *Batch fabrication and characterization of nanostructures for enhanced adhesion*. Current Applied Physics, 2006. **6**(3): p. 379-383.
78. Yao, H., et al., *Adhesion and sliding response of a biologically inspired fibrillar surface: experimental observations*. Journal of the Royal Society Interface, 2008. **5**(24): p. 723-733.
79. Kim, T.W. and B. Bhushan, *Adhesion analysis of multi-level hierarchical attachment system contacting with a rough surface*. Journal of Adhesion Science & Technology, 2007. **21**(1): p. 1-20.
80. Kim, T.W. and B. Bhushan, *Effect of stiffness of multi-level hierarchical attachment system on adhesion enhancement*. Ultramicroscopy, 2007. **107**: p. 902.
81. Northen, M.T. and K.L. Turner, *Meso-scale adhesion testing of integrated micro- and nano-scale structures*. Sensors and Actuators a-Physical, 2006. **130**: p. 583-587.

82. Lee, J., et al., *Sliding-induced adhesion of stiff polymer microfibre arrays. I. Macroscale behaviour*. Journal of the Royal Society Interface, 2008. **5**(5): p. 835.
83. Aránzazu del Campo and E. Arzt, *Design parameters and current fabrication approaches for developing bioinspired dry adhesives*. Macromolecular Bioscience, 2007. **7**(2): p. 118-127.
84. Greiner, C., A. delCampo, and E. Arzt, *Adhesion of bioinspired micropatterned surfaces: Effects of pillar radius, aspect ratio, and preload*. Langmuir, 2007. **23**(7): p. 3495-3502.
85. delCampo, A., C. Greiner, and E. Arzt, *Contact Shape Controls Adhesion of Bioinspired Fibrillar Surfaces*. Langmuir, 2007.
86. Lake, G.J. and A.G. Thomas, *Strength of highly elastic materials*. Proc. R. Soc. London, Ser A, 1967. **300**(1460): p. 108-119.
87. Hertz, H., *Über die Berührung fester elastischer Körper*. J. Reine Angew. Math., 1882. **92**: p. 156-171.
88. Glassmaker, N.J., et al., *Design of biomimetic fibrillar interfaces: 1. Making contact*. Journal of The Royal Society Interface, 2004. **1**(1): p. 23-33.
89. Aranzazu del Campo, I. C. Greiner, and Á.E. Arzt, *Patterned surfaces with pillars with controlled 3D tip geometry mimicking bioattachment devices*. Advanced Materials, 2007. **19**(15): p. 1973-1977.
90. *Special Report Technology Review, 10 Emerging Technologies That Will Change the World*. Technology Review, <http://www.technologyreview.com/article/13060/>, 2003. **106**: p. 36.
91. *International Technology Roadmap for Semiconductors*. <http://public.itrs.net/>.
92. Chou, S.Y., et al., *Sub-10 nm imprint lithography and applications*. Journal of Vacuum Science & Technology B: Microelectronics and Nanometer Structures, 1997. **15**: p. 2897-2904.
93. Roetting, O., et al. *Production of movable metallic microstructures by aligned hot embossing and reactive ion etching*. 1999. Paris, France: SPIE.
94. Becker, H. and W. Dietz, *Microfluidic devices for  $\mu$ -TAS applications fabricated by polymer hot embossing*. Proc. SPIE, 1998. **3515**: p. 177-182.
95. Casey, B.G., et al., *Nanoscale embossing of polymers using a thermoplastic die*. Microelectronic Engineering, 1999. **46**(1-4): p. 125-128.

96. Gale, M.T., *Replication techniques for diffractive optical elements*. Microelectronic Engineering, 1997. **34**(3-4): p. 321-339.
97. Kustandi, T.S., et al., *Wafer-Scale Near-Perfect Ordered Porous Alumina on Substrates by Step and Flash Imprint Lithography*. ACS Nano, 2010. **4**(5): p. 2561-2568.
98. Krishnan, R. and C.V. Thompson, *Monodomain high-aspect-ratio 2D and 3D ordered porous alumina structures with independently controlled pore spacing and diameter*. Advanced Materials, 2007. **19**(7): p. 988-992.
99. Lee, J.S., et al., *Growth of carbon nanotubes on anodic aluminum oxide templates: Fabrication of a tube-in-tube and linearly joined tube*. Chemistry of Materials, 2001. **13**(7): p. 2387-2391.
100. Im, W.S., et al., *Stepped carbon nanotubes synthesized in anodic aluminum oxide templates*. Diamond and Related Materials, 2004. **13**(4-8): p. 1214-1217.
101. Masuda, H. and K. Fukuda, *Ordered metal nanohole arrays made by a 2-step replication of honeycomb structures of anodic alumina*. Science, 1995. **268**(5216): p. 1466-1468.
102. Shingubara, S., *Fabrication of nanomaterials using porous alumina templates*. Journal of Nanoparticle Research, 2003. **5**: p. 17-30.
103. Li, A.P., et al., *Hexagonal pore arrays with a 50-420 nm interpore distance formed by self-organization in anodic alumina*. Journal of Applied Physics, 1998. **84**(11): p. 6023-6026.
104. Masuda, H., F. Hasegawa, and S. Ono, *Self-ordering of cell arrangement of anodic porous alumina formed in sulfuric acid solution*. Journal of the Electrochemical Society, 1997. **144**(5): p. L127-L130.
105. Shingubara, S., et al., *Self-organization of a porous alumina nanohole array using a sulfuric/oxalic acid mixture as electrolyte*. Electrochemical and Solid State Letters, 2004. **7**(3): p. E15-E17.
106. Asoh, H., et al., *Fabrication of ideally ordered anodic porous alumina with 63 nm hole periodicity using sulfuric acid*. Journal of Vacuum Science & Technology B, 2001. **19**(2): p. 569-572.
107. Masuda, H., K. Yada, and A. Osaka, *Self-ordering of cell configuration of anodic porous alumina with large-size pores in phosphoric acid solution*. Japanese Journal of Applied Physics Part 2-Letters, 1998. **37**(11A): p. L1340-L1342.

108. Masuda, H., et al., *Lasing from two-dimensional photonic crystals using anodic porous alumina*. Advanced Materials, 2006. **18**(2): p. 213-+.
109. Choi, J., et al., *Perfect two-dimensional porous alumina photonic crystals with duplex oxide layers*. Journal of Applied Physics, 2003. **94**(8): p. 4757-4762.
110. Granqvist, C.G.G., A. Anderson, and O. Hunderi, *Spectrally selective surface of Ni-pigmented anodic Al<sub>2</sub>O<sub>3</sub>*. Applied Physics Letters, 1979. **35**: p. 268.
111. Goad, D.G.W. and M. Moskovits, *Colloidal metal in aluminum-oxide*. Journal of Applied Physics, 1978. **49**: p. 2929.
112. Saito, M., et al., *Mircropolarizer made of the anodized alumina film*. Applied Physics Letters, 1989. **55**: p. 607.
113. Tierney, M.J. and C.R. Martin, *Transparent metal microstructures*. Journal of Physics and Chemistry, 1989. **93**: p. 2878.
114. Masuda, H., et al., *Photonic band gap in naturally occurring ordered anodic porous alumina*. Japanese Journal of Applied Physics Part 2-Letters, 2001. **40**(11B): p. L1217-L1219.
115. Oshima, H., et al., *Improvement of magnetic recording characteristics by narrowing the array pitch of nanohole patterned media*. Japanese Journal of Applied Physics Part 2-Letters & Express Letters, 2005. **44**(42-45): p. L1355-L1357.
116. Yasui, K., et al., *Patterned magnetic recording media using anodic porous alumina with single domain hole configurations of 63 nm hole interval*. Japanese Journal of Applied Physics Part 2-Letters & Express Letters, 2005. **44**(12-15): p. L469-L471.
117. Vlassiouk, I., et al., *"Direct" detection and separation of DNA using nanoporous alumina filters*. Langmuir, 2004. **20**(23): p. 9913-9915.
118. Matsumoto, F., K. Nishio, and H. Masuda, *Flow-through-type DNA array based on ideally ordered anodic porous alumina substrate*. Advanced Materials, 2004. **16**(23-24): p. 2105-+.
119. Matsumoto, F., et al., *Highly ordered nanopatterning of DNA with 40 nm diameter using anodic porous alumina substrate*. Japanese Journal of Applied Physics Part 2-Letters & Express Letters, 2005. **44**(8-11): p. L355-L358.
120. Matsumoto, F., et al., *Ideally ordered, high-density patterning of DNA on Au disk array fabricated using anodic porous alumina*. Japanese Journal of Applied Physics Part 2-Letters & Express Letters, 2004. **43**(5A): p. L640-L643.

121. Matsumoto, F., et al., *Nanometer-scale patterning of DNA in controlled intervals on a gold-disk array fabricated using ideally ordered anodic porous alumina*. Advanced Materials, 2005. **17**(13): p. 1609-+.
122. Yang, S.Y., et al., *Nanoporous membranes with ultrahigh selectivity and flux for the filtration of viruses*. Advanced Materials, 2006. **18**(6): p. 709-+.
123. Kukhta, A.V., et al., *Nanostructured alumina as a cathode of organic light-emitting devices*. Surface Science, 2002. **507**: p. 593-597.
124. Nahar, R.K. and V.K. Khanna, *Ionic doping and inversion of the characteristic of thin film porous Al<sub>2</sub>O<sub>3</sub> humidity sensor*. Sensors and Actuators B-Chemical, 1998. **46**(1): p. 35-41.
125. Sberveglieri, G., R. Murri, and N. Pinto, *Characterization of porous Al<sub>2</sub>O<sub>3</sub> SiO<sub>2</sub>/Si sensor for low and medium humidity ranges*. Sensors and Actuators B-Chemical, 1995. **23**(2-3): p. 177-180.
126. Furneaux, R.C., W.R. Righy, and D. A.P, *The formation of controlled-porosity membranes from anodically oxidized aluminum*. Nature Materials, 1989. **337**: p. 147.
127. Dalvie, S.K. and R.E. Baltus, *Transport studies with porous alumina membranes*. Journal of Membrane Science, 1992. **71**: p. 247.
128. Alwitt, R.S., *Electrochemistry Encyclopedia*, in *Anodizing2002*, Boundary Technologies, Inc.
129. Jessensky, O., F. Muller, and U. Gosele, *Self-organized formation of hexagonal pore structures in anodic alumina*. J. Electrochem. Soc., , 1998. **145**(11): p. 3735.
130. Hoar, T.P. and N.F. Mott, *A mechanism for the formation of porous anodic oxide films on aluminum*. Journal of Physical Chemistry Solids, 1959. **9**: p. 97.
131. Uchi, H., T. Kanno, and R.S. Alwitt, *Structural features of crystalline anodic alumina films*. J. Electrochem. Soc., 2001. **148**(1): p. B17.
132. Montgomery, D.C., *Design and Analysis of Experiments*. 5th Edition ed2001, Arizona State University, USA: John Wiley & Sons, Inc.
133. Fisher, R.A., *Statistical methods for research workers* 1925, Edinburgh: Oliver and Boyd.
134. Lehmann, E.L. and J.P. Romano, *Testing statistical hypothesis* 1997, New York, U.S.A: Springer.

135. Olver, F.W.J., et al., *NIST Handbook of Mathematical Functions* 2010, New York, U.S.A: Cambridge University Press.
136. O'Sullivan, J.P. and G.C. Wood, *Morphology and mechanism of formation of porous anodic films on aluminium*. Proceedings of the Royal Society of London Series A - Mathematical and Physical Sciences, 1970. **317**: p. 511-543.
137. Jessensky, O., F. Muller, and U. Gosele, *Self-organized formation of hexagonal pore arrays in anodic alumina*. Applied Physics Letters, 1998. **72**(10): p. 1173-1175.
138. Morton, K., et al., *The anti-lotus leaf effect in nanohydrodynamic bump arrays*. New Journal of Physics, 2010. **12**: p. 085008.
139. H, S., *Chemistry and physics of polycarbonates* 1964, New York, U.S.A: Interscience.
140. Christopher, W.F. and D.W. Fox, *Polycarbonates* 1962, New York, U.S.A: Reinhold.
141. Legrand, D.G. and J.T. Bendler, *Handbook of polycarbonate science and technology* 2000, New York, U.S.A: Marcel Dekker, Inc.
142. Anders, S., et al., *Engineering thermoplastics: Polycarbonates, polyacetals, polyesters, cellulose esters*, ed. L. Bottenbruch 1996, Munchen, Germany: Hanser Publishers.
143. Wu, K.J. and R.W. Odom, *Characterizing synthetic polymers by MALDI MS*. Analytical Chemistry, 1998. **70**: p. 456A-461A.
144. Waters 2690 Separations Module: Quick start guide. 28th Jan 2011 [cited 2011 28th Jan ]; Available from: <https://www.waters.com/webassets/cms/support/docs/2690qsg.pdf>.
145. Kaigala, G.V., et al., *Rapid prototyping of microfluidic devices with a wax printer*, . Lab on a Chip, 2007. **7**(3): p. 384-387.
146. Abiad, M.G., O.H. Campanella, and M.T. Carvajal, *Assessment of thermal transitions by dynamic mechanical analysis (DMA) using a novel disposable powder holder*. Pharmaceutics, 2010. **2**: p. 78-90.
147. Taylor, H., et al., *Computationally efficient modelling of pattern dependencies in the micro-embossing of thermoplastic polymers*. Microelectronic Engineering, 2009. **85**(5-6): p. 1453-1456.

148. Ferry, J.D., *Viscoelastic properties of polymers* 1960, New York, U.S.A: John Wiley and Sons, Inc.
149. Williams, M.L., R.F. Landel, and J.D. Ferry, *The Temperature Dependence of Relaxation Mechanisms in Amorphous Polymers and Other Glass-forming Liquids*. Journal of the American Chemical Society, 1955. **77**(14): p. 3701-3707.
150. Brinson, H.F. and L.C. Brinson, *Polymer engineering science and viscoelasticity: An Introduction* 2008, New York, U.S.A: Springer.
151. Gottschalch, F., et al., *Polymer issues in nanoimprinting technique*. Solid-State Electronics, 1999. **43**(6): p. 1079-1083.
152. Heyderman, L.J., et al., *Flow behaviour of thin polymer films used for hot embossing lithography*. Microelectronic Engineering, 2000. **54**(3-4): p. 229-245.
153. Scheer, H.-C., et al., *Recovery prevention via pressure control in thermal nanoimprint lithography*. Journal of Vacuum Science & Technology B: Microelectronics and Nanometer Structures, 2009. **27**(6): p. 2882-2887.
154. Chang, J.H. and S.Y. Yang, *Gas pressurized hot embossing for transcription of micro-features*. Microsystem Technologies, 2003. **10**(1): p. 76-80.
155. Hung, C., R.H. Chen, and C.R. Lin, *The Characterisation and Finite-Element Analysis of a Polymer under Hot Pressing*. The International Journal of Advanced Manufacturing Technology, 2002. **20**(3): p. 230-235.
156. Scheer, H.C. and H. Schulz, *A contribution to the flow behaviour of thin polymer films during hot embossing lithography*. Microelectronic Engineering, 2001. **56**(3-4): p. 311-332.
157. Scheer, H.C., et al., *Problems of the nanoimprinting technique for nanometer scale pattern definition*. Journal of Vacuum Science & Technology B: Microelectronics and Nanometer Structures, 1998. **16**: p. 3917-3921.
158. Gourgon, C., et al., *Influence of pattern density in nanoimprint lithography*. Journal of Vacuum Science & Technology B: Microelectronics and Nanometer Structures, 2003. **21**(1): p. 98-105.
159. Hirai, Y., et al., *Study of the resist deformation in nanoimprint lithography*. Journal of Vacuum Science & Technology B: Microelectronics and Nanometer Structures, 2001. **19**: p. 2811-2815.
160. Hirai, Y., et al. *Time dependent analysis of the resist deformation in thermal nanoimprint*. 2007. AVS.

161. Young, W.-B., *Analysis of the nanoimprint lithography with a viscous model*. Microelectronic Engineering, 2005. **77**(3-4): p. 405-411.
162. Juang, Y.J., L.J. Lee, and K.W. Koelling, *Hot embossing in microfabrication. Part II: Rheological characterization and process analysis*. Polymer Engineering & Science, 2002. **42**(3): p. 551-566.
163. Yao, D., V.L. Virupaksha, and B. Kim, *Study on squeezing flow during nonisothermal embossing of polymer microstructures*. Polymer Engineering & Science, 2005. **45**(5): p. 652-660.
164. Takagi, H., et al., *Analysis of time dependent polymer deformation based on a viscoelastic model in thermal imprint process*. Microelectronic Engineering, 2008. **85**(5-6): p. 902-906.
165. Lin, C.-R., R.-H. Chen, and C. Hung, *The characterisation and finite-element analysis of a polymer under hot pressing*. The International Journal of Advanced Manufacturing Technology, 2002. **20**(3): p. 230-235.
166. Eriksson, T. and H.K. Rasmussen, *The effects of polymer melt rheology on the replication of surface microstructures in isothermal moulding*. Journal of Non-Newtonian Fluid Mechanics, 2005. **127**(2-3): p. 191-200.
167. Guo, Y. and et al., *Study of the demolding process—implications for thermal stress, adhesion and friction control*. Journal of Micromechanics and Microengineering, 2007. **17**(1): p. 9.
168. Bird, R.B., R.C. Armstrong, and O. Hassager, *Dynamics of polymeric liquids* 1987, United States of America: John Wiley & Sons, Inc.
169. Hieber, C.A. and S.F. Shen, *A finite-element/finite difference simulation of the injection-molding filling process*. Journal of Non-Newtonian Fluid Mechanics, 1980. **7**: p. 1-32.
170. Macosko, C.W., *Rheology: Principles, measurements, and applications* 1994, United States of America: Wiley-VCH.
171. Kim, D.S., et al., *Micro-channel filling flow considering surface tension effect*. Journal of Micromechanics and Microengineering, 2002. **12**(3): p. 236.
172. Duarte, A.A., D.E. Strier, and D.H. Zanette, *The rise of a liquid in a capillary tube revisited: A hydrodynamical approach*. American Journal of Physics, 1996. **64**(4): p. 413-418.
173. Kennedy P, *Flow Analysis of Injection Molds* 1995, New York: Haser publishers.



174. Lam, Y., et al., *Simulation of particle migration of powder-resin system in injection molding* Journal of Manufacturing Science and Engineering - Transactions of the ASME, 2003. **125**(3): p. 538-547.
175. Piau, J.M. and J.F. Agassant, *Rheology for polymer melt processing* 1996, Amsterdam: Elsevier.
176. Jaszewski, R.W., et al., *Hot embossing in polymers as a direct way to pattern resist*. Microelectronic Engineering, 1998. **41-42**: p. 575-578.
177. K. Y. Suh, Y. S. Kim, and H. H. Lee, *Capillary force lithography*. Advanced Materials, 2001. **13**(18): p. 1386-1389.
178. Ho, A.Y.Y., et al., *Controlled fabrication of multi-tiered three-dimensional nanostructures in porous alumina*. Advanced Functional Materials, 2008. **18**(14): p. 2057-2063.
179. Keller, F., M.S.A. Hunter, and D.L. Robinson, *Structural Features of Oxide Coatings on Aluminum*. Journal of the Electrochemical Society, 1953. **100**(9): p. 411-419.
180. Brostow, W., H.E. Hagg Lobland, and M. Narkis, *Sliding wear, viscoelasticity, and brittleness of polymers*. Journal of Materials Research, 2006. **21**(09): p. 2422-2428.
181. Wilkes, C.E., J.W. Summers, and C.A. Daniels, *PVC handbook* 2005, Munich, Germany: Hanser Gardner Publications, Inc.
182. Youn Sang, K. and et al., *High density nanostructure transfer in soft molding using polyurethane acrylate molds and polyelectrolyte multilayers*. Nanotechnology, 2003. **14**(10): p. 1140.
183. Martin, C., L. Ressler, and J.P. Peyrade, *Study of PMMA recoveries on micrometric patterns replicated by nano-imprint lithography*. Physica E: Low-dimensional Systems and Nanostructures, 2003. **17**: p. 523-525.
184. *CRC Materials Science and Engineering Handbook*, , page 509.
185. Callister, W.D., *Materials science and engineering: An introduction (7th Edition)* 2007, New York, PA: John Wiley & Sons, Inc.
186. Auerkari, P., *Mechanical and physical properties of engineering alumina ceramics*, in *Research Notes 1792* 1996, VTT Manufacturing Technology, Technical Research Centre of Finland: Research Notes 1792.
187. 16th July 2011]; Available from: <http://www.edl-inc.com/Plastic%20expansion%20rates.htm>.

188. Garica-Vergara, S.J., et al., *Stress generated porosity in anodic alumina formed in sulphuric acid electrolyte*. Corrosion Science, 2007. **49**: p. 3772-3782.
189. Mahendra, B.C., *Contributions to the bionomics, anatomy, reproduction and development of the Indian house gecko Hemidactylus flaviviridis Ruppell. Part II. The problem of locomotion*. Proceedings of the Indian Academy of Sciences B, 1941: p. 288-306.
190. Dellit, W.-D., *Zur anatomie und physiologie der Geckozehe*. Jena. Z. Naturw., 1934. **68**: p. 613-656.
191. Sun, W.X., et al., *The nature of the gecko lizard adhesive force*. Biophysical Journal, 2005. **89**(2): p. L14-L17.
192. Hiller, U., *Untersuchungen zum feinbau und zur funktion der Haftborsten von Reptilien*. Z. Morph. Tiere. , 1968. **62**: p. 307-362.
193. Hiller, U., *Form und funktion der hausinnesorgane bei gekkoniden*. Form. Funct., 1971. **4**: p. 240-253.
194. Nosonovsky, M. and B. Bhushan, *Multiscale friction mechanisms and hierarchical surfaces in nano- and bio-tribology*. Materials Science and Engineering: R: Reports, 2007. **58**(3-5): p. 162-193.
195. Bowden, F.P. and D. Tabor, *Friction and lubrication (revised edition)*1967, London, Methuen.
196. Gao, J., et al., *Frictional Forces and Amontons' Law: From the Molecular to the Macroscopic Scale*. The Journal of Physical Chemistry B, 2004. **108**(11): p. 3410-3425.
197. Yamaguchi, T., et al., *Microscopic Modeling of the Dynamics of Frictional Adhesion in the Gecko Attachment System†*. The Journal of Physical Chemistry B, 2008. **113**(12): p. 3622-3628.
198. Bhushan, B., *Modern Tribology Handbook*2001, Boca Raton, FL: CRC Press.
199. Berman, A., C. Drummond, and J.N. Israelachivili, *Amonton's law at the molecular level*. Tribology Letters, 1998. **4**: p. 95-101.
200. Zeng, H., et al., *Frictional adhesion of patterned surfaces and implications for gecko and biomimetic systems*. Langmuir, 2009. **25**(13): p. 7486.
201. Homola, A.M., et al., *Fundamental experimental studies in tribology: The transition from "interfacial" friction of undamaged molecularly smooth surfaces to "normal" friction with wear*. Wear, 1990. **136**: p. 65.

202. Mate, C.M., et al., *Atomic-scale friction of a tungsten tip on a graphite surface*. Physical Review Letters, 1987. **59**(17): p. 1942.
203. So/rensen, M.R., K.W. Jacobsen, and P. Stoltze, *Simulations of atomic-scale sliding friction*. Physical Review B, 1996. **53**(4): p. 2101.
204. Peressadko, A. and S.N. Gorb, *When less is more: Experimental evidence for tenacity enhancement by division of contact area*. Journal of Adhesion, 2004. **80**(4): p. 247-261.
205. Majidi, C.S., R.E. Groff, and R.S. Fearing, *Attachment of fiber array adhesive through side contact*. Journal of Applied Physics, 2005. **98**(10): p. 103521-5.
206. Gere, J.M. and S.P. Timoshenko, 1997, , *Mechanics of Materials* 1997, Toronto, Canada: Cengage Learning.
207. Chen, B., P.D. Wu, and H. Gao, *Hierarchical modelling of attachment and detachment mechanisms of gecko toe adhesion*. Proceedings of the Royal Society of London - A, 2008. **464**(2094): p. 1639
208. Autumn, K. and W. Hansen, *Ultrahydrophobicity indicates a nonadhesive default state in gecko setae*. Journal of Comparative Physiology A-Sensory Neural & Behavioral Physiology, 2006.
209. Blau, P.J., *Scale Effects in Steady-State Friction*. Tribology Transactions, 1991. **34**(3): p. 335 - 342.
210. Niederberger, S. and D.H. Gracias, *Transitions from nanoscale to microscale dynamic friction mechanisms on polyethylene and silicon surfaces*. Journal of Applied Physics, 2000. **87**(6): p. 3143.
211. Adams, G.G., S. Muftu, and N.M. Azhar, *A Scale-Dependent Model for Multi-Asperity Contact and Friction*. Journal of Tribology, 2003. **125**(4): p. 700-708.
212. Wenning, L. and M.H. Muser, *Friction laws for elastic nanoscale contacts*. Europhysics Letters, 2001. **54**(5): p. 693-699.
213. Bowden, F.P. and D. Tabor, *The Area of Contact between Stationary and between Moving Surfaces*. Proceedings of the Royal Society of London. Series A. Mathematical and Physical Sciences, 1939. **169**(938): p. 391-413.
214. Israelachvili, J.N., Surf. Sci. Rep., 1992. **14**: p. 109.
215. Schubert, B., et al., *Sliding-induced adhesion of stiff polymer microfibre arrays. II. Microscale behavior*. Journal of the Royal Society Interface, 2008. **5**(25): p. 845-853

216. L. Qu, L.D., *Gecko-foot-mimetic aligned single-walled carbon nanotube dry adhesives with unique electrical and thermal properties*. Advanced Materials, 2007. **19**(22): p. 3844-3849.
217. Bhushan, B. and X. Li, *Nanomechanical characterisation of solid surfaces and thin films*. International Materials Reviews, 2003. **48**: p. 125-164.
218. Choi, S.T., S.J. Jeong, and Y.Y. Earmme, *Modified-creep experiment of an elastomer film on a rigid substrate using nanoindentation with a flat-ended cylindrical tip*. Scripta Materialia, 2008. **58**(3): p. 199-202.
219. *Nanoindentation, scratch, and elevated temperature testing of cellulose and PMMA films*, <http://cp.literature.agilent.com/litweb/pdf/5990-5761EN.pdf>, Agilent Technologies: Application Note.
220. Shooter, K.V. and D. Tabor, *The Frictional Properties of Plastics*. Proceedings of the Physical Society. Section B, 1952. **65**(9): p. 661-671.
221. Gralen, N., *Friction between Single Fibres*. Proceedings of the Royal Society of London. Series A, Mathematical and Physical Sciences, 1952. **212**(1111): p. 491-495.
222. Muser, M.H., L. Wenning, and M.O. Robbins, *Simple microscopic theory of Amontons's laws for static friction*. Physical Review Letters, 2001. **86**(7): p. 1295.
223. Schubert, B., et al., *Sliding-induced adhesion of stiff polymer microfibre arrays. II. Microscale behaviour*. Journal of the Royal Society Interface, 2008. **5**: p. 845-853.
224. Khrushchov, M.M. and E.S. Berkovich, *Methods of determining the hardness of very hard materials: The hardness of diamond*. Industrial Diamond Review, 1951. **11**: p. 42-49.
225. *The MFP instrumented nanoindenter*.
226. Doerner, M.F. and W.D. Nix, *A method for interpreting the data from depth-sensing indentation instruments*. Journal of Materials Research, 1986. **1**(4): p. 601-609.
227. Hay, J., M.R. Maschmann, and J. Baur. *Mechanical testing of carbon nanotube arrays*. 2010 12th July 2011]; Application Note]. Available from: <http://cp.literature.agilent.com/litweb/pdf/5990-5834EN.pdf>.
228. Oliver, W.C. and G.M. Pharr, *An improved technique for determining hardness and elastic modulus using load and displacement sensing indentation experiments*. Journal of Materials Research, 1992. **7**: p. 1564-1583.

- 229. Kang, M.K., et al., *Buckling of single-crystal silicon nanolines under indentation*. Journal of Nanomaterials, 2007. **2008**: p. 132728.
- 230. Chudoba, T. and F. Richter, *Investigation of creep behaviour under load during indentation experiments and its influence on hardness and modulus results*. Surface and Coatings Technology, 2001. **148**(2-3): p. 191-198.
- 231. Striegel, A.M., et al., *Modern size-exclusion liquid chromatography: Practice of gel permeation and gel filtration chromatography, 2nd Edition*2009, Hoboken, New Jersey, U.S.A: John Wiley & Sons, Inc.
- 232. *The Nano Indenter XP<sup>(R)</sup> User's Manual, Ver. 16*, in *MTS Systems Corporation*2002.